THE UNIVERSITY *of* EDINBURGH

The Response to Fire of Pressure Vessels for the Storage and Transportation of Hazardous Materials

Ian Bradley

Doctoral Thesis

The University of Edinburgh

November 2018

ACKNOWLEDGEMENTS

Top line, for making this project possible:

Prof. A M Birk, Prof. F Otremba, Prof. L Bisby

Second line, for the significant assistance they provided throughout:

Dr. S Welch, J Borch, T Hilse

Third line, for their generous financial support of the project:

EPSRC, Akzonobel (R Wade), Promat (K Both)

Fourth line, for their assistance:

G Scarponi, J Crawford, T Iannaccone, C Sklorz, L'Ecole des Mines d'Alès

Dedication: to Joy, for caring for our three little kids throughout every hour spent on this project

DECLARATION

I declare that this thesis has been composed solely by myself and that it has not been submitted, in whole or in part, in any previous application for a degree. Except where stated otherwise by reference or acknowledgment, the work presented is entirely my own.

Ian Bradley

16.11.2018

ABSTRACT

Pressure vessels present a serious hazard when exposed to fires. Boiling liquid expanding vapour explosions (BLEVEs) and other associated vessel failure events are known to have significant consequences, and be key propagators of industrial accident scenarios. Understanding the response of pressure vessels to fire, and especially the rate of pressurisation, remains a significant challenge. This study reviews the ability of existing models to capture the physical processes that drive vessel pressurisation, and the existing fire test evidence used to validate such models. The scope of existing test evidence is found to be inadequate to validate complex numerical models. This study defines and describes a set of test conditions and a novel piece of experimental apparatus that can provide detailed and reproducible test evidence in an economic manner for the purpose of numerical model validation. The equipment included a 2.6 m^3 vessel with a full cross-section (Ø1 m) glass window. A pressure compensation system maintained the window integrity, allowing combined temperature and velocity field measurements, using thermocouples and particle imaging velocimetry (PIV), to be made during fire exposure. Initial studies using ANSYS CFX indicate that the Eulerian-Eulerian multiphase model and the RPI wall boiling model are capable, when used together, of providing a good basis for simulation of the pressurisation rate, given the use of appropriate bubble-related parameters obtained by experiment.

LAY SUMMARY

Hazardous liquids and gases are often stored and transported in steel tanks capable of reaching high internal pressures at ambient temperature. In the event of a fire in the vicinity of a tank, the pressure within rises while the tank simultaneously weakens, potentially resulting in a severe explosion with serious consequences. Understanding how the pressure in tanks increases during fire exposure, and the rate of the increase, is key to understanding whether serious accidents will occur, with the aim of preventing them and raising safety levels.

Computer modelling of the pressure rise in tanks during fire remains a challenge, partly due to the limited range of experiments against which such models can be validated. This thesis describes the design and commissioning of a novel piece of equipment that gives an insight into what happens inside a tank during fire exposure. A series of tests were undertaken, and the results described, for the purpose of future computer model development and validation. Following a review of existing advanced computer models, a particular type of model was identified as having potential for future development. One such model was set-up to recreate experimental work undertaken as part of this project and the results provided numerous recommendations for further experimental and computer modelling work.

CONTENTS

LIST OF FIGURES

ABBREVIATIONS, SYMBOLS AND NOMENCLATURE

Symbols

q	heat flux
α	thermal diffusivity
ρ	density
c_p	specific heat capacity
ν	kinematic viscosity
μ	dynamic viscosity
h_{fg}	latent heat of vaporisation
k, λ	thermal conductivity
T, θ	temperature
u	velocity
τ_w	shear stress at the wall
N	nucleation site density
D	diameter
f	frequency
m	mass
x, l	distance
g	acceleration due to gravity
δ	boundary layer thickness
β	coefficient of thermal expansion (or a dimensionless ratio)
h_c	coefficient of convection
ε	emissivity

Superscript

$^+$, *, ^{x}	denotes dimensionless
"	per unit area

Subscript

b	bubble or bulk fluid
sat	saturation
w	wall
l	liquid
g	gas
0	initial time
t	thermal
v	velocity

Abbreviations

TC	thermocouple
PIV	particle imaging velocimetry
PTV	particle tracking velocimetry
PRV	pressure relief valve
DFT	directional flame thermometer
CAL	calorimeter
CTA	constant temperature anemometry
HWA	hot wire anemometry
RTD	resistance temperature detector
RPI	Rensselaer Polytechnic Institute
Eu	Eulerian
SEP	surface emissive power
DAQ	data acquisition system

Dimensionless numbers

Pr	Prandtl
Gr	Grashof
Re	Reynolds
Ra	Rayleigh
Nu	Nusselt
Ja	Jakobs
Fo	Fourier

1 INTRODUCTION

1.1 Background

A pressure vessel is any vessel capable of containing a substance at a pressure different to atmospheric pressure. In both domestic and industrial scenarios it is common for fluids to be transported, stored, or even processed in such vessels. Pressure vessels may be made from a range of metallic or composite materials. However, in industrial situations, where fire exposure is a credible hazard, steel is the most commonly used material. Industrial pressure vessels typically store fluids in cylindrical tanks with domed ends, or in spheres for very large-scale storage (with diameters in excess of 10m). This thesis investigates the response to fire of medium-scale (approximately 1m diameter) or larger pressure vessels for the transportation and storage of hazardous materials.

Pressure vessels for hazardous materials present a significant risk when exposed to an accidental fire. The potential consequences include explosion, fireball, toxic and asphyxiating clouds, projectiles and severe fires. Of the many risks associated with pressure vessels, explosive rupture is a significant concern due to the likelihood of the incident propagating, known as the domino effect (Hemmatian et al., 2015). Pressure vessel explosion is typically referred to as a boiling liquid expanding vapour explosion, or BLEVE. This term was coined over six decades ago, yet the numerous BLEVE incidents occurring since then show that industry has still not managed to understand and minimise the danger posed by pressure vessel exposure to fire.

Thankfully the number of fatalities each year due to pressure vessel incidents is low, but this should not be taken as indicative of good practice, or as reflective of an effective capacity to model and predict vessel performance in fire. It instead reflects the likelihood of fire-related vessel incidents occurring in sparsely populated areas during transportation, or on industrial facilities with established evacuation procedures (Health and Safety Executive, 2012). The fatalities and injuries that do occur, coupled with the high economical cost of such incidents, have led to the establishment of regulations covering the transportation and storage of hazardous materials, pressure vessel construction and fire protection measures in almost all countries worldwide. The fire-safety related purpose of regulations is primarily to reduce the risk of a fire event occurring, and secondly to minimise the consequences if one were to occur. In this context it is of high importance to the overall process safety strategy to understand whether a vessel will BLEVE and, if applicable, the expected time for it to do so.

The regulations applicable to pressure vessels vary extensively across country, vessel type and even content type. Test standards, including fire test standards, also vary significantly with no internationally recognised and widely accepted methodology in place. Compliance with regulations is often demonstrated through testing. The test methodologies used range from actual pressurised tank tests (albeit on a modest scale such as those by Droste, et al., (2011)), to plate tests, such as those required by U.S. regulation 49-CFR-179.18 (U.S. Government Publishing Office, 2011). Practical tests are often coupled with models that seek to interpret and apply limited results to a wide range of tank scenarios. Such models may cover a range of contents, fill levels, vessel dimensions, relief conditions and fire exposure.

Models intended to predict time to rupture must simulate two key phenomena: the deterioration of the wall yield stress as the wall increases in temperature, and the increase in wall stress due to a rise in internal pressure. Numerous models of vessel pressurisation, venting, wall strength deterioration, and rupture characteristics have been developed over the last four decades (Moodie, 1988). In general, modelling the conduction within the wall is reasonably straightforward, given knowledge of the external thermal boundary conditions and the internal fluid characteristics. A far greater challenge is modelling the pressurisation rate. Early models were typically 2D lumped-parameter models that assumed a single internal temperature value and predicted the pressure as the vapour saturation pressure of the fluid at that temperature. More advanced multi-zone models account for thermal stratification in the liquid and superheating of vapour, greatly improving the ability to accurately replicate experimental results. Recent approaches to modelling have involved computational fluid dynamics (CFD) to consider the problem in three dimensions and to capture the multiphase problem in 3D to a greater level of accuracy, for example Landucci, et al., (2016) and Shi, et al., (2012).

Despite progress over recent decades, the ability of industry and academia to reliably model the pressurisation rate of the contents of vessels during fire exposure remains limited. For reasons described within the body of this thesis, advances in modelling the pressurisation rate of vessels in fire, and hence in predicting time to failure of vessels, requires further development of three-dimensional numerical models utilising CFD.

However, modelling of turbulent multiphase flow with significant heat transfer and wall boiling is an area of active CFD research and the ability of currently available commercial codes to accurately predict previously un-tested scenarios remains quite limited (Colombo & Fairweather, 2016) (Kharangate & Mudawar, 2017). Development of improved CFD models is further hindered by the limitations in available test data suitable for

use as validation. There is an extensive set of vessel tests available in literature, however the scope of test parameters is relatively narrow (for example Anderson, et al., (1974) and Moodie, et al., (1988)). The majority of tests are horizontal bullet-type tanks containing commercial propane at a fill level of 50% or >95%, fully engulfed in an open pool fire. The resulting dataset is sufficient for calibrating a variety of model types for liquefied petroleum gas (LPG) based on the pressurisation rate. However, numerous models claim validation based on matching pressurisation rate against a limited number of tests despite failing to capture the physical processes correctly (Birk, 2000), and thus being potentially inaccurate and unreliable outside of the limited scope of validation test evidence.

Validating models against more than pressurisation rate alone requires an ability to check that the model output captures the details of the physics in a meaningful way. Achieving this is more difficult, as the instrumentation across the body of available test evidence varies significantly, and in many cases consists simply of shell thermocouples and a pressure transducer. A limited number of tests had an increased number of internal thermocouples, providing a better understanding of the fluid behaviour, however gaps remain in the knowledge of fluid behaviour, boiling and temperature distributions.

The overall goal of research in the field of pressure vessel response to fire is to improve process safety by improving our ability to predict failure. This requires the creation of more accurate models of vessel pressurisation. As described above, development and validation of improved three-dimensional models is substantially hindered by a lack of detailed characterisation of the fluid behaviour within pressure vessels during fire. The need to address this gap in knowledge gave rise to the project objectives as described below.

1.2 Project objectives

This project had two primary objectives and a secondary objective. The primary objectives were to:

- Design, build and commission test equipment capable of characterising the thermohydraulic response of vessel contents during fire engulfment
- Generate a dataset of detailed characterisation measurements, suitable for development and validation of numerical models

A secondary objective, derived from the above, was to:

- Propose methods for future development and improvement of vessel response models

1.3 Scientific contribution

The scientific contribution of this work is primarily in the production of novel test apparatus capable of characterising in detail the fluid behaviour in the specific geometry of a pressure vessel, on a scale that has not been achieved previously. Particle Imaging Velocimetry (PIV) was performed in a pressure vessel during full fire-engulfment for the first time, and the potential for the thermal and velocity boundary layer profiles to be characterised during fire engulfment has been reviewed. The results generated have been used to critique the applicability of heat transfer correlations, boundary layer thickness predictions, and boundary layer profile predictions, and to propose alternatives. The ability of PIV to characterise the internal behaviour of pressure vessels during external fire engulfment has been demonstrated and recommendations have been made to further develop the apparatus and techniques to provide additional data in the future. Recommendations have also been made to further develop CFD models of pressure vessels exposed to fire, which could in future lead to improvements in modelling of vessel-related critical accidental scenarios.

1.4 Structure of thesis

This document is divided into five main sections: a literature review, a description of the equipment and test series, analysis of the results, CFD simulation work, and conclusions and recommendations. Given the large quantity of data generated during the test series, only summaries of selected results are presented Information beneficial to further understanding the equipment or calculations, though not vitally necessary for comprehension of the main document, is given in the appendices.

1.5 Third-party contributions

The experimental part of this project involved contracted manufacture and sourcing of components across multiple countries and large-scale hazardous testing requiring heavy equipment and plant items. The challenges associated with working safely on a third-party facility around unrelated activities inevitably required practical assistance from numerous people. Where third-party assistance has been given, the specific contribution is detailed at the start of each section. Unless otherwise stated, the work described herein is that of the author. Particular recognition is given to the contributions of BAM in relation to section 3 on experimental work and of the University of Bologna in relation to section 5 on CFD modelling.

1.6 References

Anderson, C., Townsend, W., Zook, J. & Cowgill, G., 1974. *Effects of a Fire Environment on a Rail Tank Car Filled with LPG,* s.l.: US Department of Transport Report No. FRA-OR&D 75-31.

Birk, A. M., 2000. *TP 13593E Review of AFFTAC Model,* s.l.: Transportation Development Centre Transport Canada.

Colombo, M. & Fairweather, M., 2016. Accuracy of Eulerian-Eulerian, two-fluid CFD boiling models of subcooled boiling flows. *Int J. of Heat and Mass Transfer,* Volume 103.

Droste, B., Ulrich, A. & Borch, J., 2011. Brand new fire test facilities at 'BAM Test Site Technical Safety'. *Packaging, Transport, Storage and Security of Radioactive Material.*

Health and Safety Executive, 2012. *Failure Rate and Event Data for use within Land Use Planning Risk Assessments updated 28-6-201.* [Online]
Available at: http://www.hse.gov.uk/landuseplanning/failure-rates.pdf

Hemmatian, B., Planas, E., Casal, J., 2015. Fire as a primary event of domino accident sequences: The case of BLEVE. *Reliability Engineering and System Safety*, Volume 139.

Kharangate, C. R. & Mudawar, I., 2017. Review of computational studies on boiling and condensation. *Int. J. Heat and Mass Transfer,* Volume 108.

Landucci, G. et al., 2016. Modeling heat transfer and pressure build-up in LPG vessels exposed to fires. *Int J. of Thermal Sciences,* Volume 104.

Moodie, K., 1988. Experiments and Modelling:- An Overview With Particular Reference to Fire Engulfment. *Journal of Hazardous Materials,* Volume 20.

Moodie, K. et al., 1988. Fire Engulfment Tests on a 5 Tonne LPG Tank. *Journal of Hazardous Materials,* Volume 20.

Shi, J., Bi, M. & Yang, X., 2012. Experimental research on thermal stratification of liquefied gas in tanks under external thermal attack. *Experimental Thermal and Fluid Science,* Volume 41.

U.S. Government Publishing Office, 2011. *49 CFR 179.18 - Thermal Protection Systems.* [Online]
Available at: https://www.law.cornell.edu/cfr/text/49/appendix-B_to_part_179

2 LITERATURE REVIEW

2.1 Pressure vessel fire tests and regulations

2.1.1 Introduction

Hazards associated with the storage and transportation of pressure liquefied gases such as LPG can include pool fires, spill fires, jet fires, vapour cloud explosions, BLEVEs, asphyxiation and missiles. Although the probability of any individual tank being involved in an incident is arguably low (Paltrinieri, et al., 2009), the quantities and frequencies involved in the storage and transportation, along with a high societal and economic impact of such an incident when one does occur, ensures that the storage and transportation of goods in tanks capable of containing pressure significantly above ambient is a highly regulated part of industry.

As a preliminary study to designing fire test equipment capable of subjecting a pressure vessel to controlled, yet representative, conditions this section considers some of the different regulations and test procedures currently in place in the Western world covering LPG storage and transportation. It examines the medium and large-scale testing from which they were partially derived, the thermal boundary conditions imposed by the fire types to which they were subjected, and from these proposes a set of conditions which can be considered a minimum requirement for fire testing equipment design. LPG vessels are covered extensively in this section because they account for the large majority of scientific, regulatory and test literature available.

2.1.2 Hazard scenarios considered

The primary concern resulting from fire impingement of pressure vessels is loss of containment. This in turn may lead to escalation of the incident via additional accident scenarios such as a pool fire, jet fire, or a BLEVE. The type of escalation scenario depends on factors such as: the design and condition of the vessel, the presence and condition of thermal insulation systems, or the nature and degree of impingement of the fire (Birk & Cunningham, 1994). A key aim of fire tests of pressure vessels is to record the vessel shell temperature rise and internal pressure rise that can together result in a loss of containment. Testing is typically performed via direct heating of a vessel through fire engulfment, or alternatively by radiation from remote sources (see, for example, Heymes, et al., (2013)). In general, a degree of engulfment (either whole or partial) can be considered worst case and hence most actual fire tests, and corresponding furnace-based replica tests, involve flame exposure either through use of a hydrocarbon pool fire or a furnace.

2.1.3 Fire test methodology

The majority of hydrocarbon-type fire tests undertaken at present are furnace-based tests utilising a 'standard' fire curve such as the one described in BS476 pt-20 Appendix D. All furnace-based standard fire tests (including hydrocarbon-type ones) suffer from limitations as described in the public enquiry following the Piper-Alpha disaster (Lord Cullen, 1990). They seek to reproduce measurements of temperature rise within heated objects and provide a benchmark test which is conservative in the majority of cases, but they do not account for important parameters such as the fire growth, travel and decay, the radiation and convection balance, differential heating, gas velocities and erosive forces, etc.

There are numerous scenarios where existing HC test standards can be considered non-conservative, including large clean-burning fuel pool fires, compartmented fires and jet fires. Following the Piper Alpha disaster and resulting public inquiry it was concluded that the methods of test were woefully inadequate for the hazards present in the oil & gas industry. Joint industry projects were formed and led to the development of a cost-effective and reproducible jet fire test (Jet Fire Test Working Group, 1995), now adopted as an ISO standard (ISO, 2008). Similar work is being undertaken within ISO to look at a standard method of test for pressure vessels in combination with thermal protection systems.

Work undertaken by the U.K. Health and safety Executive assessed the suitability of the ISO jet fire test to represent large-scale releases (HSE, 2000). It found that the test procedure is a suitable test method, subject to adequate insulation of the test specimen to manage heat losses from the specimen, and therefore this study does not consider jet fire any further.

However, there remains no internationally recognised 'pool fire' test standard applicable to vessels. Existing pool fire standards that involve testing within a furnace are not suitable for testing pressurised vessels for obvious safety reasons. This has led to a number of national regulators and organisations publishing their own test procedures or requirements (described in the next section). However, none of these has established worldwide use.

2.1.4 Published test procedures and regulations

The International Atomic Energy Association for nuclear waste transportation vessels requires a hydrocarbon fire achieving a flame temperature of 800°C and an emissivity of 0.9 for 30 minutes, positioned 1 m below and extending 1-3 m beyond the test specimen (International Atomic Energy Association, 1996).

The UK Health & Safety Executive support a prescriptive requirement of designing or fireproofing a vessel to limit the temperature rise to 300°C for a duration of 90 minutes, as this has been shown to prevent failure of vessels. (HSE, 2000) A particular test procedure is not specified; however it is a requirement that the fireproofing system be capable of withstanding a jet fire type release. Generally the UK requirements can be considered reasonably conservative when coupled with the Liquefied Petroleum Gas Association (LPGA) codes of practice, compensating for the lack of requirements specified for fire testing.

NFPA 58 is a comprehensive guidance document, similar to the LPGA codes of practice, and covers design, operation, and maintenance among other aspects (NFPA, 2004 Edition). It includes a torch fire and firewater hose stream test procedure, subjecting the vessel to alternate heating and cooling and varying mechanical impact for a total duration of 50 minutes. The test is conducted on steel plates 1.2 m x 1.2 m by 16 mm thick, limited to a temperature rise of 427°C. The torch test can be considered far less severe than a jet fire test, with an exit velocity of 23 ms^{-1} +/-10%, approximately one quarter of that in the ISO jet fire test. The lack of insulation on the back of the plate and the fixed thickness makes the applicability of this test method questionable to thin walled vessels.

Factory Mutual, which originally defined the term BLEVE, has published “Approval Standard for Fire Protective Coatings for LP Gas Steel Storage Process Vessels and Support Structures” (Factory Mutual, 1981). It requires tests on 610 mm x 1067 mm x 16 mm plates to be positioned in a furnace preheated to 538ºC, and raised to 982°C within 20 minutes. Tests shall be performed for two hours of continuous heating and separately for one hour of heating followed by application of a hose stream followed by a further hour of heating. The FM test, like the NFPA test, is a simple pass/fail test designed for a specific fire scenario and a very specific design of vessel. It is not suitable for application as a standard intended to cover a range of vessels.

The American Petroleum Institute has published guidance documents 521 and 2510A referring to the design, construction and fireproofing consideration of LPG vessels. They do not address test procedures or shell limiting temperatures specifically, but imply a level of fireproofing consistent with 90 minutes protection to UL1709. API521 addresses the heat input to a fire engulfed vessel through an environmental factor *F* for

external insulation. The commonly used failure temperature of 427°C (800°F) is attributed to criteria specified within these API documents. API documents are widely recognised to have a number of limitations with regards to pressure relief design, failure of the F factor to represent behaviour of common fire protection materials, and reference to UL1709. Despite widespread reference for general design, they are infrequently used for the determination of fireproofing material requirements.

Gasafe (GEIE, 1993) was a comprehensive research programme conducted in France in the early 1990's investigating the ability of passive fire protection to prevent or delay the BLEVE of LPG spheres. It involved plate testing and a limited number of 1.7 m diameter butane spheres for validation. The programme was state-of-the-art at the time; however it was disbanded after completion and is not available for testing of modern fireproofing systems. The recommendations within it therefore refer to outdated materials. Despite never being a test standard, it was extensively used in France and Italy and is occasionally still referenced elsewhere.

BAM (Bundesanstalt fũr Materialforschung und -prufũng) developed a set of vessel protection test requirements intended to demonstrate compliance with German regulation TRB 801 app 25. The pass requirement is similar to the UK, in that the average steel wall must not exceed 300°C within 90 minutes, but BAM also consider a peak steel limiting temperature of 400°C. They have developed their own fire test procedure, utilising a horizontal bullet vessel above a burner arrangement, in combination with small-scale plate testing to predict performance. BAM testing is the predominant means by which protection system manufacturers in Europe qualify products, but it is not a formal test standard.

A summary of the published test procedures described above is given in Table 1.

Table 1 - Summary of published test procedures

Test procedure	Specimen	Failure criteria
IAEA	varies	survive a 30 minute HC pool fire
NFPA 58	Plates	427°C, 50 minutes torch test and hose stream exposure
FM 4971	Plates	427°C, 2 hours (including a hose stream test)
API 521/2150A/2218	makes reference to UL1709	90 minutes, 427°C often inferred (not stated)
Gasafe	Insulated plates (varying thickness)	427°C, varying durations
BAM	Insulated plates and actual vessel test	300°C, 90 minutes

2.1.5 Discussion of vessel test procedures and regulations

A number of test procedures exist (or have existed) to determine the fireproofing requirements for LPG vessels. Some of these take the form of a pass/fail test procedure on a plate of fixed size, and are inherently unsuited to assessing fireproofing requirements for a range of vessel sizes. Other test procedures use a combination of small-scale plate testing and large-scale vessel testing, which allows an assessment to be made of protection system design across a range of vessel wall thicknesses. Plate testing can be useful for predicting thermal insulation system performance and shell temperature rise if the back-face is insulated to restrict heat loss to an appropriate level; however, it must be recognised that the temperature rise of the vessel shell is a function of complex interactions between the contents and the shell, something that remains an extensive challenge to model fully in 3D CFD, as highlighted by Landucci, et al., (2016), and discussed further in section 2.3. Most industry predictions are run using relatively simple zones models empirically validated for a limited scenario window against a small number of tests (see references in section 2.3.5). All plate tests in use today are designed to be similar to a specific test (see AAR/FRA, Gasafe test or BAM tests in section 5). Plate testing is therefore not suitable as a standard method of test intended to cover a range of vessel designs or pass/fail criteria, and the results from plate tests should not be used in simple models or assessments unless supported by validation tests.

Many test procedures will prescribe the failure criteria as a limiting steel temperature of either 300°C or 427°C. Although the true failure temperature is a function of many things (including vessel design and condition, pressure release valve design and performance, inventory conditions, fire nature, degree of fire impingement, thermal protection condition and performance, etc.) testing has shown these temperatures to be broadly conservative when an appropriately designed pressure relief valve (PRV) is present, hence their acceptance worldwide.

None of the procedures or guidance notes listed above are test standards that fire protection system manufacturers can seek approval against with classification societies. A number of the procedures have points which should be considered in development of a standard test procedure. The Gasafe program and BAM procedures are of particular merit. More details on these, and other, test procedures is given in the following section.

2.1.6 Review of large-scale vessel tests

This section specifically considers tests performed on medium-scale and large-scale pressure vessels, particularly the experimental set-up, the temperatures and heat fluxes (if recorded). Commentary is provided on aspects of the test which are applicable to the goal of creating a standardised and reproducible method of test.

Table 2 - Summary of selected vessel tests referenced

Tests reported by	Vessel size	No. Tests	Fire type	Heat flux av. (max)
Townsend & Anderson, 1974	125t	2	JP-4 Pool	100 (120)
Droste & Shoen, 1988	4.9t	5	Fuel oil pool	47
		2	Heating oil pool	90-63
Moodie et al., 1988	5t	4	Diesel pool	75-90 (105)
Gasafe, 1993	2.5t	1	Butane pool	90
		1	Propane burner	80
Birk, et al., 1996	2.3t	2	Propane burner	97
Landucci, et al., 2009	2.5t	2	Diesel pool	19-56 (140) estimated
Gonzalez, et al., 2016	2.2t	7	Propane burner	110-120 kW/m^2

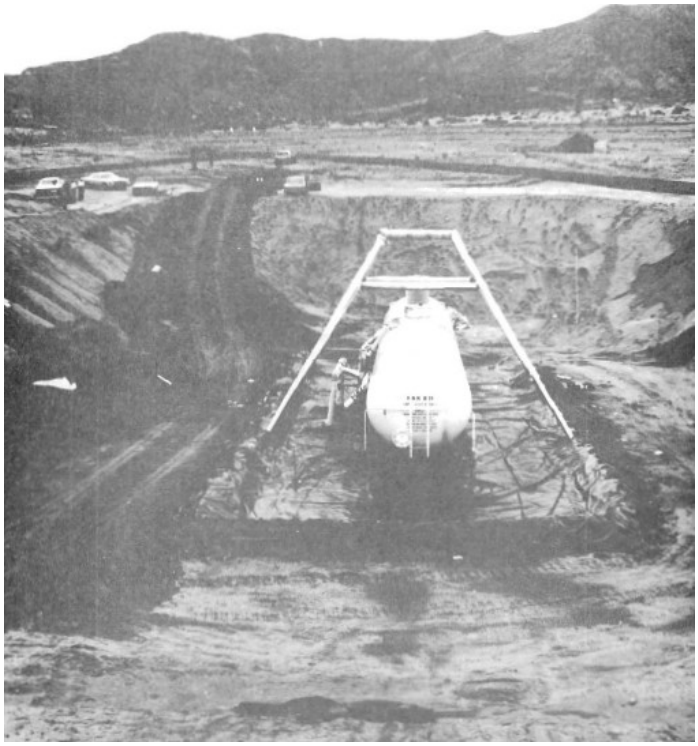

Figure 1 – Experimental set-up of test by Anderson, et al. (Anderson, et al., 1974)

The FRA/DOT, in conjunction with the RPI-AAR, conducted tests on an unprotected and protected 128,000 litre propane rail tank car as reported by Anderson, et al., (1974) and Townsend, et al., (1974). They remain the largest experiments conducted on actual pressurised vessels to-date and are still some of the largest land-based pool fire experiments in general. The vessels were Ø3.02 m x 18.41 m with a wall thickness of 15.9 mm. They were tested in a large excavation containing a 24.4 m x 9.1 m fuel pit, using JP-4 aviation fuel. Each vessel had extensive instrumentation, including a radiometer, external fire temperature TCs and 2 grids of internal thermocouples at stations ¼ and ¾ along the vessel. The TC grids measured the temperature distribution within the liquid and vapour and of the steel wall. The non-insulated vessel was described in detail in Anderson, et al., (1974). It was filled to 27.9 cm from the top with propane. During the test no direct readings were taken of the liquid level, however this can be assessed with knowledge of the vessel wall temperatures and the mass loss from the relief valve. Figure 1 shows a picture taken before the test. The A-frame over the relief valve in the middle of the vessel was used to house instrumentation from NASA to study pool and jet fires, including a radiometer. The NASA instrumentation results, also reported in Anderson, et al., (1974), indicated mean temperatures and heat fluxes much higher than those reported by Anderson (mean heat fluxes of 138 and 207 kW/m^2 at 1.2 m and 7 m above the pool respectively). This can be attributed to the influence of the relief jet and the propensity of small heat gauges to overestimate the net flux to large objects, discussed further in section 2.1.8.4. Within 45 seconds of ignition the flame temperatures reached 1090°C and then varied within a typical range for pool fires of 650°C to 1090°C. The engulfment was reasonably uniform circumferentially; however winds blew from the front of the tank to the back, leading to a temperature difference of approximately 200°C along the tank. Comparison of flame temperature data with the radiometer indicated the flame emissivity to be 0.62. The pressure release valve opened briefly at 2.2 minutes and 2.6 minutes before permanently opening at 3 minutes. After a further 7 minutes, boiling of the liquid propane caused the liquid to become isothermal, whereas thermal stratification had been observed up to that point. The test highlights the critical importance of judging the shell temperature on the basis of the maximum reliable temperature observed, rather than an average shell temperature. There is a sharp distinction between the wall temperatures in the liquid wetted areas and the vapour space areas. As the vessel pressurises and the relief valve activates, the liquid level drops exposing more wall to the vapour space. The vessel wall in this newly exposed area then exhibits a rapid increase in temperature.

Townsend, et al., (1974) calculated the net heat flux based on the change in temperature and vaporisation of the propane. They found the net flux to the propane was 99.6 kW/m^2 for the non-insulated test and 51.5 kW/m^2 for the insulated test (i.e. the insulation on the vessel halved the overall rate of heat transfer to the contents). This reduction in net flux extended the time to rupture from 24.5 minutes to 94.5 minutes. It should be noted that Anderson reported the non-insulated test as 105 kW/m^2, and this higher value is frequently referred to for this test. Variation in the heat flux reported is likely to be a consequence of the non-uniform heating of the tank. Results depend on the location, method, and data used. The NFPA and FM requirements given in Table 1 are derived from the heat flux measurements (average and range), vessel wall thickness, and wall temperature at failure of this test.

BAM have been highly active in vessel testing since the early 1980's. Droste & Schoen (1988) published results of five fire tests of 4.85 m^3 LPG vessels, three of which were not insulated and two of which had thermal insulation. The vessels were Ø1.25 m x 4.3 m with wall thicknesses of 5.9 to 6.8 mm. Non-insulated testing was intended to simulate a vessel on a pedestal, and hence 60 cm wide troughs were used around the tank base, filled with fuel oil. The propane fill level in each test was 50% and all unprotected vessels resulted in BLEVE within 7-12 minutes. The maximum wall temperatures recorded were in the region of 420-560°C. The insulated tests were conducted over 3 m x 6 m fuel oil pools to give full engulfment. Developments at BAM over 9 years were summarised by Droste (1992). The fuel oil pool fires were determined to have subjected the vessel to a net heat flux of approximately 47 kW/m^2, while a gas burner arrangement with 20 nozzles around the vessel was determined to provide a heat flux of 56 kW/m^2.

More recently, Droste, et al., (2011) described the current fire testing facility at BAM and the calibration tests that had been performed to assess the heat fluxes acting on test vessels. Two 6.65 m x 3.35 m heating oil pool fires were determined to have heat fluxes of 90.2 kW/m^2 and 63.3 kW/m^2. The only significant difference between the conditions in the two tests was that during the second test wind caused part of the vessel to remain non-engulfed in flames, giving a significantly lower overall heat input.

Current vessel tests at BAM use liquid propane burners to give more control over the degree of engulfment and the heat flux. A burner system allows improved control over the start and finish of the fire test, and reduced the environmental impact of the test. Calibration tests using water filled vessels allow direct calculation of the net heat flux to the vessel and have recorded net heat fluxes of 45-135 kW/m^2 depending on the vessel geometry. Most heat fluxes were in the region of 75-110 kW/m^2, leading Droste to conclude that

vessel tests with good engulfment are within this range. The current BAM methodology requires a successful calibration test to demonstrate the net heat flux is in this range using a water-filled vessel instrumented to act as a large calorimeter, after which the test set-up can be applied to similar vessels.

The U.K. Health and Safety Executive (Moodie, et al., 1988) presented the results of four tests conducted by the Health and Safety Laboratory on a Ø1.7 m x 4.88 m x 18 mm wall vessel, each with a varying fill level: 22%, 36%, 58% or 72%. The fire was a 6.8 m x 3.8 m pool with kerosene on water. Surrounding the test was a bund wall, as shown in Figure 2. All four tests were terminated when the vessel wall temperature reached 600°C in order to prevent BLEVE. Fire durations therefore ranged from 11.6 minutes up to 31 minutes. The test duration increased with increasing fill level, demonstrating that there is relatively insignificant heat loss from the un-wetted shell wall through both circumferential conduction and through convective/radiative loss to inventory. The heat fluxes in the fire were measured in three of the tests using three calorimeters at heights of 0.67 m, 1.17 m, and 1.67 m above the pool and 0.5 m to the side of the vessel. Heat flux readings within the three published tests generally fell within the range 75-90 kW/m^2, the data was then corrected on the basis of an assumed gauge absorptivity of approximately 0.8, and the reported peak net heat flux to a cold object was stated as being in the region of 105 kW/m^2.

Moodie (1988) also published a review of experiments and modelling, in which he listed the heat flux of the 3 tests as 96, 99 and 101 kW/m^2. Moodie, et al., (1985) presented an analysis of smaller ¼ tonne and one tonne tests performed by the HSE that preceded the above five tonne tests. They used a 4 m x 2.4 m pool fire, surrounded by a bund wall to the top of the vessel. The net heat flux to one of the ¼ tonne tests was assessed from the temperature and pressure changes within the vessel to be 97 kW/m^2. The one tonne tests were calculated as having received net heat fluxes of 118, 75, 61 kW/m^2, with the last test low due to partial engulfment caused by strong winds on the day. The HSE tests can be considered representative of vessels in pool fires except in strong wind conditions. However, the test facility was highly specialised and would not be suitable for replication across numerous locations due to the expense required.

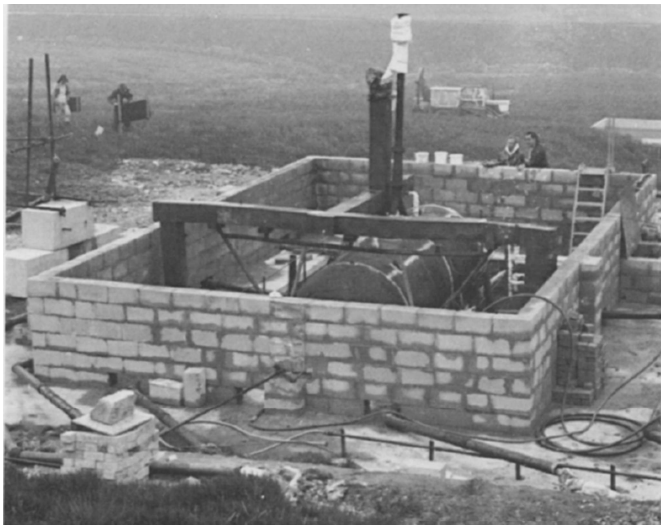

Figure 2 – HSE 5t vessel test experimental set-up (Moodie, et al., 1988)

Gasafe (GEIE, 1993) was a test programme commissioned by Groupement Européen d'Intérêt Economique to investigate and predict the performance of fireproofing on vessels. It consisted of a series of plate tests to obtain thermal data from fireproofing materials, validated against a butane pool fire engulfing a ∅1.7 m x 10 mm wall sphere positioned 2 m above a 24 m^2 pool. The sphere was 20% full of water and temperature changes were measured, allowing the net flux to the sphere to be calculated as 80 kW/m^2. The average flame temperature was 850°C, and the emissive power of the flames was estimated by the researchers as 90 kW/m^2. The butane pool fire test was used as the basis for the development of a butane burner, to recreate the conditions for subsequent testing. The burners achieved a net heat flux to the sphere of approximately 80 kW/m^2, demonstrating that a burner arrangement is capable of reproducing appropriate net heat fluxes to engulfed objects, even though the flame height and thickness are somewhat different. For a reason not clearly specified in the report future testing was based on the burner being set to follow the 'standard' hydrocarbon time temperature curve. One reason may have been to introduce a degree of conservatism, and hence a margin of safety, as the programme moved to testing in furnace environments. In private communication with the former chair of the European group of fire laboratories (EGOLF) a round-robin study of heat flux values within 'standard' hydrocarbon time-temperature tests across European furnaces was given as approximately 150 kW/m^2.

A.M. Birk has published work covering numerous pressure liquefied gas vessel tests and BLEVEs over recent years (Birk, et al., 2006). In addition to work characterising the nature of BLEVEs he has conducted tests on

vessels with defects in protection systems and partially engulfed vessels. Birk, et al., (2006) used an array of 25 low velocity propane burners to simulate a pool fire with a heat flux of 97 kW/m^2. The target vessel was Ø0.95 m x 3.07 m x 7.4 mm wall thickness. The burners engulfed 25% of the surface area of the vessel, consisting of a band approximately 1 m wide down one side. Measurement of the heating rate of 50% and 80% water-filled tests indicated the net flux to be 75-107 kW/m^2. The first propane test in the series was expected to fail within 8-10 minutes. However, the wind happened to be blowing against the flames, resulting in a lack of flame engulfment at the top of the vessel. Temperatures at the top of the vessel reached a plateau at approximately 500°C and the vessel showed no signs of rupturing, as the PRV was maintaining the pressure at 25 barg. Thirty-five minutes after the start of the test the wind changed direction, blowing the flames over the top of the vessel and causing the temperatures at the top of the vessel quickly to rise above 700°C. The vessel failed within approximately five minutes of the wind changing direction. This test shows the importance of flame engulfment, particularly at the top of the vessel. Consideration must therefore be given within any test procedure to recording the maximum temperatures reached at the top of the vessel. The burners used by Birk created a radiant, relatively low momentum flame capable of working with a variable flow rate to give a desired target heat flux. Such an array is a suitable basis on which to design a vessel test, minimising to an extent the possible susceptibility to wind-effects. Although it has the disadvantage of being relatively expensive to set-up compared to a BAM style burner, the fuel requirements during tests are likely to be lower than the BAM and Gasafe procedures using liquid burners.

Landucci, et al., (2009) analysed two diesel pool fires conducted at TNO with vessels of dimensions Ø1.25 m x 2.68 m x 5.1 mm wall. The diesel pool was 3.6 m x 2.25 m (see Figure 3), and was required to achieve a temperature of 590°C within five minutes and maintain above this temperature at a minimum of 50% of the measurement points around the vessel for the duration of the test. The vessel itself was required to meet the survivability requirements adopted by BAM (see Table 1). The first test suffered from wind effects, and the vessel was visually observed to be only partially engulfed for most of the test. The average temperature reading around the vessel was 491°C (over a range of 125-983°C). For the second test a sand wall was built, and this gave better results, with an average temperature of 725°C (range of 447°C-986°C). In general, the two tests considered by Landucci, et al., (2009) are inadequate to assess the response of a vessel to a large fire. The pool does not extend sufficiently beyond the extents of the vessel footprint to give reasonable engulfment, and both the peak and average temperatures are lower than observed in large pool fires tests. Although this

may be representative of a small-scale diesel spill fire, this is not a suitable scenario on which to base a single method of test intended to be applicable to a wider range of scenarios.

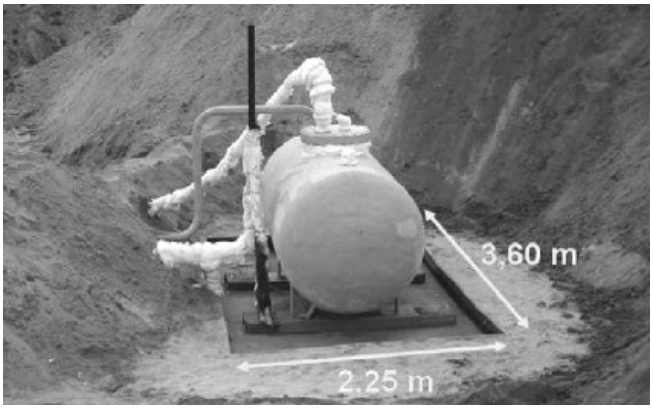

Figure 3 – Vessel test (Landucci, et al., 2009)

Gonzalez, et al., (2016) reported a series of seven full containment tests of water and 50% sodium hydroxide solution (at fill levels of 98% and 50%) undertaken by the FRA at the BAM facilities in Germany. The vessels were one-third linear-scale rail tank cars and instrumented with thermocouples secured against the outside of the jacket and tank, pressure transducers, and internal vertical lines of thermocouples. A 3.2mm thick metal jacket was fitted around the tank, with 100mm of fibreglass insulation between the jacket and the tank, to replicate existing thermal protection system practice. The fire was characterised through the use of directional flame thermometers attached to the tank to comply with the requirement of an equivalent black body flame temperature of 871°C +/- 56°C (80 kW/m^2 – 117 kW/m^2). The objective of the test programme was to determine whether full containment (no pressure relief) of sodium hydroxide solution would comply with the 100 minute survivability criteria required by regulation. The results of the test were counter to the a-priori modelling that predicted NaOH solution would pressurise slower than water. It pressurised at a similar rate. Gonzalez, et al., concluded that this is due to differences in the fluid boundary layer properties and boiling properties of NaOH compared with those of water.

2.1.7 Summary of vessel tests

A range of tests on pressure liquefied gas vessels are found in literature, ranging from lower medium-scale (Birk, Landucci et al.) to upper medium-scale (HSE, BAM), to large-scale (Anderson et al.). The average net heat fluxes measured are typically in the region of 90-105 kW/m^2, with 100-105 kW/m^2 being the value reported for the largest test ever conducted on an LPG vessel.

The large-scale tests conducted by Anderson are prohibitively expensive, and the same can be said about the HSE tests. Although the HSE test set-up seemed sufficiently resilient to wind and recreated appropriate heat fluxes, it required a specialist test facility and is therefore not practical to recreate at a number of locations for general vessel testing. The medium-scale testing performed at TNO inadequately reproduces the conditions which are expected of real pool fires, and hence is dismissed as being inappropriate examples to follow. The propane/butane burner tests conducted by BAM and the Gasafe programme could be described as medium scale, but are flexible in their design and hence have been used on a range of vessel sizes. They create net heat fluxes to a cold object of typically 80-90 kW/m^2, although BAM have shown them capable of exceeding 110 kW/m^2. Liquefied gas burner arrangements are therefore considered a suitable basis for a standardised method of test for pressure vessels and vessel protection systems. However, the work by Birk, et al., has demonstrated that even burners are subject to wind effects, and therefore environmental influences must be minimised or environmental constraints factored into any test standard.

2.1.8 Properties of hydrocarbon pool fires and thermal boundary conditions on impinged objects

2.1.8.1 Pool Fires

The heat transfer from flames to engulfed objects occurs due to both convection and radiation. The net heat flux to an engulfed object consists of the absorbed radiation and the convection terms, less the radiation emitted by the object. Radiation from ambient surroundings able to penetrate the flame can be considered negligible and ignored. The net heat flux to an engulfed object is given by equation 2.0

$$q^{"} = h\left(T_f - T_s\right) + \varepsilon_s \varepsilon_f \sigma T_f^4 - \varepsilon_s \sigma T_s^4 \qquad (2.0)$$

where:

$q^{"}$ is the heat flux (W/m^2)

h is the coefficient of convective heat transfer (W/m^2.K)

T_f, T_f is the temperature of the flame and substrate respectively (K)

ε_f, ε_s is the emissivity of the flame and substrate respectively, noting that equation 2.0 assumes the emissivity is equal to the absorptivity.

σ is the Stefan-Boltzmann constant (W/m^2K^4)

Steinhaus, et al., (2007) quote a definition of pool fires as flames established over horizontal fuel surfaces. This term includes a number of different types of fire including land spills, spills onto water, flowing liquid, and deep pools. A review of the state-of-the-art in pool fire knowledge by Joulain (1998) concluded that there was no clear definition of what a pool fire is. He described a pool fire as "characterized by the establishment of a diffusion flame on top of a horizontal fuel where buoyancy forces are the controlling transport mechanism."

This study uses the term pool fires to mean a bunded liquid pool fire, one in which a fire occurs above a horizontal fuel surface which is contained on all sides and in which the fuel is sufficiently deep to allow the maximum burning rate to be achieved. This deliberately excludes spill fires (frequently referred to as uncontained fires), in which part (or all) of the fuel perimeter has no boundary, allowing the fuel to spread and form a shallow layer. Although spill fires tend to cover larger areas than pool fires they are comparatively less severe for a given surface area. Spill fires form thin layers of fuel that lose significant heat to the underlying substrate and have reduced convective currents within the fuel. These combine to reduce the mass burning rate, which may be just one fifth of that of a corresponding deep pool fire (Steinhaus, et al., 2007), in turn reducing the surface emissive power of the flame and severity of the fire. Considering the lack of characterisation within the literature on spill fires and their reduced severity compared to pool fires they are excluded from further consideration.

Pool fires sustain burning due to vaporisation of the liquid fuel. Pools of diameter greater than 0.2 m burn predominantly due to radiative feedback to the pool (Babrauskas, 1983). As the diameter of pools increases so does the radiative feedback and the rate at which fuel is burnt. Kosecki (1989) observed this trend in studies on gasoline and kerosene, which showed a mass burning rate of 1-2 mm/min for pools less than 1 m diameter, increasing to a maximum burning rate at diameters of 3 m to 5 m. Generally accepted values for the maximum mass burning rate for various fuels on a solid substrate at ambient temperature are shown in Table 3, reproduced from Fire and Blast Investigation Group TN13 (2010). It should be added that the mass burning

rate varies from study to study, with some studies on limited fuel types giving higher values than the ones in Table 3.

Table 3 - Mass burning rates, extinction coefficient and boiling temperatures of selected fuels, reproduced from (Fire and Blast Investigation Group, 2010)

Fuel	$\dot{m}''_{\infty}$ (kg m^{-2} s^{-1})	k (m^{-1})	Approximate boiling temperature range, K
LNG	0.141	0.136	112
LPG	0.13	0.271	231-273
Propane	0.13	0.271	231
Butane	0.078	0.5	273
Gasoline	0.055	2.0	313-483
Kerosene	0.06	2.6	423-523
Diesel	0.044	1.15	438-633
Diesel – ventilation controlled	0.031	-	438-633

At diameters above 3 m most hydrocarbon fuel pool fires cannot entrain sufficient air to allow clean combustion (Raj, 2007). The soot particles therefore agglomerate to form smoke and the smoke acts as a 'shield' to radiation, reducing the surface emissive power (SEP) of the flame. The larger the pool diameter, the less air is entrained, the smokier the flame, and the lower the SEP as shown in Figure 4. The exception is fuels which do not produce smoky flames such as liquefied natural gas (LNG). These have been shown to increase in SEP with a continued increase in diameter up to 20-40 m given appropriate ventilation conditions (Fire and Blast Investigation Group, 2010).

Steinhaus, et al., (2007) presented a review of research into the field of different types of pool fires, in which they highlight the limitations in current knowledge and the difficulty in modelling the behaviour of pool fires. They refer to data on kerosene and gasoline fires on land which found approximately 20% of a flame consists of "hot spots" at a given time, but conclude "heat transfer from large-scale pool fires to adjacent objects remains a challenging problem. Important unknowns still remain"

Raj (2007) described how LNG large pool fires can be considered as a consistent and highly luminous zone at the bottom, accounting for 6-7% of the flame height, above which the emissive power decreases as height increases. The dispersion of emissive power measurements (the standard deviation divided by the mean) is very low at the base of fires and high at the top. This is attributed to opening and closing of the smoke shroud, releasing 'bursts' of radiation. Although Raj was referring specifically to LNG, the concepts of a luminous zone and smoke acting as a radiation shroud can be applied to automotive fuel and LPG pool fires.

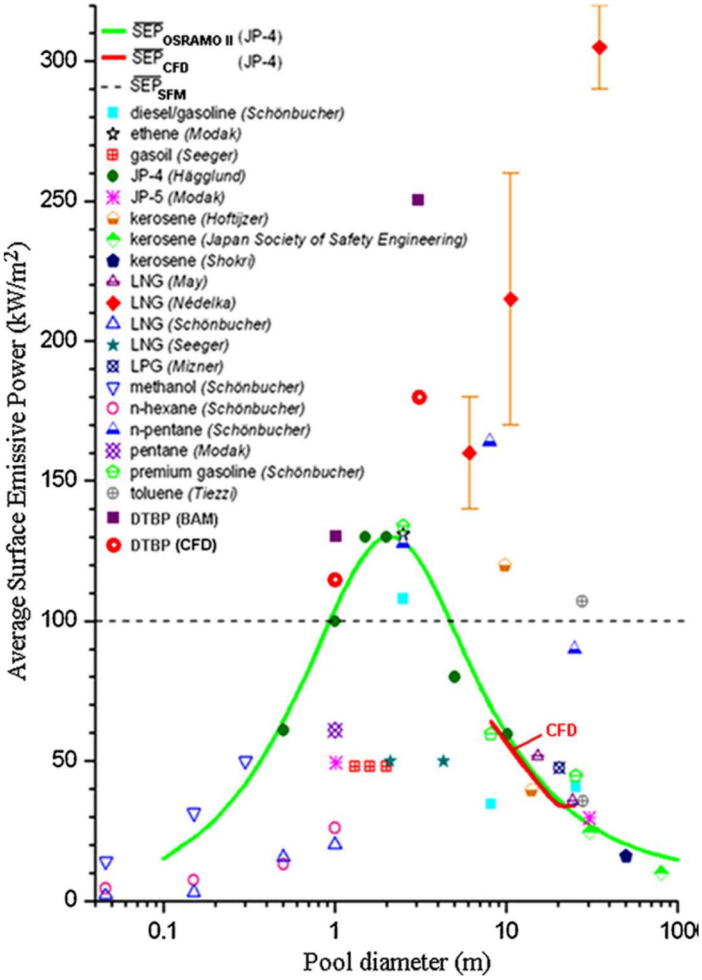

Figure 4 – Comparison of measured and modelled values of flame emissive power (reproduced from (Raj, 2007))

The temperatures and surface emissive powers of pool fires have been studied by a number of authors. Kosecki (1989) recorded gasoline maximum flame temperatures as 1000-1367°C depending on the pool diameter and the radiative fraction as 0.05-0.5 depending on the fire size.

Koski (2000) measured the temperature distribution in large pool fires using directional flame thermometers positioned 1.33 m and 1.66 m above a 6 m x 6 m JP-8 pool. All temperature measurements were within the range 600-1200°C, with the mode being 1000°C and 60% of values falling below this. Koski also commented that care must be taken when selecting a single value to represent a fire temperature as the steel will receive intermittent heating and cooling once it rises above 1000°C.

Bainbridge & Keltner (1988) recorded temperatures in a series of three 9.1 m x 18.3 m JP-4 aviation fuel pool fire tests using thermocouples on towers. They recorded a peak average temperature of 960°C, with very few temperature readings above 1300°C.

Schneider & Kent (1989) used the same 9 m x 18 m pool facility at Sandia laboratory and recorded peak average temperatures of 944-1057°C at a height of 1.4 m above the initial surface of a JP-4 fire. The data was conditionally analysed to give the temperature as 950-1100°C when flame was present.

Review of all the studies referenced herein indicates a consensus that automotive and aviation fuel pool fire average temperatures are in the region 950-1000°C and are highest at approximately 2 m above the surface of the pool. Peak temperatures in large pools are higher, up to 1300-1360°C, however the majority of the temperature readings are far below these peak readings, and the heat flux to engulfed objects cannot be equated to radiation from a black-body emitter at the peak temperature.

2.1.8.2 Surface Emissive Power

The emissive power of pool fires to targets outside the flame experiences more variation in measurement. Calculating the SEP of flames can be done using a number of methods. Infra-red thermography can be used to compare flame emissivity with that of reference plates at known emissivity (Planas-Cuchi, et al., 2003). Sudheer and Prabhu (2010) compared emissivity determined from infra-red thermography with results directly calculated from the mass burning rate. They found good correlation between the two methods, however their results are based on gasoline pool fires with a maximum diameter of 1 m. In pools above 2 m diameter, direct calculation based on the extinction coefficient tends towards a flame emissivity of 1. This does not necessarily relate to the emissive power of the flame as seen by a target outside of the flame, which decreases at large diameters due to smoke obscuration.

Other methods of calculating flame emissive power use wide-angle or narrow-angle radiometers. Narrow angle radiometers ensure the field of view is completely filled by the flame, giving a direct measure of the radiation from the flame. Their disadvantage is that radiometers which do not 'see' the full flame can give misleading results as flames are not homogenous (Planas-Cuchi & Casal, 1998). Wide angle radiometers 'see' more of the flame, however as noted by Raj (2007) the interpretation of the data may or may not consider atmospheric absorption, and may be based on the actual photographed emission surface or idealised shapes such as cylinders. When applied to an actual test such as the Montoir 35 m LNG pool fire test, such differences cause the calculated values reported by authors to vary between 275 and 175 kW/m^2.

Mudan (1984) summarises the measured emissive powers and radiation temperatures for various liquid hydrocarbon pool fires from a limited number of large-scale tests. The emissive power of a LPG pool fire on land is given as 48 kW/m^2, referencing Mizner & Eyre (1982), while the emissive power of a gasoline pool fire is given as 60 kW/m^2 (with maximum values of 130 kW/m^2).

Mizner and Eyre conducted 20 m diameter land-based pool fires of LNG, LPG and Kerosene (Mizner & Eyre, 1982). Using wide angle and narrow angle radiometers they determined the surface emissive power of the LNG fire to be 153 kW/m^2, the LPG fire to be 48 kW/m^2 and the kerosene fire to be 35 kW/m^2. It was observed that the LPG pool fire was very smoky, hence a reduction in the emissive power from 80 kW/m^2 recorded in an earlier (unpublished) 1.8 m pool fire.

In subsequent tests of LNG and LPG on water Mizner and Eyre observed an increase in LNG surface emissive powers of up to 140-225 kW/m^2 (Mizner & Eyre, 1983); however the propane surface emissive powers remained similar at 31-59 kW/m^2, due to the formation of extremely sooty flames and obscuration of radiation. The test evidence for emissive powers of LPG flames is very sparse. Testing of an LPG pool on water was also conducted by Parnaouskis (1980), but most current guidance on emissive powers of LPG pool fires refers back to the studies by Mizner and Eyre.

2.1.8.3 Heat Transfer to Objects Engulfed in Pool Fires

Keltner, et al., (1990) advise against a heat flux prediction based on an equivalent black body emitter at the average flame temperature. Such predictions underestimate the true value, as flames are intermittently present at higher temperatures and radiation is proportional to temperature to the 4th power. Conversely, predictions of net heat flux to engulfed objects based directly on heat flux measurements in flames tend to overstate the heat transfer rate (see below). Methods based on direct flame spectroscopy, such as that used by Wayne & Kinsella (1984), can be incorrectly applied by guidance documents (for example Fire and Blast Investigation Group (2010)) leading to overestimation of the heat transfer to engulfed objects. In the case of Wayne and Kinsella, this is despite the authors of the original study stating: “Lower values are appropriate in practice since the effective SEP of a pool fire takes account of the size and shape assumed for the flames, of soot shielding” and “the fact that parts of the flame will not be optically thick”.

Other methods of measuring the heat flux to engulfed objects are subject to a number of complications. The principle methods of measurement are to either utilise water-cooled calorimeters (such as Gardon or Schmidt-Boelter type gauges) or to use objects of known thermal mass to calculate the net heat flux based on a recorded temperature change. Both have advantages and disadvantages.

Using water cooled calorimeters theoretically allows a more accurate measurement as it removes the uncertainty of estimating heat losses. However, in practice it can be difficult to prevent a soot layer forming on the gauge. Inert gas can be blown on to the gauge to remove soot particulates but this may only be effective for a limited period of time. The gauges are likely to be more susceptible to variations in heat transfer coefficients due to the short length-scale involved in convective heat transfer to the small receiving plate on the gauge. They consistently give higher readings than net heat fluxes measured to large objects (discussed below). Furthermore, round-robin studies of heat flux gauge calibration have shown variability of over 10% amongst laboratories. (Blanchat, et al., 2009)

Calculating the incident or absorbed heat flux from flames using objects of known thermal mass presents a challenge as at it requires estimation of the losses. However, the use of thermally massive objects is highly useful for determining the net heat flux to objects in fire, as it avoids the problem of small-scale gauges over-estimating the net heat flux to large objects.

The heat flux to engulfed objects in aviation fuel fires has been characterised extensively at Sandia National Laboratories. Bainbridge & Keltner (1988) studied the heat flux to large objects in pool fires in a series of three tests using a large steel tube calorimeter (∅1.4 m x 6.1 m x 32 mm wall) positioned 0.9 m above the initial surface of a 9.1 m x 18.3 m JP-4 aviation fuel pool. The calorimeter recorded peak heat fluxes of 130 kW/m^2 at the bottom and the flame engulfed side, 70-110 kW/m^2 on the top and non-engulfed side. The average heat fluxes were 110 kW/m^2 at the bottom and leeward side, 70-90 kW/m^2 at the top and the windward side. This finding contradicted old models of pool fire plumes as point sources or cones/cylinders of uniform emissive power, which predicted the highest heat fluxes to engulfed objects would be on the top. It fits with the modern understanding of pool fires as consisting of different zones, with a highly luminous one at the bottom. The tests also demonstrated that even small winds have a large effect on pool fires. The flame emissivity was characterised as 0.85.

Schneider & Kent (1989) used the same test facility with a 6.35 mm thick plate calorimeter to assess the heat flux and determined the peak fluxes to be in the region 80-120 kW/m^2.

Koski & Wix (1995) used a 0.5 m x 0.5 m actively cooled plate calorimeter to record the heat flux at a range of positions and heights above a 6 m x 6 m JP-4 pool fire. All heat fluxes recorded were in the range 60-100 kW/m^2.

Kramer, et al., (2001) investigated the heat flux to a Ø1.2 m x 4.6 m x 25.4 mm wall cylindrical calorimeter 1 m above a Ø7.16 m JP-8 pool fire on water. Estimations of the net heat flux were calculated using an inverse 1-D heat transfer code from the thermal measurements of the calorimeter. The results show that even light wind conditions (<1 m/s) had a big influence on the engulfment. It took two minutes to fully engulf the calorimeter in flame, after which the light easterly wind resulted in tilting of the plume and large variations in heat transfer rate across the surface of the calorimeter. Heat fluxes of 125-150 kW/m^2 were recorded in the first 5 minutes on the flame engulfed side, followed by readings of 75-125 kW/m^2. The bottom of the calorimeter received average heat fluxes of 100 kW/m^2. The top and non-engulfed side averaged 50-75 kW/m^2. Once again, the highest heat fluxes were to the bottom and leeward side of the calorimeter. The surface emissivity of the steel was measured using two different reflectometers. It was found to be 0.8-0.85 for bare steel and 0.9-0.94 for soot-deposited steel (measured between tests).

Gregory, et al., (1989) analysed the data from a series of large pool fires conducted at Sandia Laboratories in 1983 (Bainbridge & Keltner, 1988). The flame temperatures measured were believed to be 4-12% less than the actual flame temperatures due to radiative loss from the TCs, which were positioned only 5 cm from the cool surface. Peak flux values from the test series were averaged as 115-120 kW/m^2.

Keltner, et al., (1990) highlighted the discrepancy between the heat flux measured by large objects and by small sensors. In a review of small calorimeter data, Keltner listed some of the fluxes measured as: 154 kW/m^2 (Bader 1963), 139-218 kW/m^2 (Anderson, 1974), and 161 kW/m^2 (Gregory, 1987). However, he contrasts this with heat fluxes calculated during large LPG tank tests (Anderson, et al., 1974) of 100 kW/m^2, and 109 kW/m^2 for the 1/5 scale tests that preceded this. He concluded that measured heat fluxes to large objects are consistently 20% lower than those by small calorimeters, referencing Mansfield (1983) in attributing this to a cool boundary layer surrounding the object acting as a partial shield to radiation and convection.

Table 4 - Summary of measured heat fluxes and methods in studies referenced

Test (Reference)	Fuel Type	Measurement - Method	Emissive Power / Heat Flux (kW/m^2)
Mizner & Eyre (16)	LPG	SEP - radiometer	48
Mizner & Eyre (16)	LNG land	SEP – radiometer	153
Mizner & Eyre (16)	LNG water	SEP – radiometer	140-225
Mizner & Eyre (16)	Kerosene	SEP – radiometer	38
Raj (8)	LNG	SEP -Radiometer	175-275
Wayne, Kinsella (19)	LPG	Flame emissive power - Spectroscopy	230-270
Gasafe (31)	Butane	Engulfed net heat flux - calorimeter	80
Koski & Wix (20)	JP-4	Engulfed net heat flux - calorimeter	60-100
Kramer, Koski (21)	JP-8	Engulfed net heat flux - calorimeter	50-75 top and windward, 100 bottom and leeward
Gregory, Keltner, Mata (22)	Various (10)	Engulfed net heat flux - calorimeter	Up to 115-120
Keltner, Bainbridge (10)	JP-4	Engulfed net heat flux - calorimeter	70-130 (average: 70-90 top & windward, 110 bottom & leeward)
Schneider, Kent (11)	JP-4	Engulfed net heat flux - calorimeter	80-120

2.1.8.4 Radiative Fraction

Kramer, et al., (2001), used the data from Kramer, et al., (2001) to propose models of radiative heat transfer to objects in pool fires. To explain why the net heat flux measured using thermally massive objects is less than theoretical flux they consider two scenarios: a cool boundary layer reducing heat transfer to the surface of the calorimeter, and optically thin flames, reducing flame emissivity and therefore incident radiation. Figure 5 illustrates these models.

The cool boundary layer was proposed by Kramer and Koski as the reason for absorbed heat fluxes to large objects being lower than those measured using small-scale gauges, on the premise that thermally massive objects such as vessels without thermal protection systems will cool the flame in the vicinity of the object, hence reducing heat transfer by convection, and to a smaller extent, radiation. This effect would not be observed on vessels with a thermal protection system, as the external surface would rise in temperature rapidly. The optically thin model for objects engulfed in optically thin flames is well established in radiative heat transfer theory, however it alone does not explain why thermally massive objects are subject to a lower net heat flux than small objects.

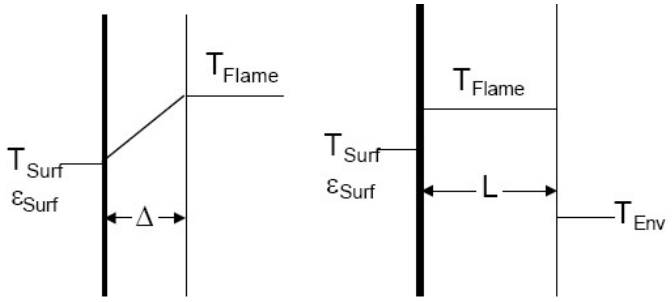

Figure 5 – Cool boundary layer and thin flame models for reduced heat flux to engulfed objects. (Adapted from (Keltner, et al., 1990))

In addition to the work at Sandia, Planas-Cuchi, et al., (1996) have observed a reduction in combustion efficiency when an object is engulfed in fire. They propose a 'hindrance factor' ξ as the ratio between the heat released in combustion of a pool fire with an obstacle, and the same pool with a free surface as a means of accounting for this. To these theories it could be added that the increase in characteristic length and reduction in corresponding convection heat transfer coefficient could be responsible for a decrease in total net heat flux measured.

The convective component of heat transfer has been estimated in a number of studies. Schneider and Kent (1989) used iteration to determine values of surface emissivity (0.46) and coefficient of convective heat transfer (40 W/m^2K) that predict a partition of 80% radiative and 20% convective heat transfer. However, this calculation relies on a best fit to measured values and is therefore subject to interpretation. Nakos and Keltner analysed similar data generated using the same facility and predicted the convective component to account for 10-20% of the total heat flux (Nakos & Keltner, 1989).

Gregory, et al., (1989) noted that variations in convective heat transfer were significant. Cylinders in vertical cross-flow will have a convective heat transfer coefficient that is greatest at the bottom, decreases at the sides, and increases again at the top. Using small calorimeter data and correlations for forced convection by Kreith (1963) they estimate the convective component at 6.5-19%. They note that the larger the radius of cylinder engulfed, the lower the convective part of the overall flux.

Nakos, et al., (1990) summarised conclusions from a wide range of test series conducted at Sandia using a range of instruments. Transpiration gauges were used in two separate tests to calculate flame emissivity values of 0.82-0.75. This compares with a flame emissivity of 0.91 calculated using a flame extinction

coefficient of 1 m^{-1}. The convective heat transfer coefficient they used within their calculations was 57 W/m^2K, referencing work by Brown, et al., (1990) and Russell & Canfield (1973) as the source.

2.1.8.5 Summary of pool fire conditions

Average temperatures in large pool fires have been characterised as typically reaching 950-1000°C, with the hottest point approximately 2 m above the surface of the fuel. The hazard presented by radiation from a non-engulfing hydrocarbon pool fire can be reasonably well characterised. The surface emissive power of different fuel types has been extensively tested and models exist to calculate the heat flux to a distant object. The types of pool fire hazards relevant to LPG vessels (gasoline, diesel, LPG fuels) all burn with smoky flames that result in a reduction in SEP as diameter increases beyond 3-4 m. It can be concluded that the pool fire engulfment scenario is thermally more severe than the non-engulfing radiant heat input scenario. It is noted, however, that pool fire heating conditions and full-engulfment may not necessarily be 'worst-case' conditions in terms of the vessel response; large-scale momentum driven fires (known as jet-fires) will typically give more severe heating conditions.

The net heat flux to cool, thermally massive, engulfed objects has been consistently measured as being lower than those recorded in pool fires using small-scale water-cooled heat flux gauges or plate calorimeters. Large calorimeters (either water-cooled or insulated) typically record a net flux of at least 20% lower than their small-scale counterparts in aviation fuel fires. On this basis it can be concluded the large-scale test evidence is representative of actual 'worst-case' scenarios, and unlikely to increase in severity with further increases in scale despite higher values reported in literature. It is concluded that average net heat fluxes to large objects engulfed in large pool fires of gasoline, diesel or LPG fuels are within the range of 80-120 kW/m^2. Peak heat fluxes of 150 kW/m^2 have been measured, but for short durations only.

To the author's knowledge, there has been no measurement of the net heat flux to large objects engulfed in large LPG pool fires other than the 1.7 m^3 sphere test performed as part of the Gasafe programme (GEIE, 1993). This remains an area of uncertainty, however a conservative estimate of the radiative component to engulfed objects is proposed as 100 kW/m^2. This was the maximum value Mizner and Eyre (1983) recorded with a radiometer having an unobstructed view of the luminous part of an LPG flame, windward of the flame

during water spill testing. The overall degree of severity of LPG pool fires on land is currently considered to be no worse than that of gasoline and diesel fires (Fire and Blast Investigation Group, 2010).

The majority of the heat transfer to cold objects in pool fires (>80%) is generally due to radiation. Optically thin flames have a lower flame emissivity and are likely to reduce the peak temperature reached by the engulfed object. Development of a fire test procedure should take into consideration the ratio between radiative and convective heat transfer, and the different optical thickness of the flames, in order to subject test specimens to representative heating conditions.

2.1.9 Proposed conditions for vessel test procedure development

Any standard test procedure needs to be sufficiently representative of the specific hazard it aims to reproduce, while being sufficiently conservative to give confidence to users that it provides an adequate measurement of the safety of the item being tested. Pool fires fuelled by gasoline/diesel/Fuel oil/LPG pool fires and LPG jet fires have been identified as the hazards.

Taking into account the heat fluxes, temperatures and environmental effects recorded by vessels subjected to hydrocarbon pool fires or pool fire simulation tests, while also considering the modes of failure of vessels and the criticality of vessel wall areas, leads to the proposal of the following requirements:

- Net heat flux to the vessel of 80-120 kW/m^2 (preferably >100 kW/m^2 to be conservative)
- Minimum radiative fraction to a cool object of 0.7
- Full engulfment in flame
- Sufficient uniformity of heating to ensure all parts of an empty vessel are exposed to a heat flux of at least 50 kW/m^2 (the minimum value recorded in actual vessel tests engulfed in pool fire)
- Use of a burner arrangement using a commercially available fuel to allow control over the degree of engulfment, rapid start-up and rapid termination of the test; propane or butane are recommended over methane due to the high radiative fraction of the total heat flux (due to their increased propensity to form soot)
- Calibration testing to assess the net heat flux to the vessel and the degree of uniformity
- Reasonable resistance to wind effects, or wind effects quantified and limitations applied to test conditions

The above recommended heat flux value is equivalent to an effective black body flame temperature of 880°C as determined by equation 2.0 as the temperature of a black-body with an emissive power per unit area of 100 kW/m^2. For a flame with an emissivity of 0.7 this heat flux value equates to a flame temperature of approximately 950°C.

A test procedure that achieves the target conditions can be considered both conservative for the large majority of pool or spill fire scenarios and sufficiently representative of 'real' pool fire conditions. Such a fire would then be a suitable basis for the generation of the experimental data necessary to meet the objectives of this study.

Furthermore, a standardised test method based on the above recommendations would be suitable as the basis for an international standard for pressure vessel testing which is non-prescriptive in vessel design or acceptance criteria.

2.2 Experimental equipment literature review

2.2.1 Introduction

This section reviews additional experimental studies and techniques applied to the following areas relevant to understanding pressure vessels in more detail:

- Studies of tanks and vessels aiming to observe or characterise the full-field flow effects
- Boiling studies intended to characterise bubble characteristics
- Turbulent free-convection boundary layer studies of subcooled fluids

Clearly, all three of the points above encompass a substantial range of works and knowledge, and this section is not intended to be exhaustive, but to highlight key works and comment on the techniques and instrumentation used.

2.2.2 Studies of bulk fluid behaviour and thermal stratification in vessels or tanks

The previous section detailed numerous pressure vessel tests that form the body of large-scale test evidence. Each of the tests described included pressure transducers, vessel wall thermocouples, and internal thermocouples (sometimes in large numbers), but were otherwise limited in the variety of instrumentation used. Internal thermocouples were typically placed in a central positioned vertical array or in a widely-spaced grid. No instrumentation was placed in the fluid close to the wall (within 10 mm) for the purposes of characterising the boundary layers formed during heating.

Venart, et al., (1984) designed and built a novel apparatus to simulate LPG vessel behaviour on a small scale. It consisted of a 40 litre horizontal cylinder with heaters between the double walls, and a full-bore observation window at one end (see Figure 6). Pressure transducers and stainless steel sheathed type J or type T thermocouples were used inside the vessel. Heat fluxes up to 65 kW/m^2 could be applied, and PRV action simulated via discharge pipes and solenoid valves. The apparatus was capable of performing a significant number of tests, varying fill rate, fluid, discharge properties, heat flux, degree of subcooling, etc.

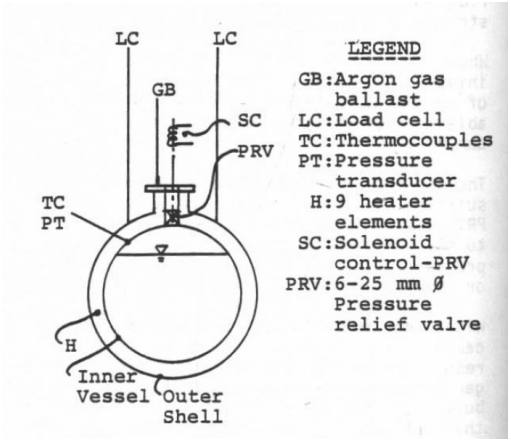

Figure 6 – Reproduced from (Venart, et al., 1984)

Sollows, et al., (1988) published work to characterise flow patterns in a horizontal cylinder (150 mm diameter) using a laser and fluorescent dye dissolved in the test fluid. The dye was visually captured in successive laser images allowing stream lines to be determined. Time-step analysis also permitted a quantitative analysis of velocities. In commentary on the technique, it was noted that there was difficulty resolving high velocities as these resulted in low concentration gradients.

Inada, et al., (1999) used a laser light sheet and holographic interferometry to assess the flow and temperature properties of air in a rectangular chamber. Photographic observations of smoke particles in the light sheet were used to capture flow effects, while holographic plates were exposed without flow and then recorded during flow effects to give isotherm patterns. An alternative technique based on the same physical principle of wavelength shifting is Laser Doppler Anemometry (LDA), also known as laser doppler velocimetry.

LDA splits a light beam and focuses the two resulting beams such that they intersect at a known distance. The scattered light is received by a probe and analysed to give a directional velocity measurement. Two disadvantages of LDA are that it returns the velocity at only the specific point at which the beams intersect and that the focal distance is at a fixed distance from the probe. LDA was considered for the current study but discounted because a wider field of flow information was targeted and the requirements to mount the probe within the pressure vessel meant practical difficulties could not be overcome.

Ganguli, et al., (2010) used particle imaging velocimetry (PIV) to characterise a 2D flow pattern within a cylindrical tank undergoing natural convection and wall boiling at a central heater. PIV uses a laser to create a 2D light sheet within the flow, and cameras perpendicular to the light sheet to record flow patterns. Flow

capture is assisted through the addition of seeding particles, of similar density to the fluid, to scatter the light sheet. The images are typically analysed using dedicated algorithms and software to create vector maps. PIV techniques have become increasingly widespread, with further studies on flow in tanks undertaken by Gandhi, et al., (2011), among others, as they are relatively inexpensive and provide a wide field of measurement.

Shi, et al., (2012) studied thermal stratification in LPG cylinders through use of PT100 thermal resistance detectors (RTDs), as an alternative to thermocouples. They are generally considered to be more accurate and more stable, however less resilient and with an upper temperature limit of approximately 500°C. Their results (obtained at a maximum heat flux of 40 kW/m^2) demonstrated that the thermal boundary layer was very thin, with the temperature at 1 mm from the wall being no greater than 3°C above the bulk fluid temperature (as recorded by RTDs at 75 mm).

2.2.3 Turbulent free convection boundary layer studies

Early studies of convective boundary layers typically used air as the test fluid and a moveable thermocouple to obtain temperature profiles (e.g. Warner and Arpaci, 1968). An increasing number of studies of water and other test fluids were conducted during the '60s and '70s, (for examples see the references within Kader (1981)). Optical techniques to visualise the flow have been undertaken by some researchers. For example, Fujii & Imura (1972) used shadowgraphy to observe flow lines of laminar and turbulent boundary layers, observing the point of detachment. They also captured flow patterns by the addition of aluminium particles, in a similar manner to PIV. Shadowgraphy is a simplified form of Shlieren photography, which is a technique that uses the refraction of light waves to visualise flow patterns. In the case of fluid boundary layers, the refraction is typically caused by thermally induced density variations. Srivastava, et al., (2004) compared shadowgraphy, Schlieren photography and interferometry as a means of characterising convective flow in a cavity and concluded that for high temperature gradients interferometry was corrupted by refraction errors, and shadowgraphy gives the best results for fluids. Purely optical techniques such as shadowgraphy were considered for the current study, however the inability to isolate a 2D plane perpendicular to the camera, and the difficulty in quantifying results, led to the techniques being discounted.

Laser doppler anemometry has been used in numerous studies to characterise boundary layers, e.g. Miyamoto, et al., (1982) and Cheesewright, et al., (1984). An alternative method of measuring flow velocities is constant temperature anemometry (CTA). CTA is a technique that uses the cooling effect of the fluid flow to

calculate the flow velocity by relating it to the calibrated values of current required to maintain a constant temperature. It is also referred to as hot-wire anemometry (HWA), or hot-film anemometry when the conductive surface is a film, as it is often when used with liquids. This method can be used to give velocity, temperature and turbulence structure measurements on a small scale, however it gives point measurements only, cannot resolve the flow direction directly, requires calibration (unlike LDA) and requires the probe to be placed in the flow.

Tsuji & Nagano (1988) performed detailed characterisation of the boundary layers formed by water in contact with a large copper surface heated to fixed temperatures. They used hot-wire anemometry to record the temperatures and velocities, commenting that the HWA method gave better results than the LDA method in past studies due to the latter measuring the properties over a volume. The hot-wire method used by Tsuji & Nagano was that developed previously by Hishida and Nagano (1978), and used tungsten wires 3.1 μm in diameter, with a cold wire upstream of two hot wire prongs. Temperatures were also measured using 0.025 mm Pt-Ro-Pt thermocouples, with results obtained differing from the HWA method by up to 15%.

Marie, et al., (1997) performed experiments with upward bubbly flow in a pipe for the purpose of investigating the effect of bubbles on the turbulence intensity. They used LDA to investigate the turbulent boundary layer characteristics without bubbles present, but instead used a conical hot film variant of CTA to measure the mean velocity and longitudinal turbulence profiles when bubbles were present.

2.2.4 Boiling studies

Boiling studies are distinguished from bubbly flow studies above by measurement or observation of the heated surface. The majority of experimental boiling studies are based on the principle of direct observation of the growing and departing bubbles, to obtain information on various bubble parameters including the bubble departure diameter (D), the bubble departure frequency (f), the nucleation site density (N), the heat transfer coefficient (h), the bubble growth rate, and the bubble waiting time (t_w). Boiling models, discussed further in section 2.4.4, typically rely on sub-models for the parameters listed above, which are themselves typically based on correlations derived from high-speed photography experiments listed below.

Boiling studies can be divided into flow boiling and pool boiling studies. They could also be further divided by numerous characteristics, including saturated or subcooled boiling, and constant heat flux or constant wall temperature heating conditions. The number of boiling studies conducted is extensive, and is beyond the

scope of the current work to describe in detail. However, the majority of boiling models in common use today use only a limited number of submodels, based on a limited number of experimental studies. Selected important experimental studies that include direct high-speed photography of bubble formation are listed below.

Flow boiling studies typically use a vertical pipe or cavity with the heated surface being either a rod (or wire) placed within the flow or a heated surface forming a side of the cavity. A window (or clear outer surface) allows direct observation of the bubbles. Means of maintaining a constant flow rate is required. Examples of such studies include: Tolubinsky & Kostanchuk (1970), Unal (1976), Lemmert & Chawla (1977), Del Valle & Kenning (1985), Basu, et al., (2002), and Situ, et al., (2004).

Pool boiling studies include Zuber (1959), Cole (1960), Ivey (1967), Petrovic, et al., (2004) and Jung & Kim (2016). Like flow boiling experiments, the majority of pool boiling studies used a clear pipe or cavity with an immersed heating wire or heating plate forming a side of the cavity.

Numerous point measurement techniques have been used to obtain flow information, although flow with a significant vapour volume fraction (or 'bubbly flow') presents a challenge to characterise due to the interaction of phases with some probe types. Marie, et al., (1997) used an Optoflow 'Photonectics' optical probe to measure void fraction and local bubble frequency with high-speed video to capture bubble shapes and velocity vectors. Optical probes have a needle-shaped tip, intended to pierce bubbles, that emits IR light. When the tip of the probe is in liquid the light will be reflected back to a receiver, whereas it will be transmitted away when the tip of the probe is in vapour. Multiple probe tips can be used to measure bubble velocities and further characteristics. Roy, et al., (1997) also used a combination of techniques to characterise bubbly flow, with LDA, dual-sensor optical probes and CTA/HFA.

Dual tip conductivity probes have been used by numerous researchers, for example Aszodi, et al., (2000), Lee, et al., (2002), Situ, et al., (2004), Yun, et al., (2008), and Ono and Sakashita (2009), for measurements of void fraction and sometimes bubble velocity. Two needle-shaped probes between 1 mm and 5 mm apart, depending on the expected bubble diameter, detect changes in the current flowing between the tips due to the different electrical resistance of fluid and vapour.

Pitot tubes have been used to measure liquid flow velocities by numerous researchers, for example Lee, et al., (2002), and Yun, et al., (2008). They are typically employed with single-phase flow, but have been used in two-phase flow with models to correlate the results back to fluid velocities.

Micro-thermocouples have been used by some researchers to directly measure liquid and gas temperatures. Warrier, et al., (2002) investigated bubble collapse rates using 250 µm type-k thermocouples attached to a micrometers to allow highly accurate positioning near the heated surface. They combined it with direct high-speed photography to capture bubble characteristics. Their results show they were able to resolve the thermal boundary layer in the region of the wall. Kim & Park (2011) performed a similar study using 12.7 µm thermocouples (again attached to a micrometer rig for positioning) and used a single camera and array of mirrors to obtain simultaneous observations from two directions. The images were then analysed using two-image orthogonal processing to reconstruct the bubble positions. These studies indicate that at low degrees of subcooling (<25°C) at the heat fluxes of interest to the current study, thermal boundary layers form in water and can be resolved within 10 mm to 20 mm of the wall.

More recently, non-invasive techniques with a wider field of measurement have been developed based on combining optical techniques. Estrada-Perez & Hassan (2010) performed Particle Tracking Velocimetry (PTV) on subcooled flow boiling of water in a vertical channel. They commented that PTV is distinguished from PIV by the smaller number of seeding particles and the direct tracking of each particle, rather than measurements being based over averaging a large number of particles as with PIV, and that PTV was preferred for two-phase flows due to the ability to distinguish between the phases. Estrada-Perez, et al., (2015) developed the technique further to include concurrent PTV, shadowgraphy and IR-thermography. A translucent indium-tin-oxide heating surface was used to allow direct IR- thermography of the surface, allowing nucleation sites to be directly observed. The laser and LED lights required for PTV and shadowgraphy were set to pulse sequentially, and the camera used for both was set to capture images accordingly. In post-experiment analysis, the shadowgraphy allowed accurate identification of bubble locations, and anomalous PTV vectors within the bubble regions could be removed to improve overall accuracy.

Jung & Kim (2016) also combined optical techniques with an indium-tin-oxide transparent film as the heating source. They used shadowgraphy, total reflectance and IR-thermography, with their focus on the influence of heating surface orientation on bubble characteristics.

The surface roughness is known to have a significant influence on boiling behaviour, however it is typically poorly characterised in most boiling studies. Goel, et al., (2017) studied subcooled pool boiling studies of water using high speed photography having first characterised the topography of the surface in detail using a digital stylus profilometer and scanning electron microscopy (SEM).

2.2.5 Discussion of experimental techniques and instrumentation relevant to pressure vessel testing

The test equipment is described in more detail in section 33, however it was clear during design of the equipment that the instrumentation must meet certain practical requirements:

- a significant quantity of instruments was required and hence affordability must be considered, given the limited budget
- instruments within the test fluid must not require frequent adjustment, as internal access of the test vessel is not trivial
- instruments must be physically robust enough to withstand field conditions, noting installation and use will be subject to physical forces associated with significant temperature gradients and opening/closing of pressure vessels using fork-lifts and cranes
- replacement of instruments would be a practical and financial challenge. Instruments should therefore be hardy enough to survive repeated test cycles

For the reasons above, consideration was given to instruments that do not require frequent calibration and have good resistance to damage or displacement due to physical movement during installation or when in-situ. As the vessel was to be fully engulfed in fire, consideration was also given to the thermal stability of the instrumentation extending from the vessel through the fire and region of significant incident radiation to a 'cool' area. Although it is possible to protect most items given sufficient money and time to design a solution, cooling systems or excessive instrumentation on the outside of the vessel would directly interfere with the fire in that area. Therefore, instrumentation that required a physical presence on the outside of the vessel in the zone of interest was discounted. Thermal insulation was planned to be used where instrumentation did, inevitably, exit the vessel, however the aim was for this to occur near the bottom of the vessel where thermal boundary layer formation is not expected due to flow instabilities (as discussed further in section 2.4).

Temperature measurement methods in the studies listed above include thermocouples, micro-thermocouples, RTDs and CTA/HWA. RTDs are considered the most accurate and stable, but their limited maximum temperature means they are prone to damage if placed in the vapour space of a fully engulfed vessel. Given the intention throughout the project to vary fill-level and to expose the vapour space to high heat fluxes these were ruled out. It was also undesirable to have different types of instrumentation within the vessel, to ensure consistency across varying locations. CTA/HWA was discounted due to the cost and their sensitivity to

calibration to achieve reliable results across a range of bubbly flow conditions. Micro-thermocouples have been shown to be capable of accurately resolving the temperature profile in bubbly flow thermal boundary layers, however equal accuracy is required when positioning the thermocouples. Micro-thermocouples are considered to be the best instruments for this purpose, however concerns over the resilience of the probe when being installed through a feedthrough, the ability of the probe to remain in position during set-up and operation of the vessel, and the increased cost, led to conventional thermocouples being selected. Various types of Inconel-sheathed insulated type-K thermocouples were compared during commissioning tests, and one selected for the primary tests (as described in section 3).

Velocity measurement methods can be divided into point-measurements such as CTA/HWA, pitot tubes, dual conductance probes, and LDA, and wide-field measurements, such as PIV/PTV, shadowgraphy, holographic interferometry, and photography of entrained particles or fluorescent dyes. The latter three methods were ruled out as they are not suited to scenarios where there is a large temperature gradient or where the plane of interest must be viewed through a substantial depth of fluid. Point-measurement techniques were also discounted as the access restrictions and external fire would make adjustment during a test impractical, limiting the set-up to measurements at only one position per test. A wide-field of velocity measurements is clearly desirable, so PIV/PTV was identified as the velocity measurement technique to implement.

Beyond the specific instrumentation described above, it was clear from the custom apparatus designed by Venart, et al., (1984) and the extensive boiling studies performed, that there is a lot to be learnt by being able to visualise the flow patterns and lading behaviour. In particular, two-phase swell on PRV activation has been observed on small-scale with low degrees of subcooling, but it remains unknown to what extent this occurs in larger vessels with greater subcooling. An early objective within the design of the apparatus for the current study was to include a full-bore window (or at least numerous sight-glasses on a full-bore blanking plate) to allow direct observation of flow, boiling and bubbles.

Given the limitations in project budget and timeframe, it was decided not to employ additional measurement techniques beyond the conventional optical video, PIV, thermocouples and pressure transducers used. With hindsight, numerous improvements can be proposed to the PIV/PTV set-up created for velocity measurement, the set-up for temperature measurement, and to additional instrumentation. There are discussed further in section 7.1.

2.3 Numerical modelling of pressure vessels

2.3.1 Introduction

Early models of the pressurisation rate of pressure liquefied gas vessels exposed to fire used a lumped parameter approach to predict pressure rise (Moodie, 1988). The failure of single zone models to reliably predict pressurisation (Birk, 2000) led to the development of multi-zone models that could account for thermal stratification. Despite the improvements in modelling capability that these models bring, they remain limited by their reliance on empirical parameters that govern the transfer of energy and mass between the various zones.

Attempts to reduce the empiricism of zone models through implementation of integral models for the thermal boundary layer formation and sub-cooled core mixing have been limited in success due to the reliance of such models on further empirical parameters, thus preventing a significant expansion in scope beyond the original zone models they sought to improve upon.

Numerical models capable of capturing flow effects across the entire vessel cross-section have superseded zone models as the predominant area of current research. Such models have the capability to capture the thermal stratification effect in detail, in both two and three dimensions, while removing a degree of empiricism necessary in zone models.

This work reviews numerical studies of pressure vessels subject to heat exposure. Related further work is reviewed focussing predominantly on studies of thermal stratification, multiphase flow and boiling of liquids in containers.

2.3.2 Previous studies on LPG vessels

Early attempts to reduce the reliance of zone models on empirical correlations for heat and mass transfer between zones implemented an integral approach to model the convection inside the liquid phase (Babe (1989), Aydemir, et al., (1984), Yu, et al., (1992)). The various zones were considered as control volumes and the conservation equations for mass and energy were solved. Natural convection in the boundary layer was modelled through integration of the partial differential equations for conservation of mass, momentum, and energy. The pressure development was obtained by a time-marching iterative procedure. Integral approaches for the boundary zone were validated against test data, however they did not remove empiricism entirely, due to the reliance on experimentally derived factors governing zone interaction.

The first dedicated CFD routine for LPG vessels subject to fire exposure appears to have been developed by Hadjisophocleus (1989). The flow field was solved in 2D for a boundary-fitted coordinate system, in a semi-implicit manner by solving the equations of conservation of mass, energy and momentum using the finite volume method. Results allowed for a range of conclusions to be drawn on the flow patterns inside a vessel. Recommendations at the time proposed: the development of a 3D model, consideration of alternative turbulence models, inclusion of mass transfer at the liquid interface, and future inclusion of the effects of boiling.

Advancements in commercial CFD codes since the early 90's have led to an increase in researchers developing pressure vessel simulations in readily available codes, particularly ANSYS Fluent and CFX.

An early attempt to model LPG vessels in ANSYS FLUENT was made by Yoon & Birk (2004). In this study, Birk and Yoon considered only the convection within the liquid, ignoring boiling and the vapour space. Simulations were performed in 3D using the volume of fluid (VOF) model for two-phase flow. The volume of fluid model, first proposed by Hirt & Nicholas (1981), is popular for multiphase flow due to its computational efficiency, resulting from the fluids sharing a single set of momentum equations. The volume fraction of the phases is tracked throughout the computational domain, but a limitation of the model lies in the phases sharing the same velocity and temperature field. The study investigated both laminar and turbulent flow, the latter using the standard k-ε model, with the primary objectives being:

1. To demonstrate that a CFD model in a commercial code could replicate experimental results
2. To calculate a parameter for pressurisation rate (ß) for a range of insulation defect scenarios

The report concluded that results are promising, and that the turbulent model gave a better match with experimental data. Further recommendations included assessing the influence of the vapour space and the effect of choosing alternative turbulence models.

Since 2004 further researchers have undertaken similar work. Bi, et al., (2011) used ANSYS Fluent to simulate an LPG vessel exposed to jet fire. The VOF multiphase model was used with the k-ε turbulence model. A similar model was used by Ren, et al., (2013) to study thermal de-stratification, however this assumed laminar flow.

The University of Bologna has been active in CFD modelling of LPG tanks since 2012. A two-dimensional model was published by D'Aulisa, et al., (2014) and was extended to different dimensions of vessel by Landucci, et al., (2016). Like the models mentioned above, Landucci used ANSYS Fluent implementing the VOF model.

Turbulence was assumed to be present from the start and modelled via the standard k-ε model. Boiling was included via the Hertz-Knudsen equations and implemented in the continuity equation.

Summary of LPG Studies

Only a limited number of CFD investigations of LPG vessel response have been performed. Each study has been able to demonstrate a reasonable match to experimental data obtained in the particular test (or tests) against which it was compared, indicating that the models are capable of being used in their current form to predict pressurisation rate at a level acceptable to industry, noting the industry benchmark is currently zone models.

However, deficiencies can be identified in the current knowledge base of numerical models of LPG tanks. The validation is predominantly based on comparison with experimentally measured pressure values, often supplemented by a small number of bulk liquid temperature measurements. It does not extend to boundary layer temperature measurements, or to fluid or flow property measurements (such as velocity or density).

Implementation of wall boiling is another considerable challenge that is either ignored or highly simplified in existing models. Handling boiling through a set of phase-change equations (e.g. the Lee or Hertz-Knudsen) approach is far from desirable, as these are based on diffusion across a flat liquid and vapour interface and assume a constant pressure and quasi- thermal equilibrium. Wall boiling is a very different scenario, influenced by a wider range of parameters and resulting in a degree of subcooling regardless of whether the liquid is at equilibrium prior to the onset of heating.

The above points imply that existing models can give results that appear reasonable, but which are not necessarily capturing the correct physical behaviour of the system. Such models consequently remain limited in their applicability to the scope of the dataset used to validate them, as is the case with current zone models.

In summary, the body of existing CFD models for LPG vessels is limited to the use of the Volume of Fluid Model in ANSYS FLUENT, and multiphase flow considered either as laminar or turbulent, the latter modelled through use of the two-equation standard k-ε model. Boiling has either been ignored or implemented based on equilibrium diffusion equations intended for a flat phase interface (Lee, Hertz-Knudsen equations). Alternative multiphase models, turbulence models and boiling models are available, but have not been studied. To improve the numerical modelling of LPG vessels recent developments in modelling subcooled boiling in closed systems should be considered.

2.3.3 Non-pressure vessel CFD models of subcooled boiling and thermal stratification

Although the number of numerical model studies dedicated to LPG vessels is limited, numerical modelling of boiling generally is a subject of active research. Prior to the widespread use of CFD, studies in the early latter half of the 20th century initially focussed on correlations between the boiling heat flux, the degree of wall superheat and the fluid and surface properties. A heat flux partitioning approach initially proposed by Rohsenow (1953) considered the total heat transfer during boiling as the sum of the heat transfer through localised nucleate boiling and convection. Subsequent developments of this concept included: adaptation of the additive method to include a correction factor intended to account for interactions between the fluid and bubbles under flow, e.g. Chen (1963); splitting the nucleate boiling heat transfer into heat transfer by evaporation and quenching following bubble departure, e.g. Rohsenow & Mikic (1969); and further development of mechanistic models of bubble growth and detachment to describe the components of the partitioning approach in a more predictive way.

The difficulty in characterising the heater surface properties of various boiling studies and differences in experimental conditions resulted in a wide range of empirical correlations being produced through to the 1990's, many of which varied in scope and even in the surface or fluid properties included. Development of such correlations has been superseded following the first implementation of a heat flux partitioning model into a two-dimensional multiphase numerical model by Kurul & Podowski (1991). This model is frequently referred to as the RPI model, after the Rensselaer Polytechnic Institute.

The RPI model makes use of numerous correlations derived from experimental data relating to bubble characteristics. In his PhD thesis Kurul (1990) lists a number of correlations which were assessed, and he concludes with an endorsement of the following: nucleation site density (Lemmert & Chawla, 1977); bubble departure diameter (Tolubinsky & Kostanchuk, 1970); and bubble departure frequency (Ceumern-Lindenstjerna, 1976), which can be related back to Cole (1960).

Numerical modelling has also been used extensively to model a wide range of boiling scenarios, on a range of scales. Large numbers of studies have focussed on the detailed development and detachment of bubbles. A broad review of such studies by Kharangate & Mudawar (2017) indicates that a substantial number have been performed using a VOF multiphase modelling approach and focussed on resolving the phase interface on a small scale. An increasing number of boiling studies use an Eulerian-Eulerian (Eu-Eu) approach, which solves separate equations for conservation of mass, energy and momentum for each phase and has additional closing

equations to handle the phase interactions. This method is considered by many to be more sophisticated, if generally less stable, and hence it is regarded as currently the most common approach for modelling two-phase flow in cases where there is a significant fraction of both phases. However, it also does not directly track the phase interphase, unlike the VOF and level-set methods, and hence its application in boiling studies has been somewhat limited.

The Eu-Eu approach considers the two phases to be interpenetrating continua, and is implemented in ANSYS FLUENT as the Eulerian model or the mixture model, and ANSYS CFX as the Eulerian-Eulerian multiphase model. A brief description of this model type is given by Krepper & Rzehak (2011): "In this approach, balance equations for mass, momentum and energy are written for each phase, i.e., gas and liquid, separately and weighted by the so-called volume fraction which represents the ensemble averaged probability of occurrence for each phase at a certain point in time and space". However, as they go on to state, closing the equations requires the use of exchange terms between the phases, giving the interfacial forces and expressions for the heat flux and mass flux. Such expressions must be derived analytically or empirically, and therefore are limited in applicability to the scope of data used for their development and validation.

Some recent studies have implemented the Eu-Eu model with a phase change model based on the Hertz-Knudsen or Lee model, e.g. Wu, et al., (2007), however the implementation of the RPI wall boiling model in ANSYS software as an option compatible with the Eu-Eu model has led to an increasing number of studies implementing it, in many cases adopting the model with very little adaptation. Brief descriptions of selected relevant developments of the RPI model are given below and summarised in Table 5.

Koncar, et al., (2004) used the Eu-Eu multiphase model in CFX 4.3 combined with the RPI wall boiling model to simulate low-pressure subcooled nucleate flow boiling of water. In their introduction, the authors highlight the importance of dedicated studies for low-pressure conditions (which they consider to be <10 bar), stating: "At low pressure, nucleated bubbles are larger and move further away from the heated wall into the cooler liquid before condensing, thus creating a different flow structure." The work claimed to be the first multi-dimensional study of boiling flow using the Eu-Eu multiphase model type at low pressure. To adapt the standard RPI boiling model built-in to CFX at the time a number of closing relationships were used by the authors. The k-ε turbulence model was used with an additional term for bubble induced turbulence in the liquid phase (Sato, et al., 1981). The grid cell next to the heated wall had a size corresponding to a Y+ value of between 50 and 80. A logarithmic wall function used for the velocity profile in the region of between the

laminar sub-layer (Y^+ = 11.23) and the core of the turbulent flow (Y^+ = 300). The bubble diameter at departure was not modelled as a linear function of subcooling (as per the built-in RPI model at the time) but instead used a mechanistic model proposed by Unal (1976) with an empirical constant added to extend the scope to heat fluxes lower than originally considered. The maximum bubble diameter after departure was prescribed as a function of the bubble diameter at departure, the distance from the heated wall, and the degree of subcooling. A further modification to the in-built CFX RPI model was a departure from a single constant saturation temperature across the entire domain, replacing it with a calculated value based on the local static pressure. The primary aim of the work by Koncar, et al., (2004) was a sensitivity analysis of the closure equations proposed, and they concluded that two aspects were particularly important to develop further: the lateral hydrodynamic mechanisms (the lift force, the wall lubrication force and mixing due to bubble-induced turbulence), and the variation of bubble diameter, both at departure and in the bulk flow, as affected by local conditions.

Krepper, et al., (2007) continued to develop a model for multiphase flow with the RPI wall boiling model within CFX for high pressure water boiling scenarios such as nuclear fuel assembly design. The turbulence model used was modified to the Shear Stress Transport (SST) model (Mentor, 1994). In their comment on the performance of the model the authors highlighted the need for further research into the wall force models (wall lubrication model, typically from Antal (1991) or Tomiyama (1998)), the momentum exchange between the fluid and bubbles, and the bubble size at departure.

Ganguli, et al., (2010) used the work by Krepper, et al., (2007) as the basis for further study on a cylindrical container of water heated by a central tube. Their work implemented a user defined function (UDF) to handle mass transfer within the bulk fluid between the liquid and vapour phase (bubbles). Gandhi, et al., (2011) used the same model to investigate water in a rectangular tank with a single and multiple heating tubes. Both studies used PIV to investigate bubble diameter to provide input data for the bubble diameter parameter required by the RPI wall boiling model implemented in Fluent.

Krepper & Rzehak (2011) further developed their previously used model to simulate dichlorodifluoromethane subcooled flow boiling. They found a significant improvement in the predicted velocity profiles was obtained through the use of a turbulent wall function designed for boiling flow (see Ramsforter, et al., (2005) and references in Krepper & Rzehak (2011)), which relates the hydrodynamic roughness to the bubble nucleation site density and bubble size (in effect, treating the wall with bubbles attached as a rough wall). In concluding,

the authors state that further improvement in the velocity profiles may be achieved through modification of the k-epsilon, k-omega turbulence models to specifically consider two phases by inclusion of source terms to account for bubble influence (see references within Krepper & Rzehak (2011)). They also concluded that the gas volume fraction could not be accurately predicted when using a single bubble diameter, and proposed replacing this with a model that could handle a range of bubble sizes.

Further work building on the recommendations given above was published by Krepper, et al., (2013) to overcome the limitations of applying a single bubble diameter. A population balance approach model was implemented, based on the MUSIG model (Lo (2000), Luas and Prasser (2007) and references in Krepper, et al., (2013)), with the addition of a source term to handle the size of bubbles generated at the wall. Improvement in modelling of bubble coalescence and break-up was also sought by moving away from accounting for bubble influence on bulk turbulence through a modification to the effective viscosity (Sato et al., 1981), to handling it though the inclusion of bubble-dependent source terms in the turbulence model equations for k, epsilon and omega. Simulation results presented indicate the above approach was able to capture the gradients in velocity and volume fractions that occur when moving from the heated surface to the bulk. The authors note, however, that calibration factors had to be introduced for the bubble coalescence and breakup models, and that further development of such models is required for reliable simulation. Bubble coalition and breakup is strongly influenced by turbulence in the two-phase flow, and the authors recommend further investigation of approaches to modelling bubble-laden turbulent flow. In their final conclusion, the authors highlight the over-prediction of the vapour volume fraction in the near-wall region with both single and multi-bubble size models. They suggest that possible reasons include the lack of a force that acts to push bubbles away from the wall, or the neglect of swarm effects in the lift and drag force models.

A general challenge when implementing the RPI model (Kurul & Podowski, 1991) relates to the necessary minimum grid size adjacent to the heated wall. Grids that are too fine prevent convergence, attributable typically to an unrealistically high volume fraction of vapour generated (either tending to a vapour volume fraction of one) or to too low a vapour volume fraction causing the simulation fluid temperature to become excessively high. Krepper & Rzehak (2011) were able to achieve convergences for non-dimensionalised coordinate for the first cell centre (Y+) value of 70 or greater. More recently, Columbo & Fairweather (2016) have achieved convergence with a heat-wall grid size based on Y^{+}=30. It must be noted, however, that coarse grids in the region of the heated wall limit the ability of the simulation to accurately predict the thermal and

velocity boundary layer profiles. Indeed, the published guidance for ANSYS CFX recommends a grid size based on a Y^+ value of one be used for heat transfer scenarios with scalable wall functions.

A number of recent studies have reviewed the wide range of correlations available for bubble departure diameter, nucleation site density and departure frequency. Prabhudharwadkar, et al., (2014) commented that attempts to improve model performance had focussed on bubble diameter at departure and bubble behaviour after departure. They reviewed recent bubble nucleation site density and bubble departure frequency models and performed a comparison of varying sub-models against Freon data produced by Morel, et al., (2009) and Roy, et al., (2002). In conclusion, they endorse the nucleation site density model of Hibiki & Ishii (2003) and a modified version of the frequency model by Situ, et al., (2004) for high pressure conditions.

In an extensive review of the applicability to low-pressure scenarios of published correlations for bubble departure diameter, bubble nucleation site density and bubble departure frequency, Cheung, et al., (2014) investigated the various possible combinations of the sub-models by Lemmert & Chawla (1977), Basu, et al., (2002), Unal (1976), Fritz (1935) and Kocamustafaogullari & Ishii (1983). They found no single combination gave best predictions for a range of experimental results they obtained. In their conclusions, the authors commented that the nucleation site density was arguably the parameter with the greatest influence on void fraction results, yet despite this no correlation takes into account the degree of subcooling. The same authors implemented a fractal model for nucleation site density in Yeoh, et al., (2014).

A further review of correlations and their applicability to high pressure boiling scenarios was performed by Murallidharan, et al., (2016), in which they discuss the experimental set-up capable of affecting the key bubble parameters of departure diameter, nucleation site density and departure frequency. They conclude that the heat flux partitioning method in combination with the Eu-Eu multiphase flow model is generally adequate, but highlight the importance of suitable nucleation site density and bubble diameter models to achieve a realistic modelling outcome.

Choi, et al., (2016) reviewed the application of the RPI boiling model to low-pressure (atmospheric) water scenarios. They compared correlations for the nucleation site density (Basu, et al., 2002) and the default CFX correlation (Koncar, et al., 2004), based on the original correlation of Lemmert & Chawla (1977), and for the bubble departure frequency (Kocamustafaogullari & Ishii (1983) and Stephan (1992)), against the default CFX 13.0 model. The model results were compared against the experimental data of Maurus, Ilchenko and Sattelmayer (2002) and found the models were generally inadequate for predictions. In concluding, the

authors proposed the model set-up by Koncar, et al., (2004) with the nucleation site density correlation proposed by Kocamustafaogullari & Ishii (1983) as giving the lowest margin of error.

A further review of the accuracy of the Eu-Eu approach with the RPI wall boiling model by Columbo & Fairweather (2016) used STAR-CCM+ to compare the predictive capability of the model against a range of datasets (Garnier, et al., (2001), Roy, et al., (1997), Bartolomej & Chanturiya (1967), Bartolomej, at al. (1982)), and atmospheric pressure water studies by Lee, et al., (2002). The authors adopted the RPI model with the Hibiki and Ishii (1983) nucleation site density. For bubble departure diameter both the Tolubinsky & Kostanchuk (1970) and the Kocamustafaogullari & Ishii (1983) correlations were tested, with the latter being preferred for its wider range of stated applicability. However, the former was adopted in many cases to achieve a better fit between modelling results and experimental data. Further contributions include the use of a second-order Reynolds stress turbulence model and the use of a polydispersed bubble diameter model, based on the moments-based S_Y population balance approach (see references therein) adapted to consider bubble break-up.

In addition to variations in surface and fluid properties, the experimental data available on boiling can be characterised as saturated or subcooled, flow or pool boiling, and high pressure and low-pressure studies. The majority of boiling studies have been performed with water as the test fluid, under subcooled high-pressure flow conditions, designed for application in cooling systems for the nuclear and other industries. No experiments exist that seek to examine in detail boiling characteristics under conditions close to those found within an LPG vessel. Studies that come closest to this scenario, such as Luke (1997) and Luke & Gorenflo (2000), typically differ in scale, the geometry and orientation of the heater surface, and the transient nature of the LPG scenario. They often differ also in terms of the heat fluxes, temperatures and internal pressures obtained under typical pool fire vessel exposure scenarios.

2.3.4 Discussion of developments in subcooled boiling modelling.

In recent years, the Eu-Eu two-fluid multiphase flow model has been increasingly used in conjunction with a heat flux partitioning wall boiling model for the purpose of modelling subcooled boiling in computational fluid dynamics codes. This framework has been shown to be capable of recreating key parameters of experimental evidence, such as void fraction and wall superheat. However, the accuracy of the wall boiling model approach

remains dependent on three key parameters: nucleation site density, bubble departure diameter, and bubble departure frequency.

Despite advances in developing mechanistic sub-models incorporating key physical properties that dictate the preceding bubble parameters, our ability to predict such behaviour is inadequate. The sub-models or correlations used are generally limited in validity to the range of experimental data upon which they were developed. In particular, the fluid type, pressure, degree of subcooling, heat flux, test equipment geometry, and bulk flow velocity all have a substantial effect.

It is therefore reasonable to conclude that the Eu-Eu multiphase model with an RPI boiling model is a reasonable framework to model the pressurisation rate of hazardous material pressure vessels, however the key bubble development parameters should be verified against experimental data and the modelling output should also be directly validated against experiments.

The necessity of experimental validation of boiling aspects presents a challenge for hazardous material modelling. The test evidence available is predominantly based on water, with a substantial number of complementary Freon tests intended to simulate water at more manageable pressures. LPG boiling studies are limited. In developing a numerical model for hazardous materials based on the Eu-Eu with RPI framework there are two aspects to consider: the sub-models and correlations used for the RPI model bubble parameters, and wider model set-up parameters including the grid size and choice of turbulence model. At present, each fluid modelled requires separate experimental validation. The equipment developed as part of this study has the potential to provide detailed data for this purpose.

It is sensible to obtain experimental data for water in the first instance because the availability of correlations for bubble parameters and the wide range of additional experimental evidence available for comparison increases the likelihood of using accurate bubble parameters. A numerical model set-up to replicate water experiments described in this thesis therefore provides the best opportunity to study the influence of various grids, turbulence models and wall functions.

Table 5 – Summary of selected Eu-Eu wall boiling simulations

Author	Software	Turbulence model	Boiling model	Validation test fluid	Experimental instrumentation	Notes
Koncar, Kljenak, Mavko, 2004	CFX 4.3	k-ε	RPI model with Unal, 1976 model for maximum bubble departure diameter	Bartel, 1999 & Lee et al., 2002 Low pressure water tests.	Electrical conductivity probes used for void fraction and vapour velocity	Saturation pressure modelled as function of local static pressure; maximum bubble diameter modelled as a function of distance from wall
Krepper, Koncar, Egorov, 2007	CFX	SST k-ω	RPI model	Bartolomej et al. 1967, 1982. High pressure water experiments	Gamma densitometry for steam volume fraction.	
Ganguli et al. 2010	FLUENT 6.3	SST k-ω	RPI model (default settings) except for bubble diameter	Water (Ra number $5.0x10^{12}$-$3.8x10^{13}$). Constant fluid properties	PIV and HFA	Mass transfer between liquid and vapour phase modelled through a UDF in the source term of the continuity equation (Fluent multiphase Mixture model used)
Gandhi et al. 2011	FLUENT 6.3	SST k-ω	RPI model (default settings)	Water (Ra number $8.5x10^{13}$-$2.6x10^{14}$). Constant fluid properties	Rectangular water tank with central vertical heating rods. PIV (10μm particles, camera min. resolution area 0.6mm)	Ganguli et al 2010. UDF used (Fluent multiphase Mixture model used)
Krepper, Rzehak, 2011	CFX	SST k-ω	RPI model	Dichlorodifluoromethane (R12). Variable properties	Deborah tests. Optical probe used for vapour volume fraction and gas velocities	Turbulent wall function for boiling flows relate hydrodynamic roughness to bubble size and nucleation site density [Koncar, Mavko, 2010]
Krepper, Rzehak, 2013	CFX	SST k-ω with bubble-induced source terms in equations for k, epsilon, omega	RPI model with MUSIG population balance model for bubble size distribution	Dichlorodifluoromethane (R12). Variable properties	As above	
Yeoh et al., 2014	Not stated	Not stated	RPI model with MUSIG population balance model for bubble size distribution	Cheung et al. 2014 Elevated pressure water tests	Gamma densitometer for void fraction measurement. High speed video for bubble size distribution.	Fractal model introduced for nucleation site density, force balance model for departure diameters includes bubble sliding
Columbo & Fairweather, 2016	STAR CCM+ v9.04	Reynold Stress Model	RPI model with a moments-based S_γ population balance approach	A range of water and Freon tests by Garnier et al., 2001, Roy et al., 1997, Bartolomej and Chanturiya, 1967, Bartolomej at al., 1982, Lee et al., 2002		Convergence achieved with near wall grid of Y^+=30

2.4 Free convection and boiling

2.4.1 Introduction

This section considers the modes of heat transfer responsible for the thermohydraulic response of the liquid phase in a full containment pressure vessel during fire. An introduction to the dominant modes of convection and boiling are given, with commentary on which modes are applicable depending on the thermal boundary conditions and the nature of the fluids within the vessel. The purpose of this section is to provide explanation of the concepts discussed in the analysis of test results, found in section 4. It must therefore be noted that the scope of this section has been strictly limited to points deemed relevant to understanding of section 4, and that extensive further information is available in the references herein.

2.4.2 Free convection

At the onset of fire, the vessel wall will be at a temperature below that required to initiate boiling. Conduction of heat through the wall will quite quickly result in free convection at the vessel wall. In cases of pressure liquefied gases the free convection is likely to be very quickly superseded as the dominant mode of heat transfer by boiling, discussed further below. However, liquids with a significant degree of subcooling may continue to have significant heat transfer by convection, either because they do boil, or because boiling occurs over only part of the heated surface.

Pure free convection is defined by the motion of the fluid (liquid or gas) being driven purely by buoyancy forces caused by density differences under gravity. This can be contrasted with forced convection, which is defined by an external force being the cause of fluid motion. In many practical scenarios convection may be mixed (both free and forced). Indeed, it could be argued that the current study of full-containment vessels does not exhibit pure free convection due to the influence of established convection cells and bubble interaction. However, given the absence of mechanical means, the term free convection is used to refer to the conditions within the vessel in the current study.

The buoyancy-driven fluid motion occurring during free convection heat transfer results in establishment of both a thermal and velocity boundary layer. A schematic illustration of this is given in Figure 7, reproduced from Bergman, et al., (2011). The flow can be characterised as either laminar or turbulent. In simplistic terms, laminar flow is that in which the fluid particle motion is predictable, turbulent flow is that in which the fluid particles move with a degree of randomness. Flow due to natural convection will typically start as laminar, and

transition to turbulent after a certain distance along the substrate in the direction of flow. The thickness of velocity boundary layers, and the heat transfer coefficient increases following transition from laminar to turbulent flow.

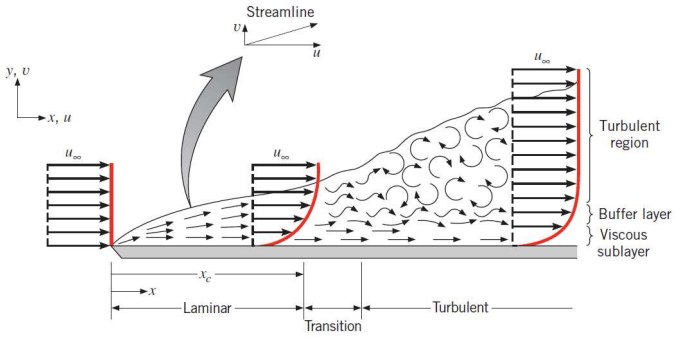

Figure 7 – Boundary layer development along a heated surface, reproduced from (Bergman, et al., 2011).

2.4.2.1 Convection Correlations and Dimensionless Numbers

The basic equation for heat transfer by convection is well known and shown in equation 2.1.

$$q'' = h_c(T_s - T_\infty) \tag{2.1}$$

where:

h_c is the convective coefficient of heat transfer (W/m^{2}K)

T_s is the surface temperature (K)

T_∞ is the bulk liquid temperature (K)

The heat transfer coefficient *h* can be related to the Nusselt number (Nu), which is a dimensionless number that expresses the ratio of convective to conductive heat transfer at a surface.

$$Nu = \frac{hL_c}{k_f} = C(Gr_L Pr)^n \tag{2.2}$$

where:

L_c is the characteristic length

k_f is the thermal conductivity of the fluid

The Nusselt number of a fluid can be further expressed in terms of its Prandtl (Pr) and Grashof (Gr) dimensionless numbers. The Prandtl number (equation 3) is an expression of the momentum diffusivity to the

thermal diffusivity, and is important when considering the thickness of thermal and velocity boundary layers. The Grashof number (equation 2.4, given for a flat plate) is an important parameter for natural convection, and is an expression of the ratio of buoyancy to viscous forces acting on a fluid. The product of the Prandtl and Grashof numbers is known as the Rayleigh number (Ra).

$$\mathrm{Pr} = \frac{\upsilon}{\alpha} \tag{2.3}$$

where:

ν is the kinematic viscosity (m^2/s)

α is the thermal diffusivity (m^2/s)

$$Gr = \frac{g\beta(T_s - T_\infty)L^3}{\upsilon^2} \tag{2.4}$$

where:

g is the acceleration due to gravity (m/s^2)

β is the coefficient of thermal expansion

A further dimensionless number relevant here is the Reynolds number (Re), which can be expressed as the ratio of inertia forces to viscous forces, and which is important in determining the transition of flow from laminar to turbulent. Pure free convective flows use the Grasfhof number in the same way.

$$Re = \frac{\rho u_\infty x}{\mu} \tag{2.5}$$

where:

ρ is the density (kg/m^3)

u_∞ is the bulk fluid velocity (m/s)

x is the distance from the leading edge in the direction of the flow (m)

μ is the dynamic viscosity of the fluid (kg/m.s)

2.4.2.2 Free convective boundary layers

The temperature and velocity profiles formed by free convection boundary layers are illustrated schematically in Figure 7. The temperature profile is similar to that which occurs under forced convection, however the

velocity profile differs as the bulk fluid has negligible velocity. Typically, the thermal and velocity boundary layers are defined as the distance until the velocity (or temperature) is within 1% of the bulk (far-field) value. The thickness of the velocity and thermal boundary layers can be approximated as:

$$\delta_v = \delta_t Pr^{1/3} \tag{2.6}$$

where:

δ is the boundary layer thickness

v, t denote the velocity and thermal boundary layers respectively

Turbulent boundary layers occur when the flow becomes unstable due to shear forces acting on the flow.

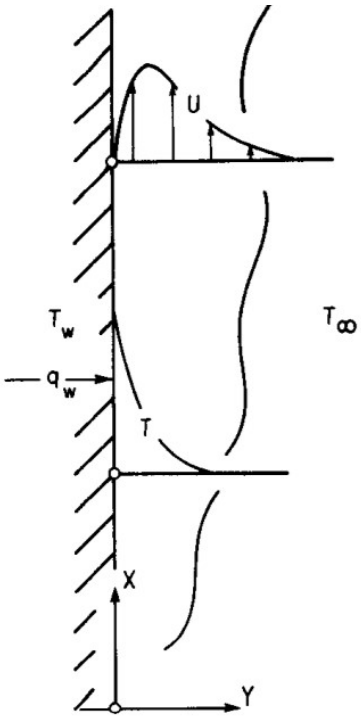

Figure 8 – Schematic of boundary layer profiles, reproduced from George Jr. & Capp (1978)

The boundary layer can be divided into various regions. Closest to the wall is the viscous sub-region, where the flow can be considered laminar and the heat transfer dominated by conduction. In this region turbulence is suppressed by viscosity. The shear velocity (or friction velocity) is an important parameter that characterises both the viscous sub-region thickness and the strength of turbulence. It can be defined as:

$$u_\tau = \left(\frac{\tau_\omega}{\rho}\right)^{1/2} \tag{2.7}$$

where:

u_τ is the friction velocity (frequently referred to as U*)

τ_w is the wall shear stress

ρ is the liquid density

At the wall, the velocity can be assumed to be zero, i.e. a non-slip condition can be applied, as shown in figure Figure 8. The shear stress can therefore be related to the velocity profile as given below:

$$\tau_s = \mu \frac{\delta u}{\delta y}\Big|_{y=0} \tag{2.8}$$

Direct measurement of the wall shear stress is difficult. Equations for estimating the value exist, such as that proposed by Blasius in equation 2.9 for hydraulically smooth pipes.

$$\tau_w = 0.0225 \rho {u_1}^2 \left(\frac{\upsilon}{u_1 \delta}\right)^{1/4} \tag{2.9}$$

where:

u_1 is an equivalent velocity outside the boundary layer in cases of forced convective flow

δ can be taken as the thickness of the boundary layer, approximated by:

$$\delta = 0.366\, x \left(\frac{\upsilon}{u_1 x}\right)^{1/5} \tag{2.10}$$

Beyond the sub-layer, turbulence dominates the transport of momentum. The remaining boundary is divided into a range of sub-regions by different authors, depending on whether temperature velocity or concentration is being considered (Kader, 1981). For forced convection situations the remaining boundary is typically considered to follow a logarithmic law of the form $\theta^+ = \alpha \ln y^+ + \beta$, where θ^+ and y^+ are the respective dimensionless temperatures and distances

Kader (1981) gave the constant α as 2.12 and β as a function of the Prandtl number. Alternative values are frequently used, such as those implemented in ANSYS FLUENT, shown in Figure 9.

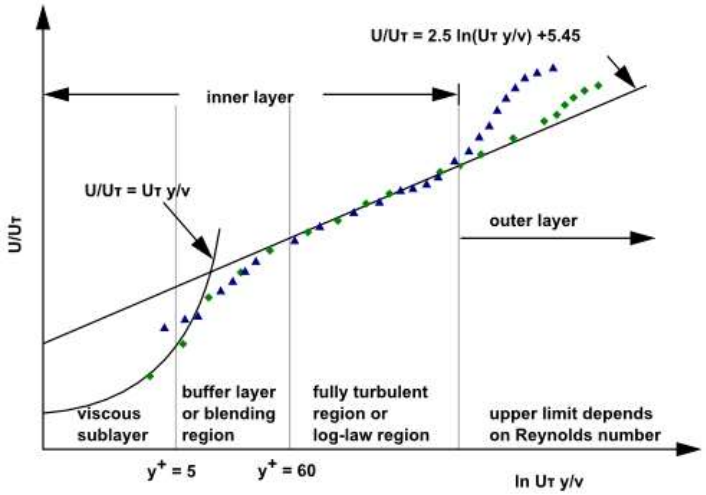

Figure 9 – Schematic of boundary layer, reproduced from Ansys support documentation (https://www.sharcnet.ca/Software/Ansys/16.2.3/en-us/help/flu_th/flu_th_sec_turb_near_wall_overview.html)

Eckert & Jackson (1950) reviewed early work in the field of turbulent free convective boundary layers, and proposed that the velocity profile fits equation 2.11, which is an adaptation of the 1/7th law first expressed by Prandtl (Oteh, 2008).

$$u = u_1 \left(\frac{y}{\delta}\right)^{1/7} \left(1 - \frac{y}{\delta}\right)^4 \tag{2.11}$$

where:

y is the distance from the wall (m)

δ is the thickness of the boundary layer (m)

u is the velocity

u_1 is an equivalent velocity outside the boundary layer in cases of forced convective flow

They also proposed the temperature profile fits equation 2.12

$$\theta = \theta_w \left[1 - \left(\frac{y}{\delta}\right)^{1/7}\right] \tag{2.12}$$

where:

θ is the difference between the temperature at the distance *y* and the bulk liquid temperature (K)

θ_w is the difference between the wall temperature and bulk liquid temperature (K)

A dimensionless plot of the shape of the profiles based on equations 2.11 and 2.12 is given in Figure 10, where:

y/δ is the distance from the wall divided by the boundary layer thickness

U/U_1 is the velocity at a given distance from the wall divided by a equivalent bulk liquid velocity

θ/θw is the difference between the temperature at a given distance from the wall and the bulk liquid temperature, divided by the difference between the wall and bulk liquid temperatures

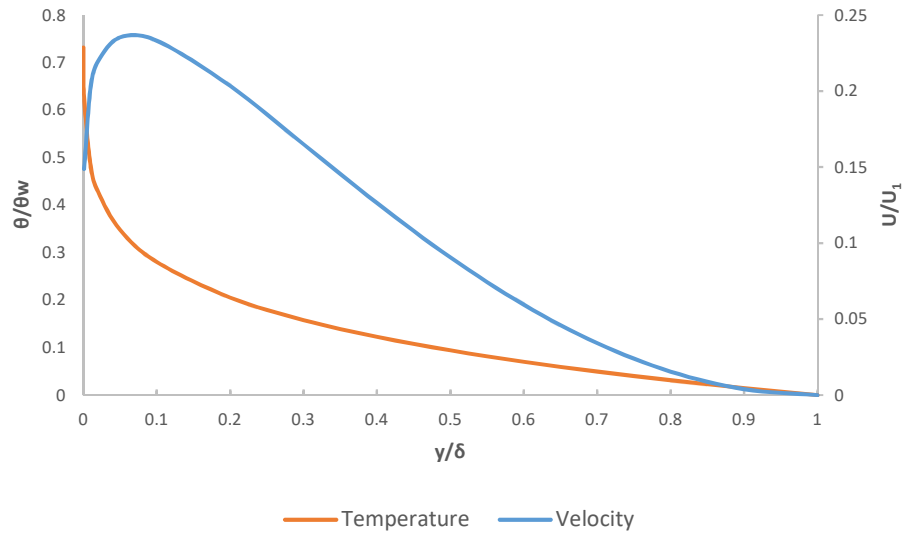

Figure 10 – Free convection turbulent boundary layer profiles proposed by Eckert & Jackson (1950)

By solving the boundary layer equations, Eckert & Jackson (1950) gave the following equations for boundary layer thickness and equivalent forced convection velocity:

$$\delta = 0.565x(Gr)^{-1/1}\ (Pr)^{-8/15}\left[1 + 0.494(Pr)^{2/3}\right]^{-1/10} \tag{2.13}$$

$$u_1 = 1.185\frac{\nu}{x}(Gr)^{1/2}\left[1 + 0.494(Pr)^{2/3}\right]^{-1/2} \tag{2.14}$$

To solve the equations above, the wall shear stress was required, and based on equation 9.

The average Nusselt number was given as below, valid over the range $10^{10} < Gr < 10^{12}$ and $1 < Pr < 50$:

$$Nu_{av} = 0.0246(Gr)^{2/5}(Pr)^{7/15}\left[1 + 0.494(Pr)^{2/3}\right]^{-2/5} \tag{2.15}$$

The experimental data was typically based on vertical plates and tubes. After 1950 a range of other studies proposed alternative equations for the boundary profiles, typically based on power laws, as above. However, a later review by George Jr. & Capp (1978) argued there was no consensus at the time of writing, citing “the lack of convincing theoretical arguments as to which dimensionless groups govern and which physical phenomena

dominate". They proposed a buoyant sub-layer, outside the thin viscous region adjacent to the wall, but close enough that convection effects are dominant. The following expressions for the temperature and velocity profiles were proposed:

$$\frac{T - T_w}{T_l} = K_2 \left(\frac{y}{\eta}\right)^{-1/3} + A(Pr) \tag{2.16}$$

$$\frac{U}{U_l} = K_1 \left(\frac{y}{\eta}\right)^{-1/3} + B(Pr) \tag{2.17}$$

where:

K2, K1, A(Pr) and B(Pr) are universal constants or functions, derived from experimental data

η is an inner length scale, given by $(\alpha^3/g\beta F_0)^{1/4}$

T_l is the inner temperature scale at a constant heat flux, given by $\left[F_0^{3/4}(g\beta\alpha)^{-1/4}\right]$

and where F is the Fourier number, β is the thermal expansion coefficient, and α is the thermal diffusivity.

The work by George Jr. & Capp (1978) is often referred to as the first wall-function approach for turbulent natural convection. Further work based on the study was performed by Versteegh & Nieuwstadt (1999). Using direct numerical simulation they were able to partially support the conclusions by George and Capp relating to the temperature profile and propose values for some of the universal constants identified. However, the velocity profile was not in good agreement with their DNS simulation and further experimental data. They proposed the following correlation for the heat transfer:

$$5Nu^{2/3}\left[(8NuGrPr^2)^{1/12} - 1\right] = (GrPr^2)^{1/3} \tag{2.18}$$

A study of temperature and velocity measurements of a turbulent free convection boundary layer over a constant temperature copper plate by Tsuji & Nagano (1989) provided important data for non-channel scenarios, in which the bulk fluid could be considered quiescent. It concluded that a logarithmic profile is valid for temperature, but not for velocity. The integral thickness of the velocity and thermal boundary layers was given as:

$$U_b\delta_U/\upsilon = 0.331\ Gr_x^{0.25} \tag{2.19}$$

$$U_b\delta_T/\upsilon = 0.646\ Gr_x^{0.151} \tag{2.20}$$

where:

$$U_b = (g\beta\Delta T_w \nu)^{1/3}$$

The maximum velocity was given as:

$$U_m/U_b = 0.408\, Gr_x^{0.16} \tag{2.21}$$

The maximum fluctuations in temperature and velocity were stated as being located at dimensionless distances of approximately $y^+ = 15$ and $y^+ = 250$, respectively.

The Nusselt number and the wall shear stress correlations were given as:

$$Nu_x = 0.110\, Gr_x^{1/3}$$

$$\tau_w/\rho U_b^2 = 0.684\, Gr_x^{1/11.9}$$

A further wall-function for the temperature and velocity profiles was proposed by Hoelling & Herwig (2005) based on a logarithmic law as shown in Figure 11.

Layer	Temperature $\Theta^\times$	Velocity $U^\times$
Viscous sublayer	$y^\times$	$\frac{1}{6}y^{\times 3} - \frac{1}{2}\Theta_0^\times y^{\times 2} + \left.\frac{\partial U^\times}{\partial y^\times}\right\|_w y^\times$
Overlap layer	$C\ln(y^\times) + D$	$\frac{C\mathrm{Pr}}{\sigma_t} y^\times \left(C[\ln(y^\times) - 2] + D - \Theta_0^\times \right) + E\ln(y^\times) + F$

with:

C	D	E	F
0.427	1.93	$0.49 \left.\frac{\partial U^\times}{\partial y^\times}\right\|_w - 2.27$	$1.28 \left.\frac{\partial U^\times}{\partial y^\times}\right\|_w + 1.28$

Figure 11 – Wall functions proposed by Hoelling & Herwig, reproduced from Hoelling & Herwig (2005)

More recently, Kiš & Herwig (2012) concluded that neither power nor logarithmic based correlations adequately capture the boundary layer profiles across both the inner (sub-viscous) and outer (fully turbulent) regions. They proposed alternative equations for the temperature and velocity profile that are not reproduced here, for brevity, but which are reliant on the temperature or velocity gradient at the wall being known. The authors noted that at y^+ values > 20 a logarithmic model may well be appropriate, and proposed the relationship between the gradients at the wall as:

$$\left|\frac{\partial \bar{u}}{\partial y}\right|_w = 199.27 \left|\frac{\partial \bar{\theta}}{\partial y}\right|_w^{2.53} + 134.19 \tag{2.22}$$

Based on a wider set of Grashof numbers than studied by Versteegh & Nieuwstadt (1999), the constants for the heat transfer correlation in the form $Nu=A(GrPr^2)^{1/C}$ were given by Kiš & Herwig (2012) as A = 0.186 and c = 3.2

2.4.2.3 Free convection heat transfer coefficient

Since 1950 further experimentally-derived correlations for free-convection heat transfer coefficients have been generated for a range of conditions, however these are typically for a heated vertical plate in contact with a fluid, a cylinder in cross-flow, or other highly specific geometries. The scale and shape of the interior of pressure vessels is not adequately described by existing correlations.

At the bottom of the vessel the wall can be considered a horizontal flat plate; at mid height it can be considered a vertical plate. The wall transitions from horizontal to the vertical through all intermediate angles. Horizontal and inclined plates exhibit higher rates of heat transfer than vertical plates as the buoyancy-driven upwards motion breaks up the boundary layer and results in plumes, as shown by the schematic illustration in Figure 12, reproduced from Bergman, et al., (2011).

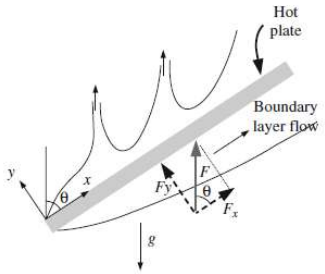

Figure 12 – Natural convection flows on the upper and lower surfaces of an inclined hot plate, reproduced from Bergman, et al., (2011)

For horizontal plates with Rayleigh numbers in the range 10^7 to $10^{11,}$ the following correlation has been proposed (Rohsenow, et al., 1998)

$$\overline{Nu_L} = 0.14Ra_L^{1/3}\left(\frac{1+0.0107Pr}{1+0.01Pr}\right) \tag{2.23}$$

Nusselt number correlations typically are given in terms of a constant surface temperature or a constant heat flux. The latter is more applicable to the current study. Widely accepted correlations for the local Nusselt number applicable to a flat plate subject to uniform heat flux are given by equations 2.24 and 2.25.

Laminar

$$Nu_x = 0.453\, Re_x^{0.8} Pr^{1/3} \qquad for\ \mathrm{Pr} \geq 0.6 \tag{2.24}$$

Turbulent

$$Nu_x = 0.0308 Re_x^{0.8} Pr^{1/3} \qquad for\ 0.6 \leq Pr \leq 60 \tag{2.25}$$

Once the local Nusselt number is known, the local temperature can be calculated using equation 8, similarly an average Nusselt number can be determined from equation 2.27.

$$T_s(x) = T_\infty + \frac{q_s^{"}}{h_x} \tag{2.26}$$

$$\overline{Nu}_L = 0.680 Re_L^{1/2} Pr^{1/3} \tag{2.27}$$

The above correlations are for forced convection. Similar correlations exist for free convection, however literature caution against the use of expressions for turbulent flow, directing users to consider experimental derivation (Bergman, et al., 2011).

The transition to turbulence in free convection is typically given in terms of a critical Rayleigh number, instead of the Reynolds number. For a vertical flat plate, the transition to turbulence occurs at approximately $Ra_c \approx 10^9$. In equation 2 the Nusselt number is expressed as the product of a constant, C, and the Rayleigh number raised to the power *n*. This common expression for the Nusselt number for free convection will typically have n = 1/4 for laminar flow and n = 1/3 for turbulent flow.

A correlation for turbulent flow on a vertical plate given under constant surface temperature conditions by Churchill & Chu (1975) is given by equation 2.28.

$$\overline{Nu}_L = \left\{0.825 + \frac{0.387 Ra_L^{1/6}}{[1 + (0.492/Pr)^{9/16}]^{8/27}}\right\}^2 \tag{2.28}$$

Equation 2.28 can also be used to approximate uniform heat flux conditions instead of a uniform surface temperature, however this is more complicated because the unknown surface temperature appears in both

the Nusselt number and the Rayleigh number. To calculate the temperature at a given point, the intermediate length, *L*, that corresponds to the average temperature must be iteratively calculated. In truly turbulent flow, Churchill & Chu (1975) proposed that the Nusselt number for uniform heat flux conditions should be identical to the constant temperature conditions (assuming $Nu \propto Ra^{1/3}$). However, knowledge of the surface temperature requires knowledge of the Nusselt number as a function of distance along the heat surface to calculate the temperature profile. Instead, and because it is often the case that $Nu \propto Ra^{1/4}$, equation 2.29 is frequently used.

$$\Delta T_x = 1.15 \left(\frac{x}{L}\right)^{1/5} \Delta T_{\frac{L}{2}} \tag{2.29}$$

Nusselt number correlations for inclined heated plates were developed by Fujii and Imura (1972) to cover both laminar and turbulent flow. For combined laminar and turbulent flow, the following was proposed for a surface exposed to constant flux:

$$Nu = 0.13 \left([GrPr]^{1/3} - [Gr_c Pr]^{1/3}\right) + 0.56 \left(Gr_c Pr \cos\theta\right)^{1/4} \tag{2.30}$$

The characteristic length suitable for use in the dimensionless numbers within such correlations is not self-evident. Flat plates typically use the ratio of the heated surface area to the heated perimeter, whereas correlations for vertical plates typically use the height of the heated length. There is also uncertainty in the critical Grashof number for transition to turbulence. It is typically reported as $1x10^9$, however Fujii and Imura referenced work done by others that reported the critical Grashof number for instabilities to occur in the laminar boundary layer as varying between $5x10^9$ and $1x10^6$. Regardless of the exact value used, the calculation gives characteristic lengths for transition to turbulence which are short, relative to the scale of pressure vessels. For example, taking the value of Gr_c to be $1x10^9$, the heated wall temperature at the liquid interface as 100°C and the bulk liquid temperature as 20°C gives a characteristic length for transition to turbulence of approximately 80-85 mm. Therefore, we can make a reasonable assumption that the turbulent flow is dominant, and therefore simplify equation 2.30 as below.

$$Nu = 0.13 \left([GrPr]^{1/3}\right) \tag{2.31}$$

Equation 2.31 is, unsurprisingly, an average of isothermal correlations reported for vertical and horizontal plates elsewhere (for example, in Bergman, et al., (2011)).

2.4.3 Pre-boiling bubble assisted convection effects

Studies of water with high degrees of subcooling and relatively low heat fluxes (Petrovic, et al., 2004) have shown that an intermediate region may be present between free convection and nucleate boiling, where the natural convection is enhanced by surface tension forces around isolated bubbles attached to the heated surface. This is known as Marangoni convection.

As discussed above, pressure vessels that contain fluid which is liquid at ambient temperature and pressure are likely to have high degrees of subcooling at the onset of fire. If the heat transfer by convection is sufficient for the wall temperature to stabilise (in a quasi-equilibrium) at a temperature below the temperature required for boiling to become significant, then convection may remain the dominant mode of heat transfer until the bulk temperature increases to the point where the rate of heat transfer by convection drops (due to a lower ΔT), and the wall temperature increases further. Clearly, this mode of heat transfer will be negligible for pressure liquefied gases and other fluids stored close to their saturation temperature.

Dissolved gases may increase the occurrence of Marangoni convection. Hazardous material in solution, or other non-flammable liquids, may contain dissolved air. At atmospheric pressure and a temperature of 25°C there is approximately 0.023 g/kg of air dissolved in water. On heating, the air dissolved may coalesce and form bubbles at the heated surface at a temperature below the vapour saturation temperature of the fluid. A study by Steinke and Kandlikar (2014) reported a nucleation temperature for air bubbles of 90.5°C, in line with other studies. The presence of bubbles attached to the heated surface has been shown to influence the heat transfer coefficient in laminar flow studies. Steinke and Kandlikar reported a decrease in heat transfer coefficient at fluxes close to 100 kW/m2 (and a corresponding increase in wall temperature). Once the heat flux was increased beyond this, the heat transfer coefficient increased and the effect of dissolved air became negligible. An earlier study on the effect of air bubbles on heat transfer by Petrovic (2004) reported an increase in the heat transfer coefficient of approximately 20%. However, it must be noted that the studies were under conditions of laminar flow (with boundary layer detachment). As discussed, heat transfer coefficients for turbulent flow are higher than laminar flow by an order of magnitude, substantially greater than the effect discussed in this section, and so it is reasonable to assume Marangoni convection has a negligible effect on the overall rate of heat transfer.

2.4.4 Boiling

Boiling is the term given to evaporation at a solid-liquid interface. It occurs when the solid surface achieves a temperature in excess of the vapour saturation temperature of the liquid (which itself is dependent on the pressure). In simplistic form, the equation for heat transfer by boiling can be stated as:

$$q_b^{"} = h_b(T_s - T_{sat}) \tag{2.32}$$

where:

$q_b^{"}$ is the heat flux due to boiling (W/m^2)

h_b is the coefficient of heat transfer due to boiling (W/m^2K)

T_s is the solid surface temperature (K)

T_{sat} is the vapour saturation pressure of the liquid (K)

The temperature difference in equation 2.32 is typically termed the excess temperature, or the superheat temperature, necessary for the initiation of boiling. As with convective heat transfer, a relatively thin thermal boundary layer will become established, with the liquid beyond the thermal boundary layer referred to as the bulk liquid. Boiling is generally characterised in terms of the liquid motion and liquid temperature, as follows:

Pool boiling

Whereby the liquid has no external applied force, and in which motion is caused solely through natural convection and mixing due to bubble motion through the liquid

Forced convective boiling

Whereby the liquid has an external force applied, and the bulk liquid has motion independent of boiling. Natural convection and bubble-assisted mixing will also contribute.

Subcooled boiling

Whereby the bulk liquid temperature is below the vapour saturation temperature. Subcooled boiling is characterised by generally small bubbles, the majority of which shrink following departure and condense in the liquid.

Saturated boiling

Whereby the bulk liquid temperature is equal to (or slightly higher than) the vapour saturation temperature. Saturated boiling is typically characterised by larger bubbles, which grow following departure and travel to the liquid-vapour surface

Pressure vessels may contain pressure liquefied gases (e.g. propane) that have a vapour saturation temperature equal to the ambient temperature, or they may contain liquids with a significant degree of subcooling (e.g. butane, NaOH solution, etc.). In practice, fire exposure will increase the pressure in the vessel, and therefore increase the vapour saturation temperature in the vessel above the bulk liquid temperature. Pressure vessel boiling scenarios can therefore be considered as subcooled boiling, although the degree of subcooling may be very small for pressure liquefied gases.

Boiling scenarios can be further divided into modes of boiling, depending on the magnitude of the heat flux applied to the solid surface. The modes can be easily visualised through use of a boiling curve, plotting the heat flux applied against the excess temperature. The first saturated pool-boiling curve for water was published by Nukiyama (1934), and is reproduced in Figure 13 from an adaptation by Bergman, et al., (2011). Point A on the chart shows the onset of nucleate boiling, below which heat transfer is solely by free convection. Between points A and B a combination of nucleate boiling and free convection occurs, and beyond point B heat transfer is considered to be by nucleate boiling (i.e. convection is negligible). Further along the line partial and complete film boiling occurs (points P and C) whereby the liquid is no longer in contact with the hot surface and the heat transfer efficiency (h_b) decreases significantly. From Figure 13 it is evident that the heat fluxes typical in pool fire scenarios (up to 120 kW/m^2) fall firmly within the partial and complete nucleate boiling regime. This is true also for alternative fluids of interest, such as ethanol, propane and butane.

Boiling is a highly complex phenomenon that is sensitive to a wide range of factors. The bubble nucleation, growth and departure process is dependent on the applied heat flux (and surface excess temperature), the liquid properties, and the surface properties and topography. Accurate characterisation of boiling surfaces is a significant challenge, typically requiring scanning electron microscopes, and is therefore extremely difficult to do on a large scale. Extensive study of water boiling has been performed over the last 60 years, particularly on scenarios and phenomena relevant to the nuclear industry. Despite the development of numerous mechanistic models to describe bubble formation and departure it remains a challenge for even state-of-the-art three-

dimensional numerical models to describe individual bubble formation and the effect it has on local fluid heat transfer characteristics, while at the same time model how a large quantity of bubbles interact across a wide field of flow. This is discussed further in section 2.3. The reliance of computational models on mechanistic sub-models for bubble behaviour, and the reliance of all models on experimentally derived correlations, limits the predictive capability of boiling models in general, and is part of the reason many sectors of industry remain reliant on simplistic models and correlations. Non-numerical models are considered further below.

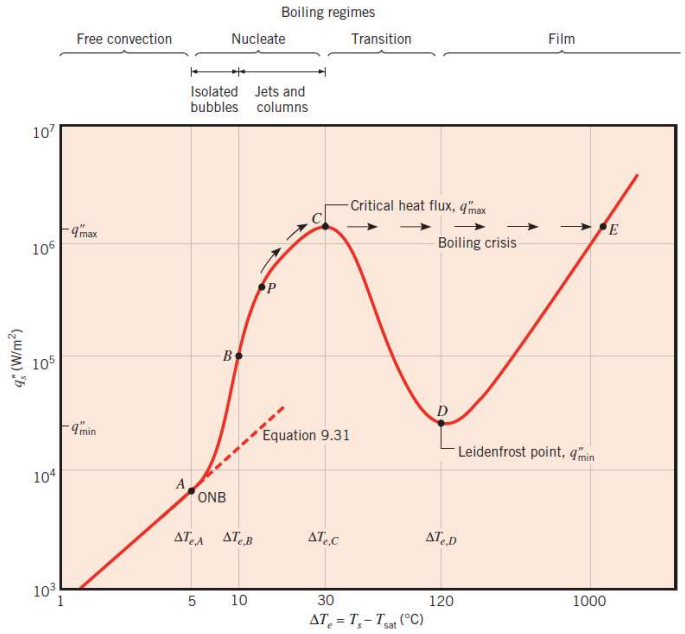

Figure 13 – Boiling curve for water at 1atm, reproduced from Bergman, et al., (2011)

The progress made in developing mechanistic models describing bubble nucleation, growth, sliding, and detachment, for pool boiling and forced convective boiling, has been supported by numerous experimental studies. A list of selected studies was given by Goel, et al., (2017). As previously observed, the majority of studies are of forced convective boiling to address specific issues within the nuclear industry. Studies of pool boiling scenarios are less common, and the majority of those performed investigate either heat fluxes significantly higher than those obtained in hydrocarbon pool fire scenarios (>>120 kW/m2) or use fluids with low degrees of subcooling (compared to the subcooling observed when the liquid is at ambient temperature, as with the transportation of hazardous materials). Analysis of results across different studies is complicated by differences in heater surface characteristics and subcooling, leading to contradictory results being reported

on the influence of heat flux on bubble diameter (Judd & Hwang, 1976), (Goel, et al., 2017). The more recent studies indicate that the departure diameter and departure frequency of bubbles increases with increasing heat flux, while the departure diameter decreases with increased subcooling.

Nucleate pool boiling

Numerous correlations have been developed for the heat transfer due to nucleate boiling in the partially developed and fully developed regimes, including those by Rohsenow (1952), Motinsi (1963), Cooper (1984) and Gorenflo (1993). The consensus among reviews of such correlations is that the inherent inaccuracy of all boiling correlations makes the choice of correlation non-critical. As such, the original correlation by Rohsenow (equation 2.33) remains in popular use. It includes an experimentally derived liquid-surface specific parameter, C, originally developed for metallic surfaces and water.

$$q_{NB}^{"} = \mu_f h_{fg} \left[\frac{(\rho_f - \rho_g)g}{\sigma}\right]^{0.5} \left[\frac{c_{pf}\Delta T_e}{c_{sf} h_{fg} Pr^n}\right]^3 \tag{2.33}$$

The wall excess temperature necessary for the onset of nucleate boiling is of interest when determining the balance between convection and boiling heat transfer mechanisms. This present work attempts to measure the wall temperature directly. Bergles and Rohsenow (1964) proposed an equation to calculate the wall super heat required. This equation was developed further by David and Anderson (1966) and Frost and Dzakowic (1967) to cover liquids other than water. This form is given by equation 2.34.

$$(T_w - T_{sat})_{ONB} = \sqrt{\left(\frac{8\sigma q^{"} T_{sat}}{k_f h_{fg} \sigma_g}\right)} Pr \tag{2.34}$$

Equation 2.34 predicts the onset of nucleate boiling for water at superheat values close to 1°C. In practice significant boiling is not observed until higher excess temperatures of up to 10°C, as the above equation is based on the assumption of a wide range of surface cavity sizes, whereas surfaces in practice (e.g. finished metallic surfaces) often do not have this.

2.4.5 Heat flux partitioning approach

The total heat flux during boiling was proposed by Rohsenow to be the sum of the heat fluxes due to both free convection and by nucleate boiling. The latter was later expanded by Bergles (1981) to the sum of the heat transfer by quenching of cool liquid replacing a bubble at the wall following departure, and by evaporation as the liquid phase turns to vapour. This approach is commonly referred to as a heat flux partitioning model. It was first incorporated into CFD by Kurul and Podowski (1990, 1991) and remains today the predominant modelling approach for including wall boiling in commercial CFD codes.

The partition approach can be described as follows:

$$q''_{net} = q''_e + q''_q + q''_{nc} \tag{2.35}$$

where:

q_e'' is the heat flux due to evaporation of liquid

q_q'' is the heat flux due to quenching

q_{nc}'' is the heat flux due to convection

Various sub-models can be used to calculate the partitioned heat fluxes, with the most common being those currently implemented in ANSYS CFX and Fluent, and summarised below:

Evaporation heat flux: q_{ev}''

$$q''_{ev} = N\, f \left(\frac{\pi D^3}{6}\right) \rho_v h_{fg} \tag{2.36}$$

where:

h_{fg} is the latent heat of evaporation (kJ/kg)

ρ_g is the density of the vapour (kg/m^3)

N is the number of nucleation sites,

D_d is the bubble departure diameter (m)

f is the bubble departure frequency (s^{-1})

Quenching flux: q_q'' (Del Valle & Kenning, 1985)

$$q''_q = A_b\, 2kf \sqrt{\frac{t_w}{\pi\alpha}} (T_w - T_l) \tag{2.37}$$

where

t_w is the bubble waiting time (s), taken by Kurul & Podowski (1991) as ($0.8/f$)

A_b is the bubble surface contact area (m^2), taken as πD^2

k is the thermal conductivity (W/m.K)

Convective flux: q_c''

$$q_c'' = (1 - A_b)h_c(T_w - T_l) \tag{2.38}$$

where:

h_c is the coefficient of convection (W/m^2K)

Different models adopt different approaches for determining h, with current commercial CFD wall boiling models typically calculating it based on turbulent wall functions (Egorov and Mentor, 2004). Selection of a value for the bulk liquid temperature, T_L, is somewhat arbitrary. In CFD models the value is typically based on the wall-function determined value at a dimensionless distance considered to be outside the boundary layer.

There are four key parameters in the above equations that are required for the model to function:

- Nucleation site density
- Bubble departure diameter
- Bubble departure frequency
- Wait time between bubble departure and initiation

The parameters above need to be determined experimentally, and consequently are typically implemented as correlations related to known parameters, such as the liquid properties and temperature. Care must be taken to consider the scope of validation of the underlying correlations during selection, with many based on convective flow boiling. Further discussion of correlations available for the above sub-models is given in section 2.4.5.1 to 2.4.5.3.

The implementation of the heat flux partitioning method in CFD differs depending on whether the wall is isothermal or whether there is a constant applied flux. The former allows for direct calculation of the partitioned terms, whereas a known constant flux value requires the partition to be determined iteratively by varying the wall superheat temperature (T_{sup}) until the combined heat transfer (q_{net}) equals the specified flux value. However, implementation of the heat flux partitioning approach is not limited to numerical methods.

The principles of the model have been frequently applied by researchers to pool boiling scenarios for many years, for example Petrovic, et al., (2004) used a partitioning model with a single term for the boiling heat transfer based on a Mikic and Rohsenow pool boiling correlation with an experimentally derived bubble departure frequency.

2.4.5.1 Nucleation site density (N)

One of the earliest models for N was given by Gaertner & Westwater (1960) relating N to the heat flux. Mikic & Rohsenow (1969) proposed a model that included the cavity size, using the Clausius-Clapeyron equation to express it in terms of fluid properties. Lemmert & Chawla (1977) proposed a model for N that was related to the liquid saturation temperature and wall excess temperature value. Kocamustafaogullari & Ishii (1983) related N to the cavity size radius (as proposed by Griffith & Wallis (1960)) and the bubble departure diameter. Yang & Kim (1988) proposed a model also related to the cavity size, but with a greater emphasis on the surface geometric parameters. These require measurement for specific substrates and substrate-fluid combinations by electron microscopy and other techniques, and consequently were not available for the current study. Wang & Dhir (1993) related N to the cavity density and contact angle with the wetted fluid. Benjamin & Balakrishnan (1997) published a correlation with a measurement of the surface roughness (R_a) as a key parameter, coupled with the wall and liquid physical properties. Basu, et al., (2002) proposed a further correlation for subcooled boiling that related N to the contact angle and the wall excess temperature. The correlation is considered, despite being developed for flow boiling as the stated range of validity includes a minimum flow speed of approximately 0.12 m/s, which is similar to bulk fluid velocities in the present study. Hibiki & Ishii (2003) proposed a model for N that developed further the approach of Yang & Kim, relating N to the cavity size and contact angle.

More recently, He, et al., (2017) studied propane, butane and other refrigerants and found the measured values of N deviated from previous correlations significantly. Their results indicated that N was proportional to the wall excess temperature, and they proposed a modification to the surface roughness constants in the correlation of Benjamin and Balakrishnan, along with an attenuation factor to improve predications for mixtures. A somewhat different approach was taken by Yeoh, et al., (2014) in applying a fractal model to a relationship for the number of cavity diameters.

As with all empirically derived correlations, the models discussed above have ranges of applicability limited to the experimental conditions on which they were based. These restrictions are typically in terms of the heat flux or wall excess temperature values, the surface and fluid properties, the degree of subcooling etc. The ranges for each correlation are not reproduced here. None of the correlations have been developed for carbon steel or painted steel surfaces, or wall excess temperatures lower than 5°C.

In comparative reviews of the various nucleation site models Kolev (2006) concluded that no single correlation adequately predicted all available datasets, and that a range of correlations were required. Numerous authors have commented that the surface topography is an important factor in determining N, however in the majority of experimental studies it was poorly characterised, leaving a significant uncertainty when applying correlations across multiple datasets.

The model proposed by Lemmert & Chawla is commonly used, but often the constants therein are replaced by alternative values proposed by Kurul & Podowski (1991). Cheung, et al., (2014) performed a detailed comparison of the models by Lemmert & Chawla (using the Kurul & Podowski constants) and Basu et al., concluding that the latter gave a higher wall superheat temperature and lower value of N. Their study also found no single correlation gives a best match to all datasets.

2.4.5.2 Bubble departure diameter (D)

An early model for the departure diameter of bubbles was proposed by Fritz (1935) and related D to the densities of the liquid and gas, the surface tension, the contact angle, and acceleration due to gravity. Kocamustafaogullari & Ishii (1983) later extended the model by Fritz to include pressures above atmospheric by inclusion of a further density related factor. Zuber (1959) assumed a relationship between the cavity dimensions and the superheated liquid film thickness, replacing the contact angle in the expression for D with the heat flux, wall excess temperature and the liquid thermal conductivity. Zeng, et al., (1993) proposed an empirical correlation for bubble diameter based on experimentally derived bubble growth parameters. However, they supported the use of the model by Zuber in the absence of such information.

Cole (1967) noted the strong relationship between bubble diameter and the Jakob number, Ja, and included it in his model to account for variations in pressure and wall excess temperature. He also noted that the contact angle is typically 50° +/- 20%.

The above models are based on determining D at the point at which the buoyancy forces and opposing hydrodynamic forces are equal for an isolated spherical bubble. Alternative models or correlations based on the same principle have been proposed by Cole & Rohsenow (1969) and Han & Griffith (1962), among others. However, numerous studies, for example Kiper (1970) and Hamzekhani, et al., (2014), have commented on the limitations of the force balance model with respect to bubble interaction and the effects of lateral forces. Alternative approaches include that of Kolev (1994), who considered the interactions between bubbles and the resultant shear forces acting on the bubble and the velocity fluctuations caused by bubble departures. Tolubinsky & Kostanchuk (1970) correlated bubble diameter with the degree of liquid subcooling and two experimentally derived parameters. The resulting correlation has been widely implemented in numerical wall boiling models.

Numerous authors have proposed correlations or models based on flow boiling experiments, including Unal (1976), Basu, et al., (2005), Situ, et al., (2005) and Chu, et al., (2011). Of these, the model by Unal (1976) is frequently used, however it is reliant on an estimate of the convective heat transfer coefficient and proposes a specific correlation in the original study which is unlikely to adequately represent conditions in the current study.

To the author's knowledge, there exists no experimental study of pool boiling that included the combination of subcooling, pressure, flow velocities and heat flux created in the current study. The correlation by Tolubinsky & Kostanchuk (1970) extended to a subcooling of 60°C, while the study by Unal included tests with a minimum heat flux of four times that of the current study, but otherwise included the pressure, subcooling and flow rates in the current study. In the study by Tolubinsky & Kostanchuk (1970) a maximum diameter of 0.47 mm was observed for a heat flux of 470 kW/m^2. The current study has a lower heat flux and flow rate, which would give larger bubbles, but a higher degree of subcooling, which would give smaller bubbles. It is therefore reasonable to expect the maximum diameter of bubbles in the current study to be within a factor of 2 of those studied by Tolubinsky & Kostanchuk.

2.4.5.3 Bubble departure frequency (f)

The bubble departure frequency was linked to the bubble departure diameter in early work by Jakob (1932), with the product of the bubble departure diameter and departure frequency found to be approximately constant (Jakob, 1949). Successive works obtained different relationships between f and D, with Hatton & Hall (1966) and Ivey (1967) proposing a relationship between the f and D^2 for the thermodynamically controlled bubble expansion, or f and $D^{3/4}$ for a transition region, as is probable under the conditions within the present study.

The established relationship between f and D means the majority of models for f include D as an input parameter. A commonly used model is that of Cole (1960), which is based on previous work by Deissler (1954) that assumes the product of f and D gives a constant rise velocity, and relates the buoyancy and drag forces acting on a free-rising bubble to give an expression for f in terms of D, g and the densities. Alternative expressions for f that also include the surface tension were proposed by Zuber (1959), Hatton & Hall (1966), Ivey (1967), Malenkov ((1972) and Kocamustafaogullari & Ishii (1995). Alternative approaches have been published more recently based on mechanistic models of the heat transfer processes taking place during the bubble growth and waiting periods. Podowski, et al., (1996) proposed a mechanistic model and Basu, et al., (2005) published such types of model intended for subcooled flow boiling predictions. Petrovic, et al., (2004) proposed a correlation for f that included both the wall excess temperature and the degree of subcooling.

2.4.6 Bubble rise velocity

Liquids with a significant degree of subcooling at the onset of fire can be assumed to be in the partial nucleate boiling regime, if boiling is present, and that bubbles will have negligible interaction between each other. Such bubbles will be of a generally spherical nature, due to surface tension exerting a dominant effect on their shape. Studies of bubble rise velocities (for example, Talaia (2007)) assert that the Stokes solution gives a reasonable approximation of the rise rate of small (<1 mm) isolated bubbles. Equation 2.39 gives a formula used to calculate the maximum rate of rise of bubbles, noting that the 1/18 factor used varies between literature. The rate of bubble rise as a function of diameter is given for various bubble and fluid combinations relevant to this study in Figure 14.

$$u_\infty = \frac{1}{18}\frac{g d^2(\rho_l - \rho_g)}{\mu_l} \tag{2.39}$$

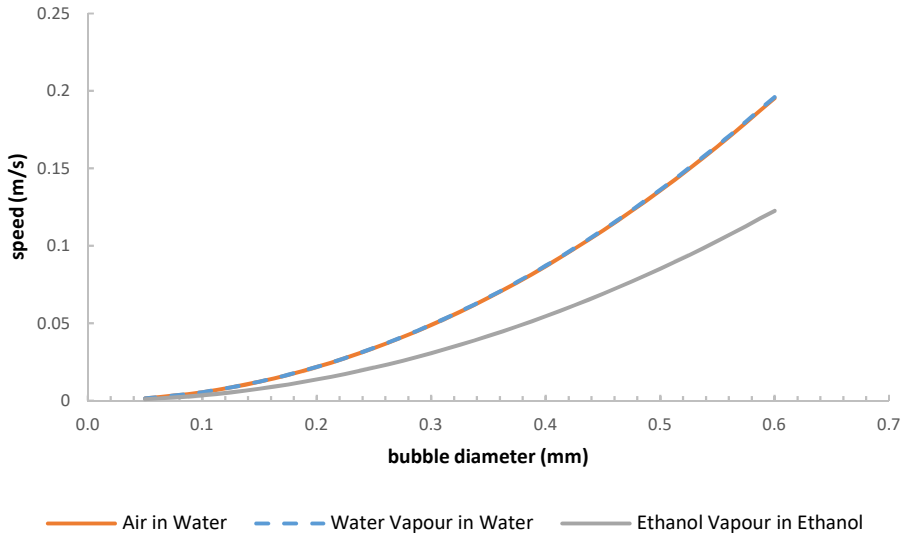

Figure 14 – Bubble terminal rise velocity in quiescent water at 20°C

2.4.7 Bubble collapse rate

Reviews of bubble condensation rates in subcooled fluids by Anjos & Buongiorno (2013) and Kolev (2007) highlight the range of correlations available to approximate the rate of bubble condensation. The consensus amongst studies is that bubbles with a Jakob number below 100 condense at a rate controlled by thermal effects, whereas bubbles with a high Jakobs number condense at a rate controlled by inertia effects. Note that the Jakobs number in this context is defined as in equation 2.40.

$$Ja_b = \frac{\rho_l}{\rho_f}\frac{c_p(T_{sat} - T_l)}{h_f} \tag{2.40}$$

Correlations for thermally controlled bubble condensation, such as those by Ranz & Marshal (1952) or Warrier, et al., (2002) are typically generated for Jakob numbers less than 60. The current study used water and ethanol at a starting temperature of 20°C, giving *Ja* numbers of approximately 230 and 930 respectively.

Bubbles moving within the boundary layer may have relatively low degrees of subcooling, and the bubble collapse rate may be dominated by thermal effects. In such cases, correlations (such as equation 2.41 quoted in Warrier, et al., (2002)) can be used to predict the bubble diameter over time. Although developed for forced convective flow boiling, it has been applied to water vapour bubbles in water for various degrees of subcooling as shown in Figure 15.

The dimensionless bubble diameter, β, is given by:

$$\beta = \frac{D}{D_0} = \left[1 - 1.8 Re_{b0}^{1/2} Pr_l^{1/3} JaFo_0\right]^{2/3} \tag{2.41}$$

where:

Re_{b0} is the bubble Reynolds number (equation 5, with substitution of the bubble relative velocity and the bubble departure diameter)

Fo_0 is the Fourier number, using the departure bubble diameter as the length term

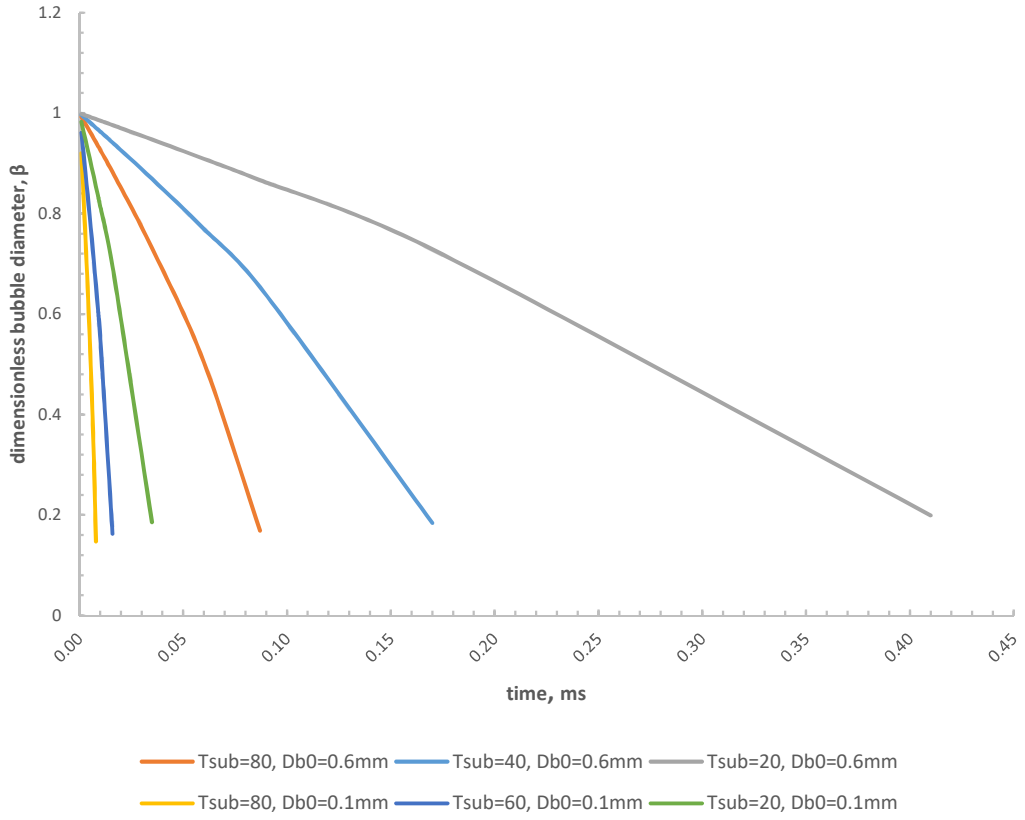

Figure 15 – Thermally controlled bubble collapse

Inertia controlled evaporation and condensation is frequently approximated by the Rayleigh-Plesset model (equation 2.42). This model is based only on mechanical effects and assumes negligible thermal effects.

$$\frac{dm_b}{dt} = F 4\pi R_b^2 \rho_g \sqrt{\frac{2}{3}\frac{p_v - p}{\rho_l}} \tag{2.42}$$

where:

m_b is the mass of the bubble (kg)

R_b is the bubble diameter (m)

p_v is the vapour pressure (Pa)

p is the liquid pressure (Pa)

ρ_l is the liquid density (kg/m^3)

F is an empirical constant

Note that the constant, F, is used to accommodate differing rates of evaporation and condensation (with condensation typically being slower than evaporation). A value of 0.01 is used in CFX by ANSYS Inc. (2013). Figure 16 shows the rate of diameter reduction for a water vapour bubble calculated using equation 2.41. It should be noted that the vapour is assumed to be at the saturation temperature, and therefore is assumed to have an internal pressure of 1 atm. The pressure differential is caused by the head of liquid exerting a greater local pressure at a depth of liquid. Figure 16 does not take into account the variation in pressure as the bubble rises, and it should be noted that the calculation is highly sensitive to the pressure values used.

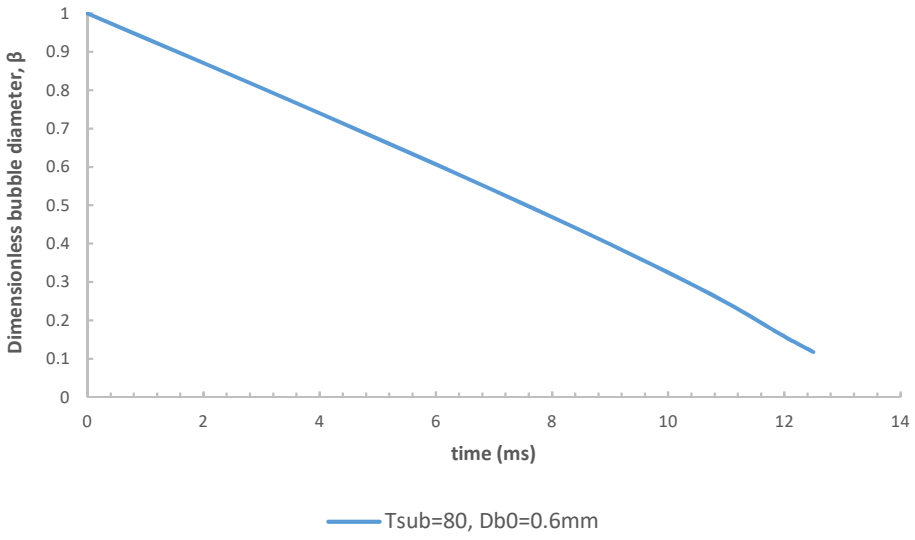

Figure 16 – Inertia controlled bubble collapse at 0.3 m depth

2.4.8 Summary

Fire engulfment of pressure vessels will rapidly result in the establishment of thermal and velocity boundary layers within the liquid phase, noting that at the bottom of the vessel the convection will be unstable. Once the temperature of the vessel wall reaches a sufficiently high excess temperature (above the vapour saturation temperature) boiling will commence. The time until boiling starts, and the magnitude of the heat transfer due to boiling will vary depending on the heat flux, the fluid properties, the degree of fluid subcooling, and the surface characteristics of the vessel. The local vapour saturation temperature will vary with the local pressure, itself a function of the overall pressure in the vessel and the location in the vessel, as the head of liquid will result in a small increase in the saturation temperature at the bottom of the vessel.

Vessels containing pressure liquefied gases will commence boiling quickly due to negligible subcooling. Vessels containing liquids with significant degrees of subcooling (e.g. hazardous materials in solution at ambient temperature) are unlikely to reach fully developed boiling quickly, with the heat transfer from the wall to the fluid taking place by a combination of partial nucleate boiling and convection.

Literature provides a number of correlations that allow an estimate of the heat transfer by convection or nucleate pool boiling, however it can be argued that none are directly applicable to the geometry and scale of the flow conditions within a pressure vessel. The non-uniformity of the geometry (and potential variations with respect to fill level), combined with the transient nature of the problem and the additional complications resulting from the combined heat transfer modes, in particular bubble interaction with flow, limit the use of correlations as a means of useful predictions. Advancement in this area requires a numerical approach capable of resolving both the bubble behaviour and boundary layers in detail.

The heat flux partitioning approach is a suitable basis for development of combined convection and boiling heat transfer models. It is based on a mechanistic analysis of bubble growth and departure and has been widely adopted for wall-boiling simulations in numerical and non-numerical models. The primary limitation of the model is the continued requirement for derivation of key parameters from experimental data, and the inherent sensitivity of boiling to changes in set-up limiting the predictive capability of boiling models in general.

2.5 Literature review summary and detailed project objectives

A summary of the key points from the preceding literature review sections is given below.

- A large amount of test data is available for LPG vessels in fully or partially engulfing hydrocarbon pool fires, however the test evidence available is limited when other fluids are considered
- In many tests the fire was characterised in simplistic terms, and at limited positions within the fire, giving significant uncertainty over the thermal boundary conditions. Future work must ensure the boundary conditions are controlled and characterised during tests.
- Internal instrumentation in vessel tests has traditionally been limited to thermocouples placed in a central position or widely-spaced grid
- Small-scale simulation tests by Venart, et al., (1984) gave early insight into flow behaviour in cylindrical vessel through the use of a full-bore viewing window and flow capture techniques
- The mechanisms of heat transfer from the shell to the fluid are known to be transient free convection and nucleate boiling. Both have been extensively studied since the mid-20th century, however the combination of both effects gives rise to turbulent multi-phase flow with wall boiling. Modelling this phenomenon remains challenging and is an area of active research
- Characterisation of bubbly flow cannot be adequately performed by temperature measurement alone. It requires local velocity measurements and bubble characterisation, which can be performed by a range of point-measurement or wide-field measurement techniques. The instrumentation should be focussed on characterising the thermal and velocity boundary layers that form within the tank, to better understand phenomena that drive and govern thermal stratification.
- Characterisation of flow behaviour in fire-engulfed pressure vessels will provide validation data for the purpose of developing numerical models of pressure vessels.
- The limited number of CFD models of vessels have typically been based on the volume-of-fluid multiphase approach, with boiling handled through a phase-change equation developed for very different scenarios to wall boiling. The majority of developments of multiphase flow model with wall boiling in the last two decades have used the Eulerian-Eulerian approach with the RPI wall boiling model.

Having reviewed the literature referenced within the current study, the project aims were further refined as given below:

2.5.1 Detailed project objectives

The driving principle behind research into pressure vessel response to fire is to improve safety through a better understanding of, and ability to predict, the factors that drive vessel pressurisation and failure. This study contributes to this through the following main objectives. Additional sub-objectives are listed following discussion of the problem within the preceding literature review.

1) To design, commission and demonstrate a novel test apparatus capable of generating experimental results that assist in the development and validation of improved models of the internal fluid dynamics during vessel fire exposure. To achieve this, the equipment (the vessel) needs to be:
    a) of realistic scale (i.e. within the scope of typical industrial use)
    b) capable of producing consistent and repeatable results
    c) re-usable over repeated test seasons (across multiple years)
    d) compatible with the BAM test facility to take advantage of the equipment for creating simulated pool fires
    e) capable of housing and protecting extensive instrumentation
    f) able to have instrumentation installed in a manner that minimises flow disruption
    g) constructed and commissioned within the project budget
    h) able to perform multiple tests per day
    i) economic

2) To generate a range of experimental data suitable for direct validation of numerical models of pressure vessels in fire over a range of fluid and fill conditions greater than currently available in literature. Information captured shall include flow characteristics, temperature distributions and rate of pressurisation. To achieve this the equipment needs to:
    a) use extensive internal instrumentation for characterisation of the thermal boundary layers and regions of stratification

b) provide a clear view of the vessel contents and internal vessel wall during tests, both above and below the liquid level, for observation of boiling phenomena

c) use extensive internal instrumentation for near-wall temperature measurements

d) be capable of showing fluid flow behaviour and velocity characterisation over a wide field of view

3) To perform a simulation of a test undertaken by the equipment designed as part of this study, using the Eulerian-Eulerian multiphase modelling approach in conjunction with a wall boiling model. Sub-objectives are to:

a) set-up a basic model (with default boiling settings and other simplified characteristics) and perform a grid independence study to assess model stability

b) assess the potential of the basic model as a future modelling approach by comparison with experimental data

c) consider the wall boiling sub-models and recommend alternative models that may be more suited to subcooled boiling

d) propose future modifications to improve model accuracy

2.6 References

Anderson, C., Townsend, W., Zook, J. & Cowgill, G., 1974. Effects of a Fire Environment on a Rail Tank Car Filled with LPG, s.l.: US Department of Transport Report No. FRA-OR&D 75-31.

Anjos, G. R. d. & Buongiorno, J., 2013. Bubble condensation heat transfer for subcooled flow boiling at PWR conditions: a critical evaluation of current correlations, s.l.: Consortium for Advanced Simulation of LWRs.

ANSYS Inc., 2013. ANSYS CFX-Solver Theory Guide, Canonsburg, PA: s.n.

Aszodi, A., Krepper, E. & Prasser, H.-M., 2000. Experimental and numerical investigation of one and two phase natural convection in storage tanks. Heat and Mass Transfer, Volume 36.

Aydemir, N. U., Sousa, A. C. M. & Venart, J. E. S., 1984. Transient Thermal Stratification in Heated Partially Filled Horizontal Cylindrical Tanks. Niagara Falls, ASME/AIChE National Heat Transfer Conference.

Babe, W. G., 1989. A Thermodynamic and Hydrodynamic Model of a Vessel Exposed to a High External Heat Flux and Containing a Pressure Liquefied Gas, s.l.: Queen's University, Ontario.

Babrauskas, V., 1983. Estimating Large Pool Fire Burning Rates. Fire Technology, Volume 19.

Bainbridge, B. L. & Keltner, N. R., 1988. Heat Transfer to Large Objects in a Pool Fire. Journal of Hazardous Materials, Volume 20.

Basu, N., Warrier, G. R. & Dhir, V. K., 2002. Onset of nucleate boiling and active nucleation site density during subcooled flow boiling. Journal of Heat Transfer, Volume 124.

Basu, N., Warrier, G. W. & Dhir, V. K., 2005. Wall heat flux partitioning during subcooled flow boiling: part 1 - model development. Journal of Heat Transfer, Volume 127.

Benjamin, R. J. & Balakrishnan, A. R., 1997. Nucleation site density in pool boiling of binary mixtures: effect of surface micro-roughness and surface and liquid physical properties. The Canadian Journal of Chemical Engineering , Volume 75.

Bergman, T. L., Lavine, A. S., Incropera, F. P. & Dewitt, D. P., 2011. Fundamentals of Heat and Mass Transfer. 7th ed. s.l.:John Wiley & Sons.

Bi, M.-S., Ren, J.-J. & Che, W., 2011. Effect of fire engulfment on thermal response of LPG tanks. J. of Haz. Mat., Volume 192.

Birk, A. & Cunningham, M., 1994. The Boiling Liquid Expanding Vapour Explosion. Journal of Loss Prevention in the Process Industries, Volume 7.

Birk, A. M., 2000. Review of AFFTAC Model, s.l.: Transport Canada - TP 13539E.

Birk, A. M., Poirer, D. & Davison, C., 2006. On the Response of 500 gal Propane Tanks to a 25% Engulfing Fire. Journal of Loss Prevention in the Process Industries, Volume 19.

Birk, A. M., Poirer, D. & Davison, C., 2006. On the Thermal Rupture of 1.9m3 Propane Pressure Vessels with Defects in their Thermal Protection Systems. Journal of Loss Prevention in the Process Industries, Volume 19.

Blanchat, T. et al., 2009. Validation Experiments to Determine Radiation Partitioning of Heat Flux to an Object in a Fully Turbulent Fire. Proceedings of the Combustion Institute, Volume 32.

Chen, J. C., 1963. A correlation for boiling heat transfer to saturated fluids in convective flow. Boston, ASME.

Cheung, S. C. P., Vahaji, S., Yeoh, G. H. & Tu, J. Y., 2014. Modeling subcooled flow boiling in vertical channels at low pressures - Part 1: Assessment of empirical correlations. Int J. of Heat and Mass Transfer, Volume 75.

Choi, Y. S., Kim, Y. T. & Lim, T. W., 2016. CFD validation for subcooled boiling under low pressure. J. of the Korean Society of Maritime Engineering, Volume 40.

Churchill, S. W. & Chu, H. H. S., 1975. Correlating equations for laminar and turbulent free convection from a vertical plate. Int. Journal of heat and Mass Transfer, Volume 18.

Cole, R., 1960. A photographic study of pool boiling in the region of the critical heat flux. Journal of the American Institute of Chemical Engineers, 6(4).

Cole, R., 1967. Bubble frequencies and departure volumes at subatmospheric pressures. AIChE Journal, 13(4).

Columbo, M. & Fairweather, M., 2016. Accuracy of Eulerian-Eulerian, two-fluid CFD boiling models of subcooled boiling flows. Int J. of Heat and Mass Transfer, Volume 103.

D'Aulisa, A. et al., 2014. CFD Modeling of LPG Vessels Under Fire Exposure Conditions. AIChE J., 60, p. 4292–4305.

Del Valle, V. H. & Kenning, D. B. R., 1985. Subcooled flow boiling at high heat flux. International Journal of Heat and Mass Transfer, 128(10).

Droste, B. & Schoen, W., 1988. Full Scale Fire Tests with Unprotected and Thermal Insulated LPG Storage Tanks. Journal of Hazardous Materials, Volume 20.

Droste, B., 1992. Fire Protection of LPG Tanks with Thin Sublimation and Intumescent Coatings. Fire Technology.

Droste, B., Ulrich, A. & Borch, J., 2011. Brand new fire test facilities at 'BAM Test Site Technical Safety'. Packaging, Transport, Storage and Security of Radioactive Material.

Eckert, E. R. G. & Jackson, T. W., 1950. Analysis of turbulent free-convection boundary layer on flat plate, s.l.: National Advisory Committee for Aeronautics.

Estrada-Perez, C. E. & Hassan, Y. A., 2010. PTV experiments of subcooled boiling flow through a vertical rectangular channel. International Journal of Multiphase Flow, Volume 36.

Estrada-Perez, C. E., Yoo, J. & Hassan, Y. A., 2015. Feasibility investigation of experimental visualization techniques to study subcooled boiling flow. International Journal of Multiphase Flow, Volume 73.

Factory Mutual, 1981. Approval Standard for Fire Protective Coatings for LP Gas Steel Storage Vessels and Process Structures. s.l.:s.n.

Fire and Blast Investigation Group, 2010. TN11: Fire Loading and Structural Response, s.l.: s.n.

Fritz, W., 1935. Berechnung des maximalvolume von dampfblasen. Phys. Z., Volume 36.

Fujii, T. & Imura, H., 1972. Natural-convection heat transfer from a plate with arbitrary inclination. International Journal of Heat and Mass Transfer, Volume 15.

Gaertner, R. F. & Westwater, J. W., 1960. Population of active sites in nucleate boiling heat transfer. Chem. Eng. Prog. 56.

Gandhi, M. S., Sathe, M. J., Joshi, J. B. & Vijayan, P. K., 2011. Two phase natural convection: CFD simulations and PIV measurement. Chemical Engineering Science, Volume 66.

Ganguli, A. A. et al., 2010. Hydrodynamics and heat transfer characteristics of passive decay heat removal systems: CFD simulations and experimental measurements. Chemical Engineering Science, Volume 65.

GEIE, 1993. Fire Protection Study on Fire Proof Tanks Containing Pressure Combustible Liquefied Gases, s.l.: s.n.

George Jr., W. K. & Capp, S. K., 1978. A theory for natural convection boundary layers next to heated surfaces. International Journal for Heat and Mass Transfer, 22(6).

Goel, P., Nayak, A. K., Kulkarni, P. P. & Joshi, J. B., 2017. Experimental study on bubble departure characteristics in subcooled nucleate pool boiling. Int. J. of Multiphase Flow, Volume 89.

Gregory, J., Keltner, N. R. & Jr., R. M., 1989. Thermal Measurements in Large Pool Fires. Journal of Heat Transfer, Volume 111.

Hadjisophocleus, G. V., 1989. Numerical Modelling of LPG Horizontal Cylindrical Tanks Subjected to Heating Environments, s.l.: The University of New Brunswick.

Hatton, A. & Hall, I., 1966. Photographic study of boiling on prepared surfaces. Third International Heat Transfer Conference.

He, J., Liu, J. & Xu, X., 2017. Analysis and experimental study of nucleation site densities in the boiling of mixed refrigerants. International Journal of Heat and Mass Transfer, Volume 105.

Heymes, F. et al., 2013. Impact of a distant wildland fire on an LPG tank. Fire safety journal, Volume 61.

Hibiki, T. & Ishii, M., 2003. Active nucleation site density in boiling systems. International Journal of Heat and Mass Transfer, Volume 46.

Hirt, C. & Nicholas, B., 1981. Volume of fluid (VOF) methods for the dynamics of free boundaries. Volume 39.

Hoelling, M. & Herwig, H., 2005. Asymptotic analysis of the near-wall region of turbulent natural convection flows. Journal of Fluid Mechanics, Volume 541.

HSE, 2000. Research Report R04.036, s.l.: s.n.

Inada, S., Taguchi, T. & Yang, W.-J., 1999. Effects of vertical fins on local heat transfer performance in a horizontal fluid layer. International Journal of Heat and Mass Transfer, 42(15).

International Atomic Energy Association, 1996. Regulations for the Safe Transport of Radioactive Material (ST-1 Revised), s.l.: s.n.

ISO, 2008. ISO22899:1:2007 Determination of the resistance to jet fires of passive fire protection materials - Part 1 general requirements, s.l.: s.n.

Ivey, H. J., 1967. Relationships between bubble frequency, departure diameter and rise velocity in nucleate boiling. International Journal of Heat and Mass Transfer, 10(8).

Jet Fire Test Working Group, 1995. Jet Fire Resistance Test of Passive Fire Protection Materials, Offshore Technology Information Report OTI 95 634., s.l.: HSE.

Joulain, P., 1998. The Behaviour of Pool Fires: State of the Art and New Insights. s.l., 27th Symposium (International) on Combustion.

Judd, R. L. & Hwang, K. S., 1976. A comprehensive model for nucleate pool boiling heat transfer including microlayer evaporation. J. Heat Transfer, 98(4).

Jung, S. & Kim, H., 2016. Effects of surface orientation on nucleate boiling heat transfer in a pool of water under atmospheric pressure. Nuclear Engineering and Design, Volume 305.

Kader, B. A., 1981. Temprature and concentration profiles in fully turbulent boundary layers. Int. Journal of Heat and Mass Transfer, 24(9).

Keltner, N. R., Nicolette, V. F., Brown, N. N. & Bainbridge, B. L., 1990. Test Unit Effects on Heat Transfer in Large Fires. Journal of Hazardous Materials, Volume 25.

Kharangate, C. R. & Mudawar, I., 2017. Review of computational studies on boiling and condensation. Int. J. Heat and Mass Transfer, Volume 108.

Kim, S.-J. & Park, G.-C., 2011. Interfacial heat transfer of condensing bubble in subcooled boiling flow at low pressure. International Journal of Heat and Mass Transfer, Volume 54.

Kiš, P. & Herwig, H., 2012. The near wall physics and wall functions for turbulent natural convection. Int. Journal of Heat and Mass Transfer, Volume 55.

Kocamustafaogullari, G. & Ishii, M., 1983. Interfacial area and nucleation site density in boiling systems. International Journal of Heat Transfer, 26(9).

Kocamustafaogullari, G. & Ishii, M., 1995. Foundation of the interfacial area transport equation and its closure relations. International Journal of Heat and Mass Transfer, 38(3).

Kolev, N. I., 1994. The influence of mutual bubble interaction on the bubble departure diameter. Experimental thermal and fluid science, Volume 8.

Kolev, N. I., 2006. Uniqueness of elementary physics driving heterogeneous nucleate boiling and flashing. Nuclear Engineering Technology, Volume 38.

Kolev, N. I., 2007. Multiphase flow dynamics 2. Berlin: Springer.

Koncar, B., Kljenak, I. & Mavko, B., 2004. Modelling of local two-phase flow parameters in upward subcooled flow boiling at low pressure. Int J. of Heat and Mass Transfer, Volume 47.

Kosecki, H., 1989. Combustion Properties of Large Liquid Pool Fires. Fire Technology, 25(3).

Koski, J. A. & Wix, S. D., 1995. Measurements in Large Pool Fires with an Actively Cooled Calorimeter, s.l.: Sandia National Laboratories Report SAND 95-0082C.

Koski, J. A., 2000. Measurement of Temperature Distribution in Large Pool Fires with the Use of Directional Flame Thermometers, s.l.: Sandia National Laboratories Report SAN02000-1165C.

Kramer, M. A., Koski, J. A. & Greiner, M., 2001. Radiation Heat Transfer to the Leeward Side of a Massive Object Suspended Over a Pool Fire. s.l., Proceedings of International Mechanical Engineering Congress and Exhibition 01.

Kramer, M. A., Koski, J. A., Greiner, M. & Lopez, C., 2001. Measurements of Heat Transfer to a Massive Cylindrical Object Engulfed in a Regulatory Pool Fire. s.l., Proceedings of ASME NHTC'01 35th National Heat Transfer Conference.

Krepper, E. & Rzehak, R., 2011. CFD for subcooled flow boiling: Simulation of DEBORAH experiments. Nuclear Engineering and Design, Volume 241.

Krepper, E., Koncar, B. & Egorov, Y., 2007. CFD modelling of subcooled boiling- Concept, validation and application to fuel assembly design. Nuclear Engineering and Design, Volume 237.

Krepper, E., Rzehak, R., Lifante, C. & Frank, T., 2013. CFD for subcooled flow boiling: Coupling wall boiling and population balance models. Nuclear Engineering and Design, Volume 255.

Kurul, N. & Podowski, M. Z., 1991. On the modeling of multidimensional effects in boiling channels. Minneapolis, MN, ANS Proc. 27th National Heat Transfer Conference.

Kurul, N., 1990. Multidimensional effects in two-phase flow including phase change. s.l.:Rensselaer Polytechnic Institute.

Landucci, G. et al., 2016. Modeling heat transfer and pressure build-up in LPG vessels exposed to fires. Int J. of Thermal Sciences, Volume 104.

Landucci, G., Molag, M., Reinders, J. & Cozzani, V., 2009. Experimental and Analytical Investigation of Thermal Coating Effectiveness for 3m3 LPG Tanks Engulfed by Fire. Journal of Hazardous Materials, Volume 161.

Lee, T. H., Park, G. C. & Lee, D. J., 2002. Local flow characteristics of subcooled boiling flow of water in a vertical concentric annulus. International Journal of Multiphase Flow, Volume 28.

Lemmert, M. & Chawla, J. M., 1977. Influence of flow velocity on surface boiling heat transfer coefficient. Heat Transfer in Boiling, Volume 237.

Lord Cullen, 1990. The Public Inquiry into the Piper Alpha Disaster, s.l.: Department of Energy.

Luke, A. & Gorenflo, D., 2000. Heat transfer and size distribution of active nucleation sites in boiling propane outside a tube. Int. J. Therm. Sci., Volume 39.

Luke, A., 1997. Pool boiling heat transfer from horizontal tubes with different surface roughness. Int. J. Refrigeration.

Malenkov, I., 1972. The frequency of vapor-bubble separation as a function of of bubble size. Fluid Mechanics Soviet Research, Volume 1.

Marie, J. L., Moursali, E. & Tran-cong, S., 1997. Similarity law and turbulence intensity profiles in a bubbly boundary layer at low void fractions. International Journal of Multiphase Flow, Volume 23.

Mikic, B. B. & Rohsenow, W. M., 1969. A new correlation of pool-boiling data including the effect of heating surface characteristics. Journal of Heat Transfer, Volume 91.

Mizner, G. A. & Eyre, J. A., 1982. Large Scale LNG and LPG Pool Fires. s.l., Institute of Chemical Engineers Symposium Series No 71.

Mizner, G. A. & Eyre, J. A., 1983. Radiation From Liquefied Gas Fires On Water. Combustion Science and Technology, Volume 35.

Moodie, K. et al., 1988. Fire Engulfment Tests on a 5 Tonne LPG Tank. Journal of Hazardous Materials, Volume 20.

Moodie, K., 1988. Experiments and Modelling:- An Overview With Particular Reference to Fire Engulfment. Journal of Hazardous Materials, Volume 20.

Moodie, K., Billinge, K. & Cutler, D. P., 1985. The Fire Engulfment of LPG Storage Tanks. s.l., Hazards VIII: IChemE Symposium Series No. 93.

Mudan, K., 1984. Thermal Radiation Hazards from Hydrocarbon Pool Fires. Progress in Energy and Combustion Science, Volume 10.

Murallidharan, J. S. et al., 2016. CFD investigation and assessment of wall heat flux partitioning model for the prediction of high pressure subcooled flow boiling. Int J. of Heat and Mass Transfer, Volume 103.

Nakos, J. T. & Keltner, N. R., 1989. The Radiative-Convective Partitioning of Heat Transfer to Structures in Large Pool Fires. Heat Transfer Phenomenon in Radiation, Combustion, and Fires, Volume 106.

Nakos, J. T., Gill, W. & Keltner, N. R., 1990. The Thermal Response of Generic Objects in JP-4 Pool Fires, s.l.: Sandia National Laboratories SAND-89-0412C.

NFPA, 2004 Edition. NFPA 58: Liquefied Petroleum Gas Code, s.l.: s.n.

Nukiyama, S., 1934. The Maximum and Minimum Values of Heat Transmittal from Metal to Boiling Water Under Atmospheric Pressure. Journal of the Japan Society of Mechanical Engineers, Volume 37.

Oteh, U., 2008. Mechanics of fluids. Bloomington: AuthorHouse.

Paltrinieri, N. et al., 2009. Risk Reduction in Road and Rail LPG Transportation by Passive Fire Protection. Journal of Hazardous Materials, Volume 167.

Petrovic, S., Robinson, T. & Judd, R. L., 2004. Marangoni heat transfer in subcooled nucleate pool boiling. Int. J. of Heat and Mass Transfer, Volume 47.

Planas-Cuchi, E. & Casal, J., 1998. Flame Temperature Distribution in a Pool Fire. Journal of Hazardous Materials, Volume 62.

Planas-Cuchi, E., Casal, J., Lancia, A. & Bordignon, L., 1996. Protection of Equipment Engulfed in a Pool Fire. Journal of Loss Prevention in the Process Industries, Volume 9.

Planas-Cuchi, E., Chatris, J., Lopez, C. & Arnaldos, J., 2003. Determination of Flame Emissivity in Hydrocarbon Pool Fires Using Infrared Thermography. Fire Technology, Volume 39.

Podowski, R. M., Drew, D. A., Lahey Jr., R. T. & Podowski, M. Z., 1996. A mechanistic model of the ebullition cycle in forced convection subcooled boiling. Kyoto, Japan, International topical meeting on nuclear reactor thermal-hydraulics.

Prabhudharwadkar, D., Lopez-de-Bertodano, M. A., Hibiki, T. & Buchanan Jr, J. R., 2014. Assessment of subcooled boiling wall boundary correlations for two-fluid model CFD. Int J. of Heat and Mass Transfer, Volume 79.

Raj, P. K., 2007. Large Hydrocarbon Fuel Pool Fires: Physical Characteristics and Thermal Emission Variations with Height. Journal of Hazardous Materials, Volume 140.

Ren, J.-J.et al., 2013. Simulation on thermal stratification and de-stratification in liquefied gas tanks. Int. J. of Hydrogen Energy, Volume 38.

Rohsenow, W. M. & Mikic, B. B., 1969. A new correlation of pool-boiling data including the fact of heating surface characteristics. Heat Transfer, pp. 245-250.

Rohsenow, W. M., 1953. Heat transfer with evaporation. s.l., University of Michigan Press.

Rohsenow, W. M., Hartnett, J. P. & Cho, Y. L., 1998. Handbook of Heat Transfer. 3rd ed. New York: McGraw-Hill.

Roy, R., Velidandla, V. & Kalra, S., 1997. Velocity field in turbulent subcooled boiling flow. Journal of Heat Transfer, Volume 119.

Sato, Y., Sadatomi, M. & Sekoguchi, K., 1981. Momentum and heat transfer in two-phase bubbly flow. International Journal of Multiphase Flow, Volume 7.

Schneider, M. E. & Kent, L. A., 1989. Measurements of Gas Velocities and Temperatures in a Large Open Pool Fire. Journal of Fire Technology, 25(1).

Shi, J., Bi, M. & Yang, X., 2012. Experimental research on thermal stratification of liquefied gas in tanks under external thermal attack. Experimental Thermal and Fluid Science, Volume 41.

Situ, R., Mi, Y., Ishii, M. & Mori, M., 2004. Photographic study of bubble behaviors in forced convection subcooled boiling. International Journal of Heat and Mass Transfer, Volume 47.

Sollows, K. F. et al., 1988. Full field flow visualisation and analysis: convection in partly filled horizontal cylinders. Experimental Heat Transfer and Fluid Mechanics.

Steinhaus, T., Welch, S., Carvel, R. & Torrero, J., 2007. Large Scale Pool Fires. Thermal Science Journal, 11(3).

Sudheer, S. & Prabhu, S. V., 2010. Measurement of Flame Emissivity of Gasoline Pool Fires. Nuclear Engineering and Design, Volume 240.

Tolubinsky, V. I. & Kostanchuk, D. M., 1970. Vapour bubbles growth rate and heat transfer intensity at subcooled water boiling. Heat Transfer, Volume 5.

Townsend, W., Anderson, C., Zook, J. & Cowgill, G., 1974. Comparison of Thermally Coated and Uninsulated Rail Tank Cars Filled with LPG Subjected to a Fire Environment, s.l.: US Department of Transport Report No. FRA-OR&D 75-32.

Tsuji, T. & Nagano, Y., 1988. Characteristics of a turbulent natural convection boundary layer along a vertical flat plates. International Journal of Heat and Mass Transfer, 31(8).

Tsuji, T. & Nagano, Y., 1989. Velocity and temperature measurements in a natural convection boundary layer along a vertical flat plate. Experimental thermal and fluid science, Volume 2.

Unal, H. C., 1976. Maximum bubble diameter, maximum bubble-growth time and bubble-growth rate during the subcooled nucleate flow boiling of water up to 17.7 MN/m2. International Journal of Heat and Mass Transfer , 19(6).

Venart, J. E. C., Sousa, A., Steward, F. & Prasad, R., 1984. Experiments on the physical modelling of LPG tank cars under accident conditions. Brugge, Int. Conf. Storage and Transport of LPG and LNG.

Versteegh, T. A. M. & Nieuwstadt, F. T. M., 1999. A direct numerical simulation of natural convection between two infinite vertical differentially heated walls scaling laws and wall functions. Int. J. of Heat and Mass Transfer, Volume 42.

Wang, C. H. & Dhir, V. K., 1993. Effect of surface wettability on active nucleation site density during pool boiling of water on a vertical surface. Journal of Heat Transfer, Volume 115.

Warrier, G. R., Basu, N. & Dhir, V. J., 2002. Interfacial heat transfer during subcooled flow boiling. Int. J. of Heat and Mass Transfer, Volume 45.

Wayne, F. & Kinsella, K., 1984. Spectral Emission Characteristics of Large Hydrocarbon Pool Fires. ASME paper, Volume 84-WA/HT-74.

Wu, H. L., Peng, X. F., Ye, P. & Gong, Y. E., 2007. Simulation of refrigerant flow boiling in serpentine tubes. Int J. of Heat and Mass Transfer, Volume 50.

Yang, S. R. & Kim, R. H., 1988. A mathematical model of the pool boiling nucleation site density in terms of the surface characteristics. International Journal of Heat and Mass Transfer, 31(6).

Yeoh, G. H., Vahaji, S., Cheung, S. C. P. & Tu, J. Y., 2014. Modeling subcooled flow boiling in vertical channels at low pressures - Part 2: Evaluation of mechanistic approach. Int J. of Heat and Mass Transfer, Volume 75.

Yoon, K. T. & Birk, A. M., 2004. Computational fluid dynamics analysis of local heating of propane tanks, s.l.: Transport Canada - TP 14357E.

Yu, C. M., Aydemir, N. U. & Venart, J. E. S., 1992. Transient free convection and thermal stratification in uniformly-heated partially-filled horizontal cylindrical and spherical vessels. Journal of Thermal Science, 1(2).

Zeng, L. Z., Klausner, J. F. & Mei, R., 1993. A unified model for the prediction of bubble detachment diameters in boiling systems - 1. pool boiling. International Journal of Heat and Mass Transfer, 36(9).

Zuber, N., 1959. Hydrodynamic aspects of boiling heat transfer (thesis), Los Angeles: Ramo-Woolridge Corporation.

3 EXPERIMENTAL WORK

3.1 Test equipment design

3.1.1 Overview

This section explains the physical design of the test equipment, including the facility, fire system, test vessel, flame shield, instrumentation, and pressure compensation system. Where an aspect of the design varies between tests, further detail can be found in section 3.2.

3.1.2 Statement of contribution

Professor A. M. Birk proposed the concept design of the pressure compensation system. The system was then built, tested, and programmed by James Crawford of Queen's University, Ontario. Pro-par Inc. of Ontario, Canada, were responsible for flange size calculations to achieve the required pressure ratings, and for production of detailed engineering drawings and vessel construction. Queen's University and BAM provided assistance with arranging shipping and customs services. Thermdyne Technologies ltd. provided assistance with Canadian contracts and ordering. Flame shield materials capable of meeting the required specification were proposed by Promat. BAM provided the test facilities, fire system (both equipment and control systems) and a data acquisition system.

3.1.3 Test equipment overview

Figure 17 shows a schematic diagram of the combined equipment. Note that the figure is not to scale, nor were all components shown present in all tests. Various aspects of the equipment are discussed below the figure. The requirement for third-party manufacture at considerable expense meant that there was little scope for design modification once the equipment had been commissioned. Therefore, the design process involved extensive planning of the test vessel, glass windows, instrumentation, pressure compensation system and flame shield in advance of commissioning in order to meet the objectives described in section 2.5. These individual aspects are described in more detail below.

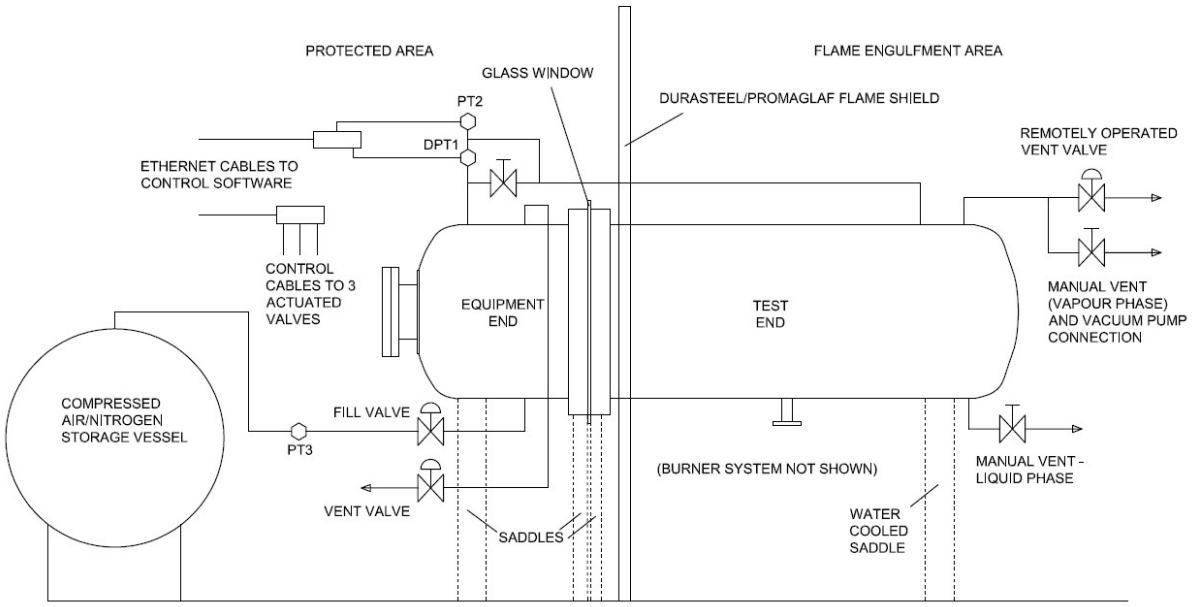

Figure 17 – Schematic of test equipment (not to scale)

3.1.3.1 Test facility

The test facility was generously provided by BAM. Their Technical Safety Test (TTS) site is located approximately 50 km south of Berlin, Germany, in a rural location specifically designed to handle hazardous tests. The fire test facility used is locally known as test pad B and was built to withstand destructive tests of LPG containment vessels. The test pad consists of a large concrete circle containing a shallow rectangular steel-lined pit. Steel I-beams within the pit support the test specimen. Rows of burners lie in between the beams. The test pit can be filled with water to protect the equipment during fire tests. Tests are controlled from a safe distance in a bunker. Large propane tanks (40,000 l capacity) and rotary pumps supply underground lines that feed the test pad burner arrangements. Two site engineers work full-time on the site with responsibility for setting-up and undertaking tests. Figure 18 shows test pad B at the BAM TTS test facility.

3.1.3.2 Fire system

Flexibility in the thermal boundary conditions was sought through use of a custom-built burner arrangement. The fuel supplied to the burner system was liquid propane, via a remote-operated rotary pump and a Coriolis mass flowmeter.

Figure 18 – BAM test pad B

Figure 19 – Control bunker

Two types of burner system were used during the project (further detailed in section 3.2). Up to the end of season one, burner heads were used on a custom frame (see Figure 18). Nozzles had an internal diameter of 1.33 mm and were spaced 150 mm apart in a grid pattern. Burner heads of 150 mm length and 50 mm diameter were used to increase the soot concentration and luminosity of the flame (by reducing the air entrainment in the high-momentum part of the pre-combustion jet).

Early burner system tests were set up for a horizontal release. The intention was to allow the horizontal momentum to drop and for the motion of the gas over the test specimen to be primarily due to buoyancy. This was considered the best way of minimising the convective component of the flame to give a high radiative fraction, as is the case in an actual pool fire. During development tests, the release was switched to vertical, as the horizontal burner array was unable to generate sufficient flame depth without being excessively affected by wind. The vertical release was maintained throughout season one. Season two instead used the BAM ring burners (a horizontal release) as the pressure rise observed in season one was too low and it was desirable to engulf more of the vessel in flame. Equipment limitations meant the original burner design could not be scaled up to achieve this.

The BAM ring burner consists of 1 mm nozzles spaced 0.5 m apart. The position, height and angle of release can be easily adjusted. The ring burner was water-cooled to minimise vaporisation in the supply lines.

3.1.3.3 Test Vessel

As identified in section 2.5, a key objective was for the vessel to have visual access over a wide cross-section during fire testing. Early design ideas included a full-diameter glass window reinforced by an outer metal lattice (or 'spider-web') design and a steel blank plate with numerous sight glasses included. The final design used a pressure compensation system, as this gave the least restrictions on view through the window and the highest maximum pressure possible during tests. The pressure compensation system is detailed further below.

The vessel diameter was set as 1 m. This represents a one third scale for rail tank cars and is a realistic scale for domestic and commercial LPG storage vessels, and it also permits direct comparison of results with work undertaken for the FRA at BAM in 2014 (Sharma and Associates Inc. & Thermdyne Technologies Ltd., 2015).

Pro-par Inc., an experienced vessel manufacturer based in Quebec, Canada, was chosen to manufacture the tank. A draft design was supplied to them, and they supplied engineering drawings prior to manufacture. Numerous iterations of designs were considered, with particular improvements made to the flange designs, the weld locations, and the fittings. Figure 20 and Figure 21 show the final engineering drawings for the vessel.

The vessel shell and flange were designed for maximum pressure of 16 bar (1600 kPa). This value was selected as the common activation pressure of relief valves on LPG tanks, with a view to use of propane as the test fluid. The full-bore flange was designed with oversized threaded rods to accommodate a 19 mm glass window. A flat-face flange type was used to maximise the area over which force was applied to the glass (to reduce the pressure on the glass and reduce the probability of failure).

A manway into the equipment end was specified to allow modification to instrumentation without the need to open the vessel. The test end had a flange on the underside designed specifically for connection to the BAM propane/butane fill system (to allow remote filling of the vessel with propane/butane in a safe manner).

Each end of the vessel was supported on two saddles. The fire exposed saddle had a hollow design to allow water cooling and prevent deformation during fire testing.

Given a need for extensive thermocouple instrumentation of test end of the vessel, and camera feeds and power supply to the equipment end, the following feedthroughs were specified: four of 1", two of ¾", ten of 0.5" and three of 0.25" nipples and couplings for instrument feedthroughs. Two of 1.5" couplings for sight-glasses were also installed in the equipment end.

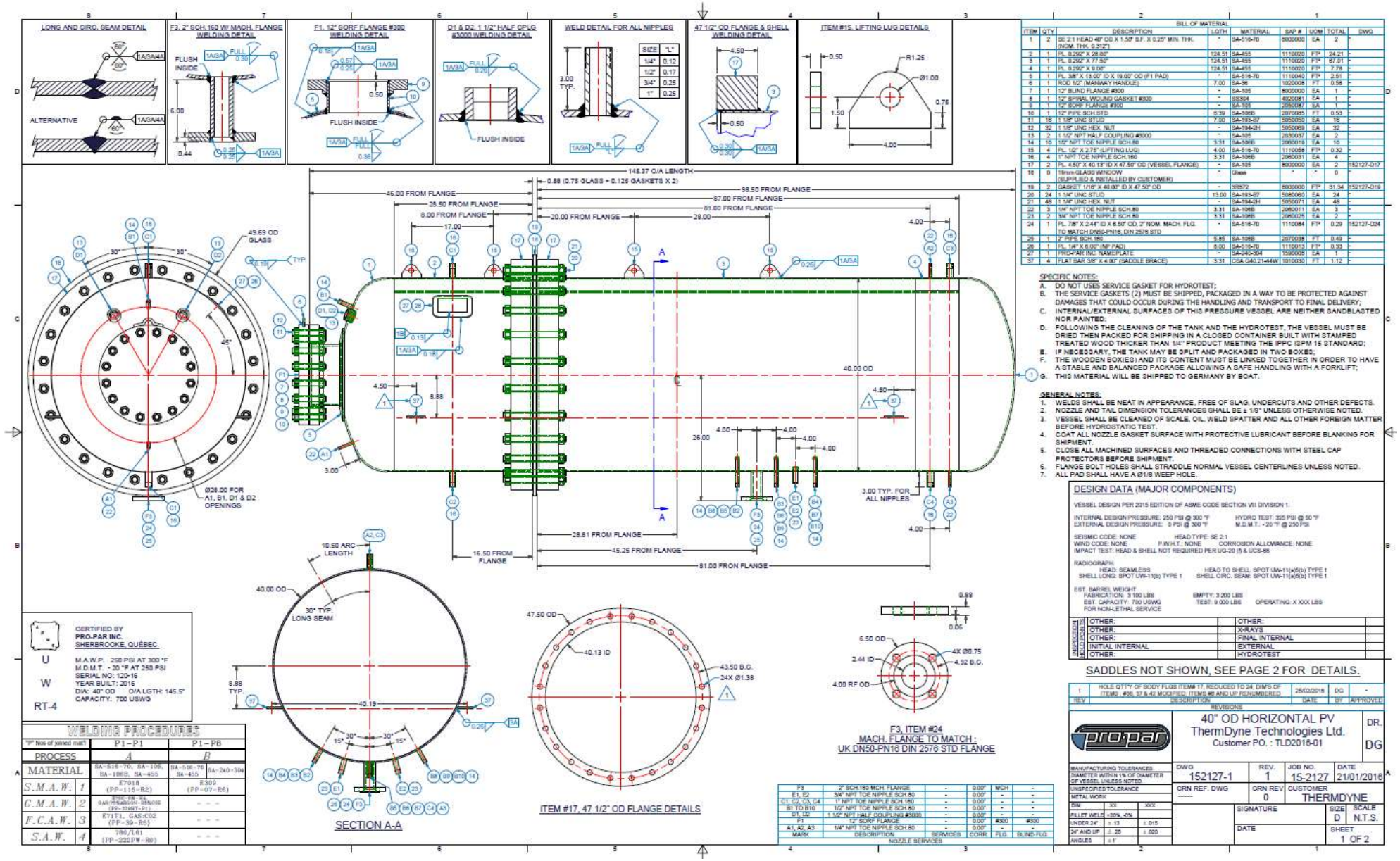

Figure 20 – Vessel design

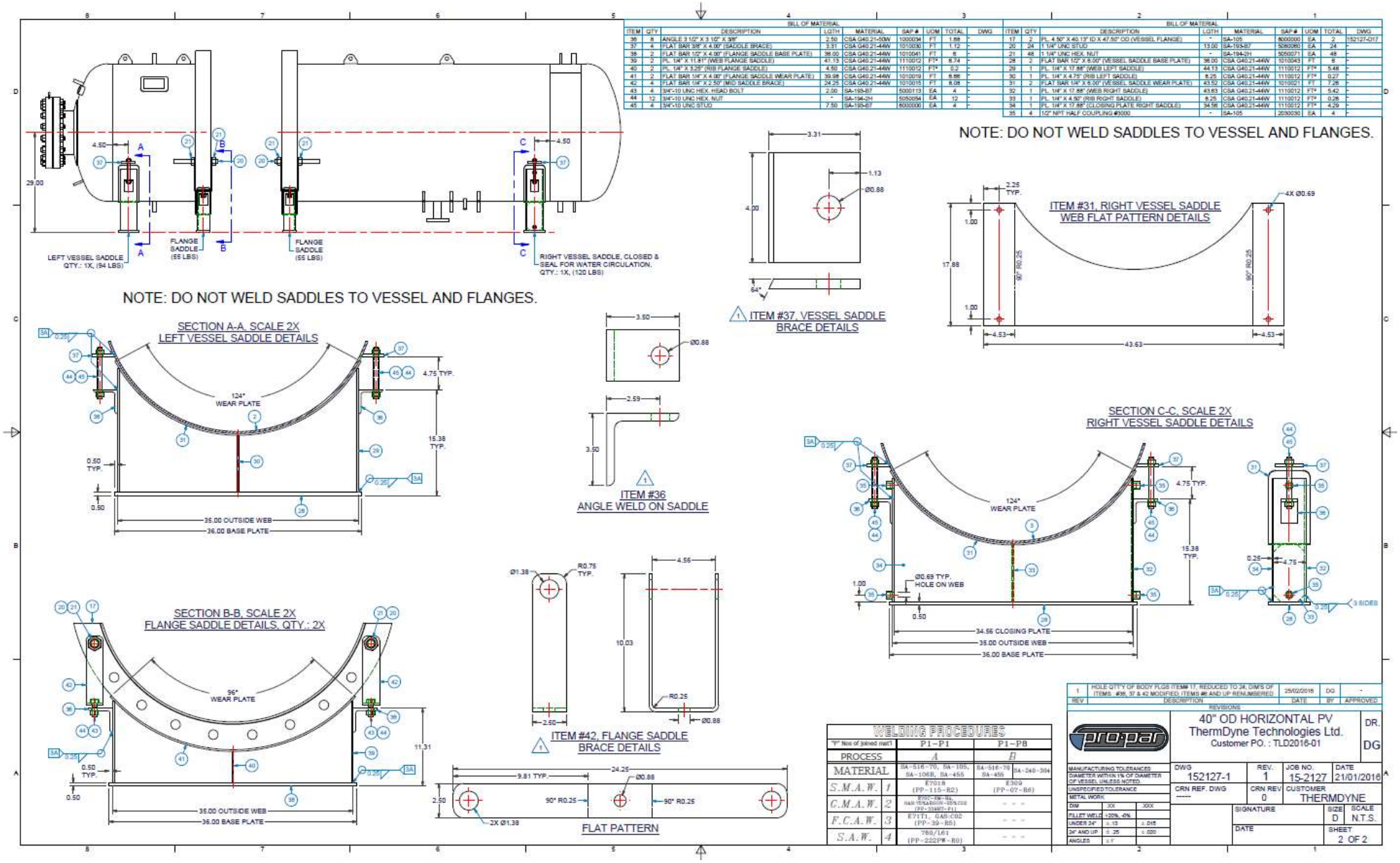

Figure 21 – Vessel support design

3.1.3.4 Glass window

The glass windows were manufactured by Trent Glass, in the U.K., to the following specification: 1315 mm x 1315 mm x 19 mm toughened low iron glass panels with 24 of 35 mm diameter holes on a radius of 552 mm. The holes were oversized to accommodate manufacturing tolerances.

Low iron glass was used to achieve a high transmissivity (0.87 at 19 mm thick, compared to approximately 0.8 for standard glass of a similar thickness). An anti-reflective film was selected in case excessive reflection interfered with the video, however this proved to be unnecessary.

The maximum permitted pressure differential across the window was calculated using equation 3.1

$$t = r\sqrt{\frac{P.K.SF}{M}} \tag{3.1}$$

Where

t is the window thickness (m)

r is the unsupported window radius (m)

P is the pressure differential (psi)

K is an empirical constant (0.75 if edges are clamped, 1.25 if unclamped)

M is the rupture modulus of the glass (psi)

The maximum pressure differential permitted across the window was calculated as 1.1 psi with a safety factor of four and a modulus of rupture of 9000 psi. It is noted that there are many formulas available to calculate the burst pressure of a circular glass window and that equation 3.1 takes no account of dynamic effects or time dependency. Despite this, the above calculation is considered a reasonable approximation given the magnitude of the safety factor assumed and the limitations in accuracy due to the susceptibility of glass to local defects.

Figure 22 – Glass window and flange bolts

3.1.3.5 Pressure Compensation System

The pressure compensation system was designed to pressurise or depressurise the equipment end of the tank to maintain a pressure differential across the glass of less than 0.5 psi. This value was selected on the basis of a factor of safety of two from the calculated break pressure differential.

Two remotely-operated pneumatically driven valves were used to control the flow of gas into and out of the equipment end of the vessel. The gas used was air or nitrogen, with the latter used for tests of flammable materials. A repurposed LPG vessel was positioned next to the equipment end and connected to the supply valve. Although both test vessel and supply vessel were rated to 16 bar, the maximum supply pressure achieved during tests was 11 bar, based on the capability of the compressor or the nitrogen storage cylinders. This resulted in a practical maximum achievable pressure below the intended design pressure.

The two ends of the vessel were connected by a 0.25” pipe to a differential pressure transducer (DPT) on the equipment side of the flame shield. When insulation or a radiation shield was present on the fire-exposed side of the vessel, the connection pipe was run underneath it to minimise heating of vapour within the pressure line. The bidirectional differential pressure transducer used had a range of +/- 2.5 psi and maximum working pressure of 300 psi.

The DPT was connected to a data acquisition system (DAQ) by a 30 m ethernet cable. The same DAQ was used to record the tank pressure and the supply tank pressure. The DAQ was connected to a laptop computer

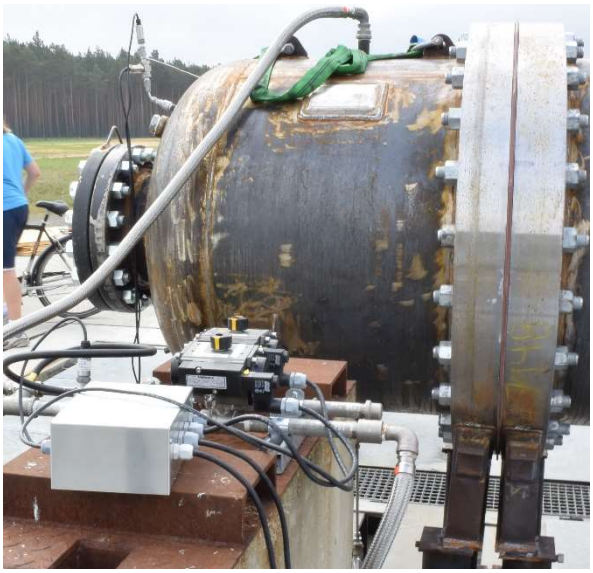

Figure 23 – Pressure compensation valves

running a programme purpose-built in MATLAB. Further details can be found in appendix 2. The software allowed the user to set separate positive and negative threshold differential pressures. On reaching the threshold a relay was activated to open either the fill or the vent valve. The rate of fill and vent was controlled by use of restrictors on the inlets and outlets.

The pressure compensation system functioned exactly as intended, and easily coped with the maximum observed pressure rise during all test seasons of 8 psi (55 kPa) per minute. Differential pressure thresholds of +0.3 psi (2kPa) and -0.4 psi (2.8 kPa) were used as default values to minimise the occurrence of valve cycling, which could happen due to the minimum cycling time of the valves giving a minimum pressure adjustment of approximately 0.5 psi (3.4 kPa) during filling.

3.1.3.6 Flame Shield

The flame shield was designed for repeated exposure to a hydrocarbon-type fire for periods of up to 30 minutes. It consisted of 9.5 mm Durasteel panels supported on a frame of steel channels, as shown in Figure 24. The Durasteel was covered with a layer of 25 mm Promaglaf FR, secured with Vicubond ceramic glue. The materials were generously provided by Promat, except for the channels, cleats, and fixings, which were generously provided by ACE Sections ltd.

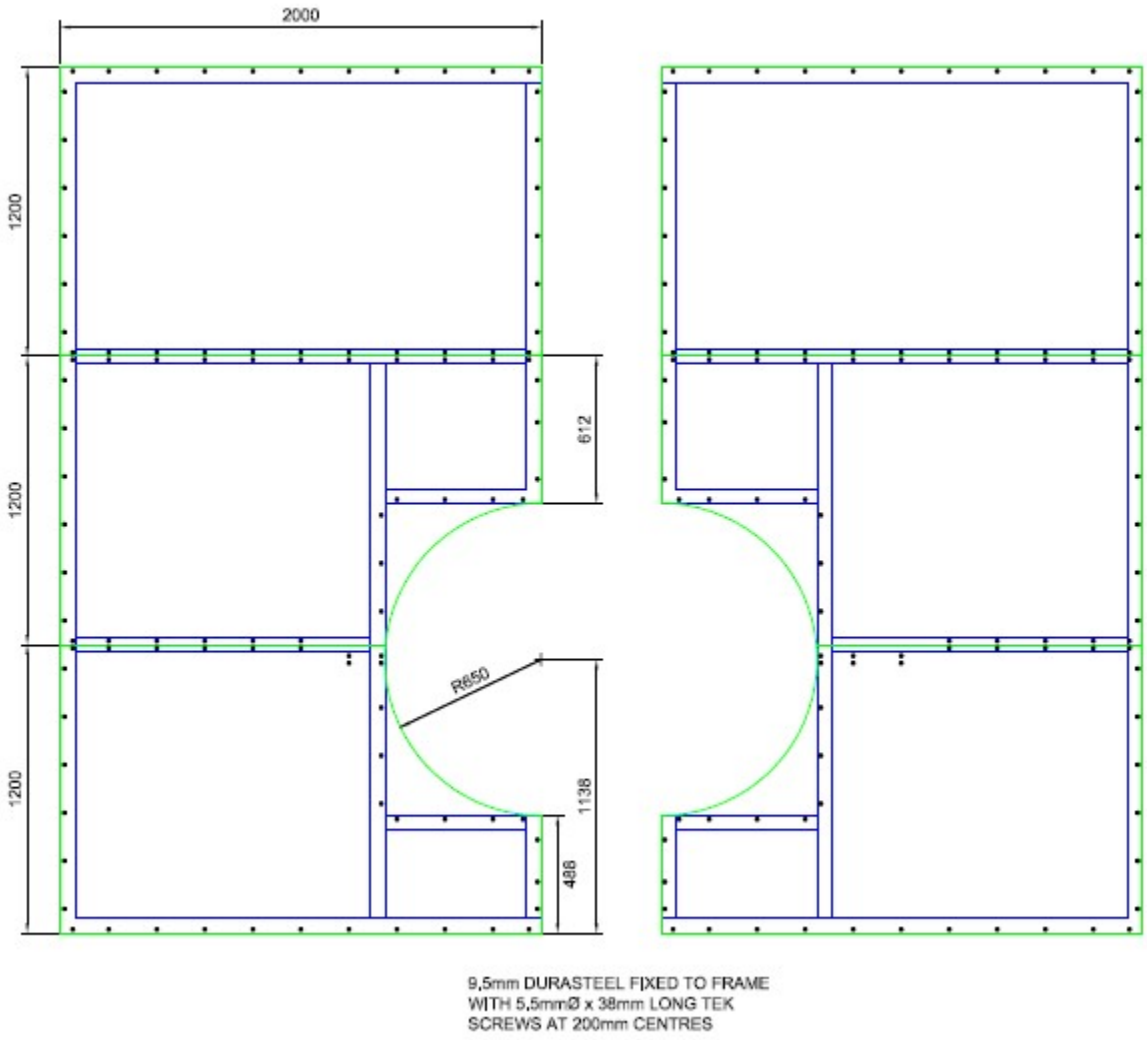

Figure 24 – Flame shield construction

Figure 25 – Supply vessel and valves (shown with flame shield incomplete)

3.1.3.7 Data acquisition

Three data acquisition systems were used. The BAM site data acquisition system (DAQ1) was used in all tests, to take advantage of existing cable and control infrastructure. Thermocouples extended from the tank under insulation to an area behind the fire wall on the north side of the vessel. Each TC for DAQ1 used a Lemo connector to interface with the BAM DAQ system, which was also connected to the meteorological instruments installed at BAM (wind speed, direction, precipitation, humidity, ambient temperature). The limited capacity of DAQ1 meant it was supplemented for test seasons one and two by DAQ2, provided by the University of Edinburgh. DAQ3 was used for the pressure compensation system, as described in appendix 2. An overview of the DAQ systems is given in Table 6.

Table 6 - Data acquisition system overview

DAQ system	Supplied by	Max channels	Used for
1	BAM	100	Test TCs and meteorological data
2	UofE	64	Test TCs
3	Queen's	8	Pressure compensation system

3.1.3.8 Thermocouples

Inconel-sheathed mineral-insulated type K thermocouples were selected for the tests due to their durability, both in terms of mechanical resilience for surviving installation and thermal resilience against flame temperatures of 1100°C. Three types of thermocouples were tested, with a combination of 1 mm and 1.5 mm ungrounded chosen to give the optimum balance between response time and stability. Thermocouples were 6 m long with 10 m PVC insulated tails. Separate Lemo connections were purchased for those to be connected to the BAM DAQ.

Thermocouple positions were designed with the primary aim of resolving the thermal boundary layer. Preliminary CFD calculations undertaken by the University of Bologna indicated the boundary could be less than 2 mm thick (Bradley, et al., 2017), which was partially confirmed through commissioning tests. With such low thicknesses, the diameter of the boundary-region thermocouples (1 mm) was a clear restriction on the ability to resolve detail. Despite this, useful results were obtained, as discussed in subsequent sections.

The exact position of the thermocouples changed slightly over time due to vessel distortion. There were also a small number of intentional modifications between season one and two. More detail on thermocouple positions is given in section 3.2.7.

The method of thermocouple attachment was designed to:

1. Minimise conduction from the vessel shell to the TC
2. Minimise the flow disruption in the region of the TC junctions.

Numerous attachment methods were considered, each of which had disadvantages. Minimal flow disruption can be achieved by installation of a feedthrough at the point of measurement, however the mass of the feedthrough and required TC insulation would have the greatest effect on the thermal boundary conditions at that point, hence this method was discounted and the thermocouples entered the vessel away from the point of measurement.

Inside the vessel, the objective of measuring liquid temperature at precise points dictated the need to fix thermocouples near the point of measurement to resist displacement due to the liquid flow. Consideration was given to attaching thermocouple support rods directly to the vessel wall, however this was expected to result in significant conduction along the support to the Inconel sheath. Instead, the support rods were fixed to a single central support in contact with the vessel top and bottom. Additional rigid spokes (steel rulers 1 mm thick and 27 mm wide) were attached to the centre of the support and extended towards the vessel wall, stopping just short of the wall to prevent contact and minimising conduction between the wall and the support. Steel rulers were chosen for their minimal cross-sectional area in the direction of flow, their rigidity, and because they provided a scale for the conventional video taken during tests.

Thermocouples were inserted through drilled holes at the bottom edge of the rulers and secured with a small amount of epoxy adhesive on the rear side. All thermocouples extended horizontally from the ruler for a minimum of 20 mm. The horizontal extension of the thermocouples was to ensure that flow disruption caused by the rulers was offset from the point of measurement. Thermocouples in contact with the wall ran horizontally along the wall for a minimum distance of 20 mm. They were secured by fine wire spot welded over the part in contact with the wall in a “Z” pattern.

3.1.3.9 Directional flame thermometers (DFTs)

Custom-built directional flame thermometers were provided by Queen's University, Ontario. They were designed to have a hemispherical view of the fire and to give an approximate black-body equivalent temperature representative of an object at that location. Further information is given in appendix 1.

3.1.3.10 Radiation Shield

A number of season one tests utilised a shield to moderate the rate of heat transfer to the vessel shell in contact with vapour. The purpose of the shield was to prolong the life of the test equipment by minimising the distortion and material property changes that would occur during partially full tests if the vessel shell were to reach high temperatures, specifically 730°C at which the steel undergoes a ferrite-austenite phase change. The shield is referred to throughout as a radiation shield after the primary mode of heat transfer that is reduced and is shown in Figure 26.

Figure 26 – Radiation shield in-situ

The radiation shield can be assumed to halve the radiation incident on the vessel, on the assumption that half radiates outwards and half inwards (neglecting temperature differences through the shield), thereby approximately halving the rate of temperature rise of the vessel shell under the shield.

It is recognised that use of a shield affects the results by reducing the radiation to the vapour and liquid surface from the vessel shell. It will also reduce the temperature gradient in the circumferential direction that occurs at the liquid-vapour boundary. The magnitude of these effects has not been quantified, however they were expected to influence the vapour temperatures primarily and the rate of pressure rise secondarily. The

liquid-wetted wall remains unaffected and the influence of the shield on the behaviour of the liquid phase was expected to be minimal. Given the focus of this study on liquid boundary layer measurements and liquid phase behaviour (see sections 2 and 5) use of the shield was considered acceptable. Note that CFD studies that include the vapour domain should either forego use of the radiation shield or quantify the radiation to the vessel shell to determine an appropriate thermal boundary condition for modelling.

3.1.3.11 Pressure transducers

A total of three pressure transducers were used during tests. The differential pressure transducer (DPT1 on Figure 17) was used by the pressure compensation system. A second pressure transducer (PT2 on Figure 17) with a maximum pressure rating of 500 psig (3.4 MPa) was connected to the test end of the vessel on the connecting tube. A third pressure transducer (PT3 on Figure 17) also rate to 500 psig (3.4 MPa) was connected to the supply tank.

3.1.3.12 Cameras

The following conventional cameras were used:

- Nikon Coolpix 9700sp (digital camera)
- Panasonic TZ80 (digital camera)
- Panasonic V250c (digital camcorder)
- Sony HDR-AS200 ActionCAM (digital camcorder)

Further details are not given here but are readily available on-line. The Panasonic V250c had a remote control, operable from outside the tank via a feedthrough connection. The Sony HDR-AS200 had a wrist-watch style remote control that functioned when held near the viewport windows. Magnetic adjustable ('gorilla') monopods or a tripod were used to support the cameras inside the equipment end of the vessel.

3.1.3.13 PIV equipment

Two specialised Flea3 cameras were used to capture PIV images.

- FL3-U3-20E4M-C (1600 x 1200 pixels, 59 fps, global shutter) with a 6.5 mm focal length C-mount lens

- FL3-U3-32S2M-CS (2080 x 1552 pixels, 60 fps, rolling shutter with global start) with a 7.5-75 mm focal length C-mount lens

The cameras were connected directly to laptops via USB 3.0 cables through a feedthrough in the equipment end of the vessel. The laptops used FlyCapture SDK software to control image acquisition. One motorised pan tilt head was available, with external operation by a wired hand controller that exited the tank via a feedthrough.

The laser system consisted of the following equipment (see Figure 27 and Figure 28):

- A 2-watt green continuous class-four laser system, from Dragon lasers
- 25 mm cylinder lens (2 of) and 50 mm cylinder lens (2 of), from Edmund optics
- 35 mm x 155 mm silver coated 4-6λ first surface mirror (3 of)
- A custom-built frame for the laser and lenses
- A custom-built mirror holder

The mirror position could be easily adjusted when the vessel was open. Most tests used the mirror in the vertical position, to give a light sheet that illuminated the middle zone of the tank on the south side. Two tests (15 & 16) use an angled mirror to illuminate the area 135° from the top on the south side. Further information on the laser positioning is given in section 4.4.6.

3.1.3.14 Vacuum pump

A two-stage rotary vane vacuum pump was used for test 22. A bypass tube and manual valve allowed the two ends of the tank to be connected, to safely allow a vacuum to be drawn without breaking the glass. It was the intention to use it for all subsequent tests, however test 22 ended up being the last test of season two.

Figure 28 – PIV mirror in the test end angled at 135°

Figure 27 – Showing laser support arms, laser, lenses, camera tripods and LEDs

3.1.4 Discussion of test equipment

Despite efforts to develop and characterise the fire system in detail, the susceptibility of the fire to environmental effects resulted in significant variations in thermal boundary conditions between tests. Inevitably the use of outdoor large-scale fires presents a fundamental issue, in that the inherent variations can never be fully eliminated. Although an argument can be made that such variability is inevitably present in practical situations, and that there is merit in included a range of boundary conditions in the test 'envelope', verification of CFD modelling clearly requires accurate specification of boundary conditions and benefits from a-priori simulations, which demand the ability to accurately recreate boundary conditions in practical work. Further work is required in this area. Additional steps can be taken to improve the consistency of results using propane burner arrangements, such as planning tests for low wind conditions and using an increased number of burners to increase vessel coverage and reduce susceptibility to wind. To move beyond the inherent variability of actual fires, consideration should be given to the use of radiant heat panels or electrical wire heating. These methods were not considered for the present study, due to time and budget limitations.

The method of thermocouple attachment was inevitably a compromise between aims of minimising both conduction and disruption. Although thermal expansion of the vessel was calculated (and considered negligible relative to the error in positioning), vessel distortion was not. Future work should use a method of attachment fixed to the vessel wall to ensure changes in relative position are minimised. Conduction can be minimised through the use of non-metallic materials under the liquid level.

The PIV system performed well, however the nature of the set-up meant that it was a challenge to ensure the light sheet was incident to the tank wall at exactly 90°. The set-up could only be completed once the tank is closed, limiting visibility. Additional remotely operated pan-tilt heads would allow conventional cameras to check for secondary (reflected) light sheets.

3.2 Test series overview

3.2.1 Test series methodology development

This section provides an overview of the important developments in methodology and practical steps taken during the test series. Note, a full chronological account of the test series is not given. Instead, this section aims to give a high-level account of the steps taken in general chronological order, and to explain decisions taken that had an influence on the results.

3.2.2 Statement of contribution

The practical elements of this project exceeded the capabilities of any one person alone within the time available. The author was involved in all aspects of the practical work, unless stated otherwise. Assistance was provided by others as follows:

Joerg Borch and Thilo Hilse, both BAM employees, provided extensive practical assistance in activities such as welding, plumbing, manual handling, electrical work and fork-lift operation. As primary engineers for the test site, they provided fire test control and DAQ1 management, and arranged hazardous activities such as crane operation.

Prof A. M. Birk provided calibration and adjustment of the laser optics and assisted with infra-red camera operation and general set-up. Giordano Scarponi and Tommaso Iannaccone provided extensive help with insulating, manual handling, plumbing, cleaning, PIV image recording and data acquisition system 2.

3.2.3 List of tests performed

Table 7 - Fire development test series

Test	Date	Vaporiser	Nozzles, orientation	Fuel flow rate (g/min)	Nozzle distance, position, notes
1-2	18.5.16	Not reported – used for commissioning of pipework and control system only			
3	18.5.16	Y	3x3 - Horizontal	600-700	0.4m, mid height
4	18.5.16	Y	*3x3 – Horizontal*	600-1200	0.25m, mid height
5	18.5.16	Y	3x3 – Horizontal	1200	0.21m, as above
6	18.5.16	Y	3x3 – Horizontal	1200	0.21m, flame direction parallel to object surface

Test	Date	Vaporiser	Nozzles, orientation	Fuel flow rate (g/min)	Nozzle distance, position, notes
7	18.5.16	N	3x3 – Horizontal	1200	0.21m, burner head air holes plugged
8	18.5.16	Y	3x3 – Horizontal	1200	0.15m
9	18.5.16	Y	3x3 – Horizontal	1200	0.5m
10	18.5.16	N	3x3 – Horizontal	1600-2000	0.5m
11	19.5.16	N	3x4 – Vertical	1200	1st row 0.12m offset, 0.65m below mid height
12	19.5.16	N	3x4 – Vertical	1200-1600	Nozzles moved so 2nd row (of 4) 0.65m directly below mid-height
13	19.5.16	N	4x4 – Vertical	2133	As above
14	20.5.16	Y	3x3 - Horizontal	1200	0.5m

Table 8 - Calibration and heated patch location test series

Test	Date	Burners	Fill level	Patch top height (see note)	Patch width	Heated sides	Notes
C1-C5	24.5.16 – 15.6.16	Not reported – tests for fire characterisation and commissioning of pressure comp. system					
C6	16.6.16	16	0.7m	LL[1] - 0.05m	0.5m	1	First test with internal TCs
C7	16.6.16	16	0.7m	LL	0.5m	1	
C8	20.6.16	16	0.7m	LL + 0.05m	0.5m	1	
C9	20.6.16	16	0.7m	LL + 0.05m	0.5m	1	
C10	21.6.16	28	0.7m	LL - 0.05m	1.0m	1	
C11	21.6.16	28	0.7m	LL + 0.05m	1.0m	1	
C12	21.6.16	28	0.7m	LL + 0.05m	1.0m	1	
C13	23.6.16	56	0.7m	LL - 0.05m	1.0m	2	
C14	23.6.16	56	0.7m	LL + 0.05m	1.0m	2	
C15	27.6.16	56	0.7m	LL + 0.05m	1.0m	2	
C16	27.6.16	56	0.5m	LL + 0.25m	1.0m	2	Possible undetected leak

Test	Date	Burners	Fill level	Patch top height (see note)	Patch width	Heated sides	Notes
C17	28.6.16	56	0.91m	LL	1.0m	2	Leak detected
C18	28.6.16	56	0.91m	LL	1.0m	2	Repeat of #17

NOTE 1: LL denotes the liquid level, which was 0.7m (74% fill level) for all test in the calibration series

NOTE 2: The fuel flow rate was 133 g per nozzle per minute for tests C1-C18

NOTE 3: The heated patch extended to the bottom of the tank for tests C6-C18

Table 9 - Test season one: water and ethanol pressurised tests

Test	Date	Test fluid	Fill	Vapour space external protection	Notes
1	31.8.16	Water	95%	Bare shell	New LEDs installed
2	31.8.16	Water	95%	Bare shell	
3	01.9.16	Water	92%	Radiation shield	
4	01.9.16	Water	92%	Radiation shield	Repeat of #3
5	20.9.16	Water	50%	Radiation shield	First test with both DAQ systems functional
6	26.9.16	Water	50%	Radiation shield	
7	26.9.16	Water	50%	Radiation shield	Rad. shield deformed, possibly unreliable results
8	27.9.16	Water	50%	Radiation shield	Small leak
9	27.9.16	Ethanol	50%	Radiation shield	Small leak
10	28.9.16	Ethanol	50%	Bare shell	
11	29.9.16	Ethanol	50%	Bare shell	Repeat of #10
12	30.9.16	Ethanol	50%	Radiation shield	Repeat of #9

NOTE 1: The fuel flow rate was 133 g per nozzle per minute for tests 1-12 (total flow rate of 450 kg/hr from all 56 nozzles)

Table 10 - Test season two: water PIV tests

Test number	Date time	Fuel flow rate (kg/hr)	Daq sync	Fill	Fly cameras	Conventional video	PIV data suitable for analysis	Notes
13	11.5.17 10:29	1000	No	0.68m (72%)	1		No	
14	11.5.17 12:11	1000	Yes	0.68m (72%)	1		No	
15	15.5.17 14:14	1200	Yes	0.68m (72%)	1 & 2 (2 only vid)		Fly 1	
16	15.5.17 15:18	1000	Yes	0.68m (72%)	1 & 2		Fly 1 & 2	
17	17.5.17 09:04	1000	Yes	0.58 (60%)			No	Poor fire engulfment
18	17.5.17 09:17	1200	Yes	0.58 (60%)	1 & 2		Fly 1	Water re-used – poor clarity
19	17.5.17 10:20	1200	Yes	0.92 (96%)	1 & 2	0937 (29fps)	Fly 1 & 2	
20	17.5.17 12:10	1000	Yes	0.92 (96%)	1 & 2	0010 (29 fps)	No	Alternated LEDs and laser
21	18.5.17 08:29	1200	Yes	0.6m (62%)	1 & 2	0014 poor clarity	No	
22	19.5.17 08:36	1200	Yes	0.6m (62%)	1	0018	Fly 1	Water degassed

NOTE 1: The vapour space had no external protection (i.e. the shell was exposed to fire) for all season two tests (13-22).

NOTE 2: Horizontal "ring burners", consisting of 0.5m spaced 1.33mm nozzles, were used for tests 13-22. The ring burners underwent minor changes in position but were generally 1.75-2.25m from the tank between the mid-height and bottom of the tank.

3.2.4 Fire development tests

Prior to the arrival of the test vessel, work was undertaken on burner system development and flame characterisation using a steel 'mock-up' of equal diameter and steel thickness, and located at an approximately equal height above the ground. The mock-up is shown in Figure 30 and Figure 32. Table 7 shows the tests performed in this manner.

The mock-up was insulated with Promaglaf on the fire exposed (outer) side, except for a 100 mm x 100 mm square cut at the middle of the curved surface. Five thermocouples (TCs) were installed at mid depth of the steel from the inside, with one being at the centre of the heated square and the four others spaced 100 mm from the centre TC in a cross (+) pattern.

The thermal data generated was used in conjunction with IR camera data (see Figure 31 and Figure 29) to estimate the flame properties and the thermal boundary conditions on the tank using some of the

methodologies later employed during fire characterisation of the test vessel engulfment (reported in section 3.3). The details of the preliminary calculations are not reported, as they are superseded by the later work reported and because the set-up was not used for actual vessel tests.

Figure 30 – Vessel mock up

Figure 32 – Vessel mock up with insulation and DFTs

Figure 31 – Showing the IR camera temporarily behind the specimen

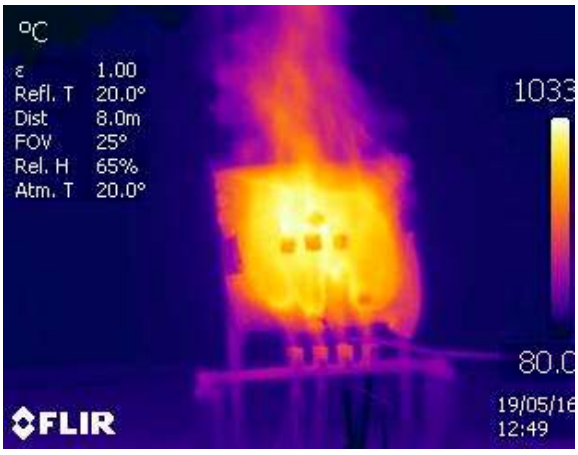

Figure 29 – A typical IR camera image

3.2.5 Fire characterisation and vessel commissioning tests

The test vessel was placed on the south-west corner of BAM test pad B. Details of the equipment design and construction are reported in section 3.1. The propane pumps, actuated valves, water pumps, ignition and pressure compensation system were controlled from a small bunker located 10 m from the vessel (see Figure 18) behind the flame shield (shown in Figure 19).

The threaded rods used to close the main flange were found to result in minor glass chips around the pre-drilled holes during insertion and extraction (see Figure 22). An attempt was made to source replacements bolts of sufficient size with a smooth shank where contact was made with the glass, however supply issues meant this could not be completed during the testing seasons. It was found that the chips had no impact on the ability of the tank to contain pressure, and that small pieces of gasket tape adequately filled chips if necessary.

The flange was initially torqued to 105 Nm, based on a suggested value provided by the vessel manufacturer, however this was found to leak at pressures above of 2 barg (201 kPa). Table 11 shows the torque found to be necessary to achieve corresponding pressures without significant leakage.

Table 11 – Pressures achieved compared with torque applied

Torque (Nm)	Pressure achieved Barg (kPa)
105	2 (201)
190	3 (301)
225	4 (401)
265	4.7 (471)
305	5 (501)

To prevent excessively rapid pressurisation/depressurisation of the equipment, end restrictors were used on the supply pipe to the vessel and the outlet of the vent valve (see Figure 23). Initial tests were performed with a steel blank plate, to avoid glass breakage, and the largest restrictors prepared; a 9 mm pipe approximately 0.3 m long was used for the supply line and a stop with a 4 mm hole for the vent valve outlet. These were found to restrict the change in pressure upon activation of the valves to approximately 0.6 psi (4.1 kPa), which was considered adequate given a calculated break pressure of approximately 1.5-2 psi (10.3-13.8 kPa). The pressure in the supply tank (visible on the left in Figure 25) affected the rate of pressure rise during fill valve

activation. Supply pressures of 5 to 9 bar (500 to 900 kPa) were tested, with the effect on minimum pressure change during a vent cycle found to be +/- 0.1 psi (0.7 kPa).

Following tests C1-C4 an alternative gasket material was used: Klinger Sealex 10 mm x 3 mm. Achieving an equivalent pressure without leak to the solid gasket was found to require an additional 1/6 turn of the nut. This took the necessary torque beyond the range of the torque wrenches available and therefore an accurate value for the torque used cannot be provided.

Thermocouples were installed at mid-height on the south side by forming thin steel (0.2 mm) into an 'L' shape with approximate dimensions: 100 mm x 10 mm x 10 mm. The short side of the 'L' was spot welded to the inside of the tank 100 mm above the mid-height of the vessel. A spacing of 50 mm was provided between each "L". Three types of type-K mineral-insulated Inconel sheathed thermocouples were installed at varying distance from the inside tank wall as given in Table 12.

Table 12 – Thermocouples positions during commissioning tests

Centre distance from wall (mm)		
1 mm Grounded	**1 mm Insulated**	**1.5 mm Insulated**
0.5 (wall)	0.5 (wall)	0.5 (wall)
5	3	2
9	7	7
13	9	13
19	14	21
24	23	31
42	38	44
62	59	

When using water as the test fluid the optical clarity was found be highly variable. If the inside surface was clean and the vessel recently filled with water, visibility was generally good. However, the water turned cloudy after each test. This is attributed to rust forming and being washed off the surface into the water by the flow. Overnight the rust would settle and clarity would partially return, however it was quickly lost during further tests as the motion of the liquid dispersed the rust particles once more. Due to the extensive effort and time required to open, clean and reclose the tank, it was decided to paint the inside tank surface with a heat resistant black matt paint. Unfortunately, it was not possible to measure the surface roughness of the curved surface in-situ, hence no quantitative information can be provided. Rolled steel has a reasonably rough surface, with an arithmetic mean deviation (R_a) typically between 12 and 25 µm. Cold rolling and other

finishing methods reduce roughness, typically to below 1 µm (Finetubes, n.d.). However, in private communication with a paint manufacturer (AkzoNobel) it was stated that corrosion can increase this to greater than 5 µm and pre-painting treatments such as grit blasting intentionally create a roughness profile of 12-15 µm. Spray paint like the one used has very fine pigments and a low viscosity (to facilitate spraying) and will typically give a smooth finish with R_a values below 1 µm (assuming a smooth surface prior to painting).

3.2.6 Season one: water and ethanol tests

The intensity of light in the tank for conventional video was considered inadequate during the commissioning tests and improved prior to season one by the installation of four custom-built light emitting diodes (LEDs), as shown in Figure 34. Each LED was 100 W (9000 Lumens) and connected to a 240 V AC driver on an 'L'-shaped aluminium heat sink. The LEDs were positioned with two just under the liquid level at 75% full, and two mid-way between these and the bottom of the vessel. A piece of square steel tube with foam pads was used to cover each light and minimise reflections or flaring.

After test 5 it was found that tank distortion had caused the central supporting rods to bend significantly. The existing rods were cut 10 mm short of the vessel top and a short section of pipe (20 mm length) was welded to the top of the vessel as a guide for the rod. This permitted vertical relative movement between the rod and the vessel.

In all tests, there is the possibility that vessel distortion changed the distance between the vessel wall and the thermocouples. Thermal expansion will also induce temporary changes in distance, particularly for TCs above the liquid surface, where temperatures, and hence expansions, are greater.

A bulge at the top of the tank approximately 200 mm from the east side of the heated zone was noticed during test 10. This distortion remained present throughout the remaining tests, leading to additional permanent deviations from the TC target wall distances to actual. Each time the tank was opened the distances were therefore remeasured, as given in Table 13.

The second data acquisition system (DAQ2) was provided by the University of Edinburgh and installed prior to season one. Synchronisation between the BAM DAQ1 and DAQ2 was achieved by simultaneous wiring to a 9V battery connector. During a test the battery was connected and the voltage jump to 9V used to synchronise the data during post-processing. The pressure compensation system was not set-up to permit synchronisation by the battery, instead a manual marker was inserted into the data by the operator at the same time the

battery was connected. The error in both synchronisation methods is estimated at +/- 1 s, due to differences in the scan time of the DAQs when set to 1 Hz, or due to user reaction time when synchronised manually.

3.2.7 Thermocouple positions for test seasons one and two

Table 13 gives the locations of each thermocouple used in and on the test vessel. Note that 'Position' in Table 13 refers to a group location as indicated in Figure 33. All thermocouples are fixed from the inside of the vessel except for those with position 'Ext'. These are affixed from the outside, on the side indicated by the additional letter.

The degrees from the top are given independently of the position or side. Where a TC is designated with degrees "C" the thermocouple is in the centre of the 2D vessel cross-section. Figure 34 and Figure 35 show the spokes in cross-section.

Distance to the wall is given to the centre of the thermocouple. A distance of 0 mm indicates the TC head is inserted into a pre-drilled hole within the wall at a target depth of 2 mm. A distance of 0.5 mm indicates a 1.0 mm diameter TC installed in contact with the wall (yet primarily in contact with the test fluid). Larger distances are secured in steel supports as described previously, and as shown in Figure 35.

Table 13 – Thermocouple positions for seasons one and two

Date	**30.6.16 (Tests 1-12)**				**09.5.17 (Tests 13-16)**				**16.5.17 (Tests 17-22)**			
TC#	Position	Degrees (from top)	Distance to wall (mm)	TC diameter (mm)	Position	Degrees (from top)	Distance to wall (mm)	TC diameter (mm)	Position	Degrees (from top)	Distance to wall (mm)	TC diameter (mm)
0	T	0	0.5	1.5	T	0	0	1.5	T	0	0	1.5
1	T	0	0.5	1.5	T	0	0.5	1.5	T	0	0.5	1.5
2	A	0	0.5	1	A	0	0.5	1	A	0	0.5	1
3	T	0	0.5	1.5	T	0	0.5	1.5	T	0	0.5	1.5
4	B	0	0.5	1	B	0	0.5	1	B	0	0.5	1
5	A	0	50	1.5	A	0	50	1.5	A	0	50	1.5
6	A	0	100	1.5	A	0	100	1.5	A	0	100	1.5
7	A	0	200	1.5	A	0	200	1.5	A	0	200	1.5
8	A	0	300	1.5	A	0	300	1.5	A	0	300	1.5
9	A	C	500	1.5	A	C	500	1.5	A	C	500	1.5
10	A	45	30	1.5	A	45	30	1.5	A	45	26	1.5
11	A	45	50	1.5	A	45	50	1.5	A	45	45	1.5
12	A	45	100	1.5	A	45	100	1.5	A	45	95	1.5
13	A	45	200	1.5	A	45	200	1.5	A	45	200	1.5
14	A	45	300	1.5	A	45	300	1.5	A	45	300	1.5
15	A	67.5	30	1.5	A	67.5	30	1.5	A	67.5	30	1.5
16	A	67.5	50	1.5	A	67.5	50	1.5	A	67.5	50	1.5
17	A	67.5	100	1.5	A	67.5	100	1.5	A	67.5	100	1.5

Date	30.6.16 (Tests 1-12)				09.5.17 (Tests 13-16)				16.5.17 (Tests 17-22)			
TC#	Position	Degrees (from top)	Distance to wall (mm)	TC diameter (mm)	Position	Degrees (from top)	Distance to wall (mm)	TC diameter (mm)	Position	Degrees (from top)	Distance to wall (mm)	TC diameter (mm)
18	A	67.5	200	1.5	A	67.5	200	1.5	A	67.5	200	1.5
19	A	67.5	300	1.5	A	67.5	300	1.5	A	67.5	300	1.5
20	A	90	30	1.5	A	90	30	1.5	A	90	30	1.5
21	A	90	50	1.5	A	90	50	1.5	A	90	50	1.5
22	A	90	100	1.5	A	90	100	1.5	A	90	100	1.5
23	A	90	200	1.5	A	90	200	1.5	A	90	200	1.5
24	A	90	300	1.5	A	90	300	1.5	A	90	300	1.5
25	A	112.5	30	1.5	A	112.5	30	1.5	A	112.5	30	1.5
26	A	112.5	50	1.5	A	112.5	50	1.5	A	112.5	50	1.5
27	A	112.5	100	1.5	A	112.5	100	1.5	A	112.5	100	1.5
28	A	112.5	200	1.5	A	112.5	200	1.5	A	112.5	200	1.5
29	A	112.5	300	1.5	A	112.5	300	1.5	A	112.5	300	1.5
30	A	135	30	1.5	A	135	30	1.5	A	135	35	1.5
31	A	135	50	1.5	A	135	50	1.5	A	135	55	1.5
32	A	135	100	1.5	A	135	100	1.5	A	135	105	1.5
33	A	135	200	1.5	A	135	200	1.5	A	135	205	1.5
34	A	135	300	1.5	A	135	300	1.5	A	135	300	1.5
35	A	157.5	30	1.5	A	157.5	30	1.5	A	157.5	30	1.5
36	A	157.5	50	1.5	A	157.5	50	1.5	A	157.5	50	1.5
37	A	157.5	100	1.5	A	157.5	100	1.5	A	157.5	100	1.5
38	A	157.5	200	1.5	A	157.5	200	1.5	A	157.5	200	1.5
39	A	157.5	300	1.5	A	157.5	300	1.5	A	157.5	300	1.5
40	A	180	30	1.5	A	180	30	1.5	A	180	30	1.5
41	A	180	50	1.5	A	180	50	1.5	A	180	50	1.5
42	A	180	100	1.5	A	180	100	1.5	A	180	100	1.5
43	A	180	200	1.5	A	180	200	1.5	A	180	200	1.5
44	A	180	300	1.5	A	180	300	1.5	A	180	300	1.5
45	B	0	100	1.5	C	0	50	1.5	C	0	50	1.5
46	B	0	200	1.5	C	0	150	1.5	C	0	150	1.5
47	B	0	300	1.5		TC dead				TC dead		
48	B	C	500	1.5	C	0	300	1.5	C	0	150	1.5
49	B	180	0.5	1.5	A	180	0	1.5	C	0	300	1.5
50	A	22.5	0.5	1	A	22.5	0.5	1	A	180	0	1.5
51	A	45	0.5	1	A	45	0.5	1	A	22.5	0.5	1
52	A	45	3	1	A	45	3	1	A	45	0.5	1
53	A	45	6	1	A	45	6	1	A	45	2.5	1
54	A	45	11	1	A	45	11	1	A	45	6	1
55	A	45	20	1	A	45	20	1	A	45	11	1
56	A	67.5	0.5	1	A	67.5	0.5	1	A	45	17	1
57	A	67.5	3	1	A	67.5	3	1	A	67.5	0.5	1
58	A	67.5	6	1	A	67.5	6	1	A	67.5	4	1
59	A	67.5	11	1	A	67.5	11	1	A	67.5	6	1
60	A	67.5	20	1	A	67.5	20	1	A	67.5	11	1
61	A	90	0.5	1	A	90	0.5	1	A	67.5	20	1
62	A	90	3	1	A	90	5	1	A	90	0.5	1
63	A	90	8	1	A	90	10	1	A	90	4	1
64	A	90	12	1	A	90	14	1	A	90	9	1
65	A	90	20	1	A	90	20	1	A	90	13	1
66	A	112.5	0.5	1	A	112.5	0.5	1	A	90	21	1
67	A	112.5	3	1	A	112.5	3	1	A	112.5	0.5	1
68	A	112.5	6	1	A	112.5	6	1	A	112.5	1.5	1
69	A	112.5	11	1	A	112.5	12	1	A	112.5	3	1
70	A	112.5	20	1	A	112.5	20	1	A	112.5	9	1
71	A	135	0.5	1	A	135	0.5	1	A	112.5	19	1
72	A	135	3	1	A	135	3	1	A	135	0.5	1

Date	30.6.16 (Tests 1-12)				09.5.17 (Tests 13-16)				16.5.17 (Tests 17-22)			
TC#	Position	Degrees (from top)	Distance to wall (mm)	TC diameter (mm)	Position	Degrees (from top)	Distance to wall (mm)	TC diameter (mm)	Position	Degrees (from top)	Distance to wall (mm)	TC diameter (mm)
73	A	135	6	1	A	135	7	1	A	135	4	1
74	A	135	11	1	A	135	11	1	A	135	12	1
75	A	135	20	1	A	135	20	1	A	135	15	1
76	A	157.5	0.5	1		TC dead				TC dead		
77	A	157.5	3	1	A	157.5	3	1	A	157.5	5	1
78	A	157.5	6	1	A	157.5	6	1	A	157.5	7	1
78	A	157.5	11	1	A	157.5	11	1	A	157.5	11	1
79	A	157.5	20	1	A	157.5	20	1	A	157.5	22	1
80	A	180	0.5	1	A	180	0.5	1	A	180	0.5	1
81		BLANK		1	A	157.5	3	1	A	180	6	1
82	A	180	6	1		Not used				Not used		
83	A	180	11	1	A	180	6	1	A	180	20	1
84	A	180	20	1	A	180	11	1	A	157.5	5	1
85	B	45	0.5	1	A	180	20	1	A	157.5	7	1
86	B	67.5	0.5	1		TC dead				TC dead		
87	B	67.5	2	1		TC dead				TC dead		
88	B	67.5	4	1	A	45	0	1	A	45	0	1
89	B	67.5	7	1	A	157.5	0.5	1	A	157.5	0.5	1
90	B	90	0.5	1	A	90	0	1	A	90	0	1
91	B	90	2	1	B	90	0.5	1	B	90	0.5	1
92	B	90	4	1	A	337.5	0	1	A	337.5	0	1
93	B	90	7	1		TC dead				TC dead		
94	B	112.5	0.5	1	A	135	0	1	A	135	0	1
95	B	112.5	2	1		TC dead				TC dead		
96	B	112.5	4	1	A	270	0	1	A	270	0	1
97	B	112.5	7	1	A	292.5	0	1	A	292.5	0	1
98	B	135	0.5	1	A	315	0	1	A	315	0	1
99	B	135	2	1	B	135	0.5	1	B	135	0.5	1
100	B	135	4	1	A	247.5	0	1	A	247.5	0	1
101	B	135	7	1	A	225	0	1	A	225	0	1
102	B	157.5	0.5	1	A	202.5	0	1	A	202.5	0	1
103	B	0	300	1.5	A	180	400	1	A	180	400	1
A1	A Ext	0		1.5	A Ext	0		1.5	A Ext	0		1.5
A2	A Ext	22.5		1.5	A Ext	22.5		1.5	A Ext	22.5		1.5
A3	A Ext	45		1.5	A Ext	45		1.5	A Ext	45		1.5
A4	A Ext	67.5		1.5	A Ext	67.5		1.5	A Ext	67.5		1.5
A5	A Ext	90		1.5	A Ext	90		1.5	A Ext	90		1.5
A6	A Ext	112.5		1.5	A Ext	112.5		1.5	A Ext	112.5		1.5
A7	A Ext	135		1.5	A Ext	135		1.5	A Ext	135		1.5
A8	T Ext	0		1.5	T Ext	0		1.5	T Ext	0		1.5
A9	T Ext	0		1.5	T Ext	0		1.5	T Ext	0		1.5
A10	B Ext	67.5		1.5	B Ext	67.5		1.5	B Ext	67.5		1.5

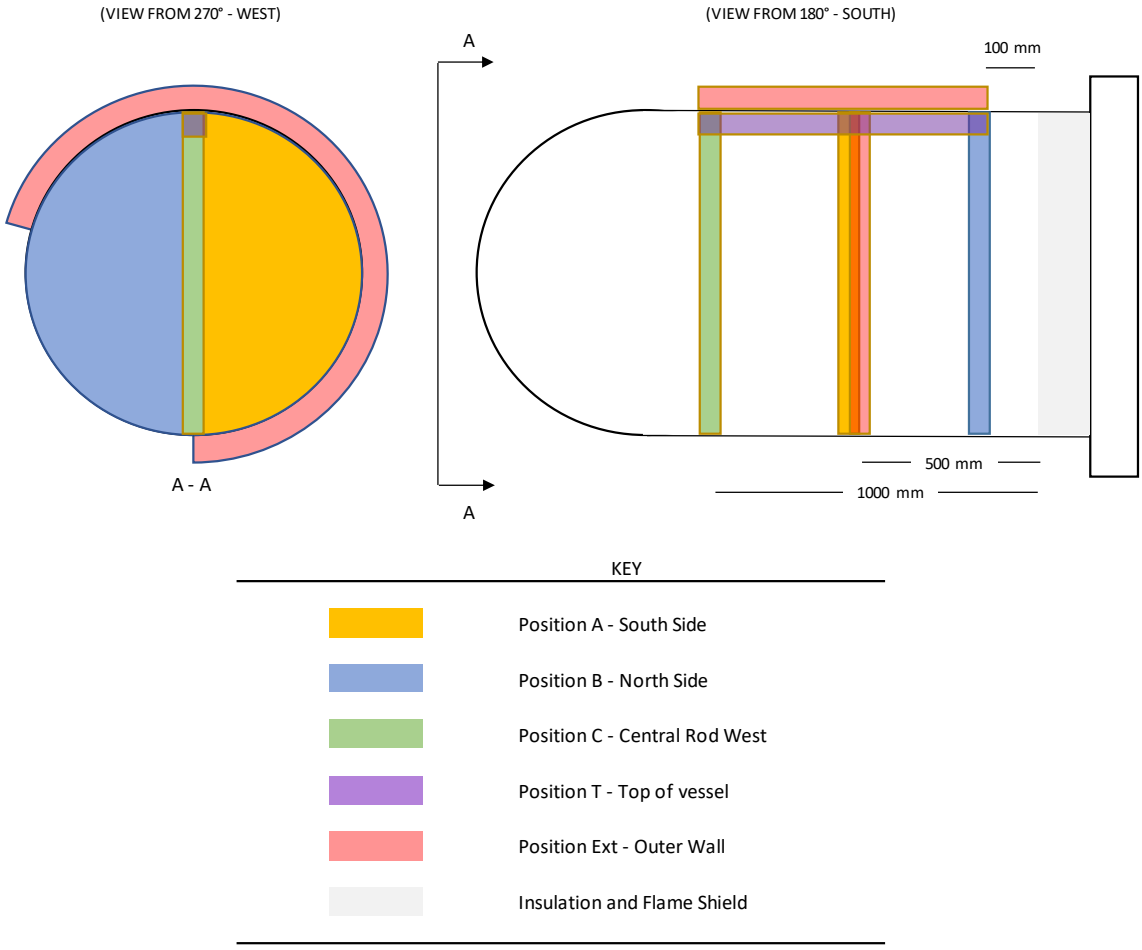

Figure 33 – Thermocouple position schematic

NOTE: Position areas may overlap, causing additional colours on the figure.

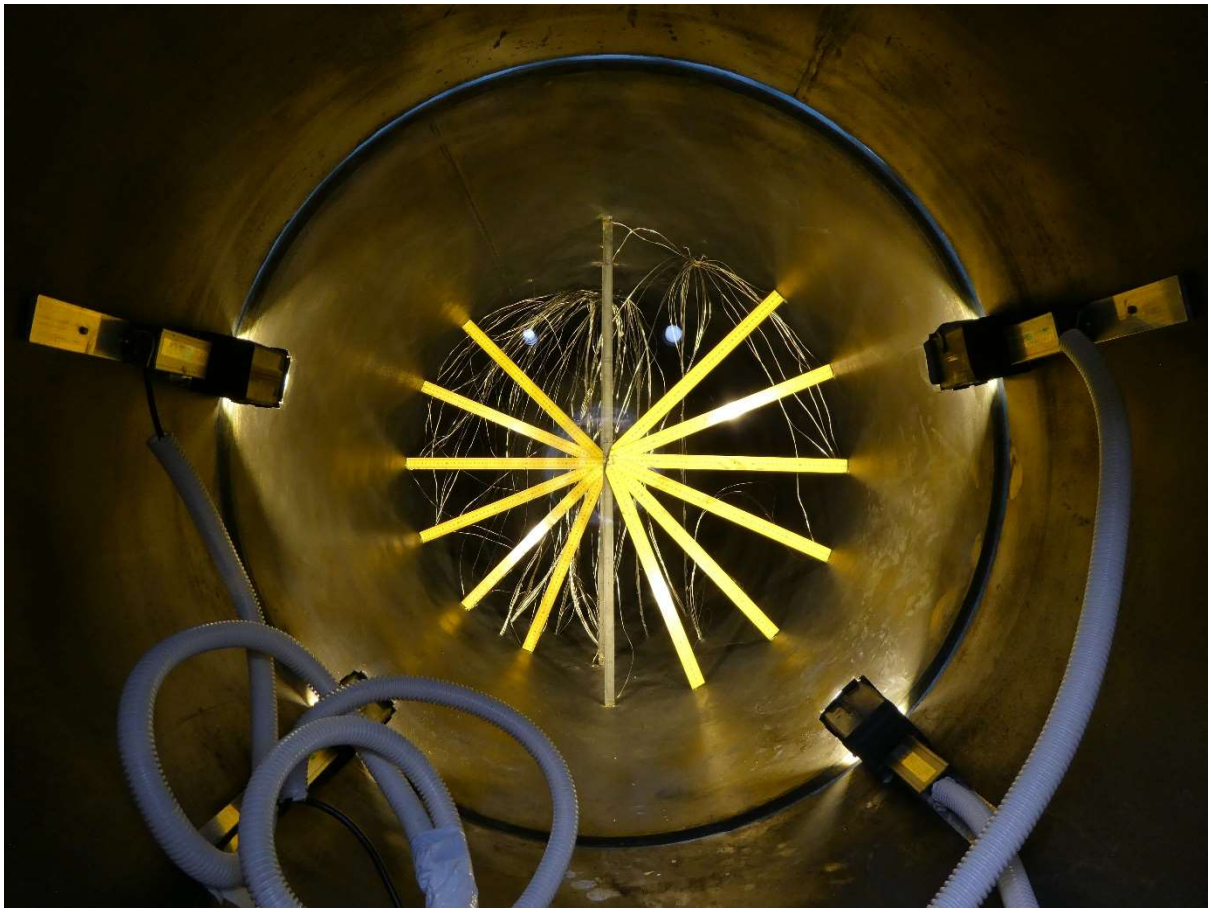

Figure 34 – View inside closed vessel (from equipment/camera end) showing TCs and LEDs

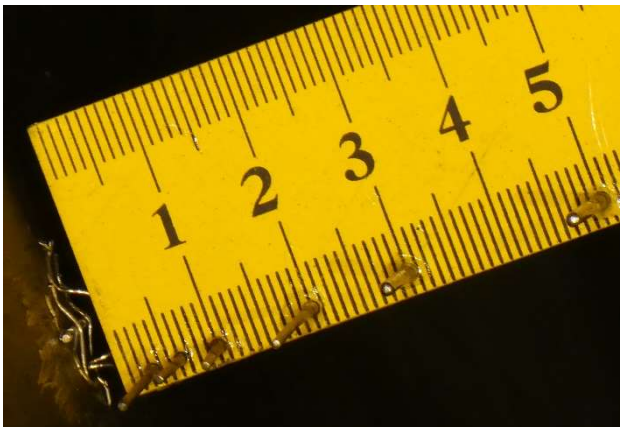

Figure 35 – Close-up of thermocouples secured in steel rule support

3.2.8 Season two: water PIV tests

The first two tests in season two (tests 13 and 14) were performed prior to implementation of the battery-based data synchronisation connection. Synchronisation has been performed during post-processing by manual comparison of time data to match significant temperatures increases. Similar comparisons made with tests that were correctly synchronised indicate the error in this approach is less than 10 seconds.

Tests 13 to 22 were performed with the test end of the tank being open to atmosphere (vented). The pressure compensation system was consequently disabled and hence no such data is available. The intention was to proceed to pressurised tests starting with test 23, however human error during preparation for the test caused the tank to over-fill and the glass window to rupture. The damage destroyed the PIV system and unfortunately resulted in premature termination of the testing season as it could not be replaced within the remaining time and budget.

The PIV set-up required tack welding of metal bars across the camera end of the vessel as shown in Figure 27. Clamps were used to secure a platform for the laser, while camera arms with locking brackets were used to secure the Flea3 cameras.

The mirror was held in a custom-built frame connected to a supporting rod, which was secured to two adjustable arms with magnetic bases. This ensured easy adjustment of the mirror position when the tank was open. Mirror positioning was performed using a laser pointer to simulate the ultimate position of the laser when the tank was closed, allowing the mirror angle to be adjusted until the laser spot fell directly on to a guide-line representing the ultimate position of the laser sheet. The tolerance of the flange bolt holes and the movement during lifting meant that the exact position of the laser could not be assured. Refinement of the laser sheet was performed after the tank was closed by adjustment of the laser position. Deviations from the required 45° angle of incidence to the mirror were evident from reflected laser sheets visible on the tank wall and mirror.

Three alternative seeding types were sourced: Vestosint 1111, Vestosint 2157 (both polymer spheres with an average diameter of 50 µm and average density of 1016 kg/m^3) and Potters AG-SL150-30-TR (silver coated hollow ceramic spheres with an average diameter of 80 µm and average density of 1500 kg/m^3). Only the Potters seeding was used following advice given regarding previous success by research groups in L'ecole des Mines (Alès, France) and Queen's University (Ontario, Canada).

Following private correspondence with a research team at Queen's University who were using PIV at the time of season two an initial seeding concentration of approximately 20 g per cubic metre of water was used. A sample of initial results was sent to Queen's University and a basic analysis performed using Dantech Dynamic Studio software. It indicated that an increased quantity of seeding was required. Consequently, tests 17 and onwards used a concentration of approximately 100 g per cubic metre of water.

The BAM test site wind speed is typically lowest early in the morning, building up following sunrise. Due to site access restrictions and set-up time the tests had to be undertaken during mid-morning to mid-afternoon. The prevailing wind was typically from a south-easterly direction, causing intermittent problems with flame engulfment on the laser sheet side (the south side) of the vessel. Some minor changes to the fire set-up were made during season two, with the aim of achieving improved flame engulfment on the south side of the vessel. An increased fuel flow rate generally improved flame engulfment, however the maximum rate used of 1200 kg/hour resulted in flames extending beyond the extremities of the flame shield and a need to limit test durations. The ring burner was tested in the positions given in Table 14, with commentary added on the fire obtained during the test. In general, the dual ring-burner configuration was unable to provide adequate engulfment of the west end of the tank. The influence of the flame shield on the wind and flame caused the flame to lean eastwards towards the shield. Figure 36 shows the typical flame distribution in test 15, where the west end of the tank is clearly not engulfed.

Test 22 used a vacuum pump to deaerate the water prior to commencing the test. Both ends of the vessel were connected via the bypass tube to allow a vacuum to be drawn without generating a significant pressure gradient across the window. The vacuum was maintained until no further 'boil-off' of air was visible. The vacuum pump was then isolated and the vessel re-pressurised, prior to both ends of the tank being isolated and the pressure compensation system being started. It was recognised that re-pressurisation would result in air going back into solution, however this is a time-dependent process and the rapid start to the test meant the mass of air in solution was significantly lower. This was evident from negligible bubble formation at the start of the test, despite the air in solution being unquantified.

Figure 36 – Typical flame distribution in test 15

Table 14 – Season two test notes

Test	Fuel flow rate (kg/hr)	Horizontal distance to vessel (m)	Vertical position relative to vessel bottom	Angle	Notes
13-14	1000	1.75	0	Horizontal	Period of weak fire
15	1200	1.75	0	Horizontal	Good fire – northerly wind
16	1000	1.75	0	Horizontal	Good fire
17	1000	1.75	0	Horizontal	Fire weak on South side
18	1200	1.75	0	Horizontal	Good fire
19	1200	1.75	0	Horizontal	Fire weak on South side
20	1000	1.25	0	Towards vessel centre	Fire weak on bottom side
21	1200	1.25 North & 1.75 South	+ 0.1 m	Horizontal	Mistake in horizontal distance but good fire
22	1200	1.75	+ 0.1 m	Horizontal	Good fire

3.3 Fire characterisation techniques

3.3.1 Statement of contribution

IR thermography practical work during the commissioning tests was led by Professor A. M. Birk. The programme required to solve the equations, and equations 3.2 and 3.3 were provided by Professor Birk.

3.3.2 Introduction

The previous section discussed the necessity of obtaining reliable experimental data for validation of numerical models. A review of previous attempts to characterise fires is given below, with focus on infra-red photography techniques to determine flame emissivity. The techniques adopted in the current study are described.

Numerous methods exist to characterise flames. One of the simplest methods is to look-up published values for the flame temperature, flame emissivity and heat transfer coefficient (from, for example, FABIG (2014)). Alternatively, the emissive power of the flame can be estimated by calculation if the value of the flame absorption coefficient is known. Published absorption characteristic data for various fuel flames can be found in, for example, Hubbard & Tien (1978) and information and equations are given in appendix 4.

Flame characterisation can be based on individual consideration of the constituent gases produced by combustion, using a simplified method proposed by Hottel (1954) in which the spectral emissivity of the constituent gases is combined with a correction factor to calculate an effective flame emissivity. This approach requires the gas temperature to be known and generally assumes flames do not exhibit grey behaviour (as it neglects the contribution from soot).

A limited set of published or calculated flame properties can be used in combination with relatively simple measurements to estimate further flame characteristics. Total heat flux measurements can be obtained using a range of different calorimeter types (including thin-skin calorimeters, thermally massive calorimeters, or water-cooled Schmidt-Boelter or Gardon type gauges) and the radiative flux obtained via a radiometer (consisting of a total heat flux gauge behind a temperature resistant glass window to prevent convection effects). Combinations of heat flux measurements and flame temperature measurements, with use of published values where necessary, allow for an estimate to be made of the radiative and convection components of the flame.

However, techniques reliant on direct temperature measurements are of questionable accuracy. Direct measurement of flame temperature and heat flux are complicated by radiation heat losses from the instrument and the influence of soot deposition. The use of published flame properties, even when based on the same fuel, may also be inappropriate due to differences in the flame shape and atmospheric conditions. Such problems have led researchers to seek more reliable means of characterising fires, leading to the adoption of Infra-red (IR) thermography techniques by numerous authors

3.3.3 Review of selected optical techniques for flame characterisation

Wayne & Kinsella (1984) performed spectroscopy measurements across the 1.2 to 3.6 µm and the 2.4 to 7.2 µm wavebands using a scanning grating monochromator. Large rectangular pools of butane, propane and naptha were studied. Optical path lengths through the flames varied from 4.3 to 20 metres. The spectral radiant emittance (in $kW/m^2\mu m$) was plotted against wavelength, and overlaid with blackbody emittance plots to identify an effective radiative temperature. In discussion, the authors stated that the propane flames became optically thick within the region of 6.5 to 9 m, and that the results were from optically thick flames, except for one test with the shorter path length of 4.3 m. No further attempt was made to estimate a soot extinction coefficient or flame emissivity as a function of thickness.

Oka & Sugawa (1989) used a fine mesh placed within a fire as the target for a perpendicularly set IR camera with a spectral range of 8-13 µm. The combined radiation was measured and the temperature determined assuming close to black body emissivity. No attempt was made to separate radiation from the mesh and the flame, nor was the emissivity of the flame considered. The temperature was also measured with thermocouples, and the ratio of results from the two methods was found to lie within 0.8 to 1.5. This study highlights the need to employ additional methods to make sense of IR readings and thermocouple readings.

Two-colour and multi-colour pyrometry are optical techniques designed to measure the temperature of a radiation source independent of emissivity. Filters ensure radiation within distinct wavelength bands is simultaneously measured. As stated by Reynolds (1964) in a review of the techniques, if the emitter is assumed to behave as a grey body, the ratio of intensities becomes independent of the emissivity, allowing the temperature to be calculated. The accuracy of this method is dependent on how closely the emitter exhibits grey body behaviour. In the context of propane flames this will require them to be optically thick, to prevent radiance being dominated by the CO_2 and H_2O wavelength bands.

Planas-Cuchi, et al., (2003) used a reference object of known emissivity (and temperature) in proximity to a flame. IR cameras with a spectral range of 7.5-13 μm were positioned to view the reference alone, the flame alone, and a view of the reference through the flame. The IR cameras gave the reference object temperature, the black body flame temperature, and the combined temperature. The energy balance equations were combined to give the temperature as a function of the emissivity, based on the assumption that flame transmissivity equals one minus the flame emissivity. The relationship between these two parameters was plotted and fitted to an equation in the form $T=A\varepsilon^b$, with this value being substituted into the energy balance equation to allow the equation to be solved for emissivity. Despite the good fit between the predicted values and experimental data, there remained a degree of subjectivity in the approach used as it required the user to choose an appropriate value for the combined emissivity to calculate a flame emissivity. Sudheer & Prabhu (2010) used the same methodology to assess the emissivity of gasoline pool fires up to 1 m in diameter.

Qian & Saito (1995) used two separate radiant sources as references for an IR camera filtered to receive 10.1-11.1 μm wavelengths. The sources were at different temperatures, and the emissivity of both was assumed to be one. IR cameras were used to measure the radiant intensity of the separate black bodies both directly and combined with flames, the latter by looking through them. By assuming the flame reflectivity is negligible, the transmissivity of the flame is calculated as the ratio of the difference in combined intensities to the difference in direct intensities. The emissivity can then be determined and used to calculate the flame temperature.

More recently, Raj & Prabhu (2017) published a study combining the method of Qian with a Wien's law approach based on integrating over the wavelength of the IR camera. However, it is unclear why adopting the Wien's integration is necessary when using a single camera (and hence single wavelength band) and assuming the flame behaves as a grey body.

The above studies have typically measured the infrared radiation in the part of the spectrum commonly known as long wavelength infrared. This avoids the strong emission bands due to the presence of hot CO_2 and H_2O, such as those at 4-4.5 μm and 2.5-3 μm. Several studies of optically thin flames have used cameras designed specifically to measure radiance in these mid wavelength infrared regions, as the flames become close to opaque at relatively low thicknesses (see for example, Rawlins, et al., (2001), Rankin, et al., (2015)).

The studies listed above that have tried to quantify both the flame emissivity and flame temperature have done so by means of determining the flame transmissivity. An alternative approach, simpler in concept, is to use an IR camera in conjunction with a temperature measuring device, such as a thermocouple, and to

determine the emissivity by adjusting it until the temperature values coincide. However, while such a method is simple, it is subject to errors due to the difficulties in measuring flame temperatures directly. Thermocouples also provide a point measurement with a relatively slow response, compared to an IR camera which captures greater spatial and temporal variations in flames.

In summary, IR thermography has been used for flame characterisation in numerous studies. Mid-wavelength IR measurements are frequently used for flames that are optically thin or produced by relatively clean burning fuels that cannot be relied upon to emit as grey bodies. Long-wavelength IR measurements are often used for optically thicker and sooty flames that can be approximated as grey bodies. The long-wavelength IR measurements described above employ grey body reference objects of known temperature and emissivity as a means of determining the flame transmissivity. However, the techniques discussed above are not capable of calculating both flame emissivity and flame temperature without a subjective user input.

3.3.4 Methodology employed in the present study

Relevant theory on IR thermography underlying the present study is given in appendix 4. The present study builds on the two-reference object principle employed by Qian & Saito (1995). The references are a directional flame thermometer (DFT) and a water-cooled calorimeter. Introducing a value for the net heat flux to a cold object and simultaneously solving the two energy balance equations for the references with two further energy balance equations for the references as viewed by the IR camera allows for derivation of the flame properties and the convective heat transfer coefficient. The calculation method is given below.

The input variables for this analysis are:

- DFT actual temperature (K)
- Calorimeter actual temperature (K)
- DFT and calorimeter black-body equivalent indicative temperatures as given by IR camera
- Fire total heat flux from calorimeter (W/m2)
- Vessel wall emissivity
- Ambient temperature (K)

The calculated outputs are:

- Calorimeter and DFT surface emissivity

- Flame temperature
- Flame emissivity
- Fire convection coefficient
- Radiation fraction (derived from the above)

The IR camera requires the user to set values of atmospheric transmissivity, distance to object, ambient temperature and surface emissivity. When the IR camera is set to an object surface emissivity of 1, the radiance measured by the IR camera is used to calculate an indicative black body temperature of the object. The black-body equivalent temperature obtained from the camera can be expressed as an energy balance equation for both the DFT and calorimeter as follows:

$$\varepsilon_{dft}\left(1-\varepsilon_{fire\ line}\right)\sigma T_{dft}^4+\left(1-\varepsilon_{dft}\right)\left(1-\varepsilon_{fire\ line}\right)\varepsilon_{fire\ vol}\sigma T_{fire}^4+\varepsilon_{fire\ line}\sigma T_{fire}^4$$
$$+\left(1-\varepsilon_{dft}\right)\left(1-\varepsilon_{fire\ line}\right)\left(1-\varepsilon_{fire\ vol}\right)\sigma T_{amb}^4=\sigma T_{dftind}^4 \quad (3.2)$$

where:

$\varepsilon_{dft}\left(1-\varepsilon_{fire\ line}\right)\sigma T_{dft}^4$

is the radiation emitted by the DFT and attenuated by the fire reaching the camera

$\left(1-\varepsilon_{dft}\right)\left(1-\varepsilon_{fire\ line}\right)\varepsilon_{fire\ vol}\sigma T_{fire}^4$

is the radiation emitted by the fire and reflected by the DFT back through the fire to the camera

$\varepsilon_{fire\ line}\sigma T_{fire}^4$

is the radiation from the fire to the camera

$\left(1-\varepsilon_{dft}\right)\left(1-\varepsilon_{fire\ line}\right)\left(1-\varepsilon_{fire\ vol}\right)\sigma T_{amb}^4$

is the ambient radiation reflected by the DFT and attenuated twice by the fire and finally reaching the camera (considered negligible)

The energy balance equation for the water-cooled calorimeter is:

$$\varepsilon_{cal}\left(1-\varepsilon_{fire\ line}\right)\sigma T_{cal}^4+\left(1-\varepsilon_{cal}\right)\left(1-\varepsilon_{fire\ line}\right)\varepsilon_{fire\ vol}\sigma T_{fire}^4+\varepsilon_{fire\ line}\sigma T_{fire}^4$$
$$+\left(1-\varepsilon_{cal}\right)\left(1-\varepsilon_{fire\ line}\right)\left(1-\varepsilon_{fire\ vol}\right)\sigma T_{amb}^4=\sigma T_{calind}^4 \quad (3.3)$$

The energy balance equations for the DFT and calorimeter once they have reached thermal equilibrium (net heat flux equal zero) are given by

DFT

$$q = h_{fire}\left(T_{fire} - T_{dft}\right) + \varepsilon_{dft}\varepsilon_{fire}\sigma T_{fire}^4 + \varepsilon_{dft}\left(1 - \varepsilon_{fire}\right)T_{amb}^4 - \varepsilon_{dft}\sigma T_{dft}^4 \quad (3.4)$$

Calorimeter

$$q = h_{fire}(T_{fire} - T_w) + \varepsilon_w\varepsilon_{fire}\sigma T_{fire}^4 + \varepsilon_w(1 - \varepsilon_{fire})T_{amb}^4 - \varepsilon_w\sigma T_w^4 \quad (3.5)$$

where:

q is heat flux (W/m^2)

h_{fire} is fire convective heat transfer coefficient (W/m^{2}K)

T_{dft} is DFT front temperature (K)

T_{fire} is fire temperature (K)

T_{amb} is ambient surroundings temperature (K)

T_w is wall temperature (K)

ε_{fire} is fire emissivity

ε_{dft} is DFT emissivity

σ is the Stefan-Boltzmann constant = 5.67x10^{-8} (W/m^{2}K^4) (approx.)

T_{wall} is cool wall temperature (K)

ε_w is cool wall emissivity

Finally, the heat flux to a cold object is calculated using a water-cooled calorimeter using equation 3.6.

$$q'' = \frac{\Delta T \dot{m} c_p}{A} \quad (3.6)$$

where:

ṁ is the mass flow rate of water

c_p is the specific heat capacity of water (calculated for the average water temperature)

A is the surface area of the calorimeter

ΔT is the time averaged difference in inlet and outlet water temperature

The radiative fraction of the total heat flux to a cold object is an important parameter in determining the severity of a fire. It is defined as:

$$f_{rad} = \frac{q_{rad}}{q_{rad} + q_{conv}} \tag{3.7}$$

Where the radiation and convection components can be separated from equation 3.7 as follows:

$$q_{conv} = h_{fire}(T_{fire} - T_w) \tag{3.8}$$

$$q_{rad} = \varepsilon_w \varepsilon_{fire} \sigma T_{fire}^4 + \varepsilon_w (1 - \varepsilon_{fire}) T_{amb}^4 - \varepsilon_w \sigma T_w^4 \tag{3.9}$$

Equations 3.2 to 3.6 can be solved simultaneously using an appropriate programme. The present study used Engineering Equation Solver (EES) by F-chart software.

Following calculation of the flame temperature, emissivity, and coefficient of convection, further information can be derived using equations 3.7 to 3.9. Refinement can also be made to the coefficient of convection at the vessel wall. The coefficient at the small calorimeter and DFTs is expected to be larger than that on the larger surface of the pressure vessel. A correlation for the convective coefficient on a flat plate (see, for example, Holman (1976)) is given in equation 3.10. This suggests the h is related to $1/D^{0.19}$.

$$h = 0.0239 \frac{k}{D} \left(\frac{\rho U D}{\mu} \right)^{0.81} \tag{3.10}$$

The analysis can be adjusted to reflect the difference between convection to the relatively small calorimeter used and the larger pressure vessel. If one value of fire heat transfer coefficient is calculated, the other can be adjusted using equation 3.11

$$h_2 = h_1 \left(\frac{D_2}{D_1} \right)^{-0.19} \tag{3.11}$$

In the present study the vessel diameter was approximately one metre and the DFT and water-cooled calorimeter had a vertical dimension 0.075 m. This would suggest that the h for the small calorimeter and DFT would be greater than the h for the vessel wall by a factor of 1.6.

Correction can also be made for the differences in fluid temperatures. The fluid properties in the convection correlation, including the thermal conductivity (k), density (ρ) and viscosity (μ). must be calculated using the

average of the surface and gas temperature. The cool calorimeter and the cool liquid wetted wall have a different average fluid temperature than the hot DFT. For example, if the same flow velocity is assumed over the small and large surfaces then the h on the small calorimeter or liquid wetted wall can be estimated from the calculated h for the DFT using equation 3.12.

$$\frac{h_{dft}}{h} = \frac{k_{dft}}{k}\left[\frac{D}{D_{dft}}\right]^{0.19}\left(\frac{\rho_{dft}}{\rho}\frac{\mu}{\mu_{dft}}\right)^{0.81} \quad (3.12)$$

3.3.4.1 Equipment Design for Fire Characterisation

General details of the equipment are reported in section 3.1. Specific features relevant to the flame characterisation are explained in more detail below.

Figure 37 shows the tank set-up for partial fire exposure, with a water-cooled calorimeter at mid-height, and a custom-made directional flame thermometer (DFT) immediately above. The exposed tank wall is black due to soot deposits from previous tests. Thermocouples measure the inlet and outlet water temperature to give the change in water temperature each second. The water supply and drain lines, and the thermocouple wires, are protected from direct flame exposure by Promaglaf ceramic blankets from Promat. Further insulation was used to protect the sides of the calorimeter from direct flame exposure. The exposed calorimeter surface area was 0.015 m^2 and the water flow rate 0.77 l/min (0.0128 kg/s). All calorimeters were connected to a data acquisition system with a scanning frequency of 1 Hz.

The thermal imager used was a FLIR A655 SC 7-13 micron camera with a 25° lens. The resolution of the camera was 640 x 480 pixels. The camera was positioned 12 m from the calorimeter.

A limited number of tests were performed with the water-cooled calorimeters during the commissioning stage to give data for flame characterisation. After test C4 the water-cooled calorimeter was removed to prevent interference with the surface of the tank near the TCs and laser sheet. The DFT data was used as a further check of future test flames.

Figure 37 – Water-cooled calorimeter position at vessel mid-height

3.3.5 Alternative fire characterisation calculation methods

3.3.5.1 Simplified method one: heat balance analysis using DFTs only

An energy balance equation can be solved for the DFT once it has reached a quasi-steady-state condition, to give the convection and radiation fractions (see, for example, Modest (1993)). This is a simplistic analysis that requires the following assumptions:

- 1D behaviour
- Steady conditions
- Uniform Fire T
- Uniform fire emissivity (uniform depth and extinction coefficient)
- No heat loss from back of DFT face
- View factor fire to DFT of (F) = 1

An energy balance on the DFT is given by equation 3.4. Under steady conditions the net heat flux equals zero. The fire emissivity in this case is due to the volume of the fire above the DFT surface. This volume radiates to the DFT with an emissivity ε_{fire}, given by equation A4.4.

The approximate heat transfer to a cool surface, equation 3.5, can also be calculated by using the properties of a cool surface (or tank wall) instead of the DFT. This assumes the cool surface does not change the fire, and that the convection coefficient is identical for the cool surface and the DFT. Neither assumption is strictly correct, giving an inherent inaccuracy to the methodology.

Direct use of equations 3.4 and 3.5 requires knowledge of the fire convection coefficient. This may be estimated from correlations in literature. One such example for forced convection on a flat plate is given by equation 3.10. Values of h_{fire} given in literature for hydrocarbon pool fires are typically in the region of 20-30 W/m^2K, as discussed and referenced in section 2.1. Further assumptions must be made about the flame temperature (or flame emissivity) and the surface emissivity, with values also available in literature.

The problem with any analysis that uses DFT data alone is the uncertainty over the fire temperature and the convective heat transfer coefficient. With a reasonable degree of confidence, the fire temperature in a large propane fire can be stated as being typically in the range of 1100°C plus or minus 100°C. However, the convective coefficient could vary between 10 –50 W/m^2K or more. For this reason, additional data is needed to have greater confidence in the calculated radiation-convection balance. A water-cooled calorimeter was used for this purpose in the current study.

3.3.5.2 Simplified method two: heat balance with DFT and water-cooled calorimeter

Measuring the net heat flux to a cool object simultaneously with DFT equilibrium temperature measurements allows for an estimation of the fire convection coefficient independent of the flame temperature and flame emissivity.

Both the DFT and the calorimeter should be constructed of the same material and should be coated or fire exposed prior to the test to give very similar surface emissivity values.

Equation 3.4 can be rearranged and rewritten as:

$$\varepsilon_{dft}\varepsilon_{fire}\sigma T_{fire}^4 + \varepsilon_{dft}\left(1-\varepsilon_{fire}\right)T_{amb}^4 = \varepsilon_{dft}\sigma T_{dft}^4 - h_{fire}\left(T_{fire} - T_{dft}\right) \quad (3.13)$$

Assuming the surface emissivity of the calorimeter and the DFT are equal, equation 3.5 can be substituted into equation 3.13, to give equation 3.14.

$$h_{fire} = \frac{q_{net} + \sigma\varepsilon_s\left(T_{cal}^4 - T_{DFT}^4\right)}{\left(T_{DFT} - T_{cal}\right)} \tag{3.14}$$

where:

q_{net} is the heat flux as measured by the water-cooled calorimeter (W/m^2)

ε_s is the emissivity of the substrate

T_{cal} is the temperature of the water-cooled calorimeter (K)

T_{DFT} is the temperature of the DFT (K)

Once the fire convection coefficient is known, the emissive power of the flame can be determined iteratively for an assumed flame temperature, and the radiation fraction can be calculated using equations 3.5 and 3.7 to 3.9.

This method is an improvement over method one, in that it gives a direct value for the fire convection coefficient, leaving the user only flame temperature and flame emissivity as the two unknown variables (neglecting surface emissivity on the basis of a reasonable knowledge of the behaviour of steel in fire). The exact flame temperature is unknown, however the fire temperature is taken to be in the range of 1100 °C plus or minus 100°C. This limits the radiative fraction range calculated by this method.

The primary limitation of this method is it still requires the user to assume a flame temperature value to calculate the flame emissivity. Equation 8 is also based on the assumption that the surface emissivity and fire convection coefficient is the same for the calorimeter and the DFT. There will be differences in practice. Alternatives to equation 3.14 that include the influence of surface emissivity and convection coefficient differences can be derived for h_{fire}., however these retain the flame temperature as a variable and are not shown here.

3.3.5.3 Simplified method 3: thermal imager iterative method

This method is a less sophisticated version of the primary methodology presented in section 3.3.4. It requires the user to start with an assumed flame temperature, but then allows all further properties to be calculated iteratively. It is subject to all the same assumptions, limitations and requirements given for the primary methodology.

Three of the energy balance equations (Equations 3.5, 3.10 and 3.13) can be solved iteratively using spreadsheet software. The following inputs are required:

1) DFT surface emissivity (estimated)
2) Calorimeter surface emissivity (estimated)
3) DFT actual temperature (K)
4) Calorimeter actual temperature (K)
5) DFT and calorimeter thermal imager indicated temperatures
6) Fire total heat flux (W/m^2)
7) Ambient temperature (K)

The flame temperature, flame emissivity, convection coefficient and radiative fraction are determined as follows:

1) For a sensible range of flame temperatures, iteratively determine the corresponding flame volume emissivity value that gives an indicated DFT temperature equal to the measured value (Equation 3.2)
2) For each combination of flame temperature and flame emissivity calculated in step 1, calculate the indicated calorimeter temperature (Equation 3.3).
3) Identify the value of flame temperature and corresponding flame emissivity that match both indicated temperature values. These are the resulting values from this method.
4) Using the flame temperature and flame emissivity identified in step 3 iteratively determine the fire convection coefficient value that gives the correct net heat flux value to the calorimeter (Equation 3.5)
5) Calculate the radiation fraction using equations 3.7 to 3.9.

The values obtained using this method can be entered into equation 3.4 to calculate the heat loss from the DFT due to internal conduction.

3.4 Fire characterisation results

3.4.1 Infrared thermography

Results from test four are given in detail as an example of the methodology described in section 3.3.4. Liquid propane was supplied to 56 burners heads (in an array four deep and seven wide on each side of the vessel) to create an engulfing pool fire simulation, as shown in Figure 38.

Figure 38 – Fire exposure during an IR characterisation test

DFTs located on the tank provided confirmation of flame stability, supported by observations. *Figure 39* shows a period affected by wind (100 – 450 s), where the flame was pushed to one side, followed by a period of stability (450 – 600 s) and then intermittent wind effects (600 – 780 s).

The water-cooled calorimeter was used to calculate the water delta T. Results are shown in Figure 40.

The heat flux to a cool surface was calculated using equation 10 to be 92-120 kW/m^2, with the average being 102 kW/m^2, for a ΔT of 25-32°C. The IR camera results are shown in Figure 41. The different line colours represent the following when viewed through the flame:

Blue: Upper DFT temperature

Green: Lower DFT temperature

Cyan: Cool wall area

Red: Water-cooled calorimeter temperature

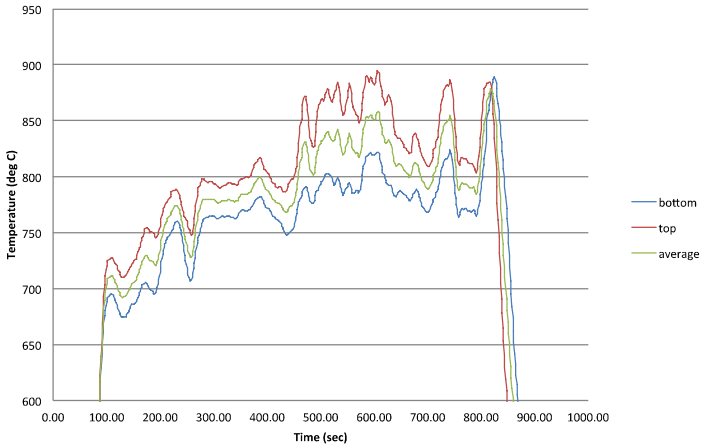

Figure 39 – DFT temperatures during test four

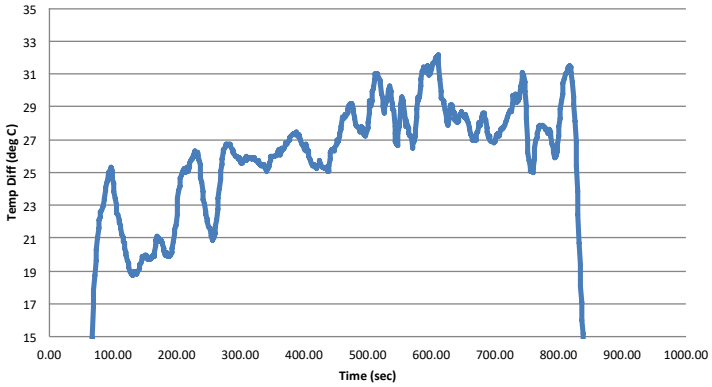

Figure 40 – Calorimeter delta T during test 4

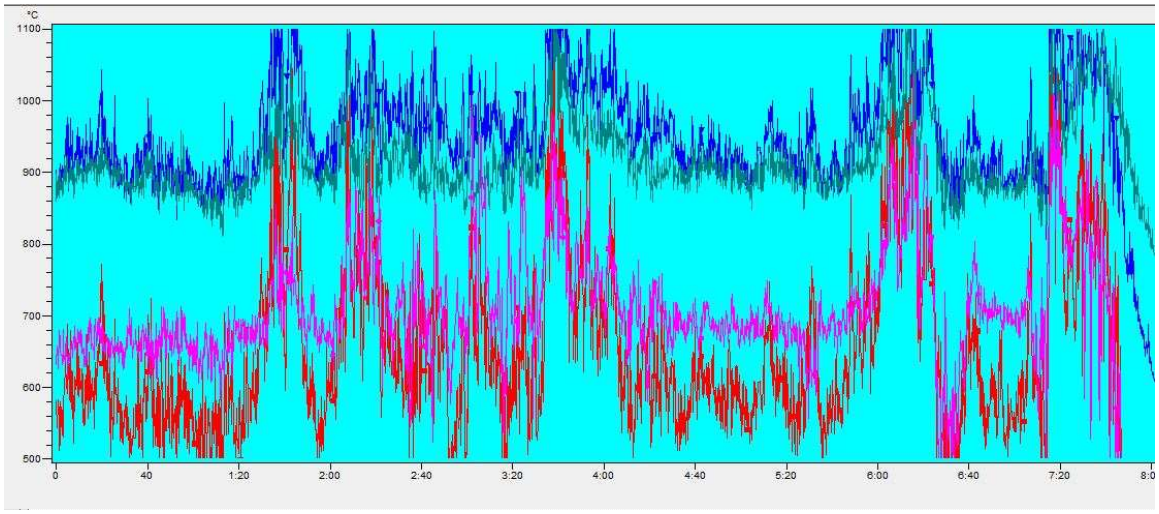

Figure 41 – IR camera measured temperatures during test 4

The necessary inputs for the calculation were obtained for the period of flame stability (450-780 s) from *Figure 39* to Figure 41 and equation 3.6, and are shown in Table 15

Table 15 – Inputs values for example calculation

Measured or calculated inputs	Measurement	Uncertainty
DFT measured temperature	830°C	+/- 10°C
DFT IR indicative temperature	900°C	+/- 10°C
Water-cooled calorimeter measured temperature	70	+/- 5°C
Water-cooled IR indicative temperature	690	+/- 10°C
Heat flux to cool object	102 kW/m^2	+/- 10 kW/m^2
Flame depth (from photographs)	0.5m	+/- 0.2m

The above inputs were used to solve equations 3.2 to 3.5 and 3.7 to 3.12 simultaneously using EES by F-chart software. The calculated outputs are given in Table 16, using a programme developed by Prof A. M. Birk of Queen's University, Ontario. The equation solving software performs an error propagation calculation based on the above specified uncertainty values.

Table 16 – Calculation results

Calculated parameter	Measurement	Uncertainty
Flame temperature	1389 K	+/- 67 K
Flame emissivity	0.33	+/- 0.1
Calorimeter emissivity	0.81	+/- 0.15
DFT emissivity	0.81	+/- 0.15
Convective heat transfer coefficient at the calorimeter	47 W/m^2K	+/- 14 W/m^2K

The values for D used in this analysis are as follows:

- Small calorimeter = 0.075 m
- DFT = 0.075 m
- Tank = 1.4 m

If the radiation is assumed to remain the same in each case, the correction for the heat transfer coefficient would give a higher convective heat transfer to the calorimeter, and hence a lower radiative fraction.

By introducing equations 3.10 to 3.12 the properties given in Table 17 can be calculated.

Table 17 – Further calculations

Further calculated parameter	Measurement	Uncertainty
Convective heat transfer coefficient at the DFT	39 W/m^2K	+/- 11 W/m^2K
Convective heat transfer coefficient at the vessel	27 W/m^2K	+/- 8 W/m^2K
Heat flux to cool vessel	90 kW/m^2	+/- 8 kW/m^2
Radiant fraction calorimeter	0.54	+/- 0.11
Radiant fraction vessel	0.69	+/- 0.07

3.4.2 Comparison with simplified methodologies

Test four was assessed using the methodologies described in section 3.3.5 using the same input parameters as defined above, except where the simplified methodologies required assumed inputs. Note that no correction has been made for the convection coefficient to take into account differences in vertical length scale or local gas properties.

Table 18 – Methodology comparison

Property	Primary method	Simplified method 1	Simplified method 2	Simplified method 3
Flame Temperature	1116°C	(1100°C)[1]	(1100°C)[1]	1105°C
Flame emissivity	0.33	0.26	0.34	0.34
Convective coefficient	27-47 W/m^2K	(25 W/m^2K)[1]	37 W/m^2K	38 W/m^2K
Radiative Fraction	0.54-0.69	0.77	0.61	0.61
Surface emissivity	0.81	(0.9)	(0.9)[1]	(0.9)

[1]Values in brackets are assumed as required by the methodology

3.4.3 Application to wider tests

It was not possible to use a water-cooled calorimeter during test five or subsequent tests, due to the need to prevent interference with the zone of primary study. Instead the data from the primary method was used to refine method 1, which involves calculation from an energy balance on the DFTs alone.

It is assumed that the flame temperature and convection coefficient remain unchanged between tests, and that differences in flame characteristics are primarily due to wind changing the shape of the flame, consequently altering the optical thickness and hence flame emissivity. Therefore, the flame temperature (1116°C), convective coefficient for the DFT (47 W/m^2K) and surface emissivity (0.81) values calculated for test four by the primary methodology are used in place of other assumptions. The average DFT temperature is taken during the stable test period and the corresponding flame emissivity is then iteratively calculated to give a net energy balance of zero. Finally, a net heat flux to a cold vessel is calculated based on the convective coefficient to a cool vessel (27 W/m^2K) to account for differences in length-scale and local gas temperatures.

The results for all season one and season two tests are given in Table 19 and Table 20, respectively.

Table 19 - Season one

Test	DFT average temp. (°C)	ε_f	q_{net} to vessel (kW/m^2)	f_{rad} to vessel
4	827	0.31	83	0.64
5	741	0.18	61	0.51
6	768	0.22	67	0.56
7	713	0.14	54	0.45
8	746	0.19	62	0.52
9	780	0.24	70	0.58
10	828	0.32	84	0.65
11	627	0.04	37	0.19
12	649	0.07	42	0.27

Table 20 – Season two

Test		DFT average temp. (°C)	ε_f	q_{net} to vessel (kW/m^2)	f_{rad} to vessel
13	**All**	759	0.21	65	0.54
	Local	881	0.41	100	0.70
14	**All**	657	0.07	42	0.30
	Local	954	0.56	126	0.77
15	**All**	640	0.06	39	0.24
	Local	870	0.39	96	0.69
16	**All**	671	0.09	45	0.34
	Local	820	0.3	81	0.64
17	**All**	654	0.07	42	0.29
	Local	834	0.33	85	0.65

Test		DFT average temp. (°C)	ε_f	q_{net} to vessel (kW/m^2)	f_{rad} to vessel
18	**All**	731	0.17	58	0.49
	Local	741	0.18	61	0.51
19	**All**	712	0.14	54	0.45
	Local	850	0.35	90	0.67
20	**All**	707	0.14	53	0.44
	Local	255	N/A		
21	**All**	826	0.31	83	0.64
	Local	796	0.26	75	0.60
22	**All**	763	0.21	66	0.55
	Local	767	0.22	67	0.56

3.4.4 Discussion of results

Significant variations in DFT temperatures and corresponding heat flux and radiative fraction values are evident across tests. Season one tests showed a distinct reduction in DFT temperatures following test 4, corresponding with the addition of a radiation shield. Tests 5 to 8 had the DFTs on the vessel below the radiation shield, however, the proximity of the shield will have changed the DFT field of view of the flame and could have also affected local gas velocities and the local convection coefficient. Tests 9 to 12 used DFTs mounted on the radiation shield. The edge of the radiation shield will have affected the local convection, as with preceding tests, however the DFTs will also have been affected by a change in their position in the flame. The increased diameter of the radiation shield will result in a potentially optically thinner flame near the DFTs, with a corresponding reduction in flame emissivity and measured temperature. The differences observed do not affect the liquid-wetted all below the radiation shield and hence the results are considered acceptable, given the level of uncertainty involved.

Season two tests had a greater number of DFTs covering a much wider area of the vessel surface. Significant spatial variations were observed, with some DFTs measuring very low temperatures, indicating a lack of flame engulfment in these areas. The methodologies do not capture intermittent engulfment, but instead provide time-averaged values. Caution must be exercised when using the results, as the physical behaviour of the system may change significantly, given slight differences in local heat flux. For example, the primary mode of heat transfer from the vessel wall to the fluid may switch between convection and boiling due to intermittent flame engulfment. This would not be captured when using a time-averaged value.

Tests 18 and 20 had intermittent fire engulfment of the laser sheet and thermocouple zone, giving variability in DFT readings. Tests 14 to 17 had a poor overall engulfment, reflected in the low average DFT values. Tests 21 and 22 had the best overall engulfment, meeting the overall heat flux target conditions for a pool fire simulation given in section 2.1.10.

The variations in heat flux described above are significant and represent a limitation of the present study. However, the variations in the radiative fraction, and the magnitude of convective heat flux specifically, are less important when considering the modelling approach adopted in section 5. The present study is concerned with modelling the liquid phase of the vessel, applying a thermal boundary condition to the region of the wall in contact with liquid. This surface will remain cool throughout the duration of the simulation and therefore the net heat flux and radiative fraction will not change throughout the simulation. It is therefore reasonable to be concerned solely with the total heat flux. This is discussed further in section 5.

3.4.5 Discussion of methodology

The methodology described herein has an inherent degree of uncertainty. Any experimental errors or inaccuracies in the measured quantities will propagate through to the calculated variables. The flame is assumed to behave as a grey body, given the sooty nature of propane flames and the optical thickness, however this assumption will introduce a further unquantified degree of inaccuracy.

It is recognised that the flame temperature, thickness, soot concentration etc. will vary over the tank surface. This method is intended to provide a spot-check at a single location and is not suitable for providing refined information on the spatial distribution of the flame.

Multiple DFTs positioned near the calorimeter were giving different indicated temperature values when viewed by the IR camera, with the upper one being hotter. This is attributed to the flame being thicker, and possibly hotter, near the upper part of the tank. The position of measuring points, such as the calorimeter and DFTs, must be carefully selected to ensure the flame depth is equal at all points viewed by the IR camera.

Variations in surface emissivity and uncertainty in measured surface temperatures caused by thermocouple conduction effects also add to the uncertainty of results. In this study, the IR camera indicated temperatures were consistently higher for the cool vessel wall than for the water-cooled calorimeter. This can be partly attributed to the indicated wall temperature being averaged over a larger area than the calorimeter spot temperature, however it is also possible that a difference in surface emissivity was a cause. The tank wall was

carbon steel with extensive soot deposits, whereas the calorimeter was new stainless steel with black paint and some soot accumulation.

The overall degree of uncertainty is considered acceptable considering the inherent inconsistency in real flame behaviour., and with further testing and validation it may be possible to eliminate certain measurements and reduce the uncertainty in calculated outputs. The calculated results show reasonable agreement with expected values. A flame temperature of 1100°C is commonly quoted in literature for propane flames, and a convection coefficient of 25 W/m^2K was also expected.

Comparing the results to the target conditions, the flame emissivity and radiative fraction is lower than desired, attributable to an insufficient flame thickness. This was evident from the lower DFT temperature of approximately 830^{o}C. It is expected that a DFT temperature of around 870^{o}C would be commensurate with a desired radiative fraction of 0.8, and it is expected this could be achieved with a small increase in the flame thickness.

3.5 References

Bradley, I. M. et al., 2017. *Experimental analysis of a pressurized vessel exposed to fires: an innovative representative scale apparatus.* Milan, The Italian Association of Chemical Engineering.

FABIG, 2014. *Technical note 13, Design Guidance for Hydrocarbon Fires ,* s.l.: s.n.

Finetubes, n.d. *Corporate website.* [Online]
Available at: http://www.finetubes.co.uk/products/technical-reference-library/tube-surface-finishes/
[Accessed March 2018].

Holman, J. P., 1976. *Heat Transfer.* 4th ed. New York: McGraw Hill Book Company.

Hottel, H. C., 1954. *Radiant-Heat Transmission.* New York: McGraw-Hill.

Hubbard, G. L. & Tien, C. L., 1978. Infrared mean absorption coefficients of luminous flames and smoke. *Journal of Heat Transfer,* Volume 100.

Modest, M. F., 1993. *Radiative Heat Transfer.* s.l.:McGraw-Hill Inc.,.

Oka, Y. & Sugawa, O., 1989. Temperature visualisation of extended flame from opening using infrared image processor. *Fire Science & Technology,* 9(2).

Planas-Cuchi, E., Chatris, J. M., Lopez, C. & Arnaldos, J., 2003. Determination of flame emissivity in hydrocarbon pool fires using infrared photography. Volume 39.

Qian, C. & Saito, K., 1995. *Measurements of pool fire temperature using IR technique.* San Antonio, Combustion Fundamentals and Applications, Combustion Institute/Central and Western States, Mexican National Section, and American Flame Research Committee.

Raj, V. C. & Prabhu, S. V., 2017. A refined methodology to determine the spatial and temporal variation in the emissivity of diffusion flames. *Int. J. of Thermal Sciences,* Volume 115.

Rankin, B. A., Ihme, M. & Gore, J. P., 2015. Quantitative model-based imaging of mid-infrared radiation from a turbulent nonpremixed jet flame and plume. *Combustion and Flame,* 162(4).

Rawlins, W. T., Lawrence, W. G., Marinelli, W. J. & Allen, M. G., 2001. *Hyperspectral infrared imaging of flames using a spectrally scanning fabry-perot filter.* s.l., 2nd joint meeting of the U.S. sections of the combustion institute.

Reynolds, P. M., 1964. A review of multicolour pyrometery for temperatures below 1500°C. *British Journal of Applied Physics,* Volume 15.

Sharma and Associates Inc. & Thermdyne Technologies Ltd., 2015. *Rail Tank Car Total Containment Fire Testing,* s.l.: Federal Railroad Administration.

Sudheer, S. & Prabhu, S. V., 2010. Measurement of flame emissivity of gasoline pool fires. *Nuclear Engineering and Design,* Volume 240.

Wayne, F. D. & Kinsella, K., 1984. Spectral emission characteristics of large hydrocarbon pool fires. *ASME paper*.

4 RESULTS AND ANALYSIS

4.1 Overview of thermal and hydraulic processes

The thermal and hydraulic processes that occur within a vessel during fire are complex. Section 2 gives the background to many of these; however, to assist understanding of the results Figure 42 gives a schematic diagram of key phenomenon.

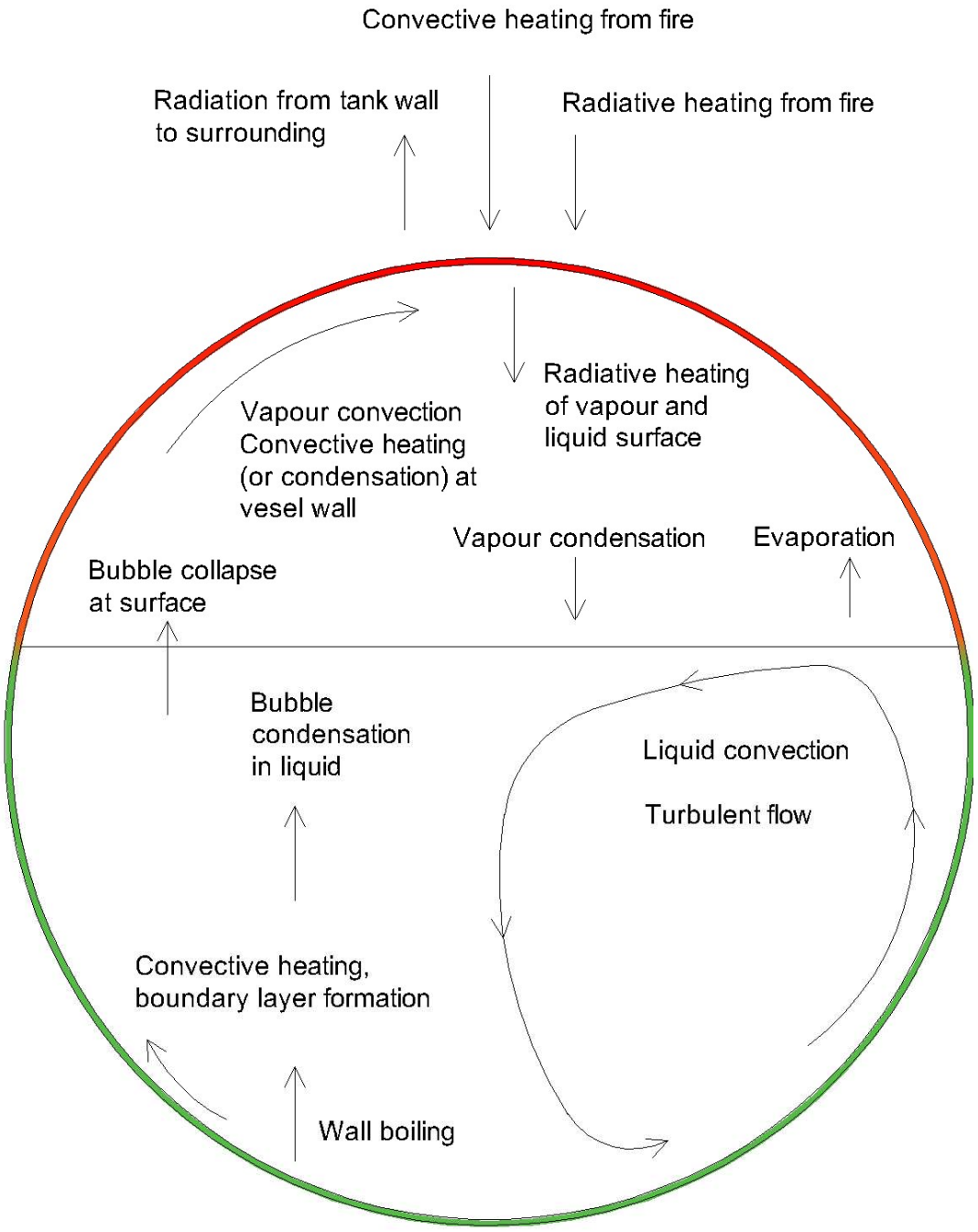

Figure 42 – Thermal and hydraulic processes inside vessel during fire (schematic)

4.2 Commissioning tests (C1-C18)

4.2.1 Objectives

The test programme objectives were to:

1. Commission the test vessel, burner arrangement and pressure compensation system
2. Compare three type-k Inconel sheathed mineral insulated thermocouples for response time and stability
3. Determine appropriate TC distances from the wall to capture thermal boundary layers
4. Assess the influence of the heated zone position relative to the liquid surface on the pressurisation rate

Results relevant to objectives two and three are not presented here. Example temperatures as a function of distance from the wall can be found in section 4.3.3.

4.2.2 Influence of heated patch location

The influence of the heated patch position in relation to the liquid surface on the pressurisation rate was studied as a secondary objective. It must be stated that the results obtained during the commissioning tests should not be relied upon quantitatively due to: the presence of minor variations throughout testing (documented and undocumented), variations in test duration, the lack of detailed fire measurements, and the possibility of leaks affecting the pressure rise. Despite this, the peak rate of pressure rise has been calculated for tests C12-C18 and given in Table 21, to allow for a qualitative comparison. Tests C1-C11 did not produce a noticeable pressure rise and are consequently not reported.

Table 21 – Summary of selected commissioning tests

Test	Fill level	Patch position	Total heated area m^2 (% of vessel test end)	Heated area to volume of water ratio m^{-1}	Peak pressurisation rate psi/min (kPa/min)
C12	0.7m	LL + 0.05m	1.0 (12%)	0.7	0.1 (0.7)
C13	0.7m	LL - 0.05m	1.9 (21%)	1.3	0.1 (0.7)
C14	0.7m	LL + 0.05m	2.1 (23%)	1.5	0.8 (5.5)
C15	0.7m	LL + 0.05m	2.1 (23%)	1.5	0.6 (4.1)
C16	0.5m	LL + 0.25m	2.1 (23%)	2.2	8 (55.2)

Test	Fill level	Patch position	Total heated area m^2 (% of vessel test end)	Heated area to volume of water ratio m^{-1}	Peak pressurisation rate psi/min (kPa/min)
C17	0.91m	LL	2.5 (28%)	1.4	N/A – Leak
C18	0.91m	LL	2.5 (28%)	1.4	3 (20.1)

Comparing test C14 with C13, and test C16 with C14, it can be concluded that the difference in pressurisation rate is significant in a manner disproportionate to the differences in heated area and ratio of heated area to liquid volume. It is therefore reasonable to conclude that the location of the heated zone relative to the liquid level has an influence on the pressurisation rate. Raising the location of heating up to and above the liquid level appears to increase the rate of pressurisation.

To explain this effect, both boiling and condensation must be considered. Boiling takes place when a sufficient superheat can be achieved at the wall in contact with the liquid. Heating of the vessel wall above the liquid level will result in temperatures above the liquid boiling temperature being established in this area. Once a quasi-equilibrium has been reached, this temperature gradient will extend down through the wall below (but close to) the liquid surface. Boiling characteristics are known to be highly sensitive to the degree of wall superheat, hence increased boiling heat transfer and vapour generation can be expected in this region. Conversely, lowering the heated patch below the liquid surface level will reduce the magnitude of superheat achieved and push the area of wall that is superheated to where a higher liquid static head of pressure increases the local boiling temperature. For example, when full, the test vessel at atmospheric pressure will have a static head of pressure of 0.1 barg (111.3 kPa), giving a local boiling temperature of 103˚C at the bottom of the vessel, reducing the rate of boiling in this region.

Vessel wall vapour space condensation may also influence the rate of pressurisation. Vapour escaping from the liquid surface will be predominantly near the vessel wall. This was confirmed by observations inside the tank during tests (vapour clouds could be seen forming near the wall-liquid surface interface and moving across the liquid surface towards the tank centre). This will be partly due to vessel curvature above mid-height (as bubbles will rise towards the wall), but predominantly because vapour released near the liquid surface level will reach the surface in greater quantities. Bubbles will gradually condense as they move through the subcooled bulk liquid. Those released near the liquid surface will have shrunk relatively little compared to those that must rise further.

Given that vapour is formed predominantly near the wall, proximity to a hot zone of vessel wall can be proposed as providing sufficient thermal energy (through radiation from the wall) to maintain the vapour in gaseous state, without it quickly condensing back to water.

A further conclusion from the heated patch tests is that condensation at the vessel wall in the vapour space has a significant role to play in reducing the pressurisation rate of partially heated vessels. This is apparent across the full range of commissioning tests. C1-C11 exhibited negligible pressurisation. The heated area was small, and the fill level of 70% left approximately 3 m^2 (approximately 30% of the total internal surface area) of insulated vapour space shell as a cool, condensing surface. Increasing the heated area caused an increase in the pressurisation rate, however the rates of pressurisation reached remained far lower than those observed during the FRA test series conducted at BAM in 2014 (Sharma and Associates Inc. & Thermdyne Technologies Ltd., 2015). Figure 43 shows that the difference is of an order of magnitude.

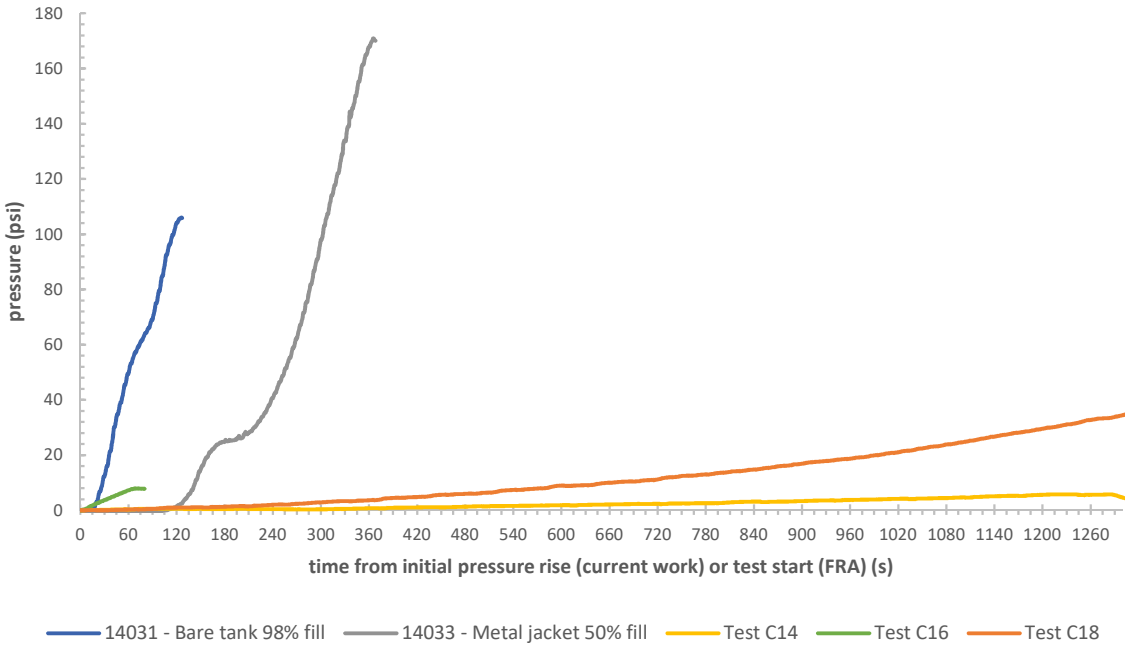

Figure 43 – Pressure comparison: selected FRA tests and current work

The magnitude of the discrepancy in pressurisation rates cannot be explained by the difference in the proportion of the vessel exposed to heat alone. The percentage of total surface area heated in the current work was 23%-28%, and hence it is reasonable to assume up to half of the discrepancy could be attributable to

this. However, this factor alone would not explain why test C16 had a higher pressurisation rate than tests C18 or C15. It is also probable that some of the discrepancy can be attributed to the fire exposure. During the FRA tests the fire was characterised as having a net heat flux of 105 kW/m^2 and a radiative fraction of 0.75 +/- 0.1 (Bradley, et al., 2016). The current work was characterised as having less severe conditions, typically in the region of 60 to 80 kW/m^2, as determined in section 3.4. The overall correlation of a reduction in heat flux with a reduction in pressurisation rate is self-evident, however the relationship should not be assumed to be approximately linear if the change in heat flux results in a change in mode of heat transfer. Below a certain value of heat flux, depending primarily on the liquid and degree of subcooling, boiling will not occur, or will be delayed, and convection will dominate. This would reduce vapour generation and potentially affect pressurisation rate.

Despite the numerous factors inevitably contributing to the differences in pressurisation rate, this work provides support for the conclusions that that condensation on the cool vapour space wall is partially responsible for the significant reduction in pressurisation rate compared with the FRA tests. The magnitude of the effect cannot be quantified in the present work, and further work with more severe fire exposures (similar to FRA levels) and a wider range of heat patch areas is recommended to confirm the validity of this conclusion.

The implication of this conclusion is that 2D zone-models designed to predict the rate of pressurisation of partially heated vessels (typically simulating defects in protection systems) are overly conservative, as they typically neglect condensation at the vessel wall.

4.3 Season one - water and ethanol pressure tests

4.3.1 Season one objectives

The objectives of season one were to:

- Determine the thermal boundary layer temperature distribution as a function of position in the tank and distance from the wall
- Determine the vessel wall temperatures as a function of position in the vessel
- Obtain estimates for bubble nucleation site density, departure frequency, and bubble departure diameter
- Obtain further pressurisation data for comparison with the FRA tests

4.3.2 Pressurisation rate

The rate of pressure rise of selected tests is shown in Figure 44. Tests at 50% fill level are shown, excluding tests 8 and 9 (due to a leak affecting results). Tests 10 and 11 used a bare tank, all other tests had a radiation shield covering the vapour space.

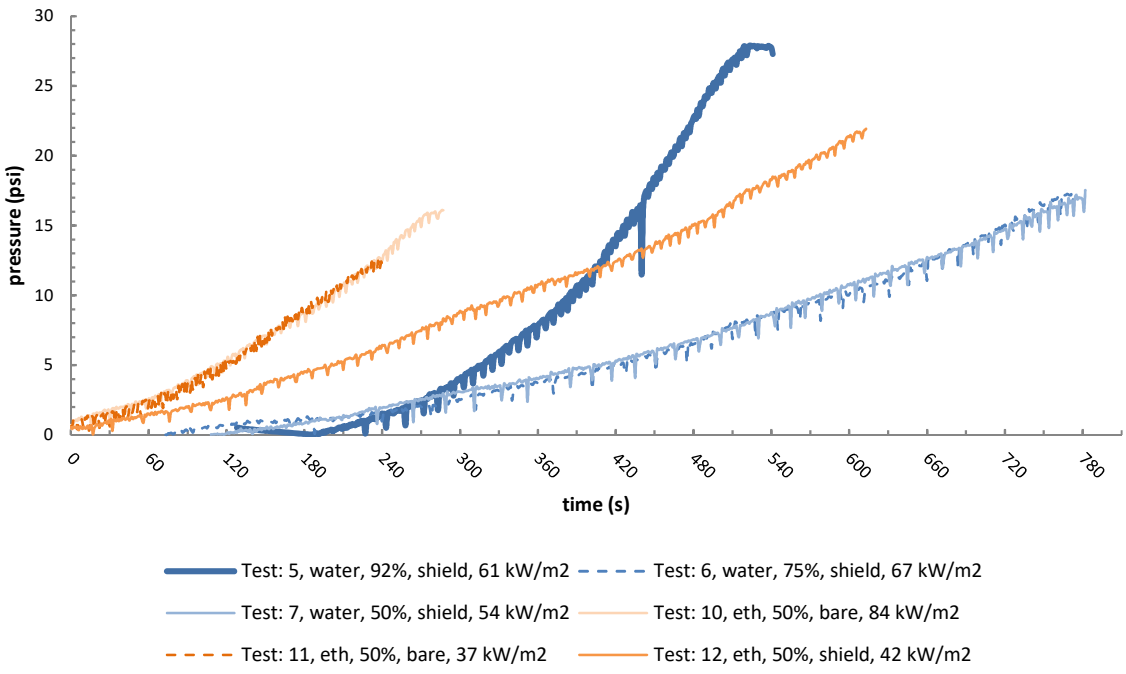

Figure 44 – Pressure rise of selected season one tests: 5-7 (Water) & 10-12 (Ethanol)

The effect of the radiation shield on the pressurisation rate can be clearly seen by comparing test 12 with tests 10 and 11. The maximum rate of pressure rise was reduced from approximately 4 psi/min to 2 psi/min. This is a greater reduction than expected (see section 3.1.3.10) however the uncertainty in the overall net heat flux to the tank outweighs the uncertainty over the performance of the radiation shield. The DFT data for season one is only useful for local assessment, as the number of DFT positions was limited. This is evident in the calculated heat flux values for tests 10 and 11 being notably different (at 84 and 37 kW/m^2 respectively), yet the rate of pressure rise being identical.

Fill level has a more complicated effect on the pressurisation rate. Tests six and seven, with fill levels of 75% and 50% respectively, exhibit the same pressure rise of approximately 2 psi/min. This contrasts with test five at a fill level of 92%, which pressurised at a higher rate, of approximately 8.5 psi/min.

Variations in heating may be the source of some deviation of the pressure rise from a theoretical value, however the magnitude of the difference indicates that there is clearly a phenomenological factor as well. Test five is therefore considered in more detail below in comparison to tests six and seven.

Test five had a delay in the onset of pressure rise of approximately 180 s, which corresponded with the delay in temperature rise in the vapour space recorded by the thermocouple 50 mm below the top of the vessel. In tests six and seven there was a similar pattern between the onset of pressure rise and the onset of temperature rise in the vapour. The reason for the delay in pressure rise or the dip in pressure in test six between 120 and 180 seconds is unclear. It is possibly related to unrecorded fire variations.

There are multiple factors affecting the pressurisation rate, which can have competing effects. These include:

- The higher fill levels will have a smaller vapour space, and therefore each mole of vapour released from the liquid surface due to bubble collapse or surface evaporation will have a proportionally greater effect on the pressure rise. Liquid thermal expansion will also result in a greater pressure increase (Boyle's law)
- A higher fill level will have a higher ratio of liquid-vapour surface area to the vapour space volume, and the maximum travel path distances for vapour molecules before they contact the liquid surface will be lower. These effects will influence the rate of condensation and evaporation.
- Vapour produced at the wall due to boiling will have a finite travel distance through the liquid before bubbles collapse, depending primarily on the degree of liquid subcooling. Increasing fill levels up to

mid-height of the vessel will potentially decrease the area of heated wall within bubble travel time of the liquid surface.

- Conversely, above mid-height of the vessel the curvature of the vessel and buoyancy of the bubbles will direct the bubble towards the thermal boundary layer, potentially reducing the rate of bubble condensation and collapse, thereby increasing the direct contribution of superheated vapour release from bubbles to the pressurisation rate.
- Higher fill levels will give a greater length of heated surface. Given constant heat flux conditions the wall will increase in temperature with increasing height (equation 2.18). Higher fill levels will therefore generally have higher liquid temperatures near the liquid surface, and hence a greater propensity to boil. Non-uniform heating conditions seen in practice are also likely to give higher wall liquid temperatures in the upper half of the vessels due to radiation from the flame plume, which is primarily incident on the upper half of the vessel and the leeward side (discussed further in section 2.1).

The above effects are considered in more detail below.

4.3.2.1 Vapour space volume and surface-liquid area ratio

Previously, the ratio of heated area of the liquid to volume of liquid was considered for the calibration test configurations. The same calculation for vapour is given in Table 22 for the three fill levels discussed in the season one tests and a fill level of 98%, close to that used during the FRA tests. The liquid-vapour interfacial area is also given.

Table 22 – Effect of fill level on system characteristics

Fill	Liquid vol. (m^3)	Vapour vol. (m^3)	Liquid heated surface (m^2)	Vapour heated surface (m^2)	Ratio of vapour heated area to vapour volume	Liquid-Vapour Interface Area (m^2)
98%	1.86	0.03	7.06	1.09	32	1.07
92%	1.83	0.07	6.79	1.36	20	1.83
75%	1.42	0.47	5.27	2.88	6	1.42
50%	0.95	0.95	4.15	3.99	4	0.95

4.3.2.2 Bubble collapse and travel distance

In section 2.4.6 and 2.4.7 it was stated that the terminal rate of bubble rise for spherical, isolated bubbles, can be approximated by Stokes' law, and the rate of collapse for inertia-controlled bubbles by the Rayleigh-Plesset model. An estimation of the travel distance can be determined as the product of the average travel velocity and the bubble life time. The former can be obtained through an integration of equation 2.24, the latter by integration of equation 2.28 (Franc, 2007). A range of bubble diameters and pressure differentials (varying with bubble departure depth below the liquid surface) were calculated, however the results are not given as all bubbles were shown to have a travel distance significantly less than 1 mm.

It can be concluded that pressure vessels containing liquids with a significant degree of subcooling will exhibit a negligible contribution to the rate of pressure rise from boiling, which occurs below the mid-height of the tank, as buoyancy will lift bubbles away from the boundary layer into the cool bulk liquid, causing rapid condensation. Bubbles released near to or above mid-height may flow within a warm layer that facilitates a greater bubble survival time and therefore may contribute more significantly to pressure rise.

4.3.2.3 Wall temperatures in contact with the liquid phase

Season one did not have thermocouples embedded in the vessel wall but did include numerous TCs partially in contact with the wall (but predominantly, given the shape of the TC, in the liquid). Although it is possible to approximate the wall temperature by back-calculation, the sensitivity of the result to the local liquid temperature, uncertainty in the local convective heat transfer coefficient, and uncertainty in the contact surface area between the wall and TC renders the calculation effectively meaningless. Instead, the reader is referred to section 4.4.2 in which comparisons are made between embedded wall TCs and contact wall TCs in season 2. During wall heat-up, the wall TCs are approximately 5-15° hotter than the contact TCs. The contact TCs will typically plateau at 95°C, indicating boiling is occurring.

One approach taken by simplified (zone) type models to estimate the wall temperature is to use established Nusselt number correlations as a means of calculating heat transfer by convection. In this way, an approximation for the wall temperature can be calculated by equations 2.1, 2.17 and 2.18. This calculation assumes the flow is turbulent and that boiling is negligible.

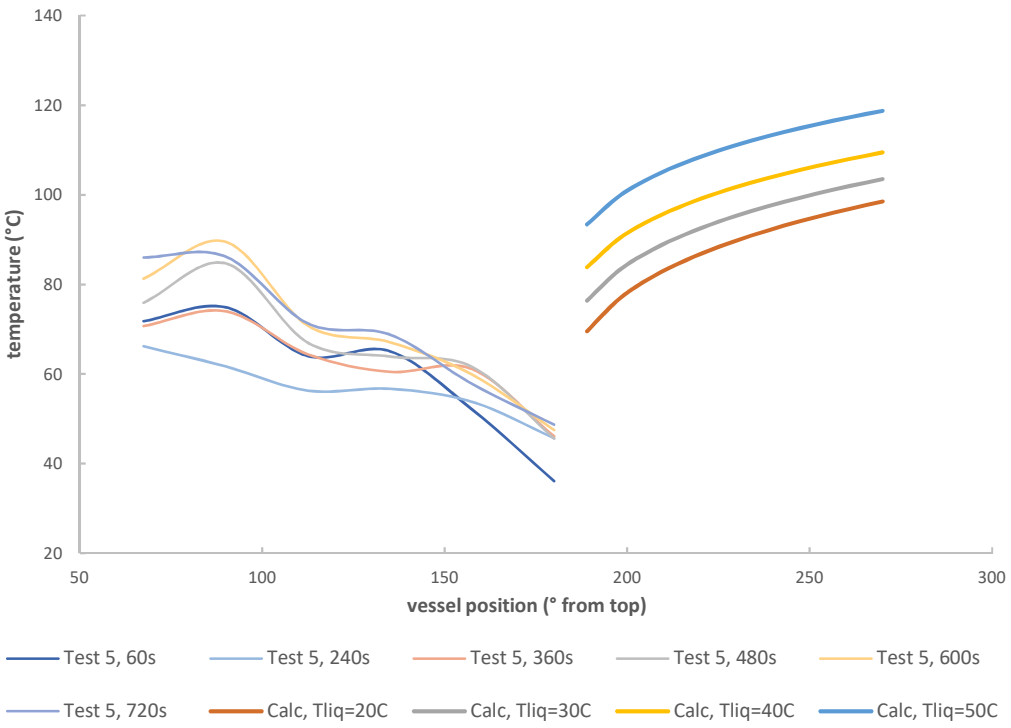

Figure 45 – Comparison of wall temperature measurements against calculated wall temperatures (assuming characteristic length of πD/4 and a heat flux of 90kW/m^2)

Figure 45 shows the results of Test 5 (Water, 50% fill, radiation shield present) against wall temperature values using equations 2.1, 2.17 and 2.18. Test 5 is chosen as it is suitably representative of the magnitude and gradient of temperature profiles across season one. It is evident that the calculation over-predicts wall temperature values near the bottom (180° +/- 45°) of the vessel. This is indicative of departure from classical boundary layer conditions, attributable to the geometry of the vessel and buoyancy acting to break-up boundary layers and thereby acting to cool the vessel shell more effectively in this region. Once the 5-15° expected increase for embedded temperatures is added, the prediction seems reasonable at higher regions in the vessel, indicating boundary layers are more stable in these regions.

A sensitivity analysis of the calculated result to the heat flux applied and the characteristic length was performed. The heat flux was found to have a similar magnitude of effect as changing the degree of subcooling, whereas the characteristic length chosen was found to have minimal effect.

The above analysis does not account for the temperature plateauing at the excess temperature (above the vapour saturation temperature) at which boiling will become significant. It is also recognised that the flow may not start as a steady turbulent flow immediately, as an initial region of laminar or unsteady flow could be

present, as reported by Venart, et al., (1984). It is not possible to estimate the time until the flow transitions from laminar to turbulent from thermocouples alone in season one. This is discussed further in section 4.5.3.

4.3.2.4 Initiation of boiling

It can be concluded that pressure vessels containing liquids with a significant degree of subcooling (e.g. hazardous materials in solution at ambient temperature) are unlikely to experience significant boiling within the range of probable heat fluxes or characteristic lengths (dictated by the likely range of fill levels) until the degree of subcooling has reduced significantly or the thickness of thermal boundary layers has increased such that the influence of subcooling is reduced. The heat transfer rate due to convection is sufficient to maintain the wall temperature below the required excess temperature until one of these phenomena occurs. For pressure liquefied gases the relatively low subcooling means this is likely to occur for a duration so short as to be negligible, if occurs at all.

The heat flux partitioning approach, described in section 2.4.5, allows an approximation to be made of the conditions under which either boiling or convection are the dominant modes of heat transfer. An example calculation for water is shown in Figure 46. Equations 2.15 and 2.20 were used to calculate the expected wall temperatures reached for a range of liquid bulk temperatures and values of heat flux, assuming only convection is present. The wall temperature values were then used to calculate the excess temperatures for input to Rohsenow's classic boiling heat transfer correlation (equation 2.22) to calculate the equivalent heat flux due to nucleate boiling. Once the boiling heat flux exceeds the original convective heat flux it is considered to be boiling dominant for the purposes of plotting the transition line in Figure 46. It must be noted that the approximation in Figure 46 is considerable. The Rohsenow equation alone can give errors of +/- 100% in heat transfer rate for a given wall excess temperature.

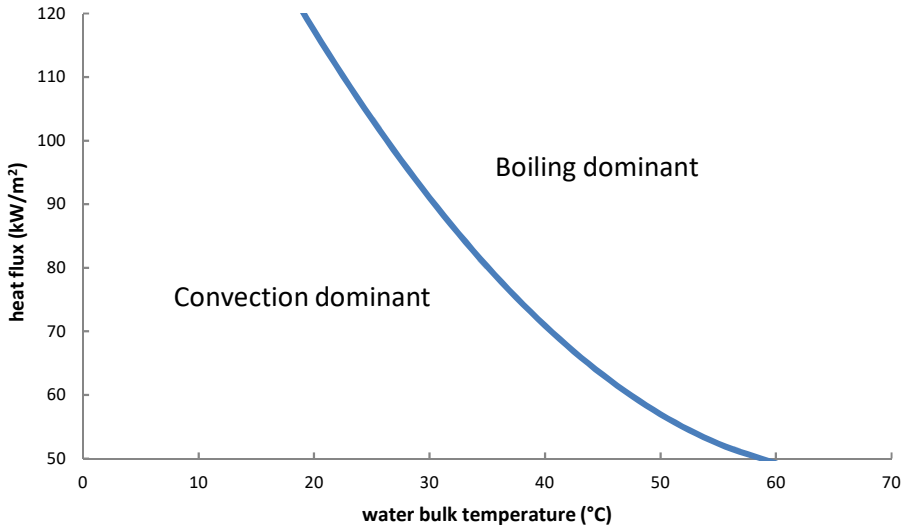

Figure 46 – Heat transfer partition for water, comparing convective flux (equations 2.15 and 2.20) with boiling heat flux (equation 2.22) – note the excess temperature at the transition varies between 8 and 12°C

4.3.2.5 Comparison with the FRA tests

Figure 47 shows the wall temperatures against time for FRA test 14038. The test was 98% water full and had a metal jacket and fibreglass insulation. Substantial variations in wall temperatures can be seen. Small variations are constant and can be attributed to the instrumentation and the nature of fire. Of more interest are the larger variations, which appear to be cyclical. The exact cause of these cyclical variations is uncertain, with variations in the fire, variations in the insulation material over time, and variations in the heat transfer coefficient being possible reasons. Another possible reason is that the variations represent a transition between boiling and convection cells, causing rapid decreases in wall temperature at boiling onset, followed by a more gradual rise as the wall temperature rises due to convection.

The closest equivalent to FRA test 14038 in the current study was test 5 (92% water full, 61 kW/m^2, with a radiation shield covering the vapour space). Both tests were fully engulfed in fire, both vessels were of similar dimensions, and the heat fluxes were similar. Test 14038 had a heat flux to the tank of approximately 35 kW/m^2, whereas test 5 was approximately 61 kW/m^2 to liquid-wetted wall and 30 kW/m^2 to the vapour space (given the radiation shield). The wetted wall thermocouple measurements from test 5 are shown in Figure 48. They exhibit fluctuations, but not the substantial variations over the approximate 10 second periods seen in the FRA test 14038. It is impossible to draw conclusions as to the cause of the cycles seen from the season one tests alone as the use of internal TCs in contact with the wall (but primarily in fluid) did not accurately capture

the wall temperatures. The analysis here has therefore been supplemented by use of season two thermocouples embedded in the wall (discussed further in section 4.4.2).

An example plot of wall temperature history is shown for test 19 (96% water fill) in Figure 49. The temperature against time is shown for thermocouples from 180 to 270° with that of DFT 9, which was located at 270°. The fluctuations in temperature measurement closely follow the variations in the DFT temperature. This trend is evident across all tests.

The above conclusion is supported by comparisons between thermocouples embedded in the wall and engulfed in the test fluid. Figure 50 compares the embedded and contact wall temperatures at three positions in the same test (test 19). It would be expected that the embedded wall TCs would record a higher temperature than those in contact with the wall. The blues lines on Figure 50 show this did occur at 135° from the top. This was also the case in the vapour space, which across season 2 showed very little difference between embedded and contact temperatures, with embedded TCs being typically 5°C hotter, occasionally up to 10°C. However, the effect shown in Figure 50 between 20 and 140 seconds at 45° and 90° from the top is of particular interest. During this period the wall temperature was decreasing, as evident from the embedded TCs, attributable to fire inconsistencies. However, the temperature of the TC in contact with the wall decreased much more slowly. From this it can be determined that the thermocouples in contact with the wall were more influenced by the flow, and that there are periods throughout the tests where the wall acts to cool the fluid.

These observations support the conclusion that variations in wall temperatures seen are due to thermal boundary condition variations or other external effects, and that the internal fluid temperatures at the wall are considerably more stable. The influence of conditions elsewhere in the vessel (i.e. below the point of interest) and the transition to boiling will both act to dampen variations in internal wall temperatures that can occur.

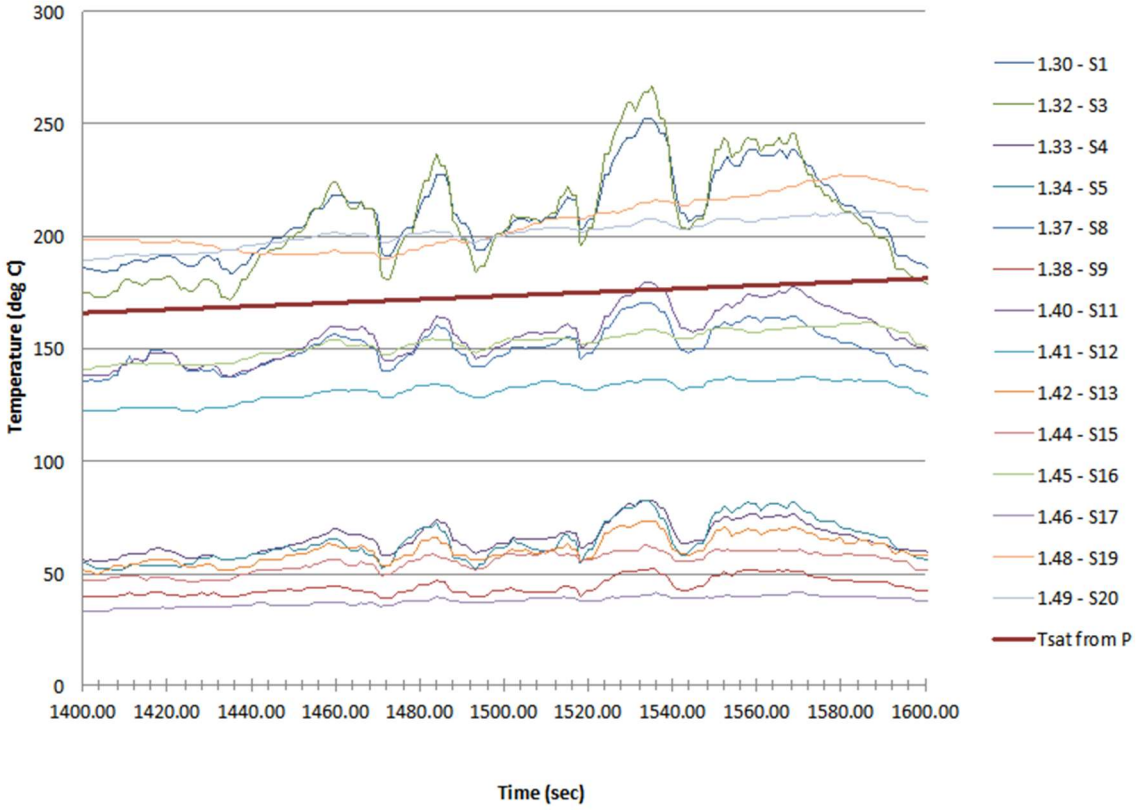

Figure 47 – Wetted wall thermocouple measurements during FRA test 14038 (water, 98% fill, metal jacket with fibreglass insulation, ~110 kW/m2)- selected duration highlighting temperature cycles shown

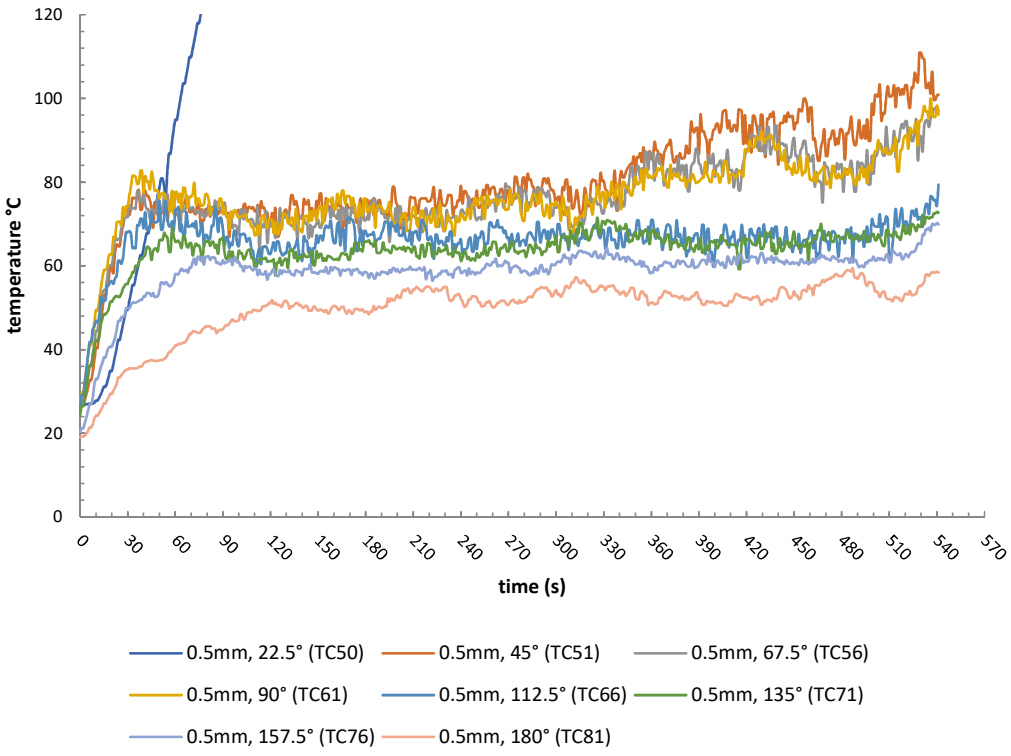

Figure 48 – Season 1 test 5, wall contact temperatures, water, 92% fill, radiation shield

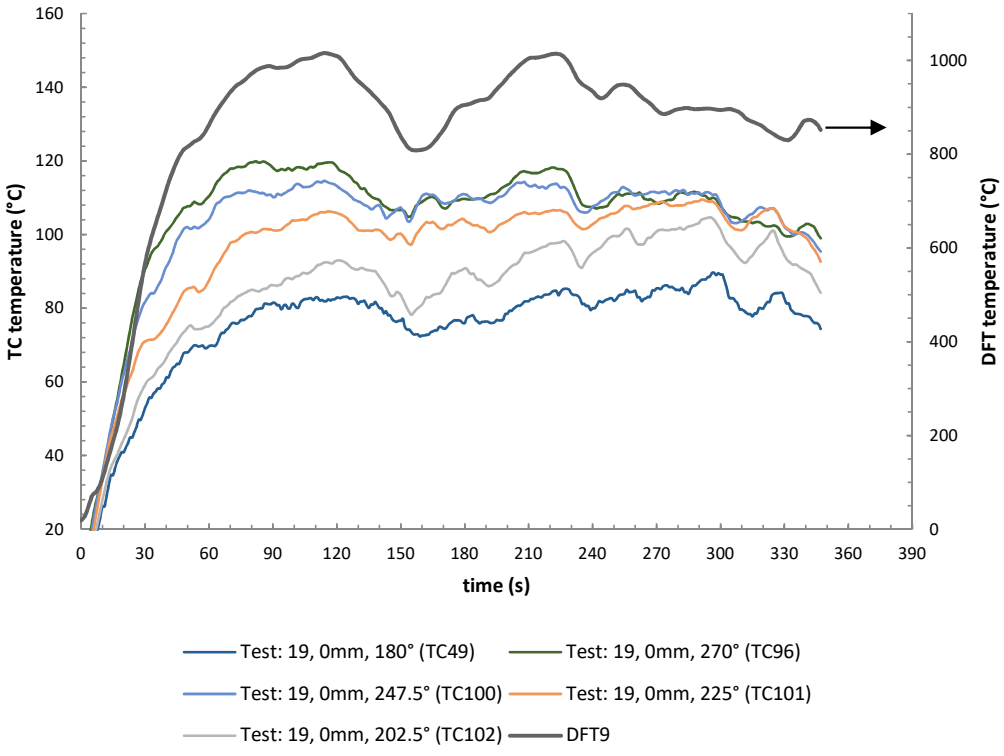

Figure 49 – Comparison of wall temperatures with DFT, test 19

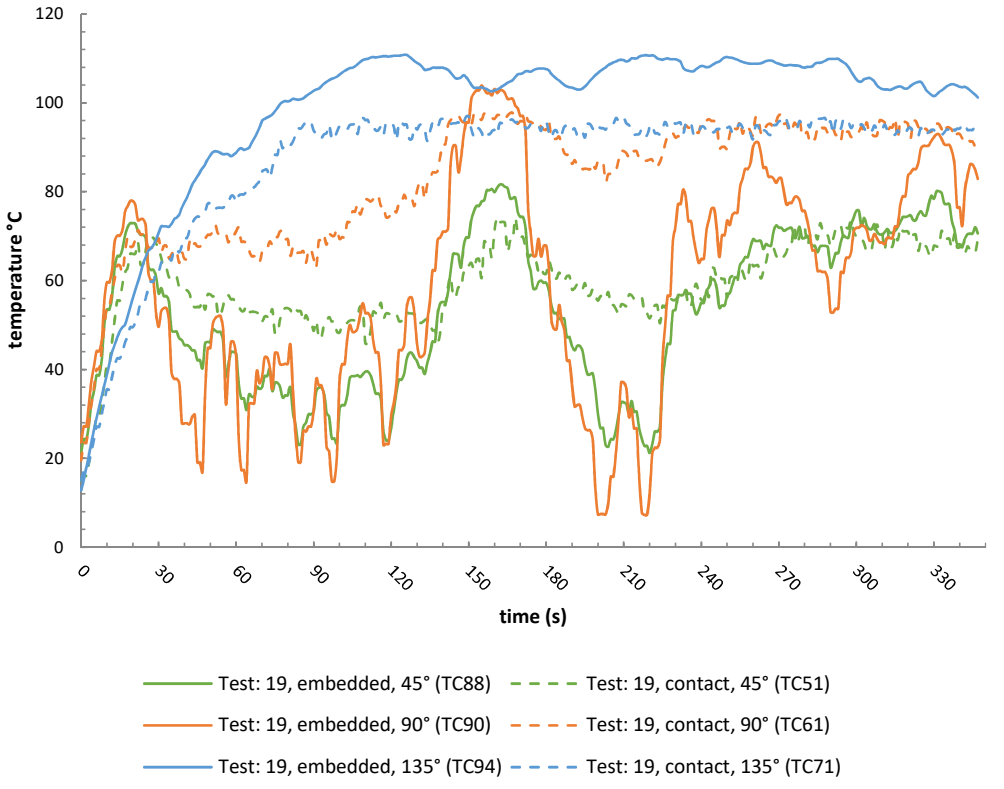

Figure 50 – Test 19 (96% water fill) comparison of embedded (solid line) and contact (dotted line) wall temperatures at 45°, 90° and 135°

4.3.3 Thermal boundary layer profiles

An example of how the temperature varies with distance from the wall at regular time increments is given in *Figure 51* and Figure 52, taken from test nine. The temperature profile can be divided into three regions. The region closest to the wall (within 3 mm) shows a clear and rapid temperature decrease with increasing distance. A larger, unstable, heat-affected zone extending from 3 mm to approximately 100-200 mm from the wall exhibits unpredictable patterns. The temperatures are generally higher than the bulk temperatures by up to 2°C, however fluctuations in the temperature profile are frequent, with local minima and maxima appearing and disappearing. Beyond the heat affected zone the temperature is more stable and increases with time and height in the vessel as the bulk liquid warms. These trends described above are present throughout season one.

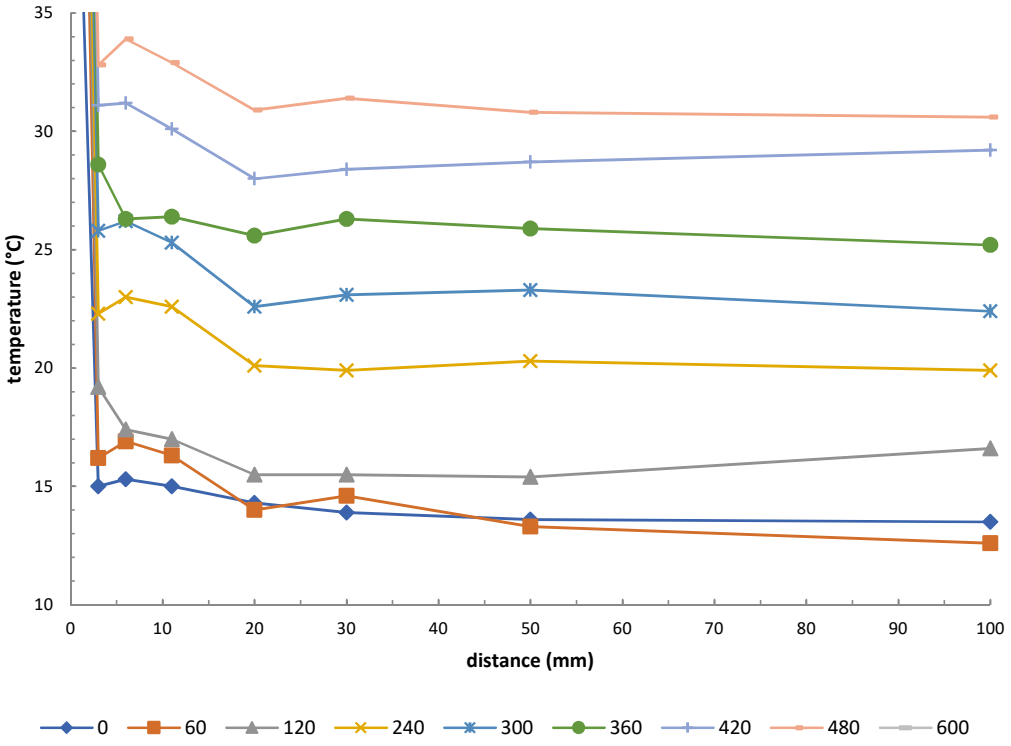

Figure 51 – Test 9, Station A, 112.5°, ethanol, 50% fill, radiation shield

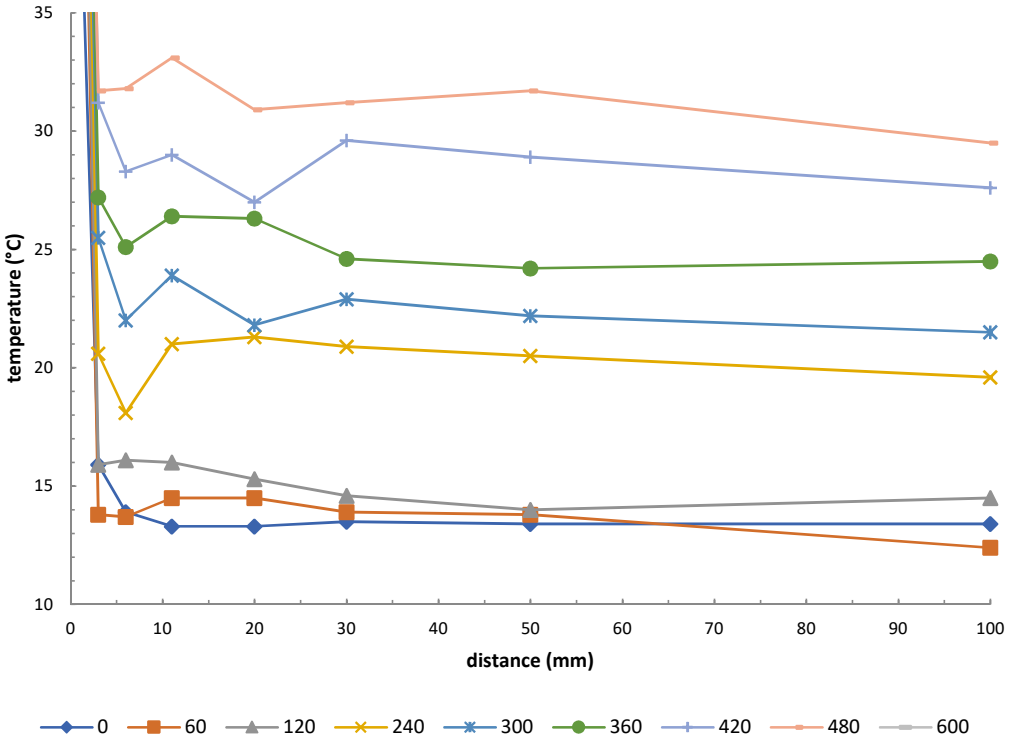

Figure 52 – Test 9, Station A, 135°, ethanol, 50% fill, radiation shield

Care should be exercised when interpreting results taken at widely-spaced time increments, as once fluctuations present in the unstable zone are averaged out they demonstrate a decrease in temperature with increasing distance from the wall, as would be expected. Figure 53 shows how the fluctuation in measured temperature values is highest nearer the wall, as indicated by a lower R-squared value, when the temperature rise is fitted to a high-order polynomial curve.

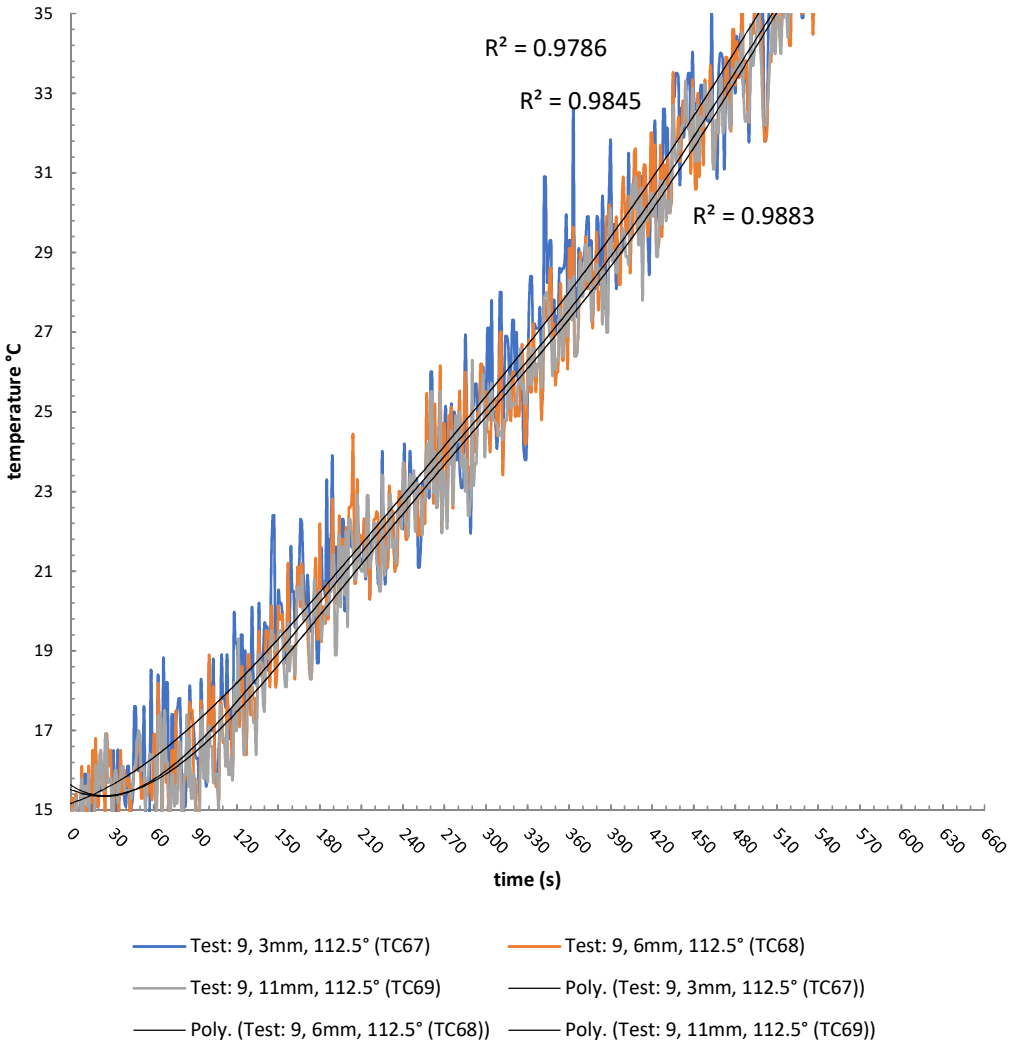

Figure 53 – Selected temperature rises measured during test 9, ethanol, 50% fill, radiation shield 112.5°, TCs at 3mm, 6mm, 11mm

The fluctuations in thermocouple readings are partly attributable to the nature of the thermocouple, with a degree of noise present in all scenarios, but primarily due to inherent variations in the flow conditions. This is visible in the bulk fluid, although to a lesser extent.

In the heat-affected zone significantly greater fluctuations are present. This can be attributed to the following:

1. Boundary layer detachment, which will occur below the mid-height of the tank due to buoyancy. When the boundary layer detaches, cooling liquid will flow in to replace it causing a temperature drop while the cooler fluid warms.
2. Flow instabilities, caused by both variations in the external thermal boundary conditions and variation in boundary layer detachment positions.

3. Turbulence, which will result in a fluctuation in the local temperature value at a given distance from the heated surface.
4. Bubbles (of air or vapour), that will have a diameter within an order of magnitude of the thermocouples. The frequency of bubble interaction with thermocouples could be significant, however this is contradicted by previous calculations of expected bubble lifetime and travel distances, indicating it is unlikely to be significant within the bulk fluid for liquids with high degrees of subcooling. It must be noted that the bubble interaction with a thermocouple is complex, and the nature of the interaction is not studied further here. The surface tension effects that dominate bubble shape will assist the bubble in flowing 'around' the thermocouple, however the proximity of the heated micro-layer around the bubble to the solid substrate may increase the heat transfer rate to the thermocouple.

4.3.4 Season one summary

It was known ahead of season one that the thermal and velocity boundary layers were expected to be thin for liquids with a high degree of subcooling and that resolving the temperature profiles would be difficult. This was proven to be the case in season one, and it was concluded that thermocouples alone were insufficient for characterisation.

More surprisingly, it was concluded that boiling was negligible at the values of heat flux and subcooling tested, due to single-phase convection being sufficient to restrict the wall temperature to below the excess value required for significant vapour generation. Bubbles were visible during tests, however these were likely to have been air bubbles coalescencing at the wall. This was in contradiction to preliminary calculations which indicated that the transition to boiling-dominant heat transfer is likely to occur at the heat flux values expected in HC pool fires for water at ambient temperature (see section 4.3.2.4, noting the approximate nature of the calculations).

The length-scales involved with pressure vessels ensure that boundary layers will transition to turbulence before they reach the mid-height of the vessel. It is unclear whether flow at approximately 135° of the vessel is fully developed turbulent flow, or whether it is unstable flow caused by variations in heating conditions and boundary layer detachment and break-up caused by buoyancy. Visually, the flow demonstrates consistent

density distortions at distances up to 30mm from the wall. It was clear at the conclusion of season one that season two would require PIV to generate detailed information.

The results from season one demonstrate that fluids with a high degree of subcooling may not experience the onset of boiling in the lower regions of the vessel until the bulk fluid has risen in temperature by a certain amount. Results also demonstrate that classical boundary layer theory under constant heat flux conditions poorly predicts the wall temperature profile observed, and that division of the wall into regions based on the angle of the vessel wall, with separate consideration for each region, may be more appropriate. Both of these findings can contribute to the validation of improved non-numerical models that seek to implement boiling and heat flux partitioning into boiling and convection.

The rate of pressurisation was an order of magnitude lower in the calibration tests than in the closest equivalent FRA test, despite similarities in vessel design and contents. This may be attributed to the difference in thermal boundary conditions, however if so, it must coincide with a change in mechanism driving pressurisation to explain the magnitude of the change. Alternatively, the fact that the vapour space steel was cooler during the tests reported herein (due to the presence of a radiation shield) may be having a significant influence on the pressurisation rate, by reducing radiative heating of the vapour and liquid surface. Either way, the results from season one would indicate that the common approach of modelling of the pressurisation rate as the vapour saturation pressure at the temperature of the liquid surface, and the surface temperature being controlled by convection currents within the liquid, is missing a factor (or factors) with significant influence on the rate of pressurisation. If this is correct, the implication is that the beta-factor (the ratio of the liquid surface temperature to the bulk temperature) approach used in simplistic models may be being empirically ‘tuned’ to match known test results but may be missing out one or more of the key factors that drive pressurisation.

4.4 Season two

4.4.1 Season two objectives

The objectives of season two were to:

- Improve wall temperature measurement to assess whether boiling was occurring
- Perform PIV tests to obtain a correlation between thermal and velocity profiles
- Progress to pressure testing, and with alternative fluids to water

As previously explained, the third objective was not met due to damage to the test equipment curtailing the test season. Season two was intended to build on, and improve on, season one through the use of additional instrumentation. Flow velocities and boiling characteristics were of particular interest, to provide information that allows detailed investigation of the balance of phenomenon that drive pressurisation.

4.4.2 Wall temperature measurements

Season two tests used thermocouples embedded in the vessel wall at 2mm depth (from the inside), as detailed in 3.2.7. An example plot of wall temperature history is shown for test 19 (96% water fill) in Figure 54.

From the Rohsenow correlation (equation 2.33) it can be reasonably assumed that the excess temperature required for water boiling is between 3°C and 9°C, depending on the degree of subcooling, and hence that boiling initiates within 60 seconds on the north side of the vessel (270° in Figure 54) and spreads to a larger area of the north side and a localised point on the south side from 120 s.

Comparison of the wall-embedded and wall-contact thermocouple positions indicates that the wall contact TCs plateau at approximately 95°C when the embedded wall TCs record values above the excess temperature required for boiling (approximately 9°C at high degrees of subcooling). On the assumption that a wall contact TC temperature of 95°C or above is representative of the presence of partial nucleate boiling, a qualitative assessment can be made of whether boiling occurred throughout season one. Table 23 gives the results of this assessment. Table 24 gives a similar assessment for season two below, but using the embedded wall thermocouples instead of the wall contact thermocouples.

It must be noted that Table 23 and Table 24 should not be relied upon quantitatively, and are only useful for guiding further analysis. Further information required to more accurately calculate the season one contact wall temperature from the contact TCs (i.e., the contact surface area and the local flow convection characteristics) is not available for the current study, and hence embedded TCs are recommended in any future work.

Based on the expected occurrence of boiling, and limitations on which tests are captured by quality videos, tests 19 and 22 and considered suitable further for analysis of wall boiling model parameters (see section 4.6).

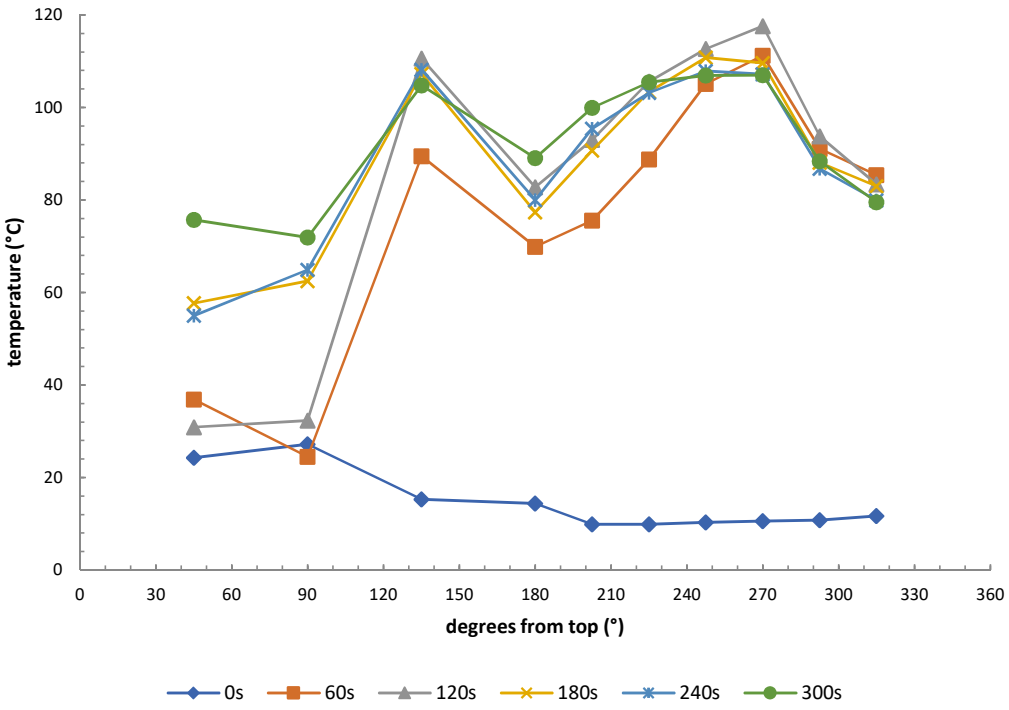

Figure 54 – Test 19 (96% water fill, full engulfment), thermocouples embedded in vessel wall

Table 23 – Qualitative assessment of boiling commencement in season one

Season 1 test	Partial nucleate boiling excess temperature reached (station A only)
5	Above 90°, 520s
6	Not reached
7	At 90°, 300s
8	At 90°, 120s
9	Not reached
10	Not reached
11	Not reached
12	At 90°, 600s

Table 24 - Qualitative assessment of boiling commencement in season two

Season 2 test	Partial nucleate boiling excess temperature reached (station A)	Partial nucleate boiling excess temperature reached (station B)
13	150-180°, 180s	Not reached
14	Not reached	Not reached
15	135-180°, 60s	180-250°, 60s
16	135°, 60s	Not reached
17	135°, 120s	225-270°, 120s
18	135°, 60s	200-270°, 60s
19	135°, 120s	200-270°, 120s
20	Not reached	Not reached
21	135°, 240s	220-250°, 240s
22	135°, 180s	250°, 120s

4.4.3 Heat transfer coefficient correlation analysis

An assessment of the applicability of selected Nusselt number correlations to the season two test data is given below. Table 25 shows the correlations used to predict the Nusselt number for each test. The measured wall temperature value at 90° (from the embedded TC) and bulk liquid temperature (from an average of TCs within 200mm of the centre) were used at 120 seconds, with this time being chosen retrospectively for expected stability of flow conditions based on PIV results (reported in section 4.4.7).

Table 25 – Nusselt number correlations

Correlation	Nusselt number (Nu_x) formula	Source
A	$0.13\ Ra_x^{1/3}$	Bergman, et al., 2011
B	$0.11\ Gr_x^{1/3}$	Tsuji & Nagano, 1989
C	$0.186\ (Ra_x Pr)^{1/3.2}$	Kiš & Herwig, 2012
D	$5\ Nu^{2/3}[(8\ Nu_x Gr_x Pr^2)^{1/12}-1] = (Gr_x Pr^2)^{1/3}$	Versteegh & Nieuwstadt, 1999
E	$\overline{Nu_L} = \left\{0.825 + \frac{0.387 Ra_x^{1/6}}{[1+(0.492/Pr)^{9/16}]^{8/27}}\right\}^2$	Churchill, & Chu, 1975
F	$\overline{Nu_L} = 0.14 Ra_L^{1/3}\left(\frac{1+0.107Pr}{1+0.01Pr}\right)$	Raithby & Holland, 1985
G	$\overline{Nu} = 0.098\ Ra^{0.345}$	Schmidt, 1956

The characteristic distance, *x*, for correlations A-D was taken as π.r/4, equivalent to half the expected flow distance (tangential to the vessel wall) from the bottom of the vessel (180°) to the location of the temperature measurement point (90°). Half of *x* was used for correlations E and F as these correlations are for the approximate average Nusselt number along the flow length. Correlation G uses the actual tank diameter and was developed as an average value for the internal of heated tanks with constant wall temperature.

Figure 55 shows the calculated Nu values for correlations A-G above, along with a reverse calculation of the Nusselt number from the measured heat flux (as reported in section 3.4.3) and temperature values (recorded by the embedded wall TC at 90°, at 120 seconds), based on a rearranged equation 2.1 substituted in to equation 2.2, to give:

$$Nu = \frac{q^{"} x}{\Delta T \, k_f} \tag{4.1}$$

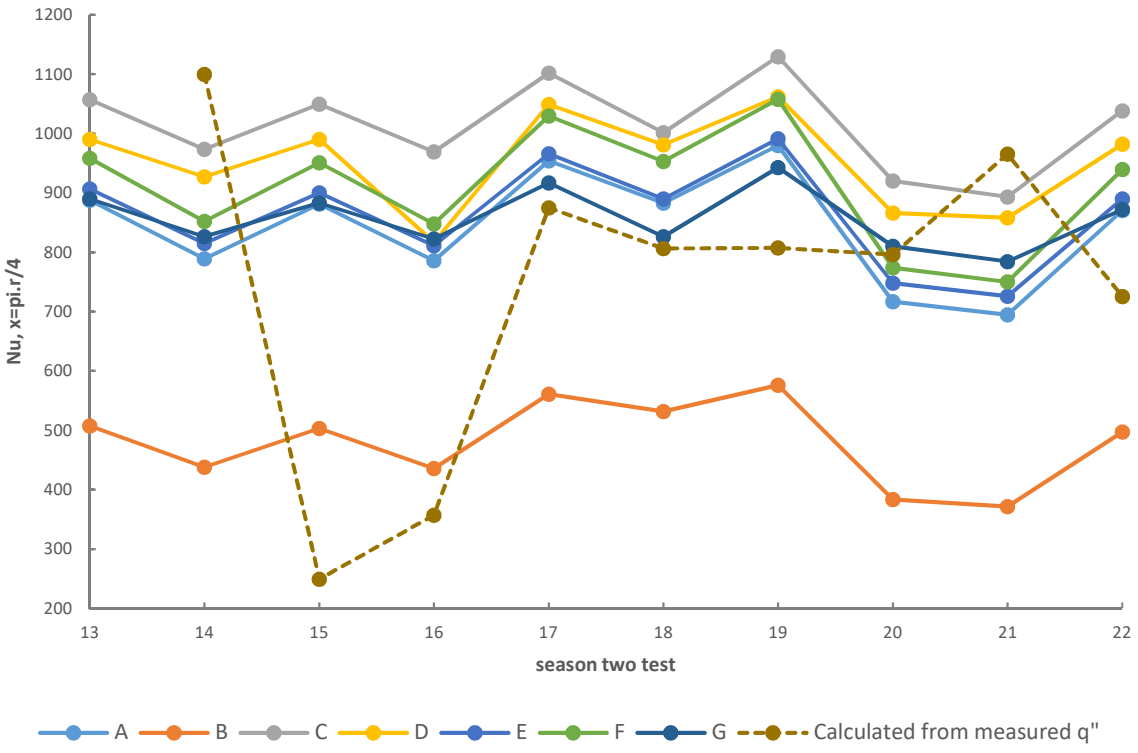

Figure 55 – Calculated Nusselt number values for season two tests (see also Table 25)

There is poor consistency in the reverse calculation results obtained from equation 4.1, making it difficult to draw reliable conclusions. Tests 15 and 16 show particularly poor agreement. The inconsistencies are caused by discrepancies between the measured heat flux and wall temperatures, giving heat transfer coefficients (and

hence Nusselt numbers) that appear to be unrealistic. Although the heat flux and temperature measurement used were taken at a similar location, the flame variations make the calculated heat flux values somewhat unreliable for use at a single point in time. For example, the heat flux used in the test 15 calculation was based on a DFT temperature of 620°C. Only 30 seconds earlier the DFT had recorded approximately 800°C. Tests 15 and 16 also had notably higher wind during the first 120 seconds, compared to other tests, possibly contributing to this variation.

Excluding tests 15 and 16, the majority of correlations show an acceptable similarity with the reverse calculated value, given the inherent variability in the method. The exception is correlation B, which was alone in excluding the Rayleigh number, and hence a length scale, and was developed based on tests with a significantly smaller length scale than can be found in pressure vessels. Correlation G is unique in that it was developed from tests which utilised a heated vessel. In the formula proposed by Schmidt, the length term, *x*, in the Rayleigh number is replaced by the vessel diameter. This removes some subjectivity, as the user does not need to choose a suitable characteristic length when calculating the Nusselt number and Rayleigh number. However, it is impossible to verify the applicability of this (or any other) correlation to alternative vessel diameters within the current study. The studies by Schmidt were based on a full vessel, and took no account of varying fill level.

The Rayleigh number correlation can be modified to introduce fill level by replacing the vessel diameter with wC/π, where w is the fraction of the wall that is wetted (calculated from the fill level) and C is the vessel circumference. The modified correlation can also be further adapted for conditions of uniform heat flux, using the methodology described by Lienhard & Lienhard (2017), which uses a modified Rayleigh number, Ra^*, defined as Ra/Nu, thereby removing the unknown temperature term from the Nusselt number equation as follows:

$$Nu = 0.098 \left[\frac{Ra^*}{Nu}\right]^{0.345}$$

And therefore

$$Nu = 0.178\, Ra^{*0.257} \tag{4.2}$$

where:

$$Ra^* = \frac{g\beta q'' \frac{wC}{\pi}}{\alpha \nu k} \tag{4.3}$$

The correlation given by equation 4.2 is plotted against the original Schmidt correlation and the reverse-calculated Nusselt number in Figure 56. The agreement with the reverse-calculated values show no improvement, however the inclusion of additional physical parameters and applicability to uniform heat flux conditions means the equation should provide a more robust correlation, applicable to a wider range of vessel diameters, fill levels and fluids. Note that the original correlation by Schmidt used the average fluid temperature to calculate the necessary parameters. As the true average is difficult to discern, equation 4.2 uses the film temperature (an average of the wall and bulk minimum liquid temperature).

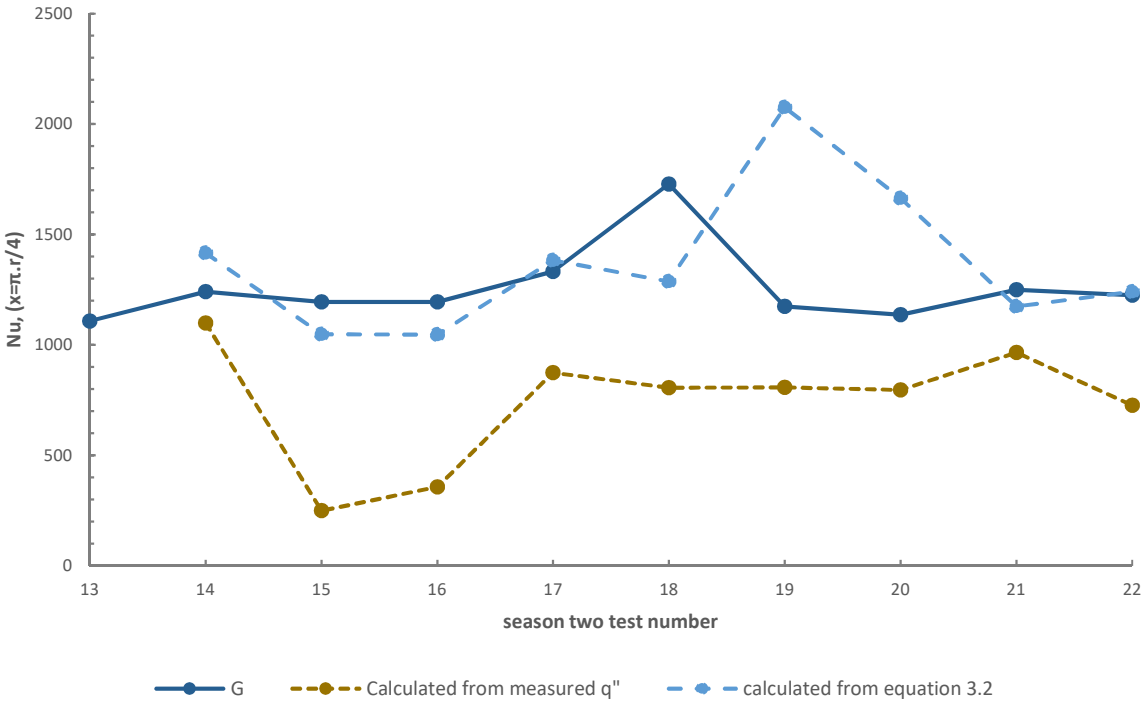

Figure 56 – Comparison of proposed Nusselt number correlation with reverse calculated values and that of Schmidt (1956)

In section 4.3.2.3 the expected wall temperatures are predicted as a function of distance along the heated length, based on a correlation for turbulent flow along surfaces exposed to a uniform heat flux proposed by Churchill and Chu (1975). A similar calculation is performed for test 22 below (using equations 2.18 and 4.2).

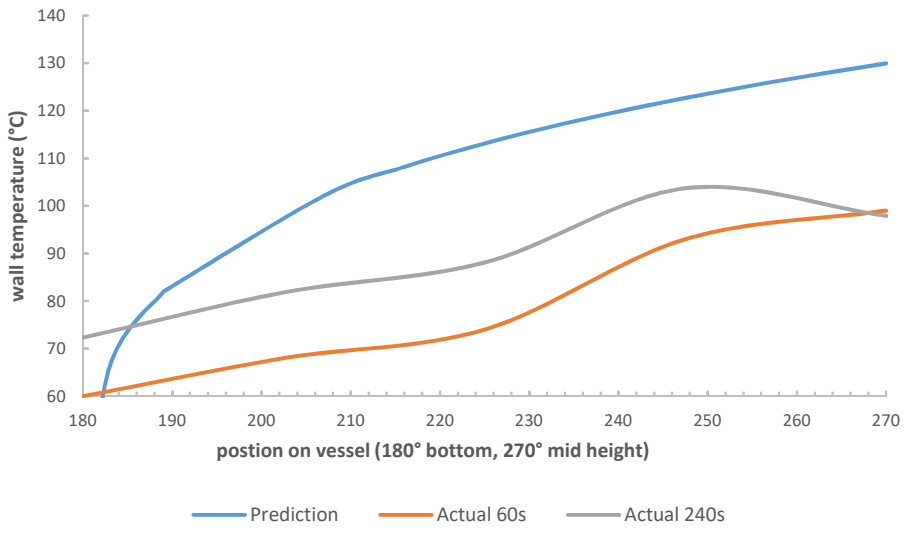

Figure 57 – Predicted vs actual wall temperatures, test 22

Figure 57 shows a significant difference between the predicted and actual values, despite a reasonable agreement between the predicted and reverse-calculated Nusselt values. Discounting the region at the bottom of the vessel from 180-190° (on the basis that equation 2.18 converges with the bulk liquid temperature at zero characteristic length, which is not true in practice) the actual temperature profile is seen to be more linear than that predicted by the methodology. This is true across season two tests in general.

The convection coefficient of fully turbulent boundary layers is known to decrease with increasing characteristic length (Bergman, et al., 2011) and the rate of temperature rise would therefore be expected to decrease as the flow moves up the vessel wall. However, the measurements in season two do not show this phenomenon well, if at all. Variations in fire intensity could be a contributing factor, however, DFT data indicates the fire was generally weaker at the bottom of the vessel and therefore there must be an alternative reason (as a weaker fire at the bottom of the tank would be expected to increase the rate of change of temperature as the heat flux increases with height, or to result in a temperature profile with multiple inflection points as the heat flux varies).

The difference observed between the actual and theoretical temperature profiles near the bottom of the vessel is attributable to the complex flow effects in the region of instability at the bottom of the vessel. Unsteady flow with multiple convection cells and plumes means the assumption of unheated fluid at the start of the turbulent boundary layer (used in the analysis shown in Figure 57) will give unrealistically low wall

temperature predictions at the bottom of the vessel (180°). Instead, local convection cells, and later warm fluid recirculation, will act to pre-heat the fluid, giving higher wall temperatures at the bottom of the vessel and the more stable temperature gradient recorded in the experiments.

The shape of the actual wall temperature measurements shown in Figure 57 may be attributable to a region of instability causing a low rate of initial temperature rise from vessel bottom (180°) to one quarter height (225°), above which a more stable boundary layer forms and the coefficient of convection starts to decrease, therefore leading to a steeper rise in temperature. Variations in fire intensity in this region may also be a factor.

4.4.4 Boundary layer thickness

Knowledge of the thickness of the thermal and velocity boundary layers is an important prerequisite for analysis of the temperature and velocity profiles within them. The thickness of the velocity boundary layer is predicted for tests 10 (ethanol, 50% fill) and test 19 (water, 96% fill) using the equations given in Table 26 and based on the measured wall temperatures at 60 seconds. The results are shown in Figure 58.

Table 26 – Boundary layer thickness prediction methods

Source	Velocity boundary layer thickness	Thermal boundary layer thickness
Eckert & Jackson (1950)	$\delta = 0.565\ x\ Gr^{-1/10} Pr^{-8/15}\left[1 + 0.494\ Pr^{2/3}\right]^{1/10}$	$\delta_v = \delta_t Pr^{1/3}$
Tsuji & Nagano (1989)	$U_b \delta_U / \upsilon = 0.331\ Gr_x^{0.250}$ $U_b = (g\beta\Delta T_w \upsilon)^{1/3}$	$U_b \delta_T / \upsilon = 0.646\ Gr_x^{0.151}$

Calculations for further tests, and alternative time periods, show little difference (as both correlations vary solely with the film temperature, which is relatively stable across tests of the same fluid).

The two correlations predict notably different thicknesses of thermal boundary layer for both tests, with that predicted by Eckert & Jackson (1950) being higher by a factor of approximately three. The velocity boundary layer predictions differ by a factor of approximately two. However, the correlation that predicts the highest thickness varies depending on the fluid; Tsuji & Nagano (1989) for water, and Eckert & Jackson (1950) for ethanol.

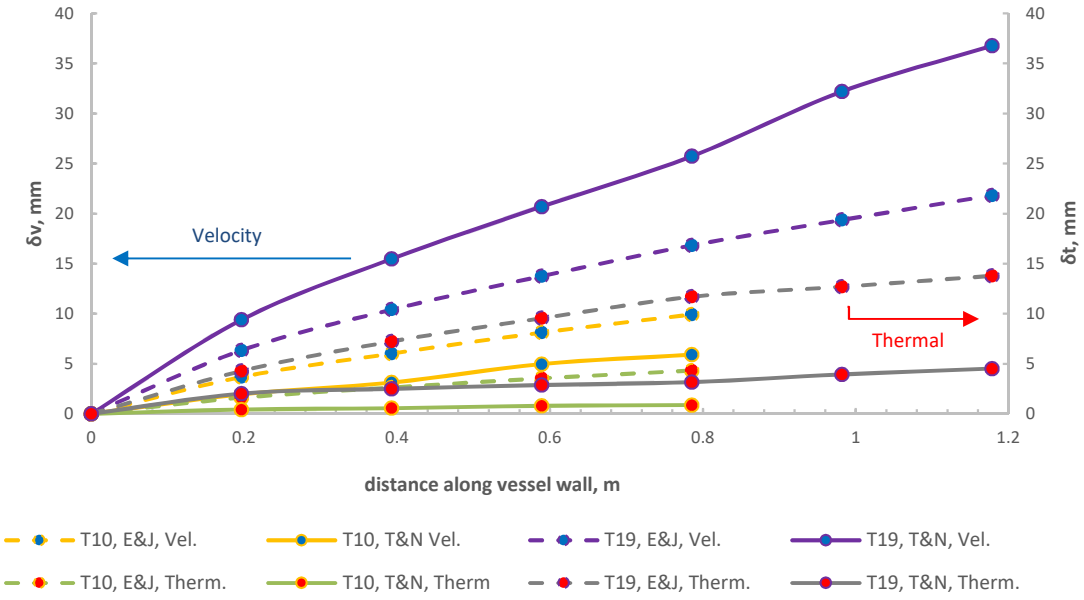

Figure 58 – Boundary layer thickness predictions for test 10 (ethanol, 50% fill, 84 kW/m^2) and test 19 (water, 96% fill, 90 kW/m^2)

4.4.5 Thermal boundary layer analysis

Obtaining thermal boundary layer thickness measurements from the thermocouple data requires further definition of a thermal boundary layer, as the frequently accepted definition of $0.99T_\infty$ does not apply in the geometric scenario of a pressure vessel. This is considered further below. Figure 59 and Figure 60 highlight the difficulty in observing a thermal boundary layer. Figure 59 shows the 'noise' within the data signal and the tendency for the lowest temperature reading to jump across thermocouples with time.

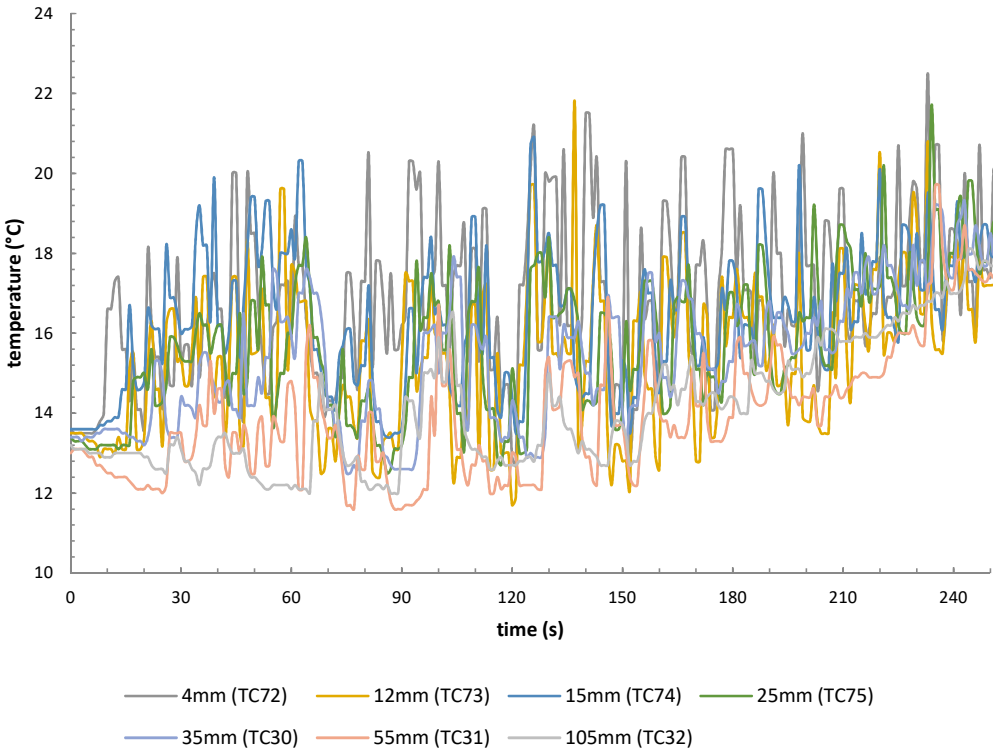

Figure 59 – Test 22, Station A, 135°

An analysis of all season one and season two tests shows that the thermal boundary layer measurements do not give a good match with the predicted values of up to 6 mm for water and 2 mm for ethanol. Figure 60 shows an example temperature profile measured in a water test. Warm layers substantially thicker than the predicted thermal boundary thickness were detected. This is unsurprising, as the correlations given in Table 26 are based on vertical plate, where buoyancy acts parallel to the plate and the primary factor driving perpendicular growth of the boundary layer is the horizontal heat flux. In a vessel geometry, buoyancy will instead act to expand the warm layer in the lower half of the vessel, and compress it in the top half.

However, it is unclear from temperature data alone whether the warm region detected represents a stable and attached boundary layer, or simply convective transport of warm liquid to the region within 50 mm of the wall by flow instabilities (e.g. eddies or plumes). Further insight is given by PIV analysis, and this is discussed further in section 4.4.7.

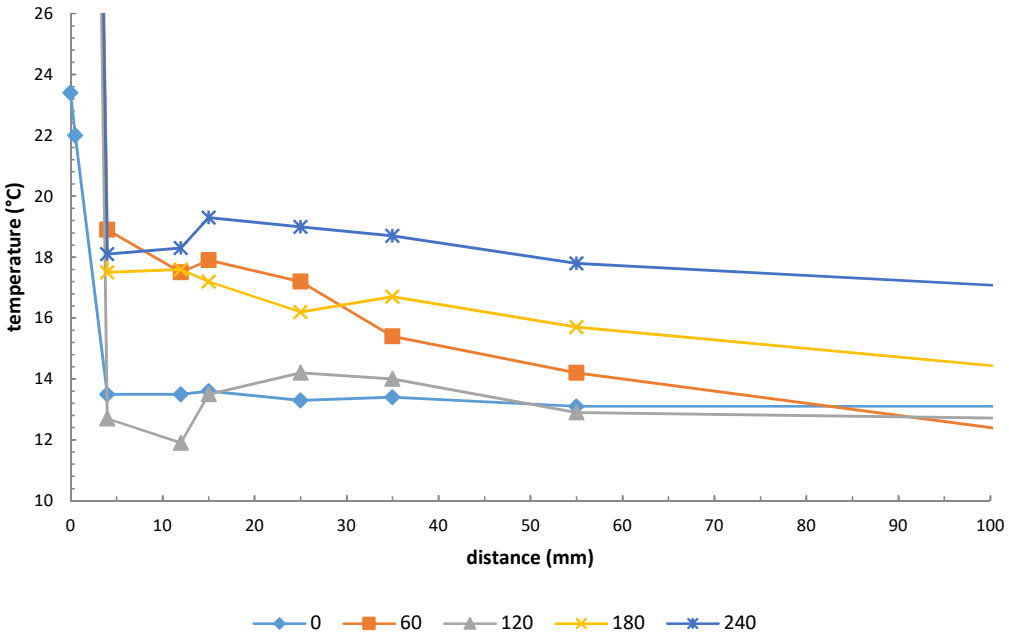

Figure 60 – Test 22 (water, 62% fill, 67 kW/m^2), Station A, 135°, temperature at 60s time intervals

Commentary on the variation in temperature profiles with position in the vessel is given below, starting from the bottom of the vessel and moving up in 22.5° increments. The following considers only water tests (season one tests 5-8 and season two tests 13-22). Commentary is reflective of general trends across all tests and illustrated by a selected example from a specific test.

*180° - Bottom of vessel (*Figure 61*)*

At the bottom of the vessel the temperature drop was rapid, occurring predominantly before the first thermocouple at approximately 5 mm from the wall. From the first liquid thermocouple to approximately 50 mm pronounced fluctuations in temperature occurred, which can be attributed to local convection cells and unstable plumes forming and moving as the boundary conditions and internal flow vary with time. At distances greater than 50 mm (rising through the centre line of the vessel) there is a steady trend for temperatures to increase in the vertical direction towards the liquid surface, albeit with some fluctuations.

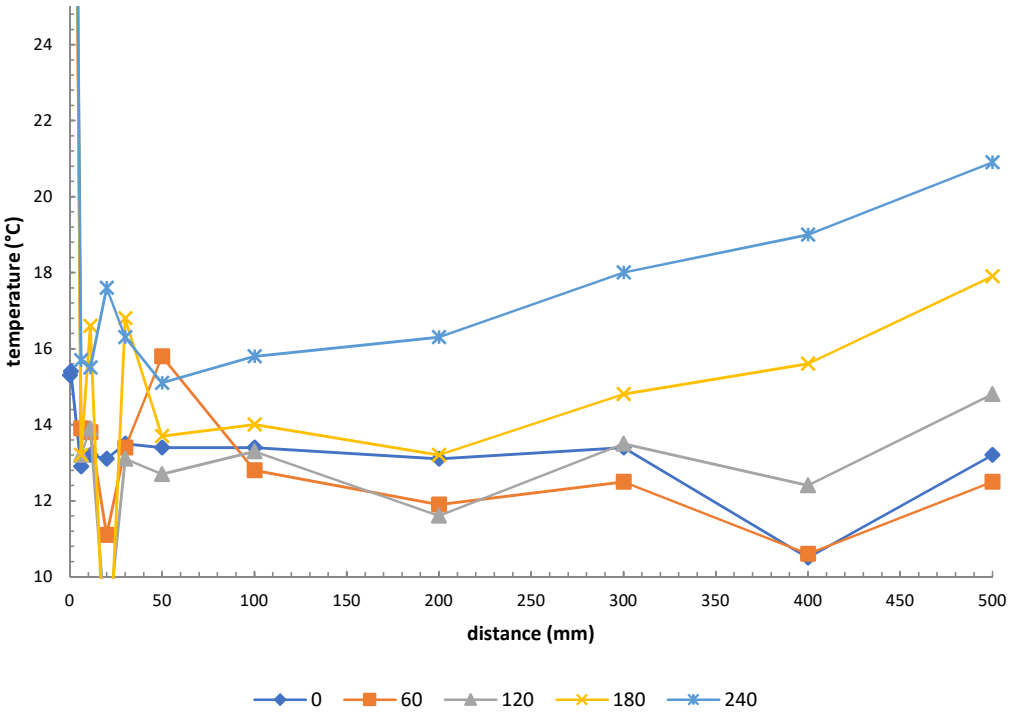

Figure 61 – Test 22, Station A, 180°

*157.5° (*Figure 62*)*

Local minima frequently occur in a region approximately 5 mm from the vessel wall, accompanied by peaks within the next 5 mm from the wall. Further minima and peaks occur infrequently in the region 10 mm to 30 mm. The warm layer typically extends to 30 mm.

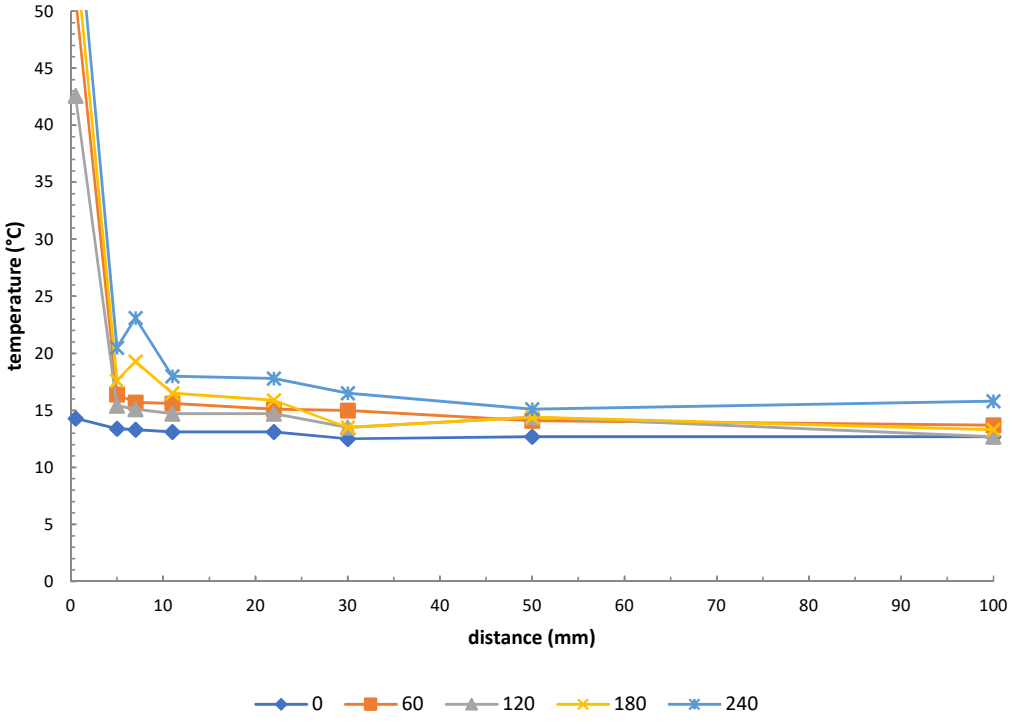

Figure 62 – Test 20, Station A, 157.5°

*135° (*Figure 63*)*

Local temperature minima and peaks are a common feature at distances of 5 to 10 mm and 10 to 20 mm, respectively, implying that cooler liquid is entrained between the thermal diffusion layer and a detached warm layer. The warm layer is thickest in this region of the vessel, typically 35 mm.

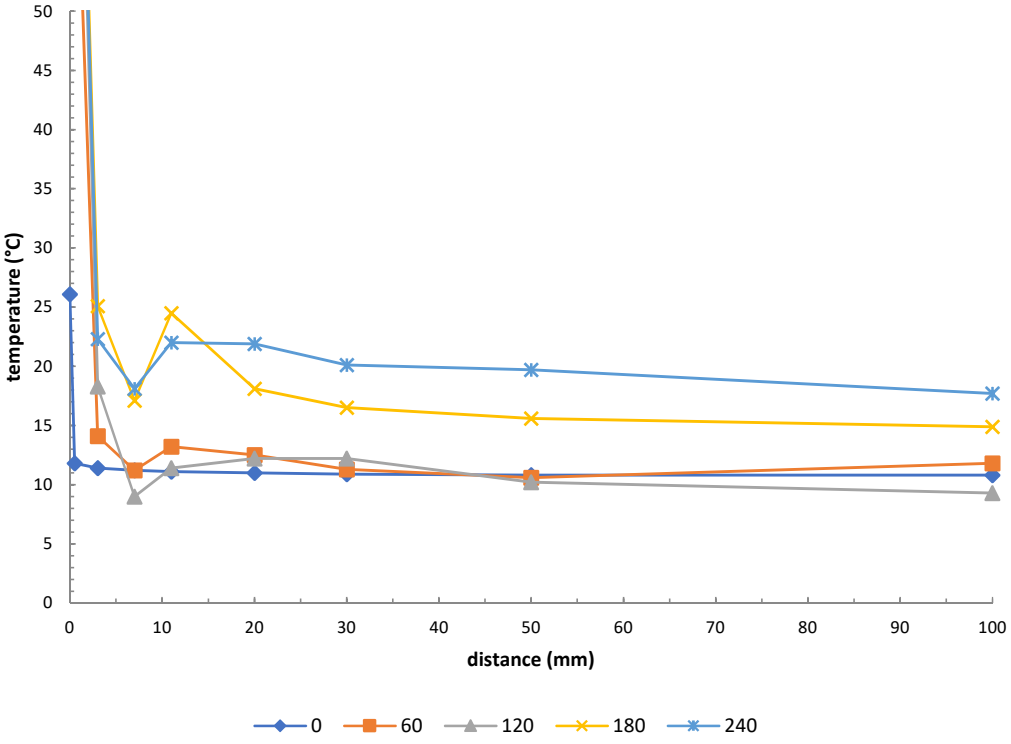

Figure 63 – Test 13, Station A, 135°

*112.5° (*Figure 64*)*

The temperature profile starts to stabilise in this region of the vessel. Peaks appear intermittently in the warm region, indicating warm fluid moving out into the bulk fluid. This can be attributed to instabilities forming and the warm layer shedding eddies, which move away from the wall into the bulk fluid, thereby causing cooler fluid to be drawn in to replace them. This would explain why some tests appear to have an intermittent thin layer of cooler liquid approximately 5 mm from the wall. The warm layer thickness is typically 30 mm.

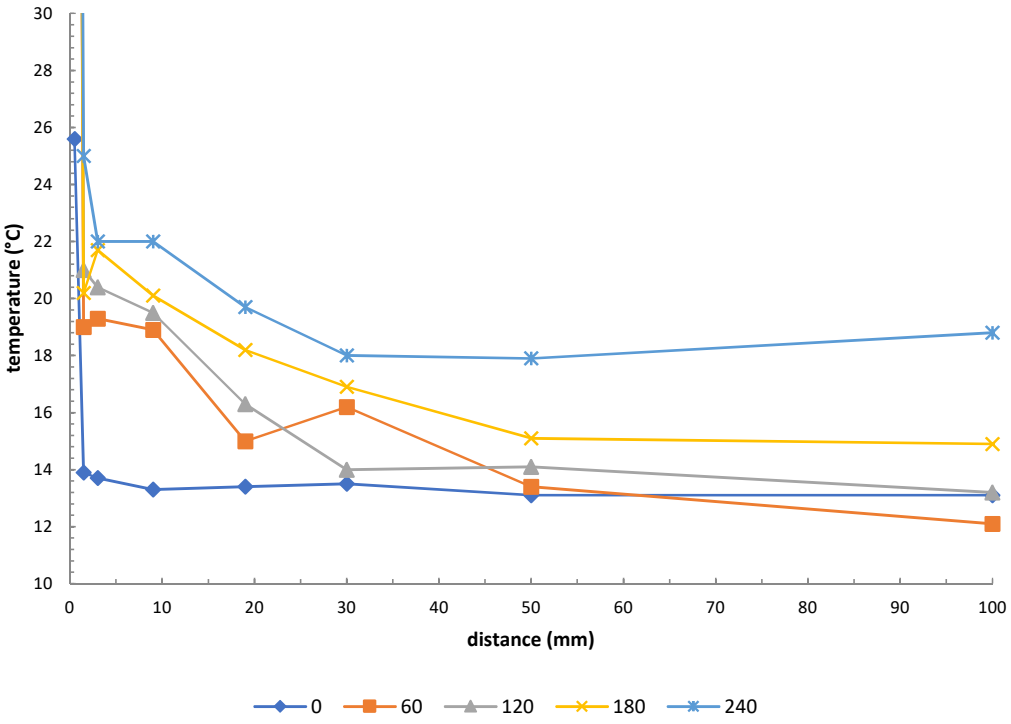

Figure 64 – Test 22, Station A, 112.5°

*90° Mid-height of vessel (*Figure 65*)*

The temperature profile at 90° is similar to that at 112.5°. From 5 mm to 30 mm the temperature decrease is approximately linear. Intermittent peaks appear, but they tend to be broader and less pronounced, possibly indicating larger eddies than lower in the vessel. The warm layer thickness is typically 30 mm.

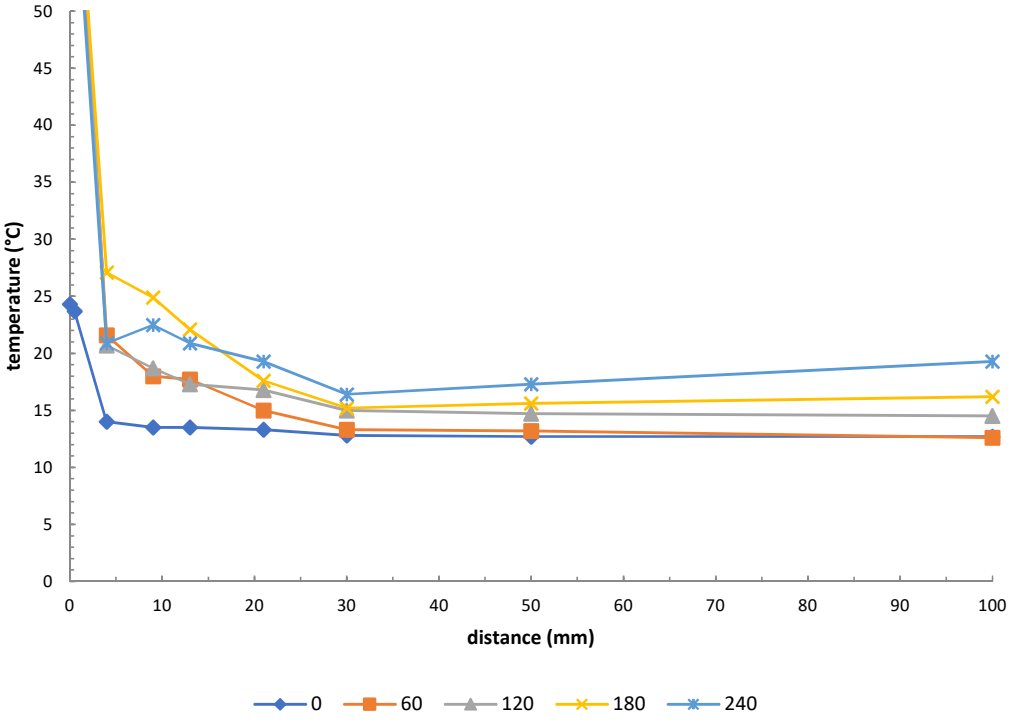

Figure 65 – Test 20, Station A, 90°

*67.5° (*Figure 66*)*

The number of tests with data above mid height is limited due to variations in fill level. Tests 19 and 20 show similar temperature profiles at 67.5° to 90°, with intermittent peaks possible. The warm layer thickness is typically 30 mm.

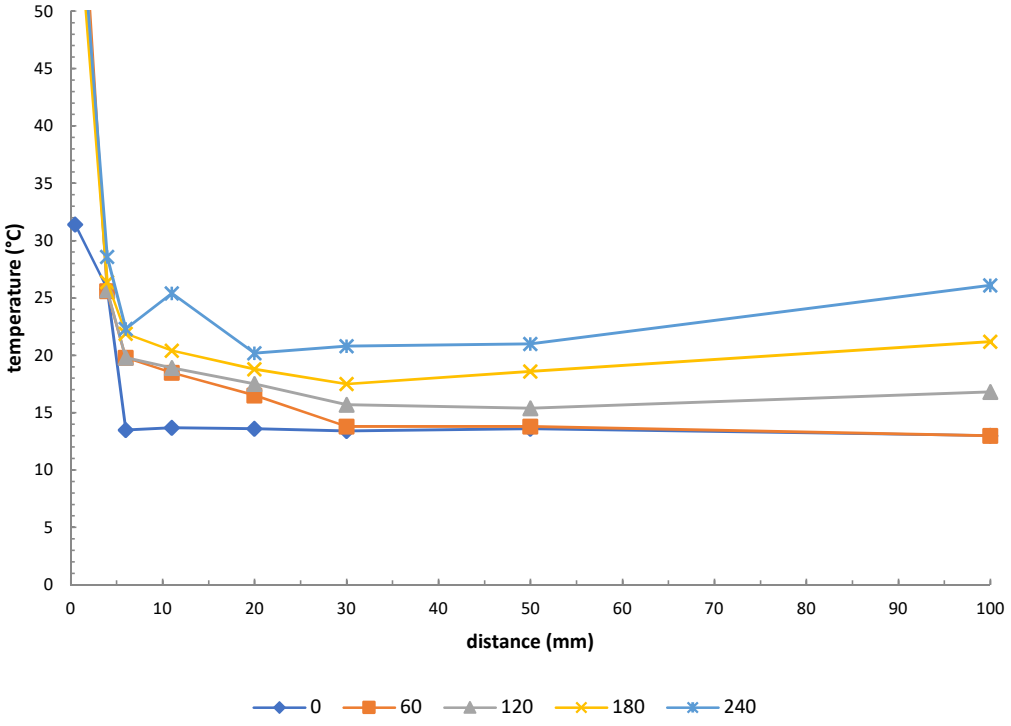

Figure 66 – Test 20, Station A, 67.5°

*45° (*Figure 67*)*

Tests 19 and 20 show a relatively flat temperature profile from distances to the wall of approximately 6 mm to 100 mm. This can be attributed to the curvature of the vessel and the presence of the liquid surface, both acting to 'collect' the rise of warm liquid from below. The combination of these factors results in an increase in warm layer thickness, up to a typical value of 50 mm or greater.

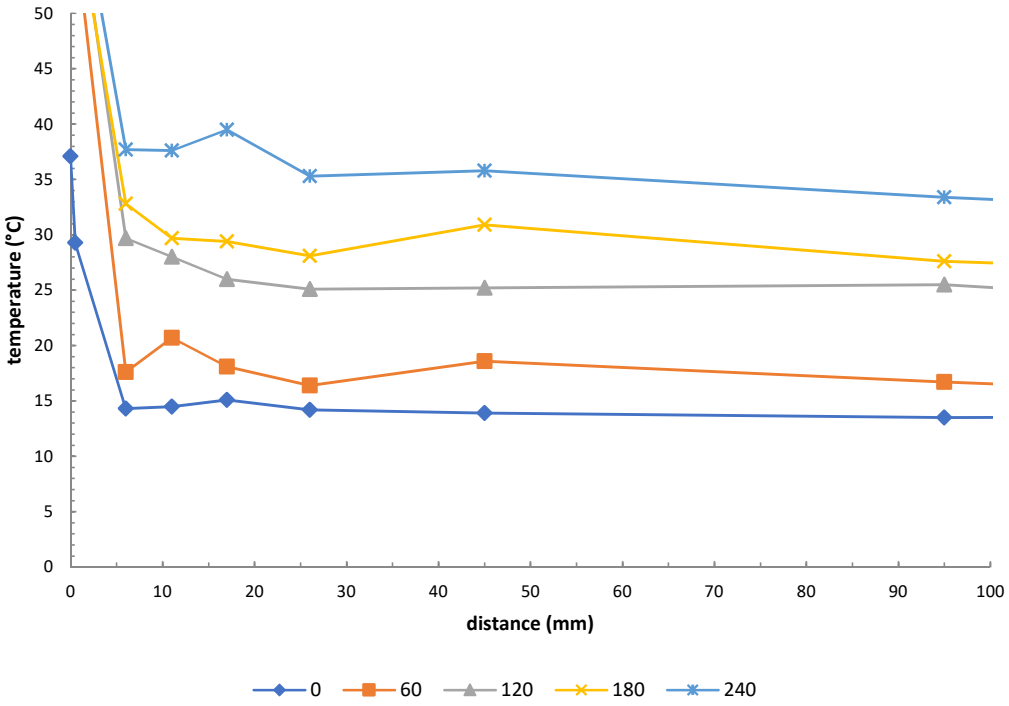

Figure 67 – Test 20, Station A, 45°

Examination of the thermocouples in the bulk fluid (taken to be 100 mm to 500 mm from the wall) between 135° and 180° (i.e. 6pm to 7.30pm on a clock) appear to show correlation of temperature only with height in the vessel. No direct correlation between proximity to the wall and temperature is evident. Given the expectation of a plume forming near the centre of the vessel, this may be an indication that the plume was small or off-set from the centre. However, it may imply that the unstable warm layer at the bottom of the vessel is only weakly mixing with the bulk fluid, either due to effective mixing within 100 mm of the wall, or due to the majority of heat transport being in the direction of the vessel wall curvature, caused by the establishment of recirculation currents within the vessel. The increased scatter in the temperature data within 100 mm of the wall at 180°, coupled with the PIV results at 135° (see section 0) would imply a combination of

these factors is occurring. There are small, unsteady plumes forming near the centre of the vessel, however a substantial fraction of the thermal energy entering the fluid in this region is transported along the vessel wall due to the establishment of flow patterns. The balance between heat transported along the boundary layers and that rising through the bulk fluid due to unstable convection at the bottom of the vessel is unknown.

4.4.6 Boundary layer temperature profiles

An introduction to the velocity and temperature profiles in free convection turbulent boundary layers is given in section 2.4. Equations developed to describe the profile of velocity and temperature change with increasing distance from the wall are commonly known as wall functions and are used with numerical modelling as a means of avoiding the need to resolve the boundary layer or when the turbulence model chosen has equations that cannot be otherwise closed at the boundary. A selection of wall function equations is used in this section to predict the temperature profile of a free convective boundary layer forming on a vertical plate in an infinite, quiescent fluid. The equations give the results in non-dimensional form, but they have been converted to dimensional form below for comparison with actual data. The models used are described in section 2.4.2.2, with further commentary on calculated inputs used below. The boundary conditions used were that of test 19 (water, 96% fill): a heat flux of 115 kW/m^2, a wall temperature of 107°C and a bulk liquid temperature of 20°C. When a characteristic length, x, was required it was taken to be one quarter of the circumference. Selected temperature measurements at 240 seconds are shown in Figure 68 for comparison.

Eckert & Jackson (1950)

The thermal boundary layer thickness was taken at 5.6 mm, from the Eckert & Jackson prediction described in section 4.4.5 above. The temperature profile is based on a power law as given by equation 2.12.

George & Capp (1978), using constants calculated by Versteegh & Nieuwstadt (1999)

The thermal boundary layer thickness was taken as 3.2 mm, from the Tsuji and Nagano (1989) prediction described in section 4.4.5 above. The temperature profile is based on a power law as given by equation 2.16.

Hölling and Herwig (2005)

The temperature gradient at the wall was taken as 176,000 K.m^{-1}, based on the definition proposed by Hölling and Herwig of:

$$\left.\frac{dT}{dy}\right|_w = \frac{q_w}{\alpha \rho c_p} \tag{4.4}$$

The turbulent Prandtl number was assumed to be constant at 0.9, as per Hölling and Herwig. The temperature profile is based on a logarithmic law as shown in Figure 9.

Kiš and Herwig (2012)

The temperature profile given by Kiš and Herwig is calculated below using the temperature gradient at the wall as proposed by Hölling and Herwig above.

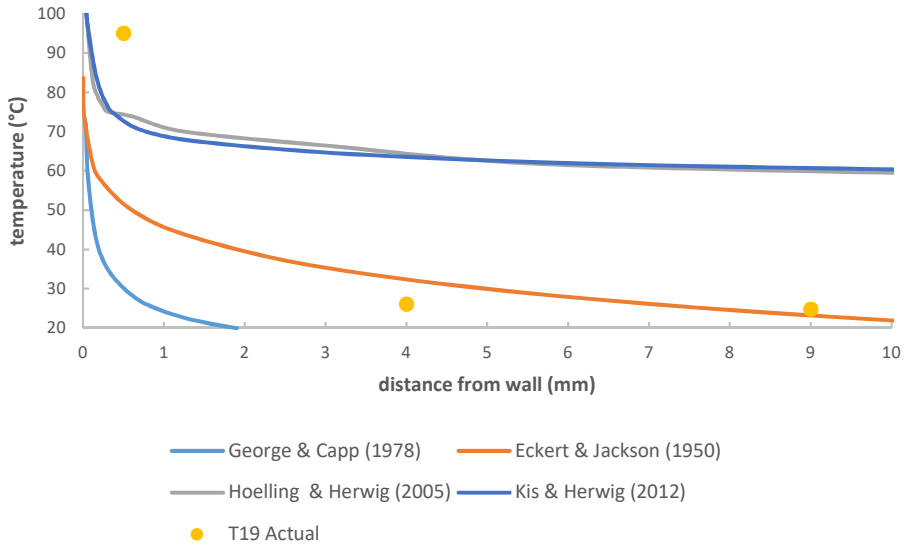

Figure 68 – Predicted thermal boundary layer profiles at mid-height (90°) for test 19 (water, 96% fill, 115 kW/m^2)

Note that the 0.5 mm reading was in contact with the vessel wall, and hence does not reflect the true fluid temperature at that distance.

The same calculations were undertaken for test 10 (ethanol, 50%) with boundary conditions set at a wall temperature of 85°C, a bulk fluid temperature of 30°C, and a heat flux of 85 kW/m^2. The wall temperature

gradient required for the Hölling & Herwig and Kiš and Herwig models was taken to be 496,000 $m.K^{-1}$, calculated using the method proposed by Hölling and Herwig above.

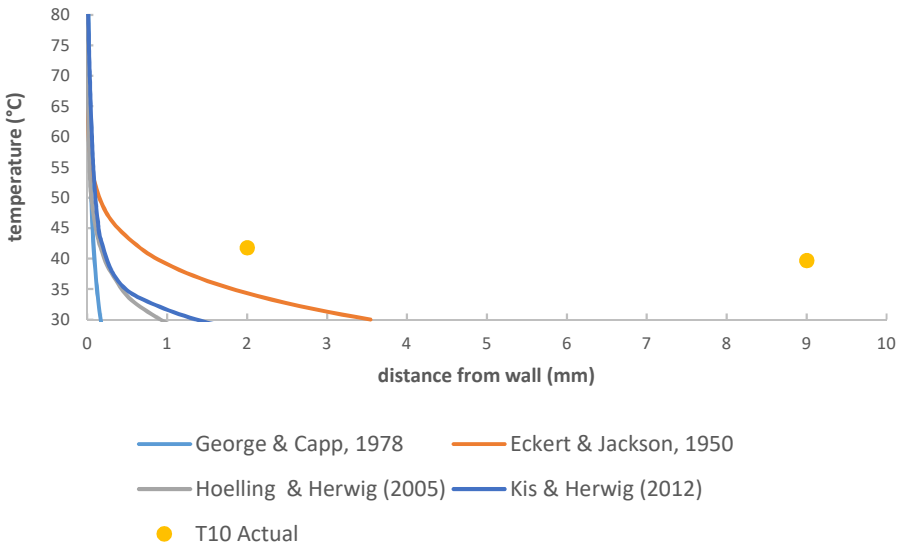

Figure 69 – Predicted thermal boundary layer profiles at mid-height (90°) for test 10 (ethanol, 50% fill, 84 kW/m²)

The predictions do not show a good fit with the test data. On the basis of water results alone, the model of Eckert and Jackson (1950) appears to give a reasonable fit, however application of the model to the ethanol test shows a large deviation. None of the other models gave reasonable predictions. Those of Hölling & Herwig (2005) and Kiš and Herwig (2012) are extremely sensitive to the wall temperature gradient, and inaccuracies here can cause the results to be clearly anomalous. The predictions from the George & Capp (1976) model gave much steeper temperature profiles than measured. However, the predictions given in Figure 68 and Figure 69 were expected to underestimate the boundary layer thickness observed in an actual pressure vessel geometry, given the previously discussed buoyancy effects acting to increase the boundary layer thickness below the mid-height of the vessel.

4.4.7 PIV results

4.4.7.1 Results overview

Analysis of the particle imaging velocimetry (PIV) results obtained in season two tests is reported in this section. PIV cameras were present in all season two tests, however the nature of the experimental set-up made fine-tuning the laser sheet position and camera focus in-situ difficult and hence numerous videos from season two were consequently judged to be unsuitable for PIV analysis. For ease of reference, information relevant to the PIV studies is summarised in Table 27.

Table 27 - Summary of tests suitable for PIV analysis

Test number	Local heat flux (kW/m^2)	Notes	Light sheet angle	Water fill level	Fly camera	Refresh rate	Times captured (1s unless stated)
15	96		135°	0.68m (72%)	Fly 1	10 Hz	60, 78, 122, 150, 253
16	81		135°	0.68m (72%)	Fly 1	10 Hz	82, 94, 130, 151, 217, 279, 293, 448, 457
					Fly 2	10 Hz	69, 111, 121, 175, 235
18	61	Water reused – poor clarity	90°	0.58 (60%)	Fly 1	10 Hz	14, 32, 57
19	90		90°	0.92 (96%)	Fly 1	10 Hz	15, 33, 50, 70, 85, 106, 138, 183, 194, 230, 249, 302
					Fly 2	5 Hz	Full duration
22	67	Water degassed	90°	0.6m (62%)	Fly 1	10 Hz	67, 101, 139, 172, 218, 282

PIV data is typically analysed through division of the image into interrogation areas and comparison of these areas across two successive frames to find the displacement that gives the best correlation between images. This displacement relates to a velocity vector. Analysis of all images was done using DynamicStudio from Dantech Dynamics. The software was made available courtesy of l'Ecole des Mines, Alès, France. The adaptive PIV algorithm was used and the interrogation area set to 16 x 16 pixels giving a resolution of 5.0 mm and 5.9 mm per pixel for tests 15-18 and 19-22, respectively, determined from image analysis as described in appendix 3. This interrogation area matched closely the maximum face size of the mesh used in section 5 (see Table 39, coarse grid maximum of 5.66 mm). An interrogation area of 32 x 32 was also tried but is not reported as this coarser resolution was a step away from mesh size used in section 5 and also offered no notable

improvement over 16 x 16 pixels in terms of vector stability and consistency. The interrogation overlap areas was set to 25% and the number of refinement steps set to three.

The dynamic studio software allows for additional analysis following calculation of the velocity vectors.

The position of the vessel surface was identified at the start of each test as the centre of the light arc on the vessel wall. The error involved in the estimation is considered negligible compared to the limitations imposed by the resolution of the PIV analysis. The following were generated to assist analysis of the data generated in season two:

- Image mean – an average of all the images taken during a 1 second period
- Vector plot – a 2D plot of velocity vectors (where arrow length is proportional to velocity)
- Profile plots – vector results along user set path lines
- Histogram – an analysis of the distribution of total velocity vectors
- Streamlines – an image displaying lines tangential to the direction of flow, highlighting eddies and changes in flow direction

During each test the laser sheet scatter at the wall grew significantly, as shown in Figure 70. This is attributed to bubbles in both the bulk fluid and at the wall. Consequently, the velocity data is lost in a growing region during the test and plots of the velocity as a function of distance from the wall can show zero values for the region closest to the wall as time progresses. This does not reflect the actual velocities in this region. Recommendations for modifications to the test set-up to reduce light scatter effects are given in section 7.2.

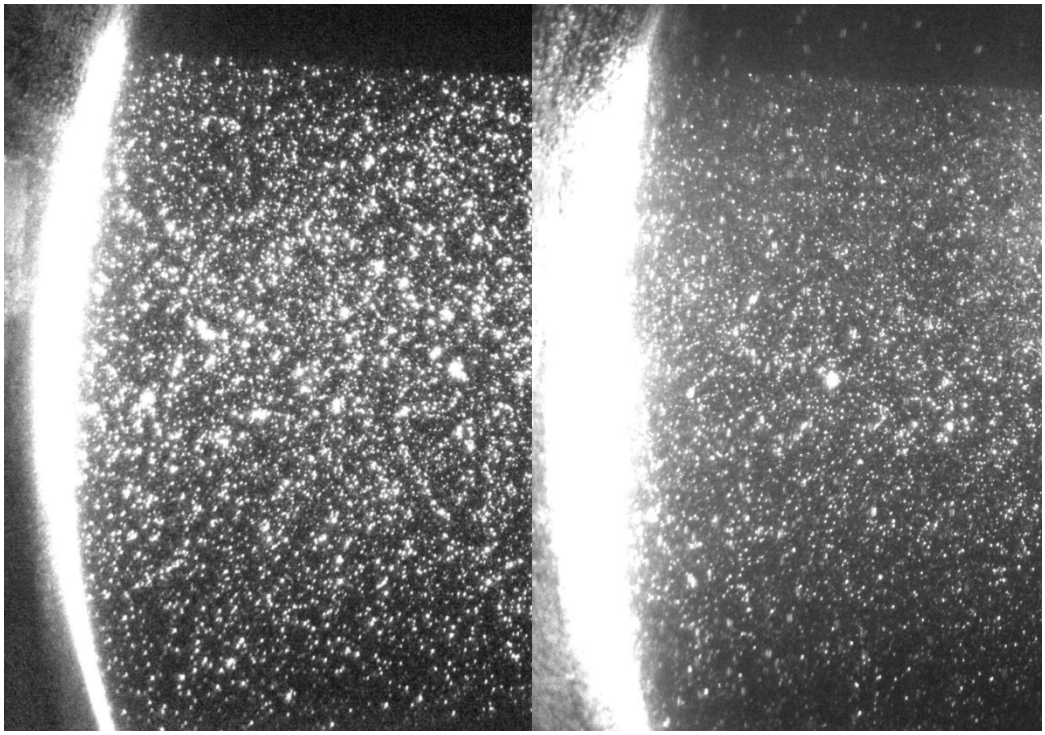

Figure 70 – Showing light scatter growth during a test, test 19 (water 96% fill). Left: 9 s, Right: 249 s

Analysis of the PIV data was further complicated by the presence of bubbles. The analysis software struggled to separate bubbles from seeding particles. Analysis of the bubble characteristics from images (described further in section 4.6.1) shows a bubble rise rate of 90 mm/s was typical. However, bubbles outside the light-plane also appeared in the videos, due to scattering of light. Depending on the distance of the bubble from the camera the rise velocity could appear substantially different, with bubbles in-front of the light plane appearing to rise faster and resulting in a small number of anomalously high velocity vector readings. Recommendations for modifications to the test set-up to reduce bubble influence are given in section 7.2.

The PIV results were taken at either 90° or 135° from the top, at position A in Figure 33 (a plane approximately 800 mm from the glass window). Results were analysed to give an image mean, streamlines, a vector plot, and a histogram of total velocities for tests in which good quality results were obtained.

Figure 72 to Figure 87 give the PIV results at selected times showing the boundary layer at maximum size and highlighting changes over time. All figures include a scale and a green line indicating the position of the wall.

4.4.7.2 Test 15

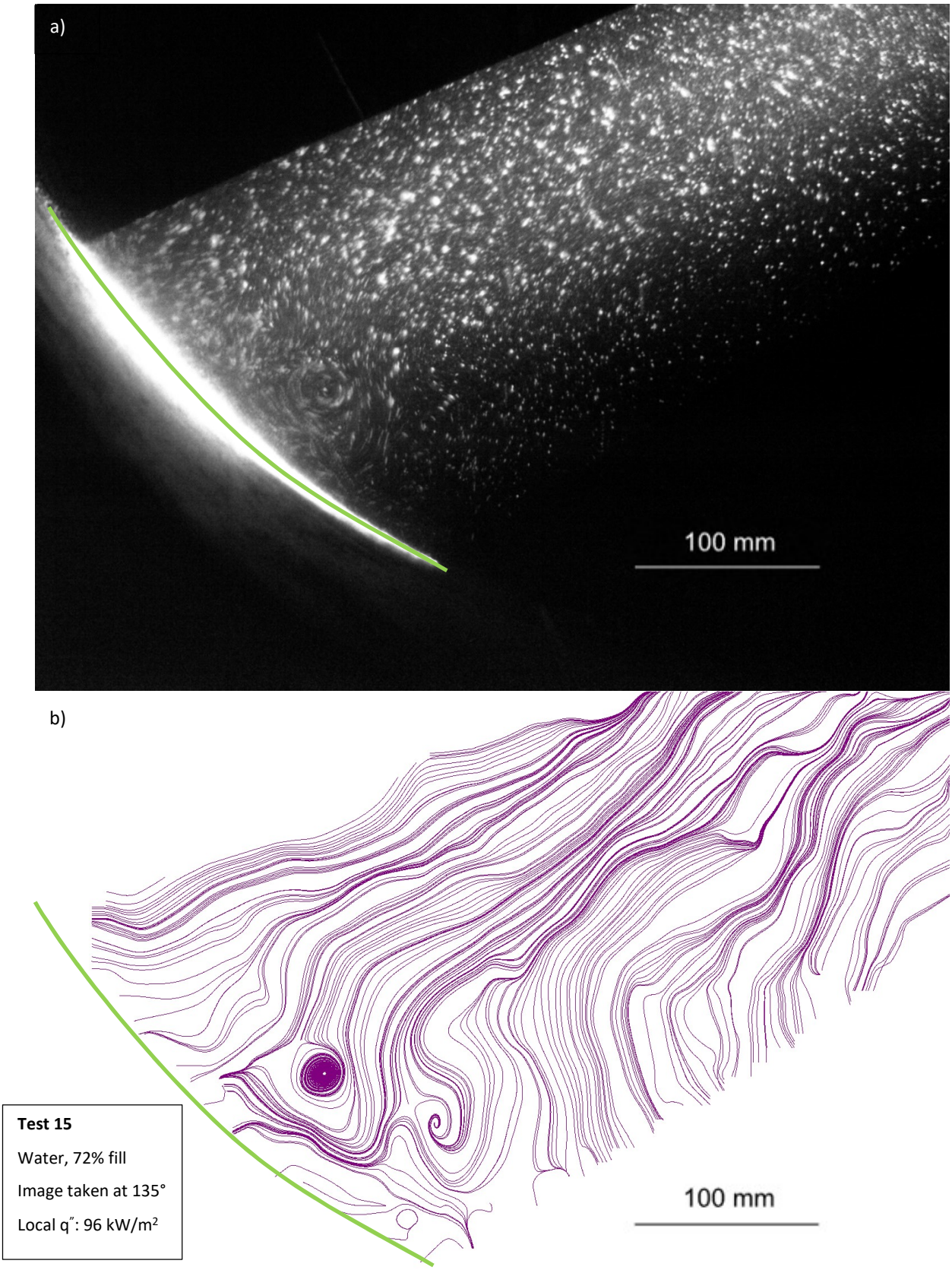

Figure 71 – Test 15, 60 seconds, a) image mean, b) streamlines

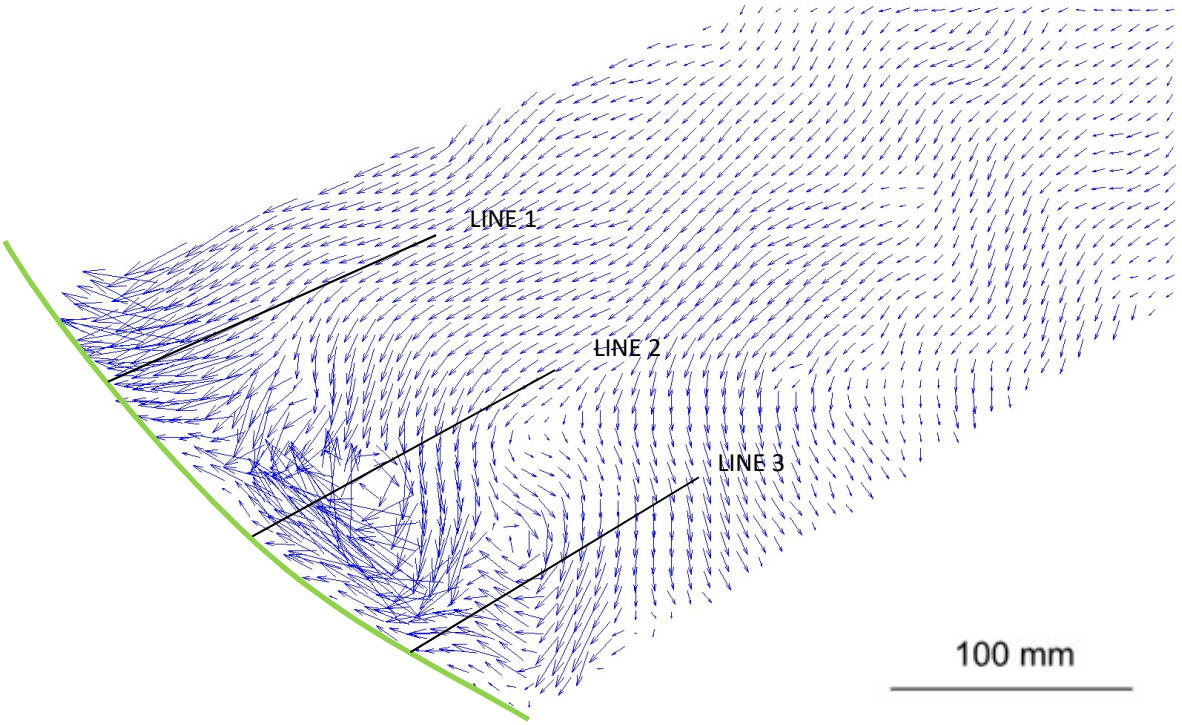

Figure 72 – Test 15, 60 seconds, vector plot showing profile plot line positions

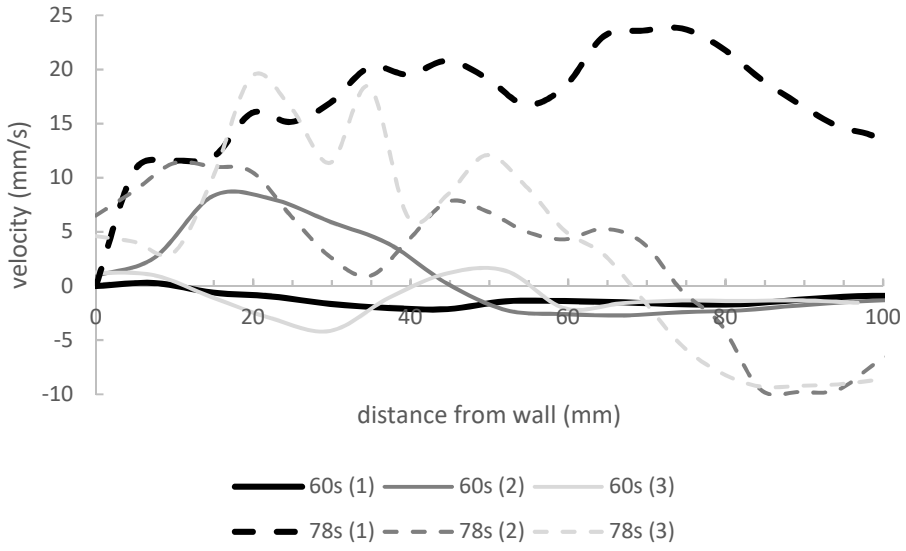

Figure 73 – Y-velocities along profile plot lines (1),(2),(3)

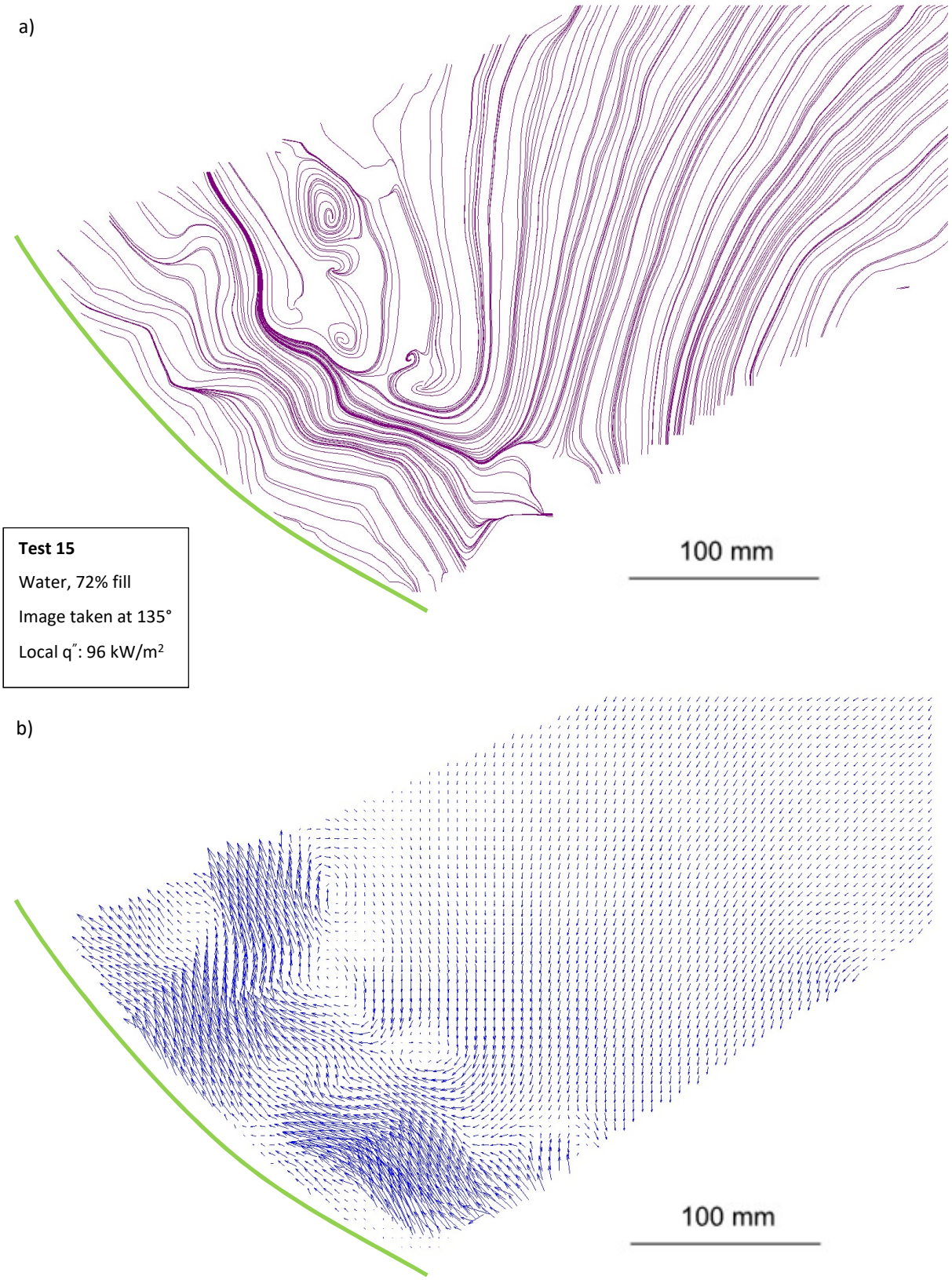

Figure 74 – Test 15, 78 seconds, a) streamlines, b) vector plot

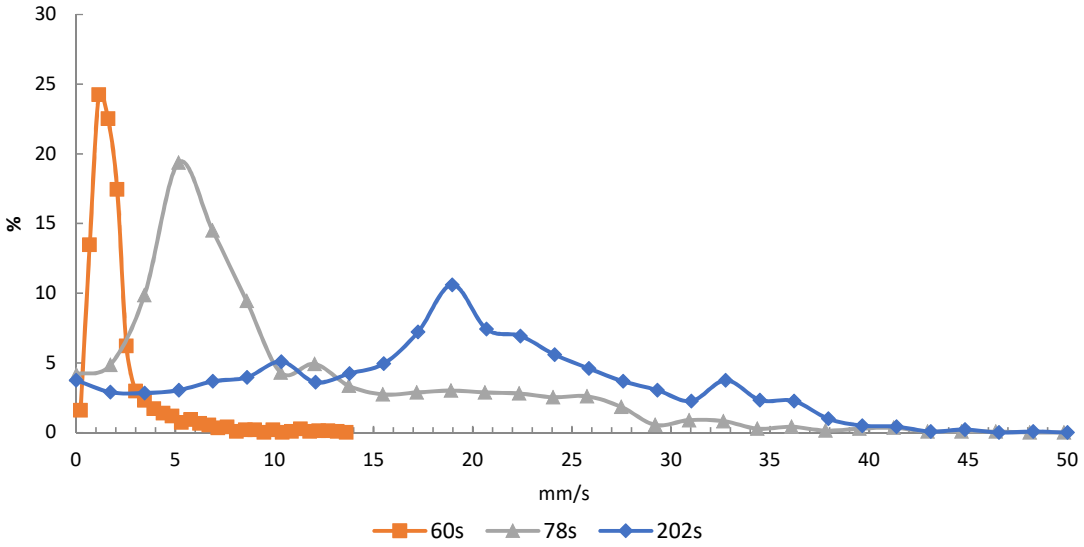

Figure 75 – Test 15, histogram of overall velocity values at selected times

4.4.7.3 Test 16

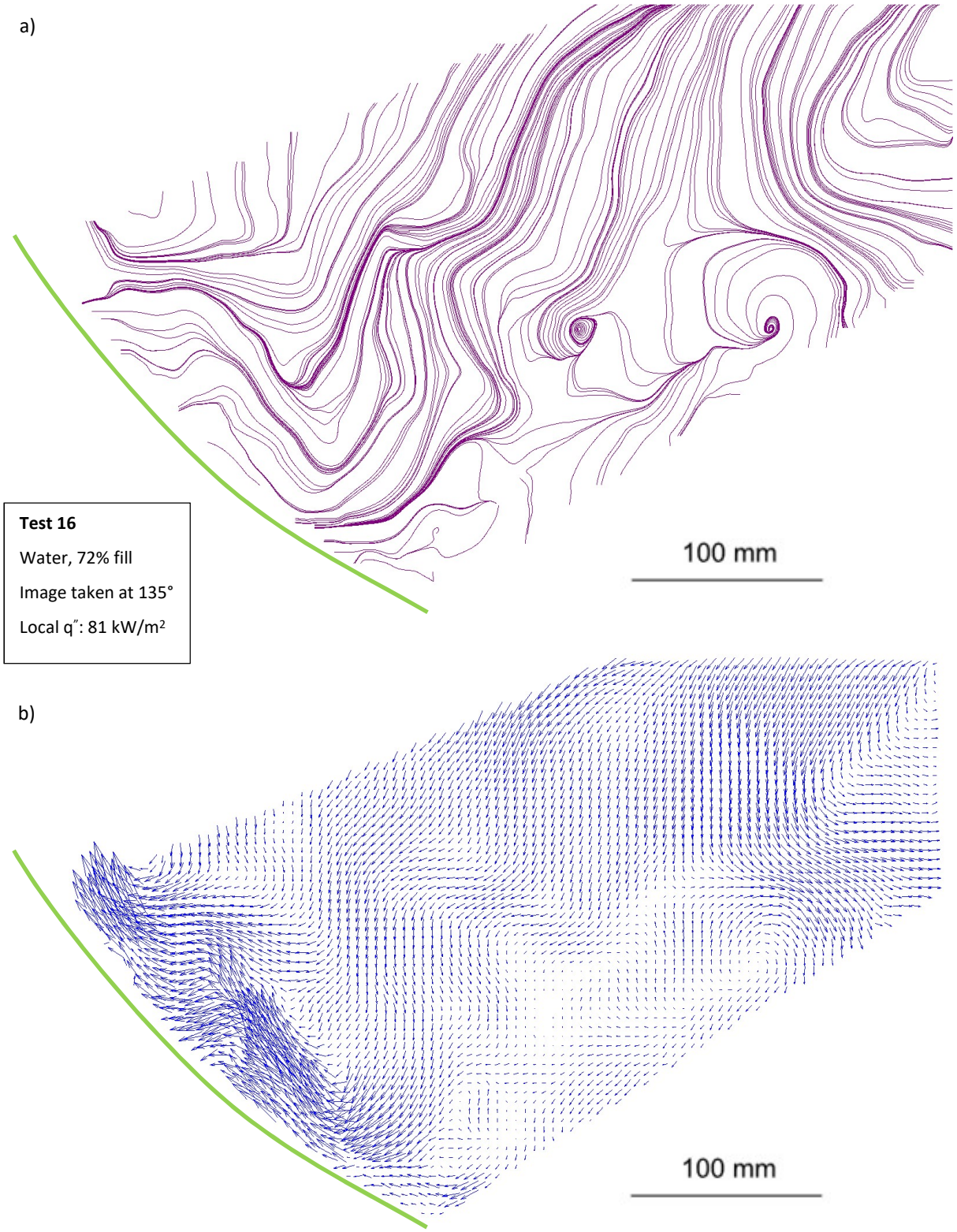

Figure 76 – Test 16, 54 seconds, a) streamlines, b) vector plot

4.4.7.4 Discussion of results at 135°

The PIV results from test 15 show the flow behaviour in a region where the buoyancy is acting at approximately 45° to a tangent of the vessel wall. Figure 71 and Figure 74 show the stream lines at 60 and 78 seconds. These images (supported by observations throughout tests 15 and 16) show the flow varied substantially with time, indicating it is unsteady. Boundary layer detachment and eddy formation can be seen in the image means, streamlines and vector plots above, however eddy formation is intermittent and the thickness of the warm boundary layer increases between detachment and eddy formation. The travel direction of the eddy centre is generally in the direction of the boundary layer flow when the eddy is within 100 mm of the vessel wall (i.e., within the warm layer previously described). Eddies outside the warm layer, having moved into the bulk fluid, predominantly rotate in the direction expected from the flow, however, some counter-rotating eddies were observed, highlighting the unstable and varying nature of the flow beyond the boundary layer.

Figure 75 shows that after 60 seconds the generally quiescent fluid (indicated by a large proportion of small velocities (<3 mm/s) starts to show an increase in the maximum velocity values observed and a greater spread. This is indicative of a greater spread in the bulk liquid velocities, and an increasingly thick warm layer with a range of flow rates.

At 60 seconds into test 15 the maximum velocity was in the region of 5-10 mm/s, occurring at 10-20 mm from the wall. Analysis of video clips indicate that this is near the edge of the velocity boundary layer, in the region where small eddies are forming. As the test progresses, the number of bubbles visible starts to increase substantially. The histograms of velocities (Figure 75) show a small quantity of velocities up to 50 mm/s. These are likely to be attributable to the influence of bubbles being included in the algorithm calculations, however the effect cannot be readily quantified.

In test 15 many bubbles were observed after approximately 80 seconds. This increased light scatter, as previously discussed, and made the results less reliable. At 60 seconds the boundary layer thickness can be approximated as 10 mm thick based on y-velocity data and supported by video observations. Peak Y-velocity readings of 40-50 mm occur in locations coincident with an eddy.

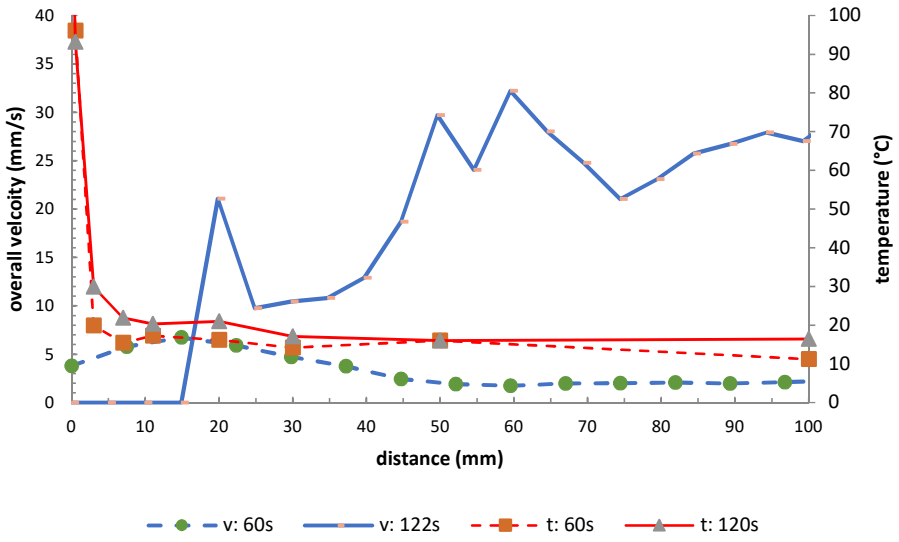

Figure 77 – Velocity and temperature profiles, test 15

Figure 77 shows the measured velocity and temperature profiles overlaid at the position of profile plot line 1, located as shown in Figure 72. The overall velocity maximum at approximately 15 mm coincides with a local, small temperature peak. Video observation and the PIV data support the conclusion that these frequently observed peaks are due to the presence of boundary layer detachment and eddy formation.

The results of test 16 support the analysis given for test 15 above. In summary, the fluid behaviour inside the vessel at 135° can be characterised as having a very thin thermal boundary layer, extending less than 5 mm from the wall. The velocity boundary layer is thicker, but is unstable in this region. Frequent detachment and eddies can be observed. The detached boundary flow creates a warm layer approximately 20-30 mm thick, with local variations in flow velocities in this region. After 120 seconds the warm region is less well defined, as the flow has become more unstable, driven primarily by boiling effects.

The light scatter at the wall makes it impossible to accurately resolve the velocities within the first 5 mm from the season two data. On the basis of well-established boundary layer theory, it can be assumed that the maximum velocity in the boundary layer lies within this unresolved region. The bulk flow velocity in the region 100-300 mm from the wall can be assumed to be approximately 20 mm/s after 120 seconds on the basis of the histogram plots, supported by the profile plots and vector images.

4.4.7.5 Test 18

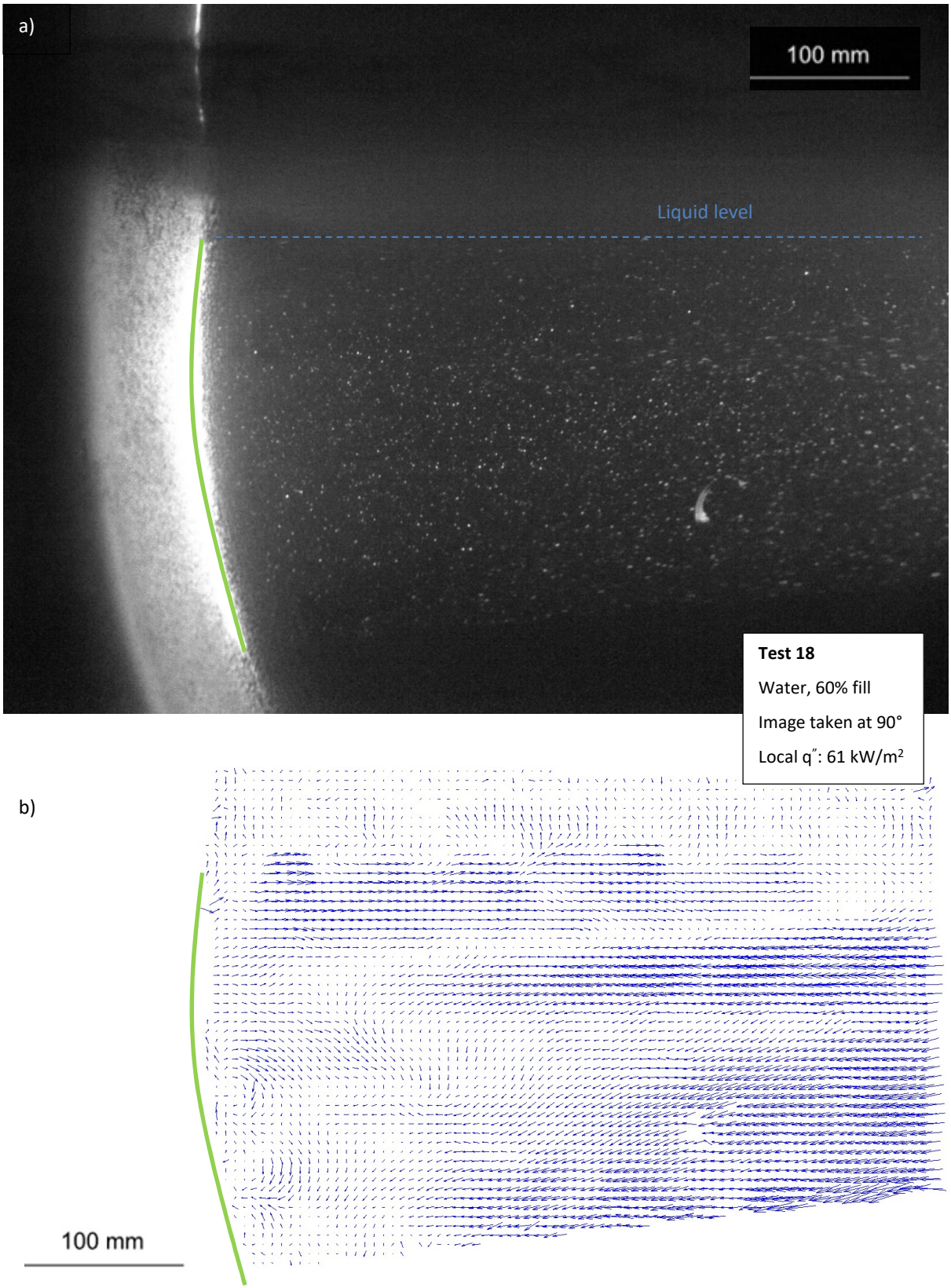

Figure 78 – Test 18, 14 seconds, a) image mean, b) vector plot

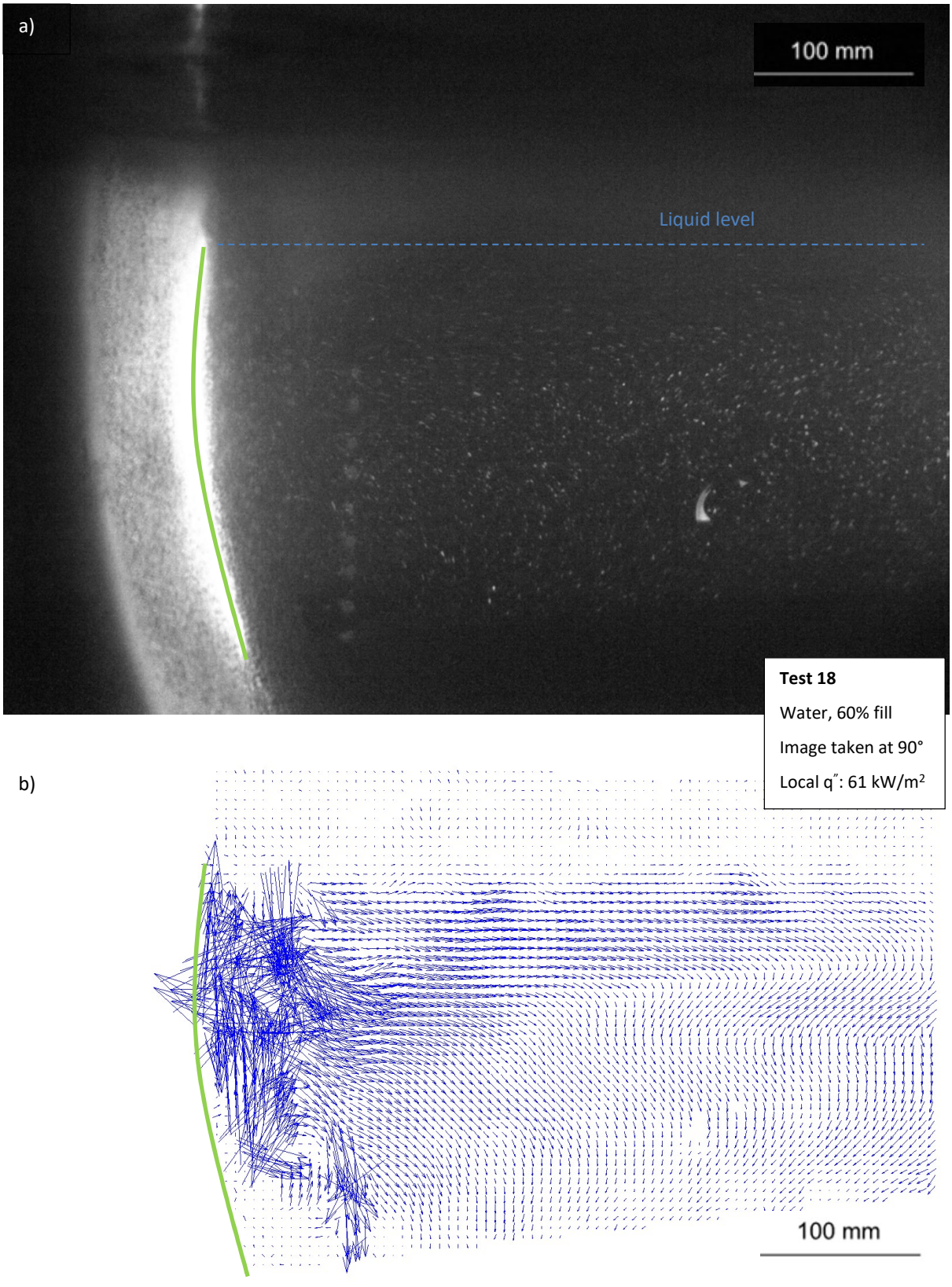

Figure 79 – Test 18, 32 seconds, a) image mean, b) vector plot

4.4.7.6 Test 19

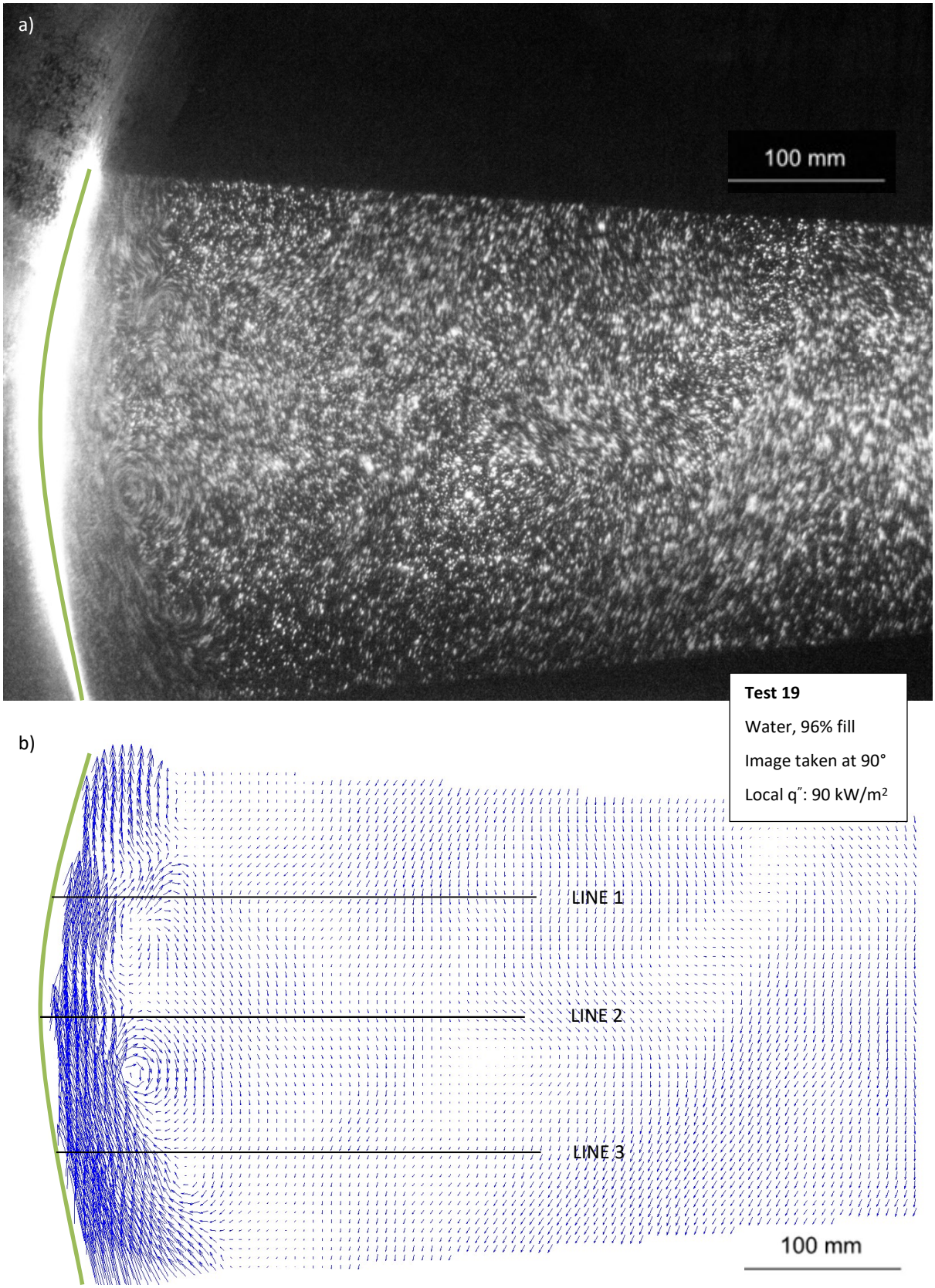

Figure 80 – Test 19, 33 seconds, a) image mean, b) vector plot

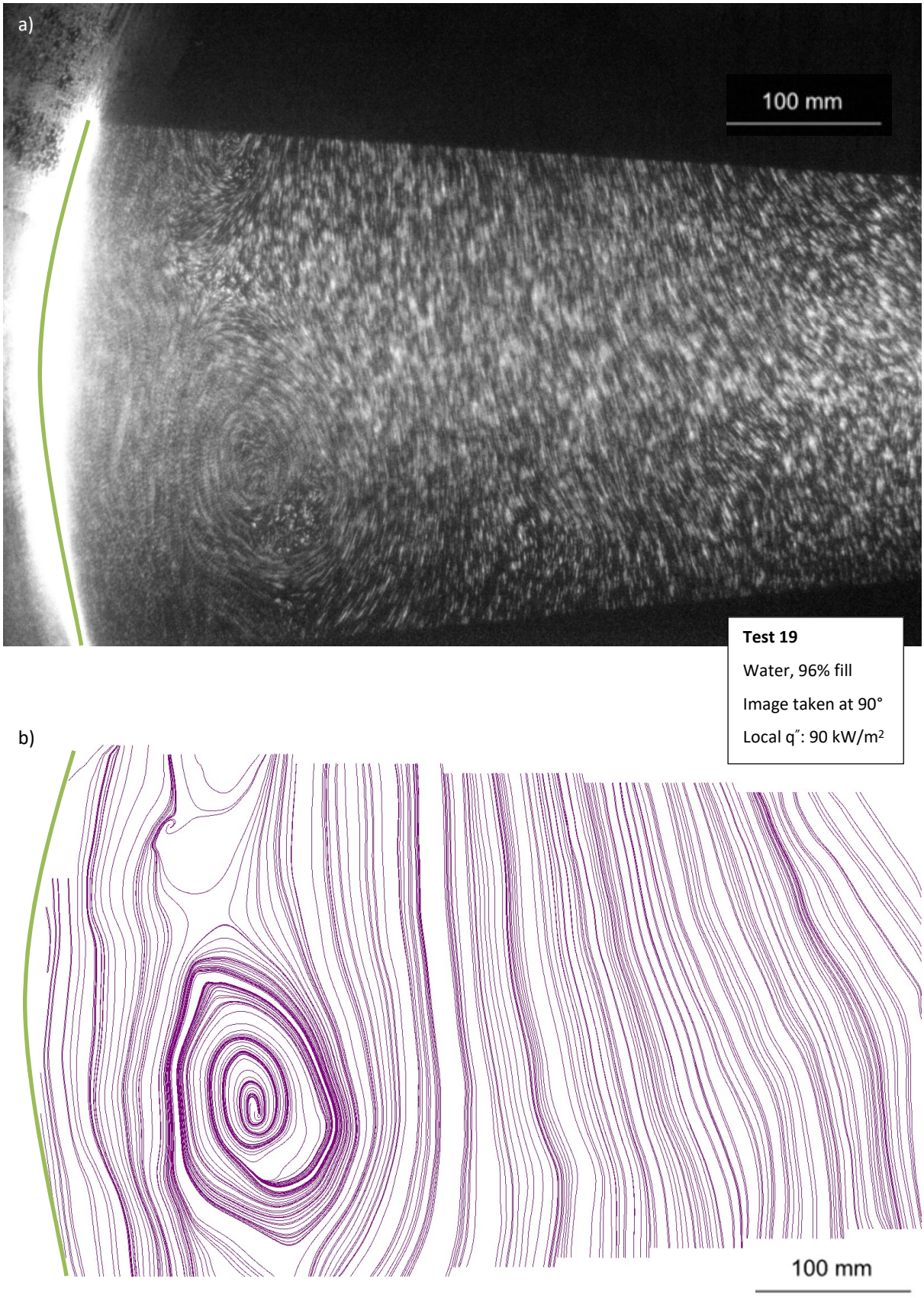

Figure 81 – Test 19, 50 seconds, a) image mean, b) streamlines

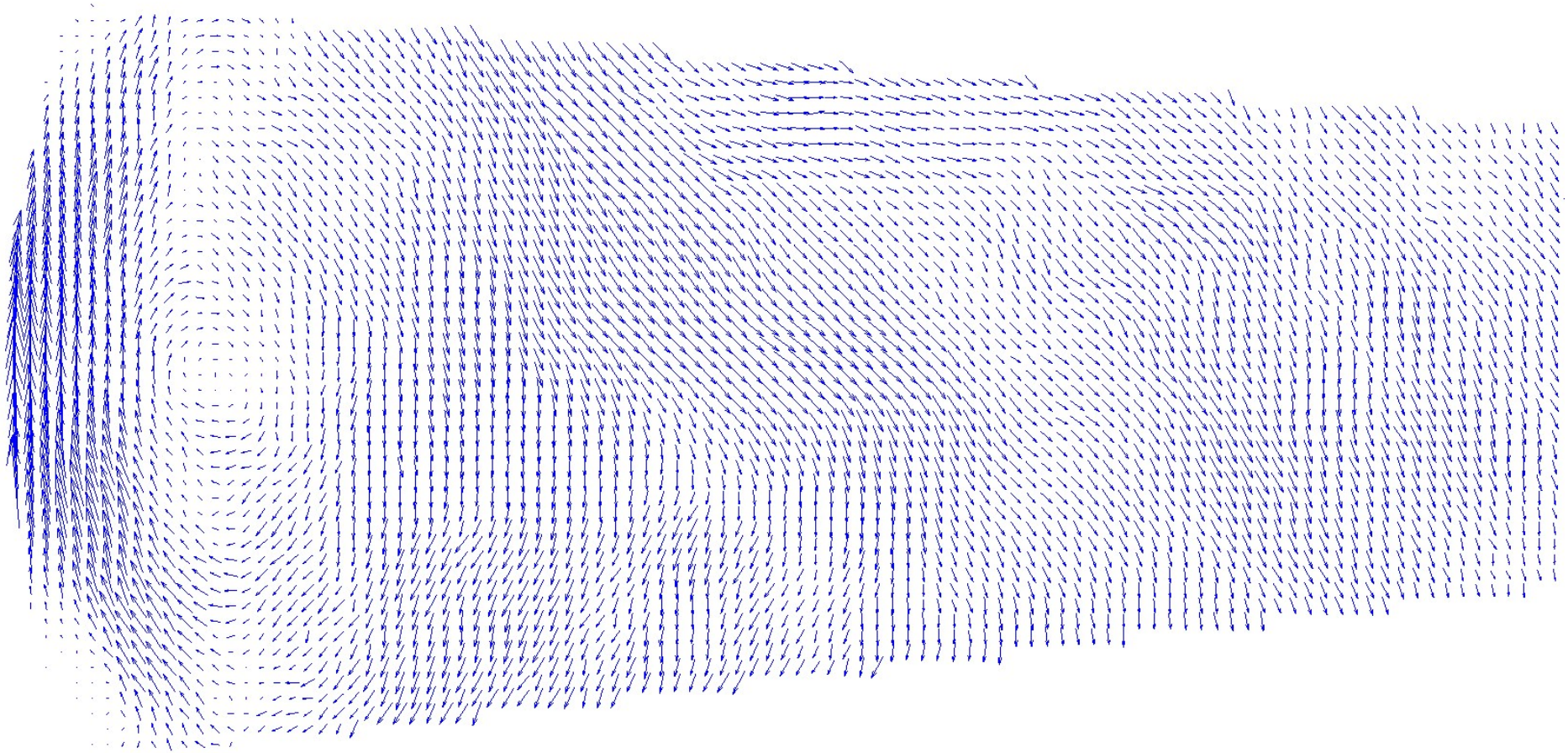

Figure 82 – Test 19, vector plot of average across 0-200 seconds

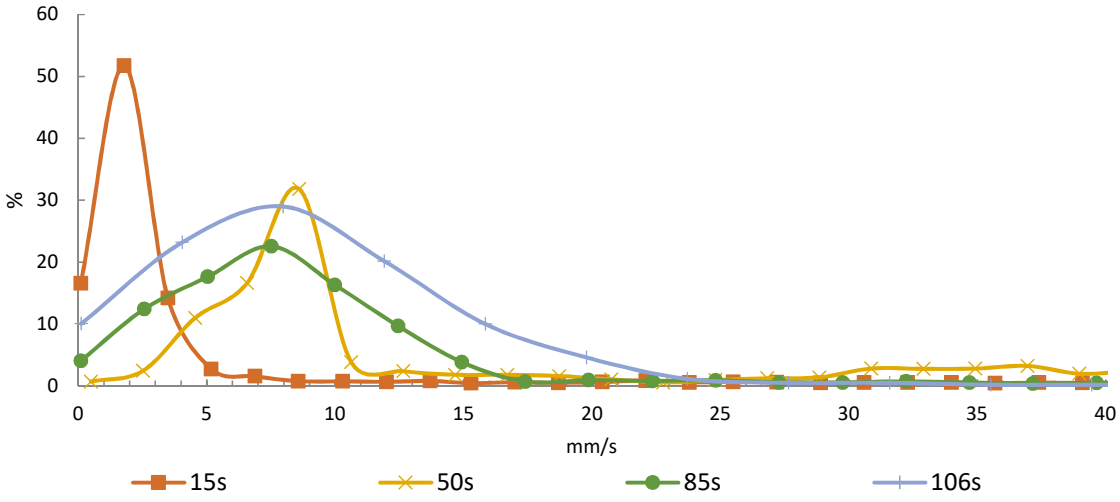

Figure 83 – Test 19, histogram of velocity measurements

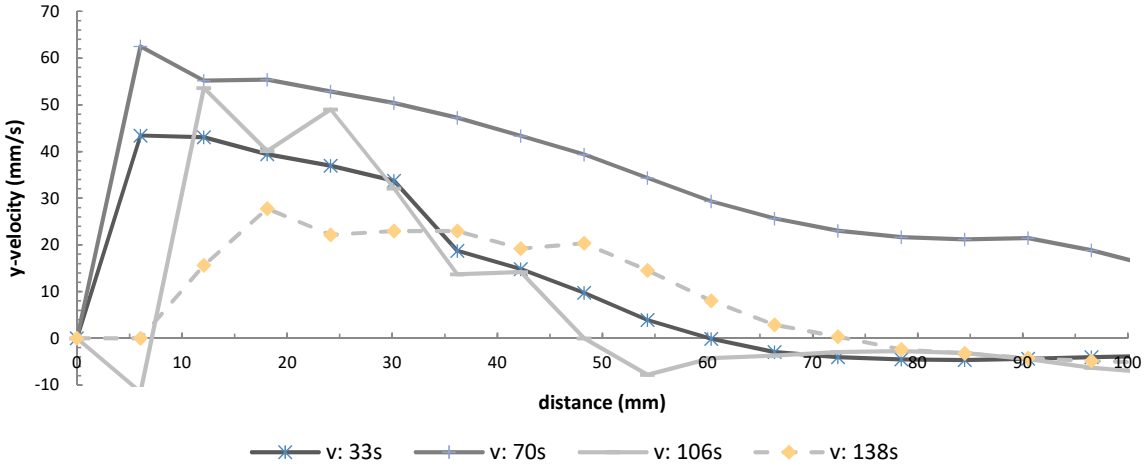

Figure 84 – Y-velocity variation with distance from wall, test 19 (water, 96% fill, line 2)

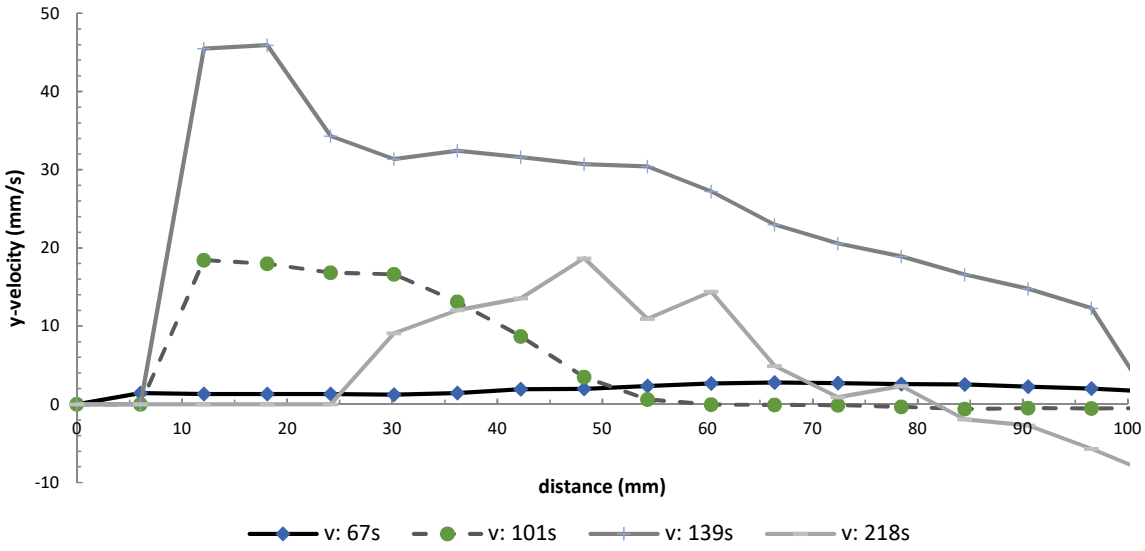

Figure 85 – Y-velocity variation with distance from wall, test 22 (water, 62% fill, line 2)

4.4.7.7 Test 22

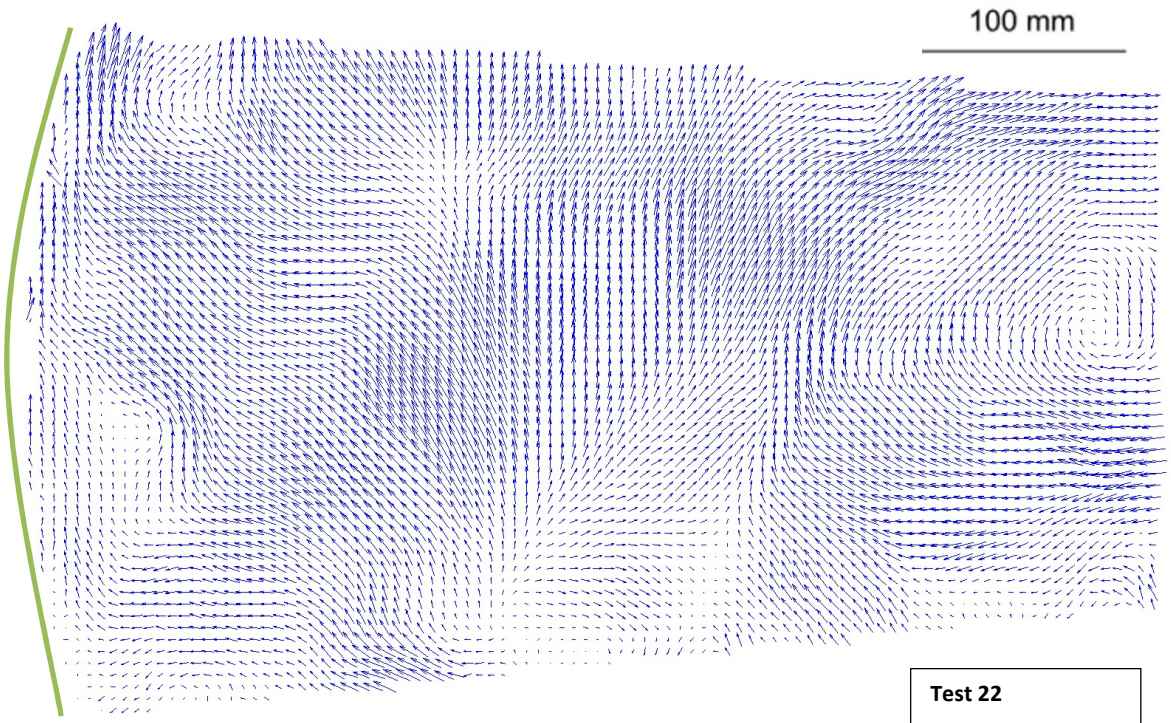

Figure 86 – Test 22, 67 seconds, vector plot

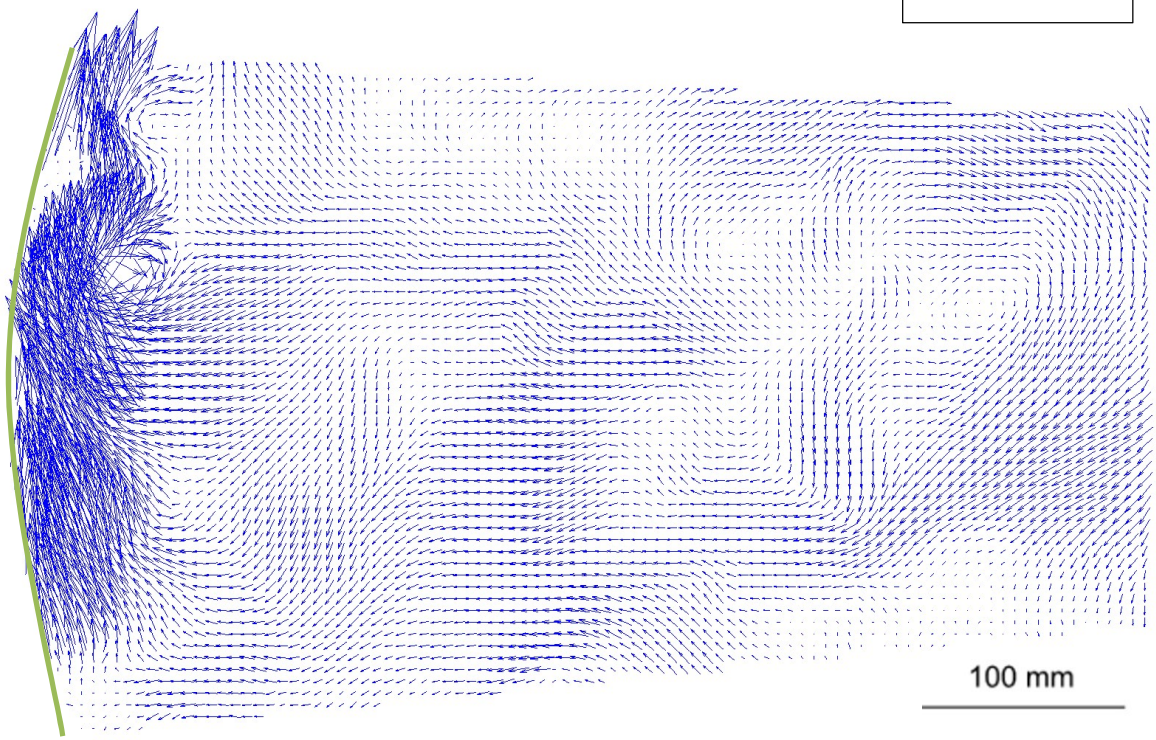

Figure 87 – Test 22, 101 seconds, vector plot

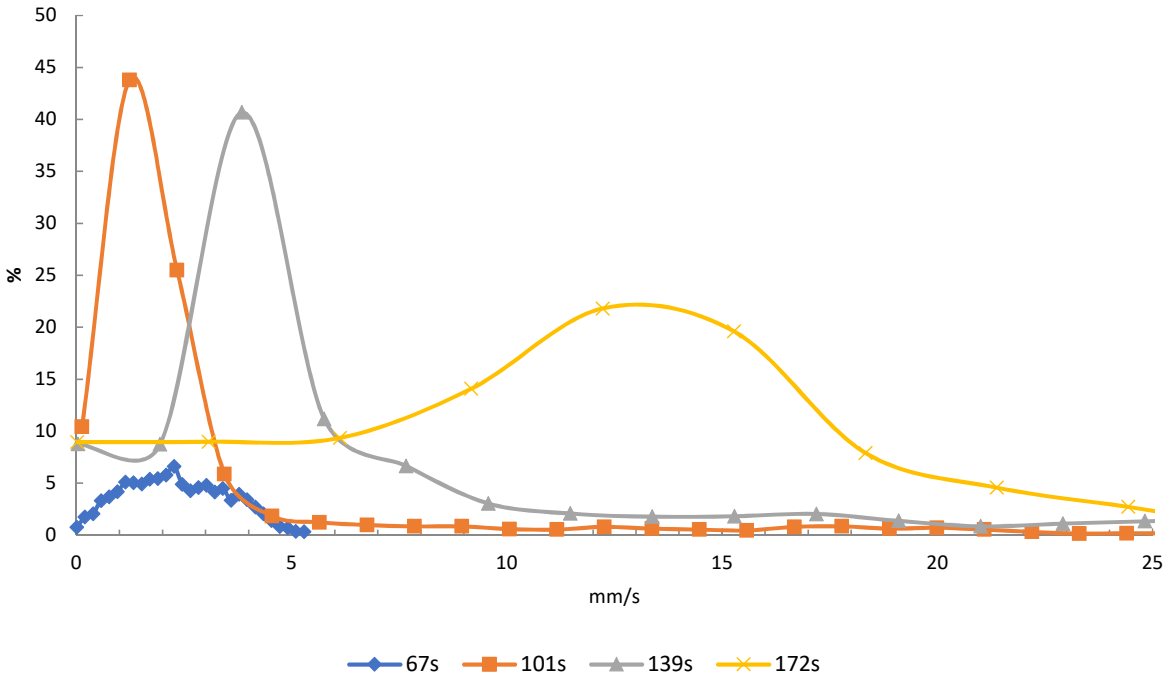

Figure 88 – Test 22 -histogram of velocity measurements

4.4.7.8 Discussion of results at 90°

The PIV camera used for test 18 analysis was positioned to include the liquid surface. During the test the motion of the surface and reflection meant the exact position was difficult to determine, however the flow just beneath the surface can be observed in Figure 78 and Figure 79. The results confirm that the liquid phase flows away from the vessel wall towards the middle. The flow is approximately 100 mm deep, however it thins as it approaches the middle of the tank as the cooler liquid at the bottom mixes with cooler bulk fluid beneath. At 14 seconds a counter-flow can be seen back towards the wall, however by 32 seconds this counter flow has gone, replaced by a gentle flow in the general downward direction.

Tests 19 and 22 were undertaken with the flow captured at vessel mid-height. Figure 82 shows a time-averaged vector plot of the first 200 seconds of test 19 (water, 96% fill, captured at 5 Hz), giving a good representation of the general nature of the flow. At 90° a velocity boundary layer is clearly visible in the region of the wall. On conventional video seeding particles can be observed to flow parallel with a tangent to the wall at the closest point. An estimate of the velocity in this region is 50-70 mm/s, as can be seen in Figure 84. Test 22 recorded a maximum of 40-50 mm/s, however the light scatter was greater in this test, which probably prevented higher values from being observed.

Tests 19 and 22 show a positive y-velocity value (upwards flow) to a distance of typically 50-100 mm from the wall. In some instances, the upwards flow can extend to 150 mm. At 90° the flow does not completely detach in a way observed

in test 15 (at 135°). Instead eddies typically form at the edge of the boundary layer, where the distance from the wall at which the y-velocity turns negative. The number of eddies observed at any one time within the illuminated zone at 90° was typically one, although on occasion two or three were also observed. Video evidence and the PIV analysis supports an anecdotal conclusion that the eddies observed at the vessel mid-height are bigger but less frequent (at 135° two or three eddies are typical).

The y-velocity plots show that the maximum overall velocity increases until approximately 180 to 240 seconds into the test, after which it decreases. Video analysis indicates that this is due to a deterioration in the quality of the data captured due to increased boiling effects resulting in further light scatter. It is not representative of an actual decrease in fluid velocities. The y-velocities usually show a peak value at approximately 60 to 150 seconds, after which the increasingly irregular flow has higher overall velocities but occurring in a less predictable manner and thereby showing significant variability in the y-velocities.

The time-averaged velocity vectors of test 19 (over 0-200 seconds) provide a more stable dataset for further analysis. Every row of vectors was re-plotted by the distance from the vessel wall, and the average calculated of all velocity values at each distance. The resulting average velocity in the y-direction as a function of distance from the wall is shown in Figure 89. It indicates that the warm, buoyant region has an average thickness of approximately 100 mm. Figure 90 shows just the warm region, including the maximum value as well as the average. Varying severity of light scatter means multiple zero values are included in the average, and the maximum is considered a more realistic reflection of the temperature profile over the distance 10-50 mm from the wall. At distances below 10 mm the results are artificially low due to light scatter causing a loss of PIV measurement.

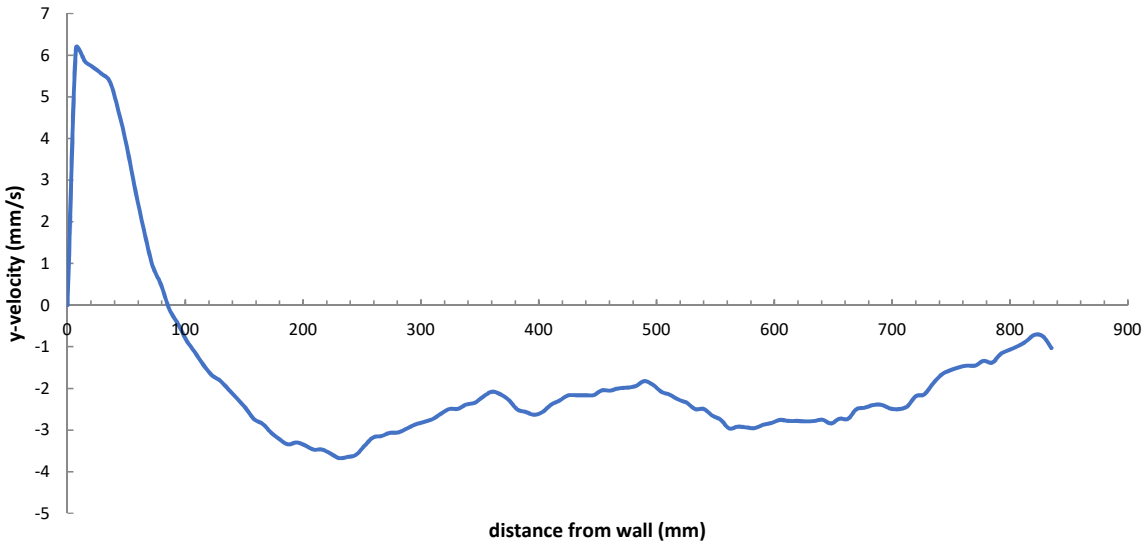

Figure 89 – Y-velocity average at 90°, test 19, (time averaged over 0-200 seconds)

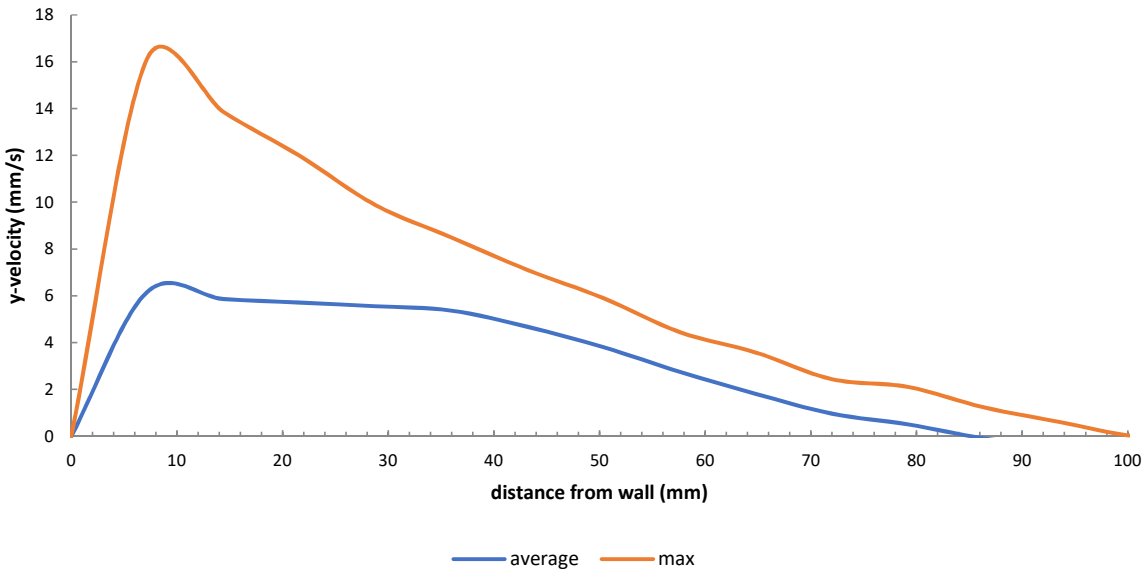

Figure 90 – Y-velocity average and maximum at 90°, test 19 (time averaged over 0-200 seconds)

4.4.7.9 Discussion of flow patterns

The two major parameters that were varied between tests were the fill level and the heat flux. A reduction in heat flux clearly delayed the occurrence of significant boiling, as evidenced by a delay in significant light scatter and less noise in the velocity vector plots further into test 22 (67 kW/m^2) than test 19 (90 kW/m^2). Beyond this difference the influence of heat flux could not be observed in the test. There was no significant difference in the maximum y-velocities or the thickness of velocity boundary layer between the two tests. This would support the hypothesis that an increase in heat flux increases the pressurisation rate via mechanisms beyond those solely attributed to the convection boundary layers. Changes in the boiling characteristics, leading to an increase in the rate of vapour generation at the wall, increased bubble interaction with the bulk fluid, increasing temperature of the vapour by radiative heating, and increased vapour release due to bubble collapse on the surface are likely to contribute to the increased rate of pressure rise to some extent.

The effect of fill level on flow patterns can be inferred through comparison of tests 18 (60), 19 (96) and 22 (62). Test 18 showed that the region where the boundary layer meets the liquid surface grows quite quickly and becomes rather chaotic, frequently producing eddies in this area. As time progresses, the region under the surface (captured in test 22) experiences incursions of local flow patterns from above, typically coming from near the middle of the tank. This can be attributed to variations in heat flow on the north and south of the tank leading to unsymmetrical behaviour. Further down from the liquid surface (captured in test 19) the bulk flow is much calmer. Local flow patterns and eddies typically come from below or from the direction of the wall. It is reasonable to assume that at high and low fill levels the reduced surface area of liquid surface will result in the warm layer at the liquid surface extending deeper into the liquid. This may, in turn, promote vapour release from the surface by promoting boiling in the region below the liquid surface and by reducing the rate of bubble condensation near the surface.

An indicative diagram of the flow within a vessel approximately 60 seconds after fire engulfment can be made by combining the temperature and PIV results with observations made throughout all tests. Figure 91 and Figure 92 show the general direction of flow and regions of temperature distributions within a vessel and at 90° and 135° in more detail. The figures are intended to be representative of a uniformly heated 1m diameter vessel filled to 60% with water. Note that the colours represent different regions of temperatures (red hottest, through orange, yellow and green, to blue coldest) however these are not indicative of specific values. The magnitude of the velocities is not shown.

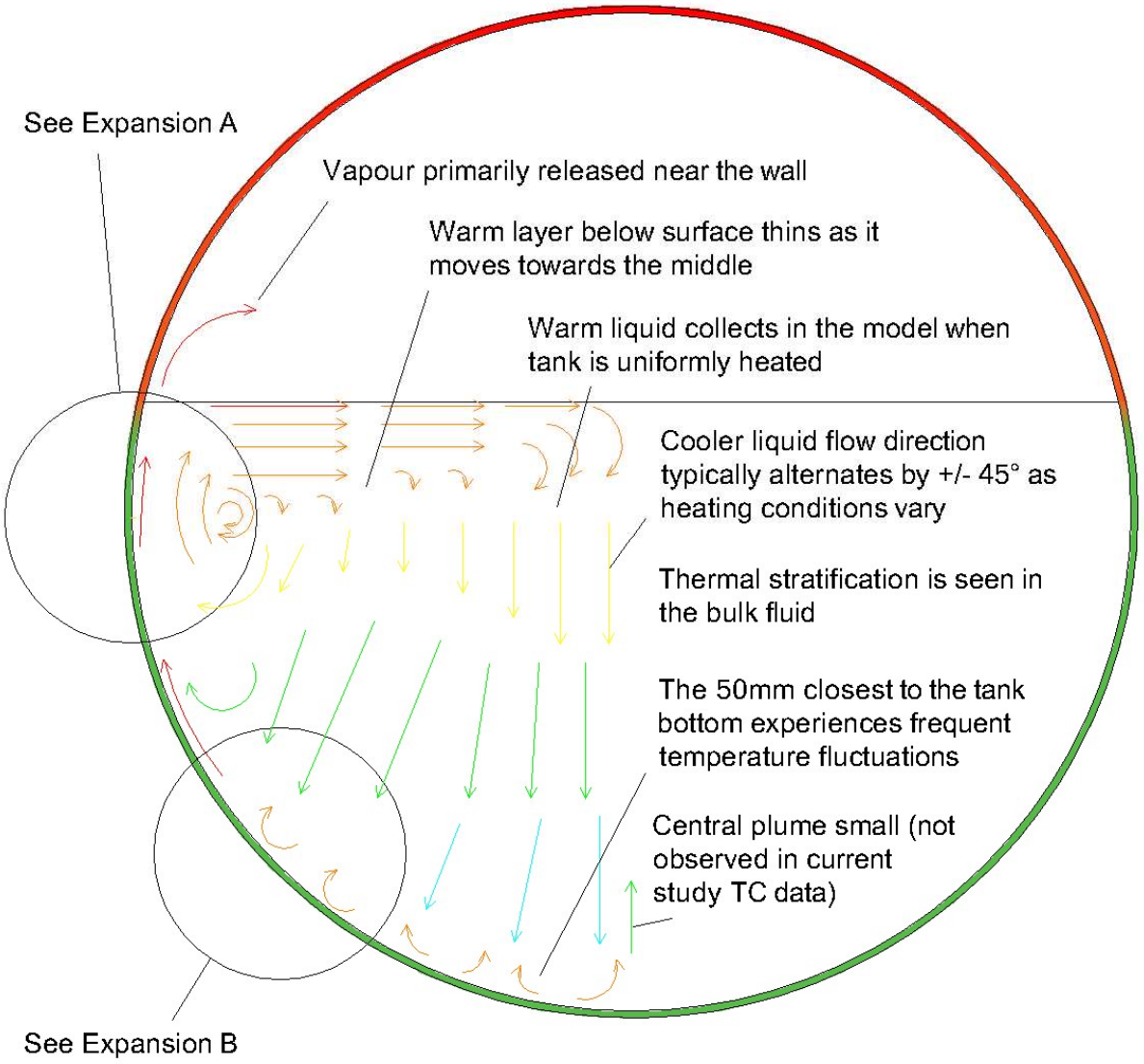

Figure 91 – Schematic diagram of flow inside 60% full vessel at 60 seconds

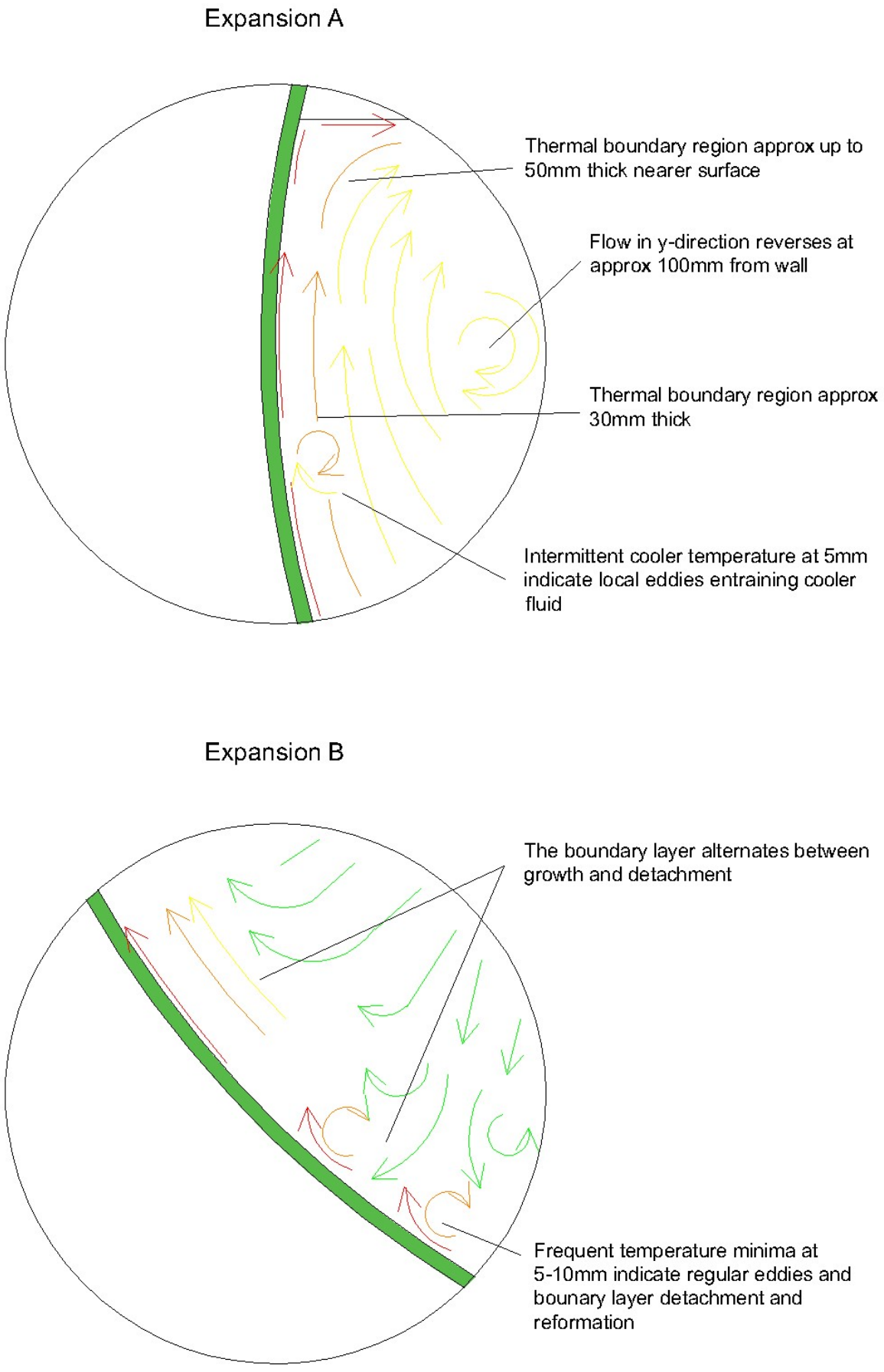

Figure 92 – Schematic diagram of flow at 90° and 135° in vessel at 60 seconds

4.4.8 Boundary layer velocity profiles

The wall function models of boundary layers described in section 4.4.6 were considered for application to the velocity boundary layer profiles. The George & Capp (1978) model is omitted as it does not provide an equation for the outer velocity boundary layer. Models by Kis & Herwig (2012) and Hölling & Herwig (2005) are not presented here because the resulting values are unphysical (orders of magnitude from what can be expected) due partly to the dependence on the velocity gradient at the wall (which is unknown as the PIV light scatter) and partly to the test 19 experimental conditions being far outside the range of Grashof numbers and dimensionless distance values (y^+) for which they are applicable. The Eckert & Jackson (1950) model, based on a modified $1/7^{th}$ power law originally proposed by Prandtl, has been used to calculate a velocity profile using a boundary layer thickness of 100 mm and a maximum velocity of 70 mm/s, based on test 19 observations described above.

An alternative model by Henkes & Hoogendorn (1990) is also given, with the required temperature gradient at the wall set to approximately 170,000 as per the method proposed by Hölling & Herwig (equation 4.4). Figure 93 overlays the velocity boundary layer profiles predicted with the test 19 measured velocity results and the time averaged 0-200 seconds maximum velocity.

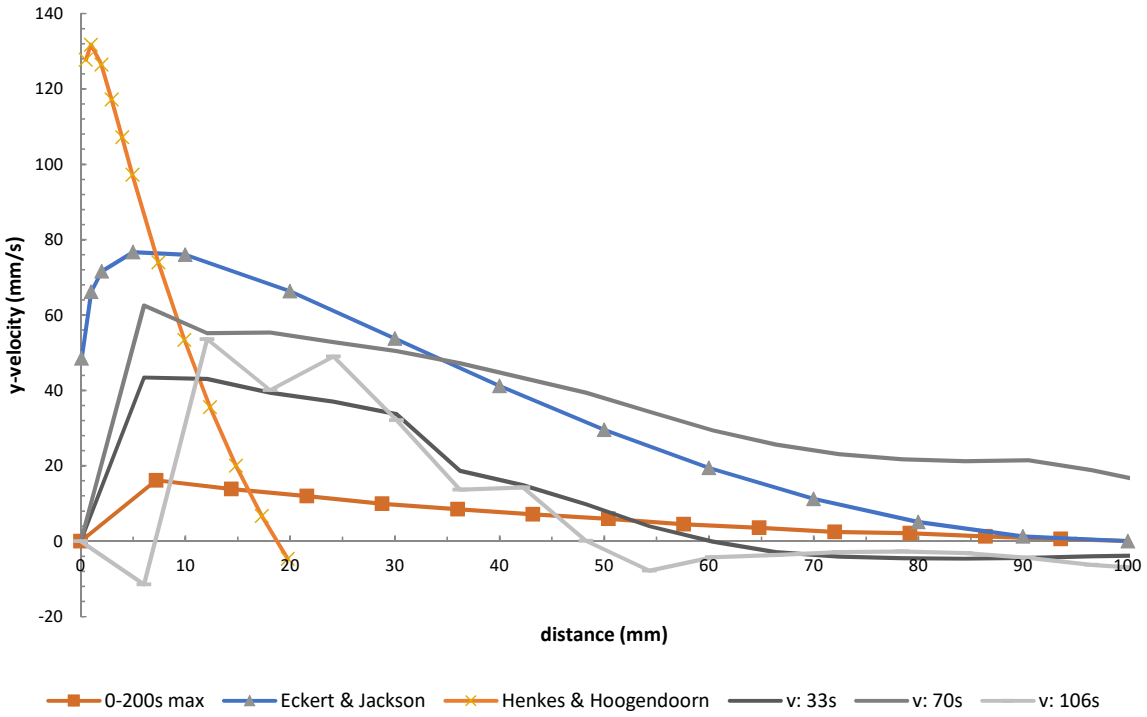

Figure 93 – Comparison of predicted and measured velocity profiles at 90°, test 19

The variation in measured velocity profile with time makes it impossible for a comprehensive fit to be achieved. Instead, close fit at 60 to 120 seconds is sought, as during this time the boundary layers were the most stable and the least affected by boiling. The Henkes and Hoogendoorn model does not give a good prediction of any velocity profile observed, primarily because of the thin boundary layer predicted. The Eckert and Jackson model requires a boundary layer thickness and reference velocity as inputs, for which the experimental values obtained from test 19 were used in Figure 93 above and therefore, unsurprisingly, shows a better fit with the experimental data. Given the scatter in results, the Eckert and Jackson model gives a reasonable approximation of the shape of the boundary layer captured at 70 and 106 seconds.

Figure 94 below shows a schematic view of the two boundary profile shapes studied in literature. On the left-hand side, natural convection in narrow channels is considered, on the right-hand side a semi-infinite fluid is considered. At the centre-line of the narrow channel the y-velocity is zero, but there remains a significant rate of velocity change at this point. The effectively infinite fluid on the right, more similar to that studied by Tsuji and Nagano (1988), has a negligible rate of velocity change once the temperature nears that of the bulk fluid.

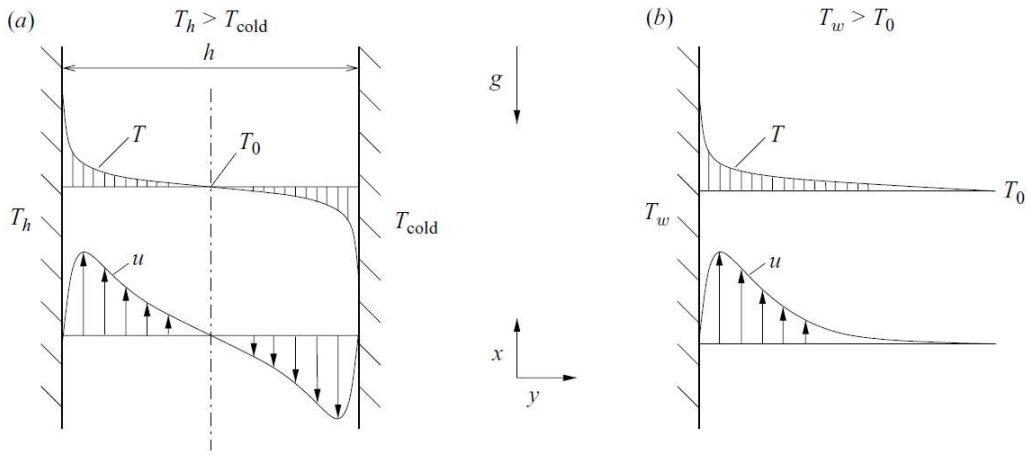

FIGURE 1. Natural convection along walls with heat transfer: (*a*) vertical channel of infinite extent (one-dimensional flow and temperature field) for example investigated by Versteegh & Nieuwstadt (1999); (*b*) hot vertical plate, measured by Tsuji & Nagano (1988*a*, *b*), Tsuji *et al.* (1991).

Figure 94 – Comparison of profile types investigated - reproduced from Hoelling & Herwig (2005)

The velocity profile in a pressure vessel will fit neither of the profiles shown in Figure 94. A good indication of the generic velocity profile across the width of the vessel at mid height is given in Figure 89.

Applying a best-fit curve to the downward flow region (between 100 and 500 mm) and then integrating it with respect to the distance from the wall and multiplying by the average density in the region, gives the cool bulk fluid flow per linear metre in in the downward direction (kg/m/s). The total mass of the upward flow in the warm region must equal that of the bulk downward flow. Therefore, assuming the Eckert and Jackson velocity profile is a reasonable approximation of the velocity profile in the warm region, integration of the Eckert and Jackson formula as below allows the maximum velocity (u_{max}) to be determined iteratively from knowledge of the measured width of warm region (δ) in equation 4.5 and previously calculated downward flow rate.

$$\int_0^{\delta} u\, dy = \int_0^{d} \frac{u_{max}}{0.537} \left(\frac{y}{\delta}\right)^{1/7} \left(1 - \frac{y}{\delta}\right)^{4} \tag{4.5}$$

The solution to equation 4.5 can be determined numerically using appropriate tools. Applying it to the time-averaged results for 0-200s across test 19 gives a predicted maximum velocity of 57 mm/s to give a warm layer momentum flow of 1.03 kg/m/s to equal the same flow in the opposite direction of the bulk liquid. The calculation above assumed the density in the bulk and warm fluid regions to be equal, based on minimal temperature gradients in the fluid within the first 200 seconds of the test (excluding the thermal diffusion boundary layer, which has negligible volume). A plot of the

upwards flow velocities calculated using the above method against the PIV data at mid-height of the vessel in test 19 is shown in Figure 95.

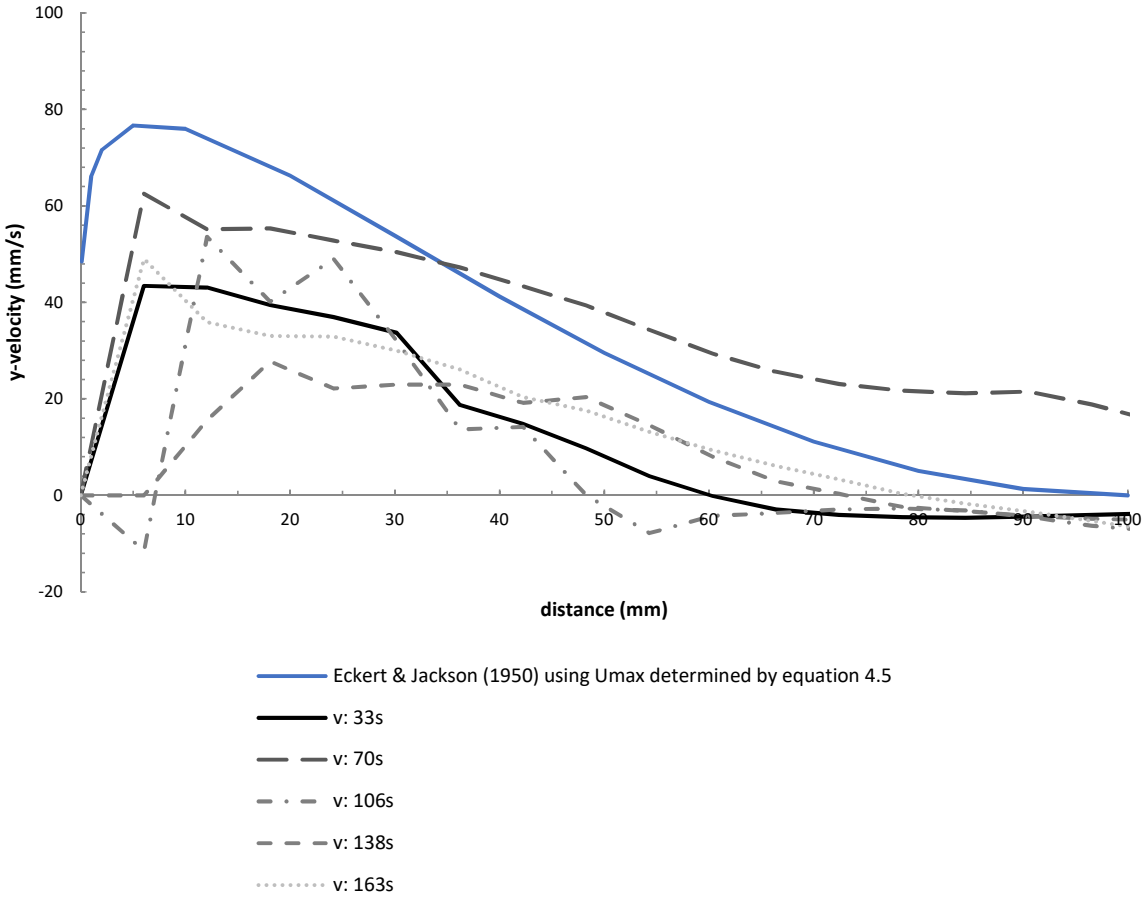

Figure 95 – Comparison of velocity profile prediction and experimental data

The maximum velocity predicted (77 mm/s) is close to the peak experimental values recorded during test 19 (70 mm/s) and the shape of the predicted velocity profile also shows an acceptable match with experimental data, allowing for the variation in measured results with time.

As discussed previously, the scatter in measured velocity profile shapes reflects the occurrence of instabilities and the movement of eddies into the bulk flow. However, when time-averaged over 0-200 seconds in test 19 (water, 96% fill) the velocity profile showed an approximately linear decrease in velocity from a wall distance of 10 mm to the edge of the warm layer (approximately 100 mm). To the author's knowledge, no correlation based on experimental data or theoretical model has proposed a linear relationship between velocity and distance, although the temperature profile across narrow channels is distinctly closer to linear than that in semi-infinite fluids (as shown in Figure 94). Given that a

pressure vessel geometry is different to both such arrangements, future investigation on whether the velocity profile in the warm layer outside the thermal diffusion boundary layer can be approximated by a linear relationship is recommended.

Models of pressure vessels that use a momentum integral method to predict boundary layer thickness, and hence the thermal stratification, typically rely on entrainment coefficients to model the heat transfer and mass flux from the boundary layer to the bulk fluid.

However, results obtained within this study indicate that simplification of the system to one of mass transfer between two zones solely by entrainment of mass from one homogenous cool zone to a homogenous warm zone is insufficient to describe the behaviour of the fluid inside the pressure vessel. The relationship between the thickness of a velocity boundary layer and the thermal boundary layer is complicated by wall boiling, buoyancy, unsteady flow and eddies. Bulk fluid may be entrained in the outer velocity boundary layer long before it encounters a significant temperature profile. The heat transfer into the bulk liquid along the edge of the boundary layer may therefore be lower than that predicted by simple entrainment calculations.

Very quickly the thermal and velocity boundary layers reach a period of maximum stability, whereby the profile shapes are closest to what would be predicted by literature (accepting differences due to geometry). After approximately 60 to 120 seconds the shape of the velocity profile is heavily disrupted by unstable flow, eddies and boiling. The thermal boundary layer growth after 120 seconds is minimal, and the further growth that does occur can be attributed to the bulk fluid becoming warmer.

4.5 Boundary layer further analysis

4.5.1 Dimensionless analysis of the boundary layers

Three tests were chosen for dimensionless analysis based on the quality of data and an adequate heat flux. They were: test 10 (ethanol, 50% fill, 84 kW/m^2), test 19 (water, 96% fill, 90 kW/m^2) and test 22 (water, 62% fill, 67 kW/m^2). Prior to non-dimensionalising the data, temperature values for specific times intervals were obtained from a 30-second moving-average trendline to reduce noise effects. The values were taken at an angle of 112.5° (this particular spoke had the highest concentration of thermocouples nearest the wall) except for the wall temperature value, which is taken at 135° (as there was no embedded TC present at 112.5° and the results from the TC at 90° were unreliable).

Table 28 – Data for dimensionless analysis

	Test 10					Test 19				Test 22				
Time	**Wall**	**2 mm**	**9 mm**	**13 mm**	**100 mm**	**Wall**	**1.5 mm**	**3 mm**	**9 mm**	**Wall**	**1.5 mm**	**3 mm**	**9 mm**	**30 mm**
120 s						108	17.8	18.0	17.8	103.6	19.6	19.2	18.0	14.5
240 s	86.0	41.8	39.7	38.3	30.0	109.4	22.5	21.0	22.0	105.2	22.7	21.8	20.7	18.0

Two methods of non-dimensionalising the data were considered. The first approach used is that adopted by Tsuji & Nagano (1989), among others, and uses a characteristic temperature and velocity as shown below:

$y^+ \ (= u_* y/\nu)$ is the dimensionless distance from the wall

$T^+ \ = (T_w - T)/t_*$ is the dimensionless temperature

Where

$t_* \ \left(= q_w/\rho c_p u_*\right)$ is the friction temperature

$u_* \left[= \ (\tau_w/\rho)^{1/2}\right]$ is the friction velocity

and τ_w is the wall shear stress determined in accordance with the formula proposed by Blasius (equation 2.9).

The characteristic flow velocity and the boundary layer thickness required to estimate the wall shear stress were calculated using the correlations for maximum velocity and boundary layer thickness proposed within the same study by Tsuji & Nagano (1989). For comparison, the values were also calculated using the methodology proposed by Eckert & Jackson (1950) as detailed in section 4.4.4.

The measured values converted to dimensionless form by this method are given for water in Table 29 and ethanol in Table 30.

Table 29 – Dimensionless distance and temperature values from water tests

Time		Test 19			Test 22			
	Parameter - Method	1.5 mm	3 mm	9 mm	1.5 mm	3 mm	9 mm	30 mm
120 s	y^+ -T&N	39	77	232	37	73	217	2350
240 s	y^+ -T&N	39	76	231	38	75	223	2411
240 s	y^+ -E&J	29	58	174	28	56	168	1813
120 s	T^+ T&N	36	36	36	39	39	40	41
240 s	T^+ T&N	35	35	35	38	39	39	41
240 s	T^+ E&J	26	27	26	25	25	26	27

Table 30 – Dimensionless distance and temperature values from ethanol tests

Time		Test 10			
	Parameter - Method	2 mm	9 mm	13 mm	100 mm
240 s	y^+ -T&N	15	69	100	771
240 s	T^+ T&N	5.7	6.0	6.2	7.2

Figure 96 shows the measured T^+ vs y^+ point values from the actual test against the correlation for the viscous sublayer proposed by Tsuji & Nagano (1989) and numerous authors of $T^+ = Pr\ y^+$. The parameters calculated from test data are shown for both the Tsuji & Nagano (1989) and Eckert & Jackson (1950) methods. The latter requires the maximum velocity as an input. For water tests 70 mm/s was used, based on the peak measured value obtained during season 2 (occurring in test 19). Velocity measurements were not available for the ethanol test (test 10) so only the Tsuji & Nagano method was used.

As discussed in section 4.4.5, in the available literature the temperature gradient outside of the thermal boundary layer predicted on flat plate has been fitted to both power and logarithmic based equations, with neither providing a robust fit in all cases. There is greater consensus among authors that the temperature and velocity profiles follow a logarithmic profile in the outer part of boundary layers, and therefore a modified logarithmic profile has been fitted to the data as shown in Figure 96, based on the form proposed by Hoelling & Herwig (2005) of:

$$T^+ = C \ln(y^+) + D.$$

The gradient of a trendline through the measured data, *C*, was found to give good agreement with a factor of $Pr^{-1/2}$, where the Pr number is calculated using the bulk fluid temperature T_b.

The intercept, *D*, can be calculated on the assumption that the coolest fluid temperature T_b is at a distance midway between the wall and the centre of the vessel (i.e. half the vessel radius) as follows:

1. Calculate a bulk fluid dimensionless temperature, T_b^+, as $(T_w-T_b)/t^*$
2. Calculate a bulk fluid dimensionless distance, y_b^+, as $(u^*r/2v)$
3. Calculate D as $T_b^+ - Pr^{-0.5} ln(y_b^+)$

The resulting equations are:

Water:

$$T^+ = 0.58\, ln(y^+) + 35.7 \tag{4.6}$$

Ethanol:

$$T^+ = 0.31\, ln(y^+) + 4.8 \tag{4.7}$$

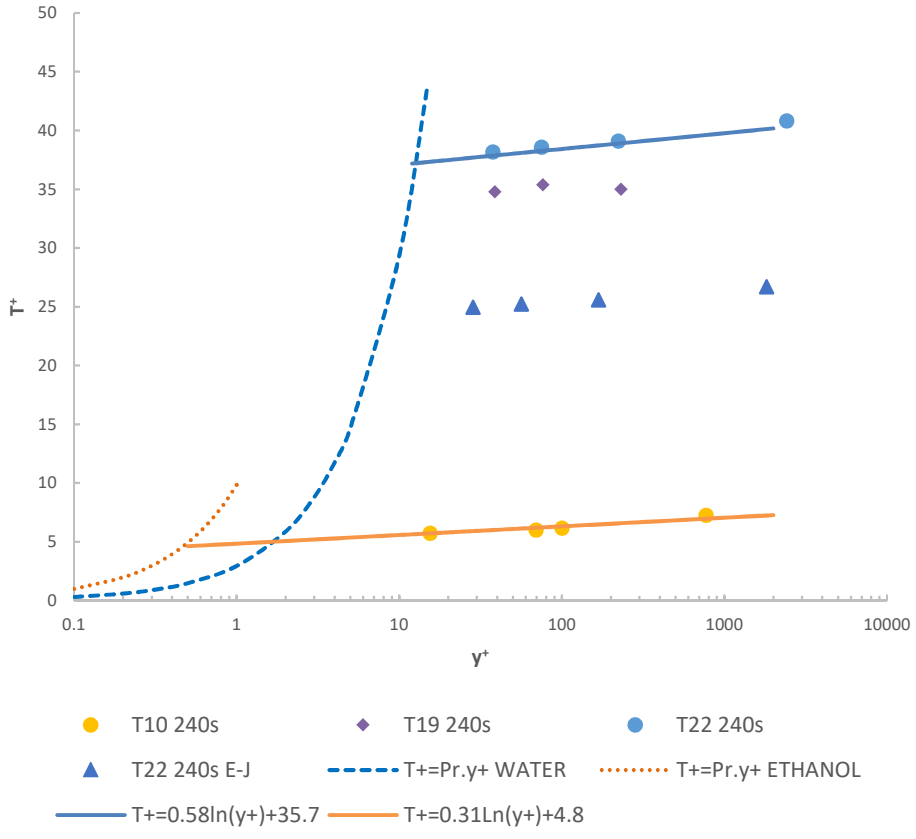

Figure 96 – Dimensionless temperature plot for test 10 (ethanol, 50% fill, 84 kW/m^2), test 19 (water, 96% fill, 90 kW/m^2) and test 22 (water, 62% fill, 67 kW/m^2. Methodology of Tsuji and Nagano (1989)

The second method of non-dimensionalising the data uses a characteristic parameter proposed by Hoelling & Herwig (2005). They defined a characteristic parameter that avoided use of the wall shear stress, which does not govern the flow in the outer boundary and hence was considered by them to be unsuitable for use across the whole boundary layer. The non-dimensional form of the distance and temperature were given as:

$$y^x = \frac{y}{\delta};\ \delta = \frac{T_c}{|\partial T/\partial y|_w}$$

$$\Theta^x = \frac{T_h - T}{T_c}$$

where the temperature gradient at the wall and the characteristic temperature can be related back to the heat flux and physical properties of the fluid as follows:

$$T_c \equiv \left(\frac{a^2}{g\beta}.\left|\frac{\partial T}{\partial y}\right|_w^3\right)^{1/4}$$

$$= \left(\left[\frac{q_w}{\rho c_p}\right]^3 \frac{1}{ag\beta}\right)^{1/4}$$

The data in dimensionless form in accordance with this method is given for water in Table 31 and ethanol in Table 32.

Table 31 – Dimensionless water data, H & H method

Time		Test 19			Test 22			
	Parameter	1.5 mm	3 mm	9 mm	1.5 mm	3 mm	9 mm	30 mm
120 s	y^x	21	41	124	20	40	119	1325
240 s	y^x	21	41	124	20	40	120	1330
120 s	T^x	7.0	7.0	7.0	7.3	7.3	7.4	7.7
240 s	T^x	6.9	7.0	6.9	7.2	7.3	7.4	7.7

Table 32 - Dimensionless ethanol data, H & H method

Time		Test 10			
	Parameter	2 mm	9 mm	13 mm	100 mm
240 s	y^x	60	271	392	3012
240 s	T^x	2.7	2.8	2.9	3.4

Figure 97 shows selected results in dimensionless form along with the two correlations proposed by Hölling and Herwig for the viscous sublayer ($\theta^x=y^x$), and for the turbulent part of the boundary layer. For comparison, the profile predicted by Eckert & Jackson (1950) is also shown in this dimensionless form.

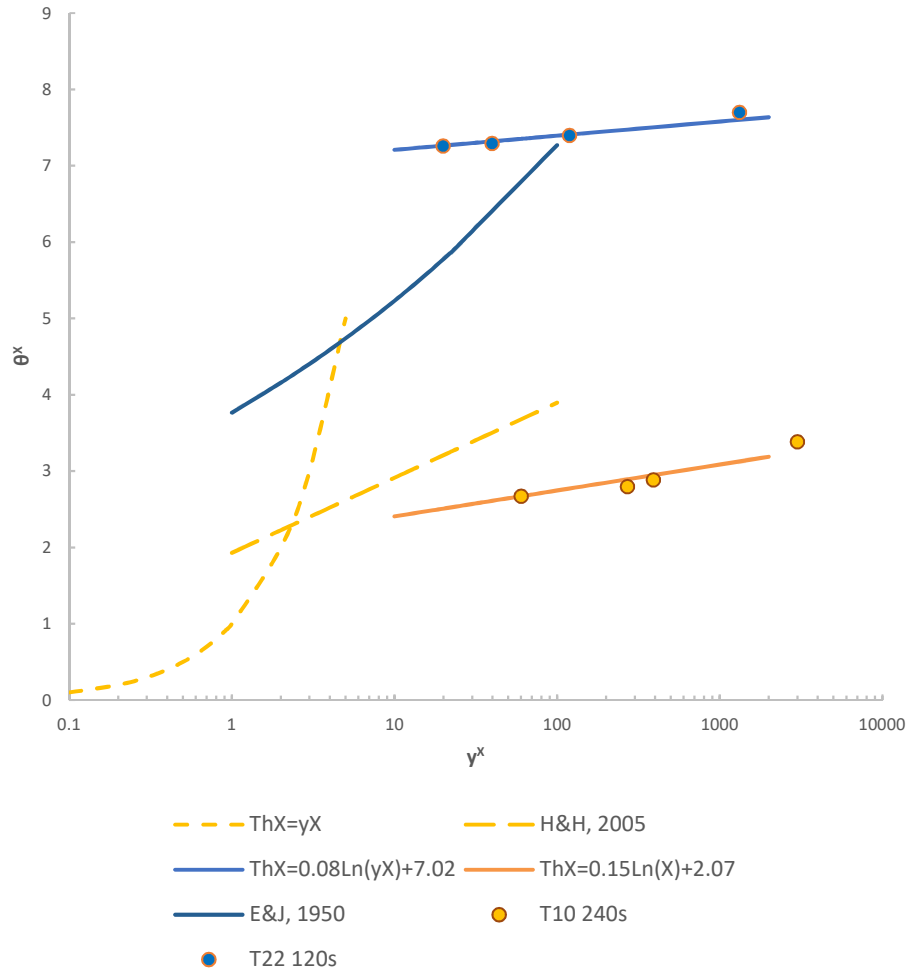

Figure 97 – Dimensionless temperature plot for test 10 (ethanol, 50% fill, 84 kW/m^2) and test 22 (water, 62% fill, 67 kW/m^2. Methodology of Hölling and Herwig (2005)

A logarithmic profile can be fitted to the test data in the form of $\theta^x = C \ln (y^x) + D$. The gradient of a trendline through the measured data showed a reasonable correlation with $0.047Pr^{0.5}$. The constant D can be calculated as follows:

1) calculate $\theta_b{}^x$ for the bulk fluid temperature as $(T_w-T_b)/T_c$
2) calculate a bulk fluid dimensionless distance y^x as $r/2\delta$.
3) calculate D as $\theta_b{}^x - (0.047\ Pr^{0.5}\ y^x)$

When converted from dimensionless values into actual values, the temperature profiles predicted by the two methods are unsurprisingly similar (given they are fitted to the same data), as shown in Figure 98.

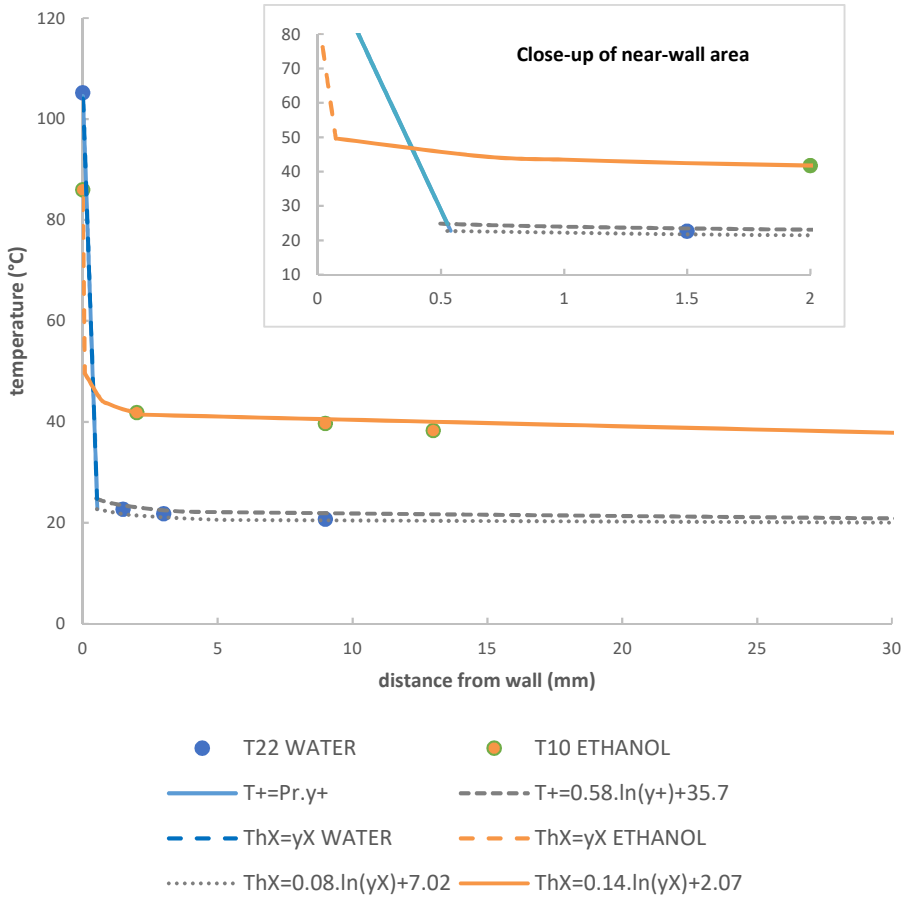

Figure 98 – Comparison of temperature profiles predicted by dimensionless analysis methods with modified constants

The velocity profile in the boundary layer can be non-dimensionalised and analysed in the same manner as above, however the uncertainty in the thickness of the boundary layer and maximum velocity (due to the inability to resolve near wall data in the current study) make an alternative to the Eckert & Jackson profile of no practical benefit until near-wall data is available. Such analysis is therefore not reported here. Future work should focus on resolving the velocity profile near the wall (within 5 mm) in greater detail to assess whether an alternative profile provides a better fit with the time-averaged data.

4.5.1.1 Discussion of dimensionless analysis

The method proposed above allows for prediction of a temperature profile that shows reasonable fit with the test data generated in this study. Of the two methods used to non-dimensionalise the data, that of Hölling and Herwig is preferred due to the reliance of the method on fundamental material and system properties that can be measured and characterised in a reliable manner.

Both methods consist of a linear profile in the viscous laminar sub-region and a logarithmic profile in the turbulent region, which also continues into the bulk fluid. The transition between the two profiles occurs at a dimensionless distance that varies by fluid and methodology, but is easily determined by the point of intersection. A transition (or buffer) region between the laminar and fully turbulent regions, which is well established by experiments, was not captured by the current experimental study and has not been included in the methods herein. The inability of the thermocouples used in the current study to accurately resolve temperatures on a scale sufficiently small to characterise the region means this has been omitted. In practice, the temperature profile will exhibit a smooth curve between the linear and logarithmic profiles. Characterising this in detail for the levels of subcooling used in the current study would require alternative instrumentation within 1 mm of the vessel wall.

The scope of the current study is limited. Fluids include water and ethanol, covering a range of Prandtl numbers $2.3 < Pr < 17$ and a range of Grashof number $4x10^{10} < Gr < 1x10^{12}$. The degree of subcooling studied was $45 < T_{sub} < 88$. Only atmospheric pressure studies were undertaken.

Further work should seek to extend the scope of the available test data. Modifications to instrumentation should also be considered to allow more accurate characterisation of transition zone temperature profiles. An alternative method of fixing instrumentation should be considered that ensures a fixed distance from the vessel wall as the vessel undergoes thermal expansion (and possibly distortion). Finally, the attempts to control and characterise the heat flux within the current study have been inadequate, leading to significant uncertainties in defining the characteristic parameters used for non-dimensionalising the data, and to unsteady flow behaviour, giving the appearance of anomalous data. Alternative means of applying thermal boundary conditions under more controlled conditions must be devised.

4.5.2 Multiphase (bubbly) flow effects

Flow with a significant vapour volume fraction is commonly referred to as bubbly flow. The presence of bubbles in a flow changes the temperature and velocity profiles within the boundary, and typically increases the degree of turbulence.

Numerical modelling of two-phase flows using the Eulerian-Eulerian framework typically assumes that the liquid-phase turbulence is enhanced by the bubbles. Numerous studies have included an additional term in the liquid effective viscosity to account for this, following the method proposed by Sato, et al., (1981). More recent studies have instead included terms directly within the equations for k and ε or ω (Krepper, et al., 2013).

Numerous studies have also investigated the boundary layer profiles in bubbly flow and proposed modifications to velocity profiles and wall functions. Examples include Hassan (2016), Marie, et al., (1997) and Mikielewicz (2003). The latter also proposed a modified thermal boundary profile.

The modified profiles given in references above are all based on the logarithmic profile commonly used for turbulent flows beyond the viscous sub layer (and transition region) but with a range of additional factors included to account for bubble effects. However, all the studies listed above (and references therein) are applicable to flow boiling conditions. To the knowledge of the author, there are no experimental studies that have characterised the effect of bubbly flow on free convective velocity profiles in a quiescent fluid. The current study does not provide sufficient information for a dimensionless correlation to be obtained, given the restrictions in instrumentation and test scope, the novel geometry, and most importantly the limited vapour volume fraction. Consequently, proposing a form of equation for a wall function that includes a void fraction term cannot be done within the current study.

4.5.3 Recommendations for future investigation

Classic boundary layer theory divides the velocity boundary layer into a viscous region of laminar flow nearest the wall, a transition (or buffer) region, and a fully turbulent region that is considered to obey a logarithmic (or power) law. The time averaged velocity profile results suggest a fourth region may be identified, whereby the time-averaged y-velocity decreases in an approximately linear manner with distance (see section 0), although the difficulties in defining a boundary layer in a pressure vessel configuration make it debatable whether this should be considered within the boundary layer or the bulk flow.

The thermal boundary profile has been shown to fit a modified two-equation approach (see previous section) with the potential for future inclusion of an additional term to account for the vapour fraction/boiling effects.

The time-averaged y-velocity profile is more complex, as the velocity is zero at the wall, peaks at an unknown distance from the wall, and then decreases until it becomes negative. At least two, and possibly three, equations are required to adequately capture the profile for wall functions. There is also potential for future inclusion of an additional term to account for the vapour fraction/boiling effects in such equations following future work to characterise the near-wall characteristics.

The duration from onset of fire until the boundary layer flow transitions from laminar to transient is unlikely to be affected by wall boiling. The length scales typical in actual pressure vessels, the variations in thermal boundary conditions that will occur in practice, and the heat sink of the wall and fluid, mean that the flow is likely to transition to turbulent before significant wall boiling occurs. This hypothesis cannot be validated within the current study as the light scatter at the wall prevented measurements from being obtained within the first few millimetres of the wall throughout the test. The recommendations given in section 7 may permit measurement of the time to transition in future work.

4.5.4 Heat transfer to the bulk fluid by turbulence effects

In a hypothetical scenario where the thermal load on a large vessel is uniform and constant, the thermal and velocity boundary layer profiles will quickly reach a quasi-stable scenario, after which further development will be slow and driven by changes in the bulk fluid properties.

Changes to the bulk fluid temperature distribution will be driven by numerous mechanisms. Firstly, the warm fluid rising will flow along the top of the vessel and a convection cell (or cells) will become established. However, the well-established vertical temperature gradients measured indicate that the thermal energy accumulates at the top of the vessel, having flown across to the centre and met warm fluid coming from the other direction. The influence on the edge of the boundary layer is probably small.

Boiling has an un-quantified influence on the bulk fluid. Boiling analysis in section 4.6 indicates the void fraction in the current study is low (at 4 $x10^{-7}$) and can be considered negligible. However, the bubbles evidently have a rate of condensation far lower than predicted by the simplistic hydrodynamic model given in section 2.4.7. Bubbles were observed throughout each season two test in the bulk fluid, passing through the illuminated area without noticeable change in rate of rise or collapse. Heat transfer from the bubbles to the bulk fluid may be significant at higher volume fractions, which will be observed at lower degrees of subcooling, however it is considered to have a minor contribution to bulk fluid temperature rise, other than via the effect it has on the flow behaviour of the thermal boundary layer and warm region.

It is proposed that an important mechanism for bulk fluid temperature increases is the entrainment of warm liquid into the bulk, more specifically through eddy incursions into the bulk fluid. Time-averaged data within the current study indicates the warm region (beyond the thermal diffusion boundary layer but before the slow-moving bulk fluid) extends from approximately 30 mm to 100 mm. Within this region the velocity profile may be approximated by a linear relationship (noting that this is beyond the region expected to obey a logarithmic law), whereas the temperature gradient is expected to be minimal and can be assumed to be either negligible or also represented by a linear relationship.

4.5.5 Discussion on the implications to modelling

The thermal boundary layer stabilises quickly and remains small throughout the tests. This implies that a type of simplistic two-zone model that assumes constant growth of a boundary layer does not capture the physical mechanisms driving pressurisation. The boundary layers are governed by the wall temperature and the bulk fluid properties, and the wall temperatures are inherently limited by boiling. The results from the commissioning tests, season one and season two together support a conclusion that pressurisation is driven by more than convective heating driving the liquid surface temperature. This statement is supported by the disproportionately significant effect on pressurisation rate of reducing the vapour space wall temperatures shown in the commissioning tests and season one, and the significant effect on reducing the vapour space volume to small amounts (<10% of vessel volume) in season one, the stability of the thermal boundary layer temperature profiles shown in season one and two, with fluid temperatures at the wall and liquid surface limited by wall boiling.

The contribution of boiling to the pressure rise is unknown and requires further study to assess its significance. Boiling may affect the pressure rise in two ways: the direct addition of moles of superheated vapour following bubble collapse at the surface, which do not condense due to further superheating of vapour through radiation from the vapour-space wall; or through heating of the fluid outside the thermal diffusion boundary layer due to bubble condensation causing growth of the thermal boundary layer and thereby increasing wall temperatures (and thus promoting further boiling and convective heat transfer).

The heat transfer from the boundary layer to the bulk fluid will occur through a range of mechanisms:

1) entrainment of warm liquid via eddies and plumes (near the bottom of the vessel)

2) diffusion and advection from the warm layer above

3) bubble condensation in the bulk fluid.

The first mechanism is proposed as the most significant for the current study (with high degrees of subcooling), with the latter two less so due to gentle movement of the warm layer and a low void fraction.

The correlations proposed in the current study may have applicability in incremental developments of zone or momentum integral models of pressure vessels. However, it is recognised that the scope of the current study (in terms of fluids, governing dimensionless numbers and thermal boundary conditions) is limited, and hence further validation studies are necessary before implementation.

For reasons stated throughout, attempts to improve models of pressure vessels should be focussed on numerical-models, as simplified models (integral models or zone models) are unable to resolve the complex flow patterns that occur.

4.6 Boiling analysis

The heat flux partitioning method for partial nucleate boiling originally proposed by Rohsenow, and first implemented in a numerical model by Kurul and Podowski (1990), is described in section 2.4. It is reliant on sub-models of three primary parameters:

- Bubble departure diameter
- Bubble departure frequency
- Bubble nucleation site density

Numerous models have been proposed to predict these values for water, and selected models compared against experimental data in this section.

4.6.1 Measured values

Test 22 from season 2 was analysed for an indication of the key bubble parameters. Only this one test is suitable for direct comparison, as no others had degasification applied prior to commencement of the fire (numerous further degasified tests had been planned but could not be performed for the reason described in section 3.2.8). This test was deaerated by application of a vacuum pump prior to commencement of fire until no further boiling could be seen. Unfortunately, the pressure transducers connected were not rated for below 1 atm (101 kPa) and so a calculation cannot be made to estimate the concentration of remaining dissolved air.

The PIV images taken by the Flea3 cameras are not suitable for analysis of bubble sizes. Despite the application of several particle-tracking algorithms in Dantech Dynamic studios, the bubbles could not be reliably separated from the seeding.

This is attributed to bubbles scattering significantly less light than the silver-coated seeding particles, and the aperture size and shutter speed of the camera being such that only the largest bubbles were bright enough to be captured.

Large bubbles were occasionally identified, however, they rarely remained in the light sheet for long enough to give sensible (i.e. positive y-velocity) results from the particle tracking algorithms.

Figure 99 shows the bubble with the position marked. The position of the bubble also is marked for the 13 frames (representing 1.3 s) immediately preceding and after that shown. The rise velocity can be calculated across the frames as 95 mm/s prior to the frame and 85 mm/s after. The bubble is approximately 6 pixels wide, corresponding to a diameter of 2 mm. However, the Cole correlation (see main report section 2.4) predicts a bubble diameter of 0.4 mm for this measured velocity, with the discrepancy probably attributable to light scattering.

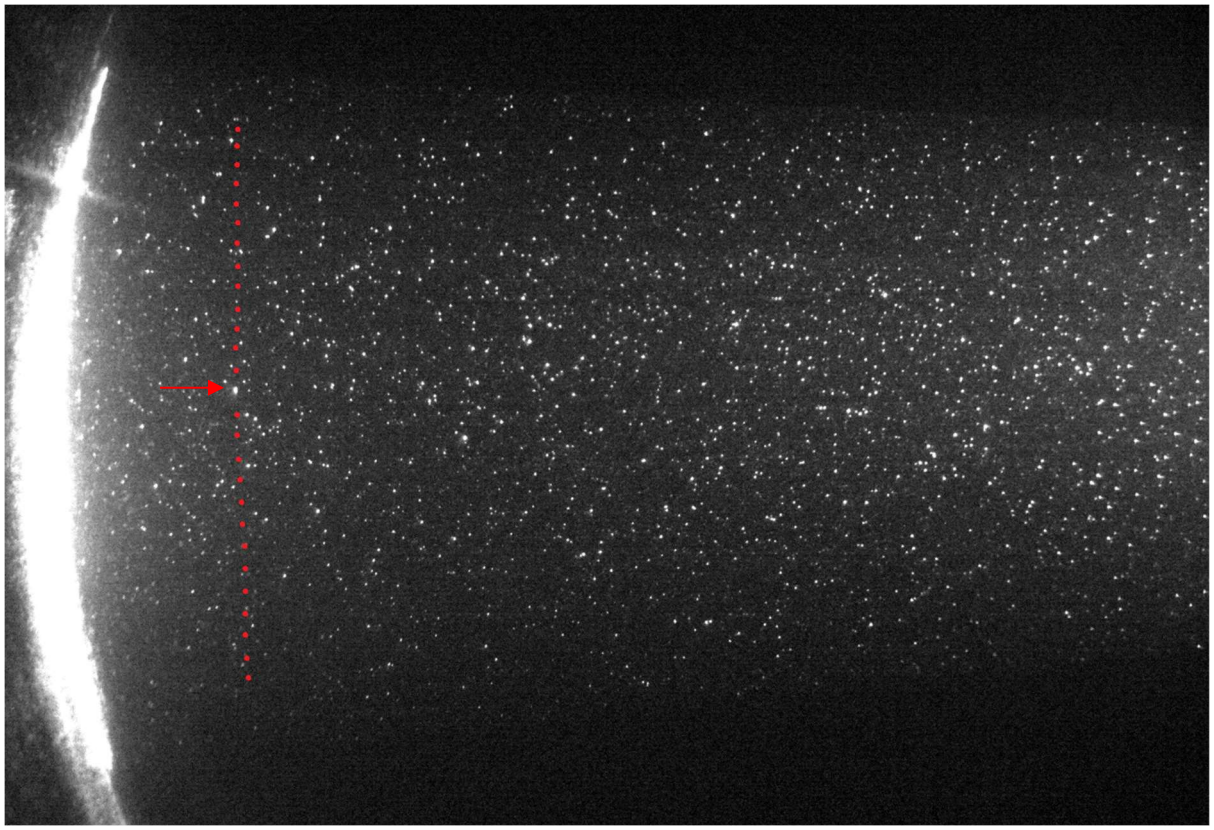

Figure 99 – Bubble rise positions at 10 Hz

An analysis of individual frames taken with a conventional camera was performed to obtain values for bubble nucleation site density, bubble diameter and bubble departure frequency. Only frames taken after 150 seconds were considered, due to the higher magnification and the more developed boiling. To obtain the nucleation site density, N, an area of 200 x 40 pixels was drawn near the laser arc immediately outside the area saturated with light. Figure 100 shows the analysed

area in red, with bubbles identified by a blue pixel. Areas that appear as intermediate brightness were typically not marked as bubbles, due to the presence of lighter-shaded areas being visible at the start of the test in the same location. These are attributed to reflection due to the surface topography. The area examined was converted to an area of $1.3x10^{-4}$ m^2 and then multiplied by a geometric factor of 3.9 (to account for the angle between the wall and the camera line of sight) to give a final area of $5.0x10^{-4}$ m^2.

The bubble diameter is based on the typical number of pixels occupied by the bright centre of the bubble. Surrounding mid-shade areas are attributed to light scattering as described above. The bubble departure frequency was too low for analysis on a frame-by-frame basis, instead well-defined bubbles were watched for residence time on the wall. Multiple bubbles were assessed and an average value to be determined. The results of this bubble characteristic analysis are given in Table 33.

Table 33 – Measured bubble characteristics

Nucleation site density	Departure diameter	Departure frequency
160,000	0.25 mm	1/30
+/- 15%	+/- 50%	+/- 60%

The frames between 150 seconds and 240 seconds were compared for the nucleation site density and departure diameter. No significant difference was observed between the results, given the margins of error involved.

4.6.2 Nucleation site density (N)

Table 34 shows a comparison of the nucleation site density given by selected models for a range of wall excess temperatures, relating to the peak wall temperature measured at 90, 120, 180 and 240 seconds. Also shown are the measured values obtained over a period of 150-240 seconds. The video shows that the measured values were reasonably stable over that period.

Table 34 - Active nucleation site density comparison

Wall temperature (°C)	Lemmert & Chawla (1977)	Kocamustafaogullari & Ishii (1983)	Wang & Dhir (1993)[1]	Benjamin & Balakrishnan (1997)[2]	Hibiki & Ishii (2003)	Measured values from test 22
102.5	1,000	2,000	10,000	0	0	-
104.3	2,000	20,000	310,000	0	0	-
106	5,000	90,000	1,640,000	5,000	0	160,000
107.7	8,000	265,000	7,335,000	15,000	0	160,000

[1]value of θ taken as 38°, as per Basu, et al., (2002) based on dataset by Bergles & Rohsenow (1964)

[2]value of R_a taken as 1 µm, as per mid-range of applicability for Benjamin & Balakrishnan (1997)

The only nucleation site density model within an order of magnitude of the observed values was that of Kocamustafaogullari & Ishii (1983). However, it was based on the bubble diameter by the same authors which was over an order of magnitude larger than those observed in the current study. Use of the measured bubble diameter in their model resulted in an order of magnitude reduction in the site density.

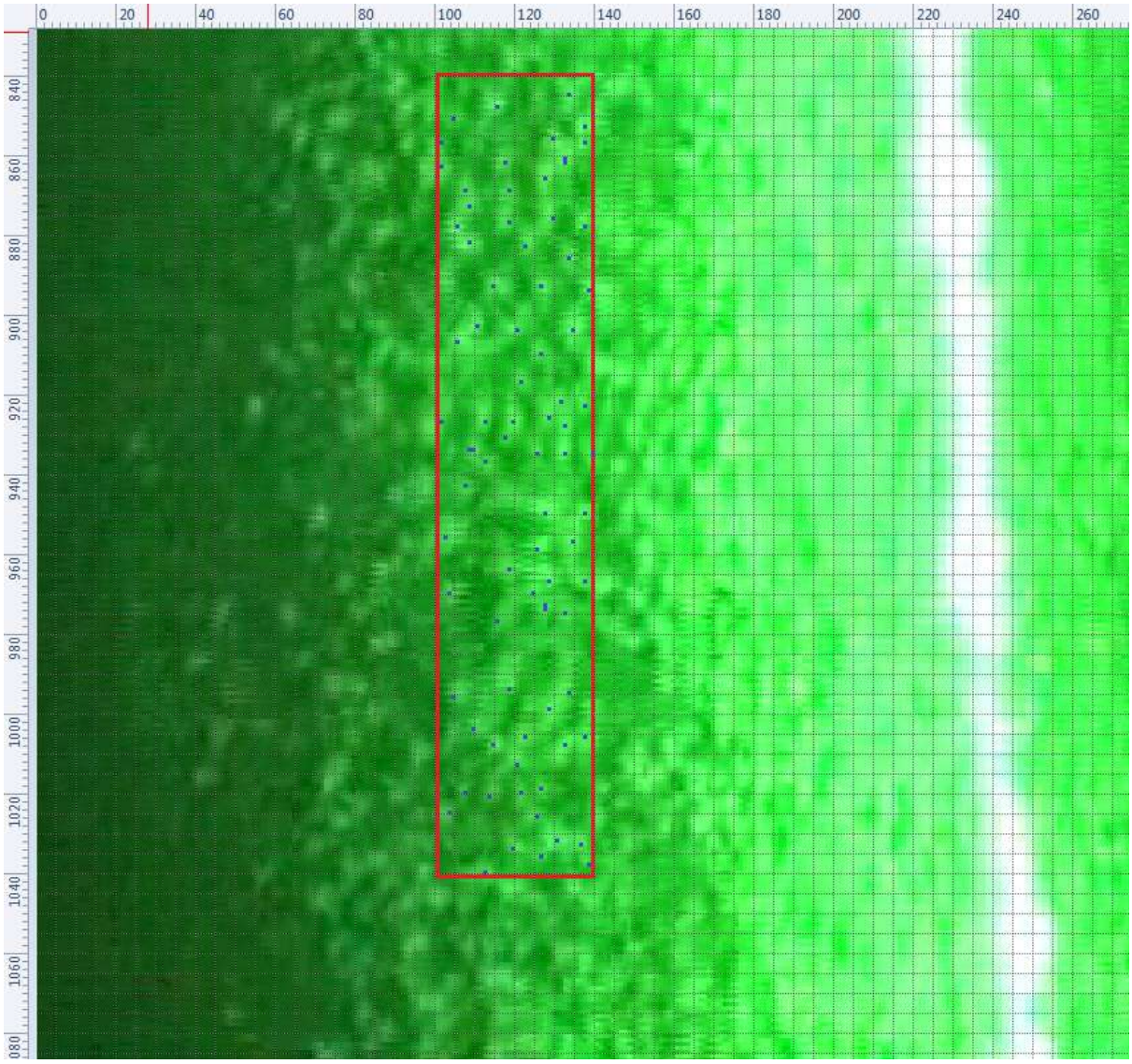

Figure 100 – Nucleation site density calculation example

4.6.3 Bubble departure diameter (D)

Table 35 shows the predicted bubble diameters against the observed values from test 22.

Table 35 – Bubble diameter (mm) comparison

Wall temperature (°C)	Fritz (1935)[1]	Zuber (1959)	Cole (1967)	Tolubinsky & Kostanchuk (1970)[2]	Unal (1976)[3]	Kocamustafaogullari & Ishii (1983)[1]	Measured values from test 22
102.5	4.2	0.9	16.5	0.3	0.1	3.9	-
104.3		1.0	28.4				-
106		1.2	39.7				0.25
107.7		1.3	50.9				0.25

[1] Theta set to 80° as per Rogers et al., (1994)

[2] d_{ref} set to 1.3mm and ΔT_{ref} set to 53°C as per Krepper & Rzehak (2011)

[3] H calculated as per Unal (1976) proposed correlation for flat plates, using a reference velocity of 0.13 m/s and a characteristic length of $\pi.r/4$

The bubble diameter models of Tolubinsky & Kostanchuk (1970) showed the best agreement with the measured values, followed by that of Unal (1976).

4.6.4 Bubble departure frequency (f)

Table 36 shows the predicted bubble departure frequencies against the observed values from test 22.

Table 36 - Bubble departure frequency comparison

Wall temperature (°C)	Cole (1960)[1]	Zuber (1959)[1]	Kocamustafaogullari & Ishii (1995)[1]	Podowski, et al., (1996)[1,2]	Petrovic, et al., (2004)	Measured values from test 22
102.5	210	310	620	0.07	0.009	-
104.3				0.08	0.05	-
106				0.09	0.14	0.033
107.7				0.10	0.32	0.033

[1] Bubble diameter taken as 0.3 mm as per measured values

[2] Cavity radius unknown, value assumed to be 0.3 µm as referenced in Basu, et al., (2002)

Only the departure frequency models by Podowski, et al., (1996) and Petrovic, et al., (2004) were within an order of magnitude of the measured values.

4.6.5 Comparison of heat flux partition predictions

The heat flux partition model divides the heat transfer into convection, evaporation and quenching. Commonly used formulas for this partition, based on the method of Kurul & Podowski (1991), are given below by equations 2.35 to 2.38.

To identify the best combination of models to represent the current study, the area influenced by nucleate boiling and the total vapour production are calculated for various combinations and compared against the actual value below. The coefficient of convection, h_c, was calculated from equation 4.2 based on a characteristic length of $\pi.r/4$.

All 64 combinations of the following models were assessed: Nucleation site models from Wang & Dhir (1993), Lemmert & Chawla (1977), Benjamin & Balakrishnan (1997), and Kocamustafaogullari & Ishii (1983); departure diameter models from Zuber (1959), Kocamustafaogullari & Ishii (1983), Tolubinsky & Kostanchuk (1970), and Unal (1976); departure frequency models from Cole (1960), Kocamustafaogullari & Ishii (1983), Petrovic, et al., (2004), and Podowski, et al., (1996).

Selected results are shown in Table 37 below. Models are referred to by the initials of the authors.

Table 37 – Comparison of bubble parameter effect on heat flux partition predictions

Nucleation Site Model	Departure Diameter Model	Frequency Model	q_{ev}" (W/m^2)	q_q" (W/m^2)	h_c ($W/m^2.K$)	mass evaporation rate ($kg/m^2.s$)
As measured	**As measured**	**As measured**	**0.06**	**0.005**	**1122**	**2.55E-08**
K & I	T & K	Pet. et al.	1.50	0.024	1175	6.63E-07
K & I	Unal	Pet. et al.	0.06	0.003	1096	2.46E-08
K & I	T & K	Pod. et al.	0.50	0.014	1175	2.21E-07
L & C	**T & K**	**Cole**	**31.72**	**0.625**	**1089**	**1.40E-05**
L & C	Unal	Cole	1.17	0.069	1087	5.19E-07
L & C	T & K	Pet. et al.	0.05	0.024	1089	2.00E-08
L & C	T & K	Pod. et al.	0.02	0.014	1089	6.67E-09
B & B	T & K	Pet. et al.	0.08	0.024	1092	3.75E-08

Highlighted in Table 37 are the calculated values from the measured data and the default models within the ANSYS Fluent and CFX programmes. It can be seen that the default models poorly predicted the measured values. This is perhaps unsurprising, as these nucleation site density and departure frequency models are based on saturated boiling and do not take into account subcooling. The best match was obtained using the nucleation site density model by Kocamustafaogullari & Ishii (1983) and the frequency model by Petrovic, et al., (2004). The latter was developed from

subcooled pool boiling studies of water and the good match is therefore unsurprisingly. The former is a correlation which includes the bubble diameter, and therefore takes into account the degree of subcooling indirectly, when the model by Tolubinsky & Kostanchuk (1970) is used to predict D_b.

The frequency model by Podowski, et al., (1996) actually gave the best match with experimental data. However, this must be considered fortuitous due to the assumption of the important cavity radius parameter. As this information is not typically known outside of laboratory conditions (and was not known in the current study) this model is considered no further at present, however it does show promise for future use should further information on cavity sizes become available.

Both the departure diameter models by Tolubinsky & Kostanchuk (1970) and Unal (1976) gave reasonable results and both take into consideration the degree of subcooling. The former predicted departure diameters closer to the measured value, however the over-estimate of both the nucleation site density and frequency by other models meant an under-estimate by the latter gave the closest overall mass evaporation value. Considering the inverse relationship between frequency and bubble diameter, it would seem reasonable to apply either Unal model.

4.6.6 Bubble Behaviour Analysis

The bubble rise velocity and rate of condensation can be estimated using the measured and predicted bubble diameters above. The bubble models can be categorised as those which consider hydrodynamic effects only, and those which also consider thermal effects. The theoretical terminal rate of bubble rise models by Cole and Zuber, based on hydrodynamic effects only, are given below compared with a typical measured value during the tests. These models give a relative velocity assuming a quiescent liquid, and do not account for liquid velocity effects on the bubble.

Table 38 – Bubble rise rate comparison

Cole	Zuber	Measured
30 mm/s	180 mm/s	90 mm/s

Conventional video indicates that the absolute rate of bubble rise observed in the water tests was in the region of 90 mm/s. This is an absolute value. It is not possible to give an exact relative value, however given the location at which the measurement was taken, and the results presented in section 0, it is reasonable to assume the relative velocity is within the range 40-90 mm/s.

Bubble condensation models that include thermal effects rely on the heat flux between phases being known, which in turn requires knowledge of the heat transfer coefficient. In numerical codes this is typically calculated from the Nusselt number, which itself has a significant degree of uncertainty. Throughout seasons one and two significant numbers of bubbles were captured on video in the bulk flow. It is evident that the bubble collapse rate described in section 2.4.7 is not representative of those seen in practice. Further work should investigate the cause and effect of this phenomenon.

4.7 References

ANSYS, Inc., 2018. ANSYS Fluent User's Guide, Release 19.0, Equation (6.68).. In: s.l.:s.n.

Basu, N., Warrier, G. R. & Dhir, V. K., 2002. Onset of nucleate boiling and active nucleation site density during subcooled flow boiling. *Journal of Heat Transfer,* Volume 124.

Benjamin, R. J. & Balakrishnan, A. R., 1997. Nucleation site density in pool boiling of binary mixtures: effect of surface micro-roughness and surface and liquid physical properties. *The Canadian Journal of Chemical Engineering ,* Volume 75.

Bergles, A. E. & Rohsenow, W. M., 1964. The determination of forced convection surface-boiling heat transfer. *ASME Journal of Heat Transfer,* Volume 1.

Bergman, T. L., Lavine, A. S., Incropera, F. P. & Dewitt, D. P., 2011. *Fundamentals of Heat and Mass Transfer.* 7th ed. s.l.:John Wiley & Sons.

Bradley, I. M. et al., 2016. *Development and characterisation of an engulfing hydrocarbon pool fire test for hazardous materials pressure vessels.* Edinburgh, 1st Conference on Fire and Blast.

CFD Online, n.d. *Turbulence intensity.* [Online]
Available at: https://www.cfd-online.com/Wiki/Turbulence_intensity

Cole, R., 1960. A photographic study of pool boiling in the region of the critical heat flux. *Journal of the American Institute of Chemical Engineers,* 6(4).

Cole, R., 1967. Bubble frequencies and departure volumes at subatmospheric pressures. *AIChE Journal,* 13(4).

Del Valle, V. H. & Kenning, D. B. R., 1985. Subcooled flow boiling at high heat flux. *International Journal of Heat and Mass Transfer,* 128(10).

Eckert, E. R. G. & Jackson, T. W., 1950. *Analysis of turbulent free-convection boundary layer on flat plate,* s.l.: National Advisory Committee for Aeronautics.

Franc, J.-P., 2007. *Fluid dynaimcs of cavitation and cavitating turbopumps.* Vienna: CISM International Centre for Mechanical Sciences.

Fritz, W., 1935. Berechnung des maximalvolume von dampfblasen. *Phys. Z.,* Volume 36.

George Jr., W. K. & Capp, S. K., 1978. A theory for natural convection boundary layers next to heated surfaces. *International Journal for Heat and Mass Transfer,* 22(6).

Hassan, Y. A., 2016. Multi-scale full-field measurements and near-wall modeling of turbulent subcooled boiling flow using innovative experimental techniques. *Nuclear Engineering and Design,* Volume 299.

Henkes, R. A. W. N. & Hoogendorn, C. J., 1990. Numerical determination of wall functions for the turbulent natural convection boundary layer. *Int. Journal of Heat and Mass Transfer,* 33(6).

Hibiki, T. & Ishii, M., 2003. Active nucleation site density in boiling systems. *International Journal of Heat and Mass Transfer,* Volume 46.

Hoelling, M. & Herwig, H., 2005. Asymptotic analysis of the near-wall region of turbulent natural conection flows. *Journal of Fluid Mechanics,* Volume 541.

Kiš, P. & Herwig, H., 2012. The near wall physics and wall functions for turbulent natural convection. *Int. Journal of Heat and Mass Transfer,* Volume 55.

Kocamustafaogullari, G. & Ishii, M., 1983. Interfacial area and nucleation site density in boiling systems. *International Journal of Heat Transfer,* 26(9).

Kocamustafaogullari, G. & Ishii, M., 1995. Foundation of the interfacial area transport equation and its closure relations. *International Journal of Heat and Mass Transfer,* 38(3).

Krepper, E. & Rzehak, R., 2011. CFD for subcooled flow boiling: Simulation of DEBORAH experiments. *Nuclear Engineering and Design,* Volume 241.

Krepper, E., Rzehak, R., Lifante, C. & Frank, T., 2013. CFD for subcooled flow boiling: Coupling wall boiling and population balance models. *Nucelar Engineering and Design,* Volume 255.

Kurul, N. & Podowski, M. Z., 1991. *On the modelling of multidimensional effects in boiling channels.* s.l., ANS proc. 27th national heat transfer conference.

Lemmert, M. & Chawla, J. M., 1977. Influence of flow velocity on surface boiling heat transfer coefficient.

Lienhard , J. H. & Lienhard, J. H., 2017. *A heat transfer textbook.* 4th ed. Cambridge: Phlogiston Press.

Marie, J. L., Moursali, E. & Tran-cong, S., 1997. Similarity law and turbulence intensity profiles in a bubbly boundary layer at low void fractions. *International Journal of Multiphase Flow,* Volume 23.

Mikielewicz, D., 2003. Hydrodynamics and heat transfer in bubbly flow in the turbulent boundary layer. *International Journal of Heat and Mass Transfer,* 46(2).

Petrovic, S., Robinson, T. & Judd, R. L., 2004. Marangoni heat transfer in subcooled nucleate pool boiling. *Int. J. of Heat and Mass Transfer,* Volume 47.

Podowski, R. M., Drew, D. A., Lahey Jr., R. T. & Podowski, M. Z., 1996. *A mechanistic model of the ebullition cycle in forced convection subcooled boiling.* Kyoto, Japan, International topical meeting on nuclear reactor thermal-hydraulics.

Raithby, G. & Holland, K., 1985. Chapter 6. In: W. Rohsenow & E. G. (. J.P. Hartnett, eds. *Heat Transfer Fundamentals.* New York: McGraw-Hill.

Sato, Y., Sadatomi, M. & Sekoguchi, K., 1981. Momentum and heat transfer in two-phase bubbly flow. *International Journal of Multiphase Flow,* Volume 7.

Sharma and Associates Inc. & Thermdyne Technologies Ltd., 2015. *Rail Tank Car Total Containment Fire Testing,* s.l.: Federal Railroad Administration.

Tolubinsky, V. I. & Kostanchuk, D. M., 1970. Vapour bubbles growth rate and heat transfer intensity at subcooled water boiling. *Heat Transfer,* Volume 5.

Tsuji, T. & Nagano, Y., 1989. Velocity and temperature measurements in a natural convection boundary layer along a vertical flat plate. *Experimental thermal and fluid science,* Volume 2.

Unal, H. C., 1976. Maximum bubble diameter, maximum bubble-growth time and bubble-growth rate during the subcooled nucleate flow boiling of water up to 17.7 MN/m2. *International Journal of Heat and Mass Transfer ,* 19(6).

Venart, J. E. C., Sousa, A., Steward, F. & Prasad, R., 1984. *Experiments on the physical modelling of LPG tank cars under accident conditions.* Brugge, Int. Conf. Storage and Transport of LPG and LNG.

Versteegh, T. A. M. & Nieuwstadt, F. T. M., 1999. A direct numerical simulation of natural convection between two infinite vertical differentially heated walls scaling laws and wall functions. *Int. J. of Heat and Mass Transfer,* Volume 42.

Wang, C. H. & Dhir, V. K., 1993. Effect of surface wettability on active nucletion site density during pool boiling of water on a vertical surface. *Journal of Heat Transfer,* Volume 115.

Zuber, N., 1959. *Hydrodynamic aspects of boiling heat transfer (thesis),* Los Angeles: Ramo-Woolridge Corporation.

5 CFD MODEL

5.1 Design of model

5.1.1 Statement of contribution

The models described herein were designed by the author of the current study, and set-up in CFX by Tommaso Iannaccone, using an initial mesh template provided by Giordano Scarponi. The simulations were executed by Christian Sklorz using the BAM computer cluster in Berlin. Third party assistance was necessary to undertake the simulations due to the computing cluster availability coinciding with the schedule for experimental work.

5.1.2 Objectives of the Model

As described in section 2.3, the Eulerian-Eulerian model with the RPI wall boiling model has become a popular model for researchers seeking to analyse multiphase flow and boiling in tanks and pipes. The primary aim of the simulation described in this section was to apply the same modelling approach to a pressure vessel scenario, and assess whether the model in a basic form can recreate and predict the pressure rise and fluid characteristics observed in tests. A secondary aim was to provide recommendations on modifications to the basic model to improve the predictive capability.

5.1.3 Modelling Approach

A transient Reynolds-Averaged Navier Stokes (RANS) equations computation fluid dynamics simulation was set up in ANSYS CFX v17.2. RANS models introduce averaged and fluctuating terms into the governing equations for conservation of mass, momentum and energy given by equation 5.1 to 5.3 respectively. Such models are often referred to as statistical turbulence models due to the averaging involved in determining the equations (ANSYS Inc., 2013).

Governing conservation equations

Continuity

$$\frac{\partial \rho}{\partial t} + \nabla \cdot (\rho \boldsymbol{u}) = 0 \tag{5.1}$$

Momentum

$$\frac{\partial}{\partial t}(\rho \boldsymbol{u}) + \nabla \cdot (\rho u u) = -\nabla p + \nabla \cdot \tau + S_M \tag{5.2}$$

Energy

$$\frac{\partial (\rho e)}{\partial t} + \nabla \cdot (\boldsymbol{u} \rho e) = \nabla \cdot (\lambda \nabla T) - p \nabla \cdot u + \tau : \nabla u + \tag{5.3}$$

where:

ρ is the density

u is the velocity

p is the pressure

(ρe) is the total energy per unit volume

τ is the stress tensor

S_M, S_E are source terms for momentum and energy equation respectively.

The model geometry was a two-dimensional cross-section of the lower half of a vessel, replicating the initial fluid phase in a 50% full vessel with an internal diameter of one metre as shown in Figure 101. Both the assumption of two-dimensional fluid behaviour and consideration of only the liquid phase are simplifications made to increase the simulation efficiency. It is recognised that the absence of a domain for the initial vapour phase prevents modelling of pressurisation rate, however, the focus of this model was on the boiling and flow dynamics of the subcooled liquid for comparison against real-scale experiments performed with water. It is also recognised that multiphase flow is inherently a three-dimensional scenario and that the assumption of two-dimensional flow will introduce discrepancies between experimental and simulation results due to flow in the direction of the axis of vessel being unaccounted for in the simulation. To minimise flow in the direction of the axis of the vessel, and thereby the discrepancy between simulations and experiments, the experimental set-up was designed to produce uniform heating along the axis of the vessel, and to ensure measurements were taken at the middle of a uniform area. The experimental data generated is also available for use in development of future three-dimensional models.

All parameters not specifically described within this section can be assumed to be taken as the default values recommended by ANSYS in the wall boiling model tutorials. This design choice was made to focus the present study on the influence of the RPI model parameters identified in section 2.3.3. A base scenario was set up to use the default wall boiling parameters within CFX, as described below. The base scenario was then compared with a modified boiling characteristics model, using wall boiling parameters taken from the experimental measurements described in section 4.6.1. To reflect common practice, the wall-boiling model was implemented using the CFX default settings except where described in this section.

a)

b)

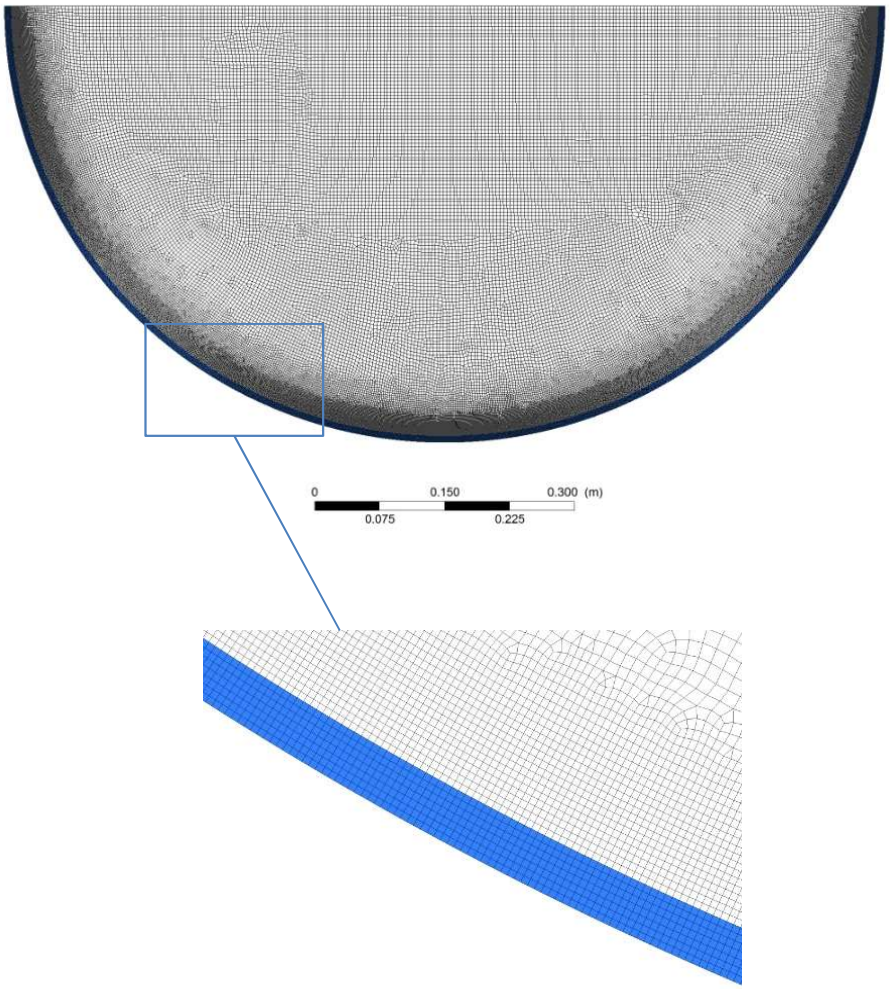

Figure 101 – Mesh used in the present study: a) overview, b) detail close to tank wall (blue shaded area).

5.1.3.1 Grid design

The governing equations were solved for each control volume resulting from the spatial discretisation of the domain. The liquid domain and tank wall were modelled through the construction of an unstructured mesh, featuring 72,245 elements. Mesh independence of the results was evaluated through running the same simulation on two other different grids and comparing results: a finer one, with 118,415 elements, and a coarser one, with 36,620 elements. The meshes consisted of a structured inflation layer of 10 to 18 cells thickness, followed by an unstructured region. The meshes were chosen partly based on preliminary studies (Scarponi, et al., 2016) of the inflation layer cell size that permitted convergence. As described in section 2.3.3, as near-wall cells reduce in size the void fraction tends to increase. Excessive

void fractions in the near wall region leads to an over-estimation of the heat transfer to the liquid phase when using a constant heat flux, which in turn leads to excessive liquid temperatures and convergence issues. Initial runs with a finer near-wall cell size failed to produce convergence. As discussed in section 4.4.7, the PIV analysis interrogation area was selected to give the best match possible with the maximum grid size (a PIV analysis area of 5.0 to 5.9mm, compared with a maximum face size of 5.7mm in the coarse mesh).

Table 39 - Grid features for results independence study

Item	Coarser	Base case	Finer
Max. face size (m)	$5.657 \cdot 10^{-3}$	$4.000 \cdot 10^{-3}$	$2.800 \cdot 10^{-3}$
Min. size (m)	$1.414 \cdot 10^{-4}$	$1.000 \cdot 10^{-4}$	$7.000 \cdot 10^{-5}$
No. of nodes	37157	72918	119580
No of elements	36620	72245	118415
First layer thickness	$1.000 \cdot 10^{-3}$	$1.000 \cdot 10^{-3}$	$1.000 \cdot 10^{-3}$
Growth rate	1.2	1.2	1.1
Maximum layers	10	10	18

Table 40 - Governing equations for a turbulent multiphase simulation

ID	Equations	Parameters definition
A	$\frac{\partial}{\partial t}(r_\alpha \rho_\alpha) + \nabla \cdot (r_\alpha \rho_\alpha \boldsymbol{u_\alpha}) = S_{MS\alpha} + \sum_{\beta=1}^{N_p} \Gamma_{\alpha\beta}$	r_α: volume fraction of phase α ρ_α: density of phase α u_α: velocity vector for phase α $S_{MS\alpha}$: user specified mass source terms $\Gamma_{\alpha\beta}$: mass flow rate per unit volume from phase α to β
B	$\sum_{r_\alpha=1}^{N_p} r_\alpha = 1$	N_p: number of phases
C	$\frac{\partial}{\partial t}(r_\alpha \rho_\alpha u_\alpha) + \nabla \cdot (r_\alpha(\rho_\alpha u_\alpha u_\alpha)) = -r_\alpha \nabla p_\alpha + \nabla \cdot (r_\alpha \mu_\alpha(\nabla u_\alpha + (\nabla u_\alpha)^T)) + \sum_{r_\alpha=1}^{N_p}(\Gamma^+_{\alpha\beta} u_\alpha - \Gamma^+_{\beta\alpha} u_\alpha) + S_{M\alpha} + M_\alpha$	u_α: velocity vector for phase α p_α: pressure distribution for phase α μ_α: dynamic viscosity for phase α M_α: interfacial forces acting on phase α
D	$\frac{\partial}{\partial t}(r_\alpha \rho_\alpha e_\alpha) + \nabla \cdot (r_\alpha \rho_\alpha u_\alpha e_\alpha) = \nabla \cdot (r_\alpha \lambda_\alpha \nabla T_\alpha) + r_\alpha \tau_\alpha : \nabla u_\alpha + Q_\alpha$	λ_α: effective thermal conductivity for phase α e_α: internal energy of phase α $\tau_\alpha : \nabla u_\alpha$: viscous dissipation term Q_α: interphase heat transfer to phase α across interfaces with other phases
E	$\frac{\partial}{\partial t}(r_\alpha \rho_\alpha k_\alpha) + \nabla \cdot \left(r_\alpha \left(\rho_\alpha k_\alpha u_\alpha - \left(\mu_\alpha + \frac{\mu_{T\alpha}}{\sigma_k} \right) \nabla k_\alpha \right) \right) = r_\alpha (P_\alpha - \rho_\alpha \varepsilon_\alpha)$	k_α: turbulent kinetic energy. $\mu_{T\alpha}$: turbulent viscosity (see eq. G) $\sigma_k = 1.00$: turbulence standard k-ε model constant. ε_α: turbulence dissipation rate P_α: turbulence production due to viscous forces

ID	Equations	Parameters definition
F	$\frac{\partial}{\partial t}(r_\alpha \rho_\alpha \varepsilon_\alpha) + \nabla \cdot \left(r_\alpha \left(\rho_\alpha \varepsilon_\alpha u_\alpha - \left(\mu_\alpha + \frac{\mu_{T\alpha}}{\sigma_\varepsilon} \right) \nabla \varepsilon_\alpha \right) \right) = r_\alpha \frac{\varepsilon_\alpha}{k_\alpha} (C_{\varepsilon 1} P_\alpha - C_{\varepsilon 2} \rho_\alpha \varepsilon_\alpha)$	$\sigma_\varepsilon = 1.30$, $C_{\varepsilon 1} = 1.44$; $C_{\varepsilon 2} = 1.92$ are the turbulence standard k-ε model constants.
G	$\mu_{T\alpha} = \frac{\rho_\alpha C_\mu {k_\alpha}^2}{\varepsilon_\alpha}$	$C_\mu = 0.09$ turbulence standard k-ε model constant.
H	$\nu_{td} = \frac{\nu_{tc}}{Pr_t} \rightarrow \mu_{td} = \frac{\rho_d}{\rho_c} \frac{\mu_{tc}}{Pr_t}$	ν_{td}: dispersed phase kinematic turbulent viscosity ν_{tc}: continuous phase kinematic turbulent viscosity Pr_t: turbulent Prandtl number:

5.1.3.2 Multiphase model

For the present study, the Eu-Eu inhomogeneous approach was chosen. This model was selected over the volume of fluid (VOF) multiphase model due to the limitation of the VOF model whereby the phases share the same temperature and velocity field. This is evidently not the case in subcooled wall boiling, where the vapour phase will have a higher temperature and, post bubble departure, a higher velocity. The differences between the models, and hence the justification for selection of the Eu-Eu approach, is described further in section 2.3. In the inhomogeneous multiphase model each separate phase possesses its own flow field and the fluids interact via interphase transfer terms (closure relationships). There are different sub-models available for modelling the interfacial area density and the interphase transfer terms. In this work the particle model was used. This is an appropriate sub-model when one of the phases is continuous and the other dispersed, like vapour bubbles generated during boiling. The dispersed phase particles are assumed to be spherical.

For the steam-water flow regime, the energy equation is solved for the liquid phase, whilst vapour was assumed to be at the saturation temperature everywhere. The interfacial momentum transfer between the two phases was modelled in terms of drag force using the model by Ishii & Zuber (1979). In this simplified model non-drag forces are not considered.

Particle induced turbulence for bubbly flow was modelled using the Sato, et al., (1981) eddy viscosity model for the continuous phase.

Heat transfer was modelled through the two-resistance option, meaning that each of the two phases has a different heat transfer coefficient. For the continuous liquid phase, interphase heat transfer coefficient was calculated using the model proposed by Ranz & Marshall (1952):

$$h_{lg} = \frac{k_l}{d_b} Nu = \frac{k_l}{d_b}(2 + 0.6Re^{0.5}Pr^{0.33}) \quad (5.4)$$

The vapour phase was assumed to have zero resistance, which has the effect of assuming mass transfer occurs extremely quickly between the liquid and vapour, minimising differences in species concentration across the interface between phases. In practical terms, implementation of the zero-resistance model for the vapour phase results in the interfacial temperature being the same as the phase temperature, which is equal to saturation condition in this simulation. The zero-resistance model was chosen based on the wide acceptance for dispersed spherical gas bubbles in liquid, and for its computational efficiency.

5.1.3.3 Turbulence model

A first estimation of Rayleigh number (Ra) of 1 x 10^{12} suggests that the flow inside the heated tank is turbulent (noting that transition from a laminar to turbulent regime in natural convection is considered to happen for 10^8 < Ra < 10^{10}).

For the present study, turbulence for the continuous phase and the dispersed phase were evaluated using different models. For the continuous liquid phase, the k-ε turbulence model was used. It is a well-known two-equation model (see equations E, F and G in Table 40) already used in other fluid dynamic studies of hazardous materials vessels by D'Aulisa, et al., (2014) and numerous boiling studies. Although the majority of recent studies state that k-ω (SST) method is to be preferred this is not a unanimous position (as discussed in section 2.3). The k-ε turbulence model was adopted in the present study because the grid size chosen (reasoning discussed above) was too coarse to allow resolution of the viscous sublayer and instead required the use of wall functions in the near wall region, ruling out the k-ω or k-ω (SST) method (these are not discussed further here but are treated extensively elsewhere in Launder & Spalding (1974)). It would be preferable to resolve the boundary layer using a refined grid, however, the currently available literature shows this has not been possible to date due to the convergence issues described above. It therefore remains, at present, necessary to use wall functions.

The turbulent behaviour of the vapour bubbles was modelled by means of the dispersed phase zero equation using equation H in Table 40.

To account for the interphase turbulent dispersion force, the Favre average drag model was activated, with the CFX default value used for the dispersion coefficient. For further details refer to Burns, et al., (2004).

5.1.3.4 Fluid properties

The model assumed constant properties both for liquid and vapour phase. Use of fixed properties is a substantial simplification to be rectified in future work through more accurate specification of boiling parameters to achieve an accurate vapour volume fraction. It was implemented in the present study to promote convergence and model stability by avoiding the known tendency of the Eu-Eu model with RPI wall boiling model to over-estimate void fractions in the near wall region (Krepper, et al., 2013), which leads to an over-estimation of the heat transfer to the liquid phase and, in turn, to excessive liquid temperatures. Initial runs with variable properties frequently resulted in the liquid temperature continuously rising until the simulation failed to achieve convergence.

Buoyancy effects were accounted for using the Boussinesq approximation, which considers density as a constant value in all solved equations except for the buoyancy term in the momentum equation.

Table 41 - Liquid water and vapour physical properties used in this work

Item	Value	Units
Liquid water		
Density	954	$kg\ m^{-3}$
Dynamic viscosity	$2.9136 \cdot 10^{-4}$	Pa s
Specific heat capacity	4216	$J\ kg^{-1}\ K^{-1}$
Thermal conductivity	0.6067	$W\ m^{-1}\ K^{-1}$
Thermal expansion	$2.1 \cdot 10^{-4}$	K^{-1}
Buoyancy reference density	954	$kg\ m^{-3}$
Buoyancy reference temperature	318.15	K
Vapour		
Density	0.540	$kg\ m^{-3}$
Dynamic viscosity	$1.2162 \cdot 10^{-5}$	Pa s
Specific heat capacity	2069	$J\ kg^{-1}\ K^{-1}$
Thermal conductivity	0.02475	$W\ m^{-1}\ K^{-1}$

5.1.3.5 Boundary and initial condition

A symmetry boundary condition was employed for the two transversal planes that enclose the liquid region (+/- Z faces), accounting for symmetry in the axial direction of the tank, as well as at the two small portions of steel wall adjacent to the liquid-vapour interface.

The face located at the liquid-vapour interface was modelled as a degassing outlet. This boundary condition allows the dispersed phase (bubbles) to flow out of the domain, while the continuous phase sees this boundary as a free-slip wall and does not leave the domain.

A constant heat flux of 100 kW/m² was imposed at the outer wall of the tank, simulating a situation of full engulfment in a hydrocarbon fire. Given the parallel timeframe of performing experiments and simulations it was not possible to use a magnitude of total heat equivalent to an actual test described in section 3.4.3. Instead, the value used was selected based on the target conditions described in section 2.1.9. The application of a constant total heat flux value is a simplification which is appropriate for modelling the liquid-filled zone only in the present study. It would not be appropriate for modelling the vapour space of a vessel, given the rise in substrate temperature in the vapour space, resulting in a reduction in net heat flux over time at a rate related to the radiative fraction of the total heat flux. Future work that includes the vapour space would need to model radiation and convection separately and consider thermal losses due to radiation from the vessel shell itself.

Initial conditions were set up to reproduce the experimental test conditions where possible. At the beginning of the simulation the water inside the tank was considered motionless, at a temperature of 293.15 K, at an absolute pressure of 1 atm (101 kPa), and in thermal equilibrium with the steel wall (also set to 293.15 K).

The turbulence kinetic energy was set to an initial value of $1.0x10^{-30}$ m²/s² and turbulence dissipation rate set as 1.0×10^{-15} m²/s³.

For the vapour phase, saturation conditions were assumed to be valid throughout the entire simulation and the initial temperature was set to 373.15 K.

In order to give the RPI boiling model an initial seed of vapour phase, the vapour volume fraction is initialized to 1.0×10^{-15}.

Table 42 - Initial and boundary conditions specifications

Item	Value	Units
Absolute pressure	101325	Pa
Liquid temperature	293.15	K
Steel temperature	293.15	K
Vapour temperature	373.15	K
Liquid velocity	0	m s^{-1}
Vapour velocity	0	m s^{-1}
Turbulence kinetic energy	$1x10^{-30}$	m^2 s^{-2}
Turbulence dissipation rate	$1x10^{-15}$	m^2 s^{-3}
Liquid volume fraction	$(1-1x10^{-15})$	-
Vapour volume fraction	$1x10^{-15}$	-
Wall heat flux	100000	W m^{-2}

5.1.3.6 Boiling model

Subcooled wall boiling takes place when the liquid temperature exceeds the saturation temperature in close proximity to the wall, despite the bulk average liquid temperature being below the saturation temperature.

Evaporation starts at nucleation sites, where vapour bubbles grow and eventually detach when external forces exceed surface tension forces. The wall total area is partitioned into a cumulative area affected by bubble growth, and the remaining area which is not. The wall heat transfer to the liquid may be described by single phase convective heat transfer in the area not affected. The remaining part of wall heat flux is used to provide energy for liquid evaporation and for superheating the liquid that replaces vapour bubbles once they have detached from the wall. This latter phenomenon is known as quenching.

The model describes the total wall heat flux as a sum of three terms:

$q_w = q_c + q_e + q_q$

Where q_c is the heat flux for convective heating of the liquid phase on the wall area fraction not affected by bubble formation; q_e is the heat flux for evaporation of the superheated microlayer and q_q is the heat flux for quenching between bubble departure and formation.

For the base case, all RPI model settings were taken from default ANSYS CFX v17.2 settings. The modified boiling characteristics models used values taken from experimental data for bubble departure diameter, departure frequency and nucleation site density. The differences in these parameters are described below.

For both cases the vapour phase temperature was kept constant at the saturation condition for atmospheric pressure, the onset of boiling superheating was set to 0.05 K, and the maximum area fraction of bubble influence was set to 0.8. Use of the RPI sub-models for bubble diameter and quenching heat flux require a value for the bulk liquid temperature (T_l). To achieve results independent of meshing, the default liquid characteristic temperature is estimated using the logarithmic form of temperature wall functions. For further details refer to Egorov & Menter (2004).

<u>Base case – CFX default parameters</u>

Bubble departure diameter (D_b) was estimated using the model of Tolubinsky & Kostanchuk (1970) with default settings. This model depends only on the degree of liquid sub-cooling and was originally proposed based on horizontal heater surfaces in contact with water at high pressures.

$$D_b[mm] = \min\left[0.6\ \exp\left(-\frac{\Delta T_{sub,l}}{45\ [K]}\right), 1.4\right] \tag{5.5}$$

The model used to estimate wall nucleation site density (N) was that of Lemmert & Chawla (1977), based on pool boiling of saturated water. The model has been modified somewhat in implementation in CFX, and when implemented with the default settings is as follows:

$$N\ [m^{-2}] = \ 793840\ [m^{-2}] \cdot (\frac{\Delta T_{su}}{10\ [K]})^{1.805} \tag{5.6}$$

The bubble departure frequency (f) was estimated using the model of Cole (1960), taking the drag coefficient factor (C_d) as one.

$$f\ [s^{-1}] = \sqrt{\frac{4g(\rho_l - \rho_g)}{3C_d D_b \rho_l}} \tag{5.7}$$

Modified boiling characteristics case

The source of the values used are given in section 4.6.1. For ease of reference the values are repeated below:

- D_b: 0.25mm
- f: 0.033
- N: 160,000

Note that both the base case and modified boiling characteristics case used f as the basis of the bubble waiting time (tw = 0.8/f). The changes implemented are expected to decrease the bubble departure diameter slightly, decrease the departure frequency by 4 orders of magnitude, and increase the nucleation site density by a factor of 20.

5.1.3.7 Analysis type and solver settings

Three transient simulations were run for the base case (including the finer and coarser mesh for the grid independence study) and one further transient simulation for the modified boiling characteristics case, each lasting for a total time of 120 seconds. The simulations were limited to this time as it matched that after which the PIV data quality deteriorated within the experimental work described in section 4.4.7. Adaptive time stepping was used, based on a maximum Courant number value of 1.0. The initial time step size was set to 0.001 seconds, with a maximum allowable time step of 0.02 seconds.

A summary of solver and analysis settings is given in Table 43.

Table 43 - Solver and additional settings summary

Item	Option/value
Analysis settings:	
Total time	120 s
Initial timestep	0.001 s
Maximum timestep	0.02 s
Minimum timestep	0.001 s
Courant number	1
Solver control:	
Advection scheme	high resolution
Transient scheme	second order backward Euler
Turbulence numerics	high resolution
Convergence - min/max coeff. loops	1/20
Convergence criteria - residual RMS	$1.0 \cdot 10^{-4}$
Conservation target	0.01
Fluid specific models:	
Liquid heat transfer model	thermal energy
Liquid buoyancy model	Boussinesq
Liquid reference temperature	45°C
Liquid turbulence model	k-e scalable
Vapour heat transfer model	Isothermal
Vapour fluid temperature	saturation temp.
Vapour buoyancy model	Boussinesq
Vapour reference temperature	saturation temp.
Vapour turbulence model	dispersed phase zero equation
Fluid-pair models:	
Surface tension coefficient	0.038 N/m
Interphase transfer	particle model
Momentum transfer	Ishii-Zuber
Turbulence transfer	Sato enhanced
Mass transfer	phase change
Wall boiling model	RPI
Heat transfer model	2 resistance: liquid: Ranz-Marshall, vapour: zero-resistance
Boundary conditions:	
Interface model	conservative interface flux
Mesh connection	GGI

5.2 Results

5.2.1 Statement of contribution

Following completion of the simulations on the BAM server, extraction of the raw data and images was performed by Christian Sklorz, except for grid independence study tabulated values which were extracted by Tommaso Iannaccone. Analysis of the data was performed by the author of the current study.

5.2.2 Grid Independence Study

The base, finer and coarser mesh simulations have been directly compared. Figure 102 shows the predicted velocity boundary layer profiles for the three cases at 120s. Figure 103 shows the equivalent temperature profiles. Figure 104 and Figure 105 compare the deviation between the grid independence study cases for the temperature and velocity profiles, respectively.

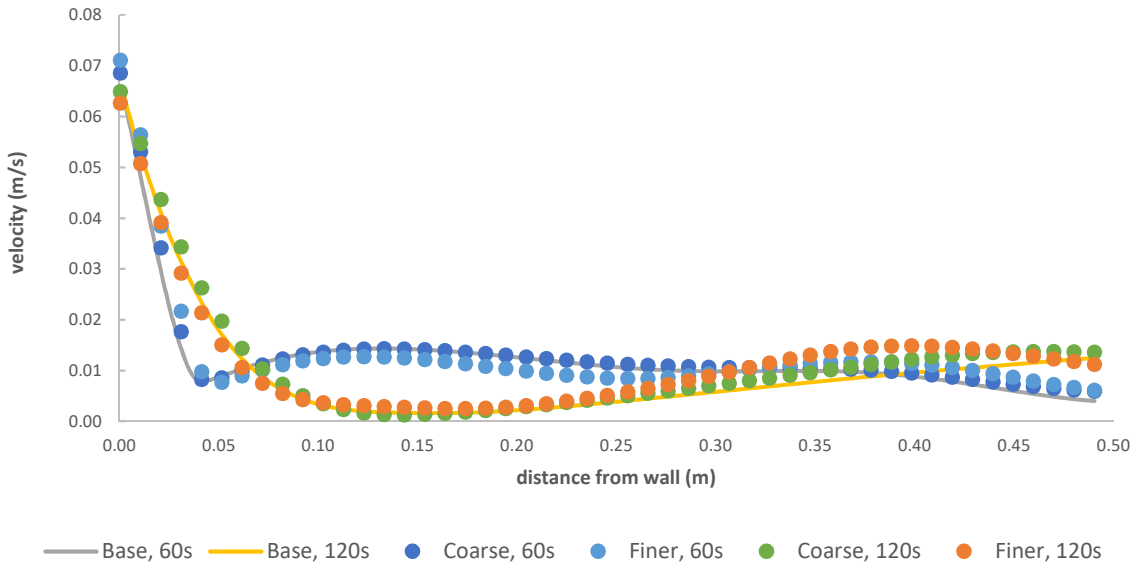

Figure 102 – Velocity profiles at 0.4m height (along a horizontal line)

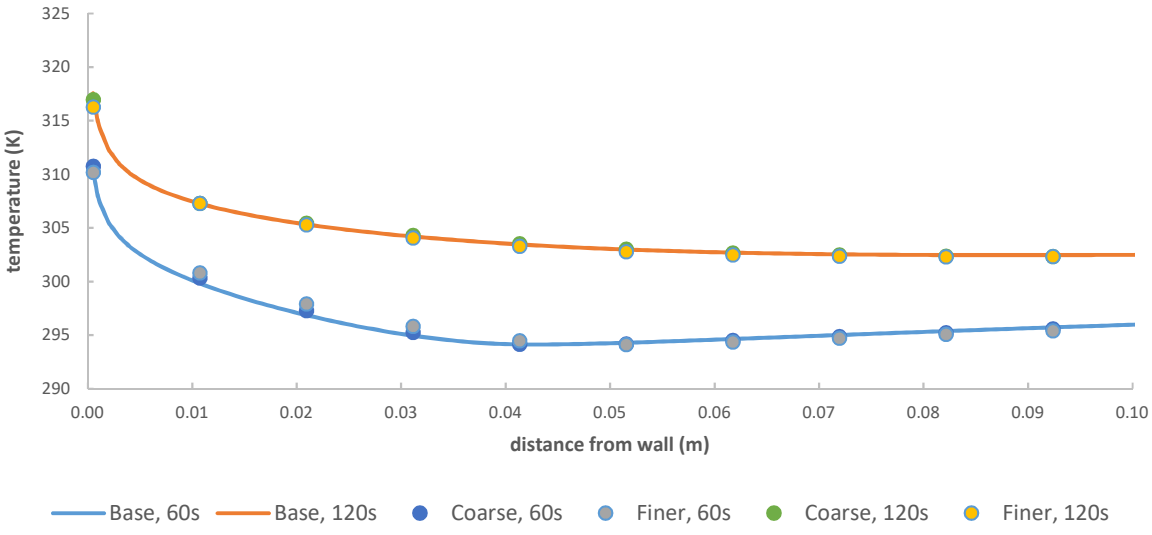

Figure 103 – Temperature profiles at 0.4m height (along a horizontal line)

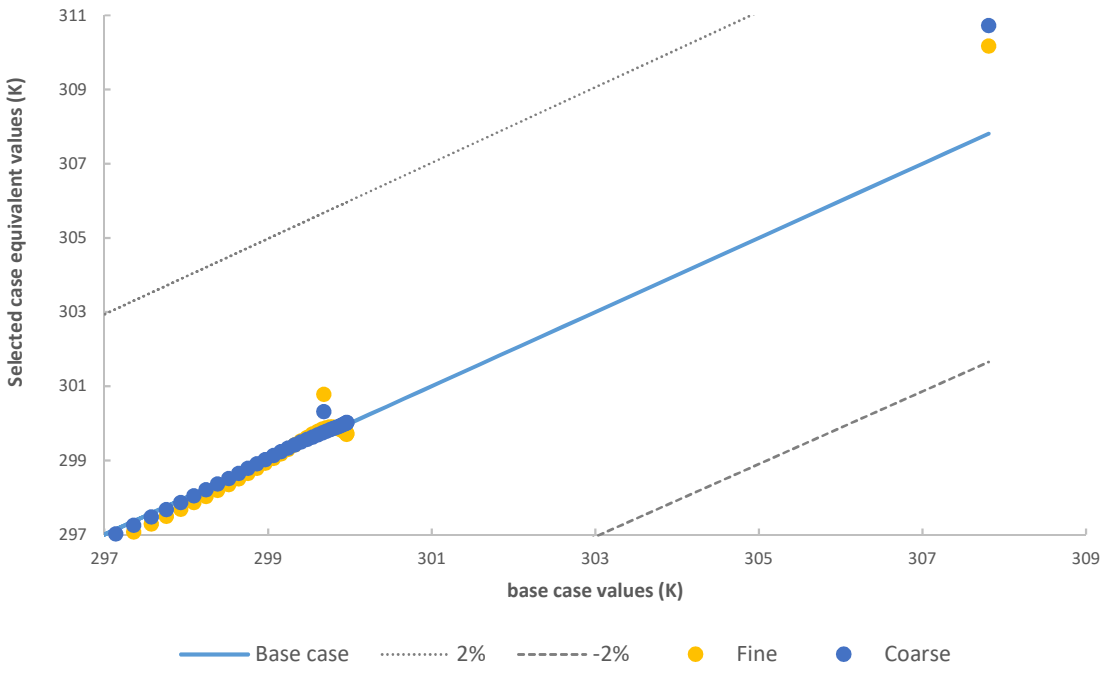

Figure 104 – Comparison of temperature values across the 3 different grids

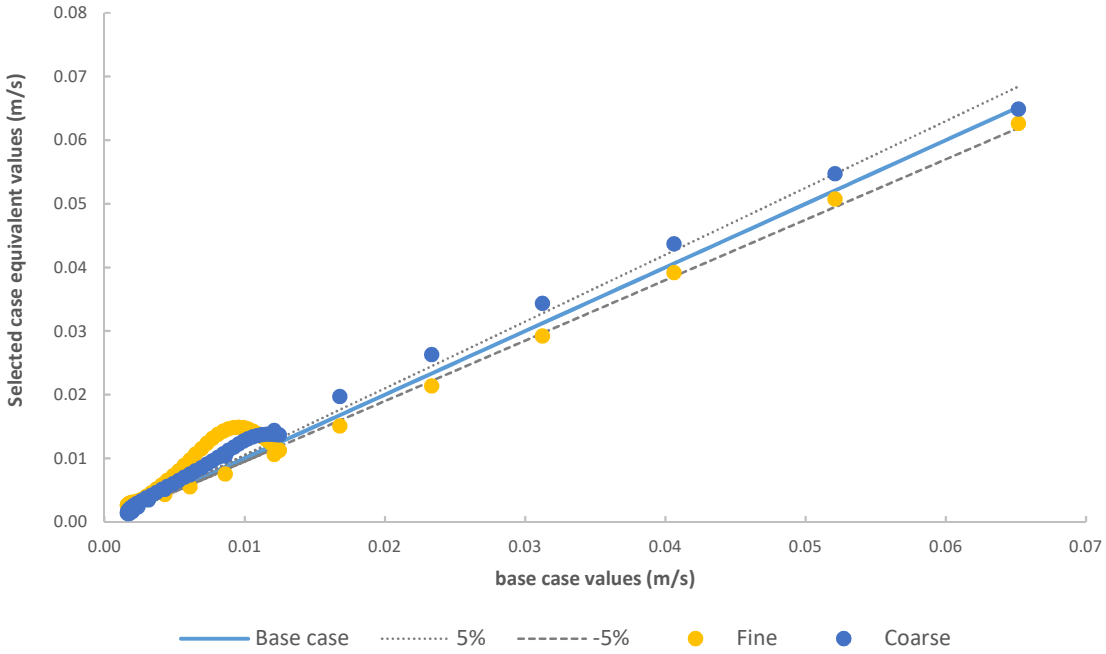

Figure 105 – Comparison of velocity values across the 3 different grids

The grid independence study shows reasonable agreement between the different grid study cases. The temperature variations between studies are typically within +/1%. Velocity variations are greater, with differences of up to 50% recorded, however this number disguises the fact that variations in the boundary region were closer to 5%. The convection cells that form in the bulk fluid during the simulation are not symmetrical, attributed to numerical instabilities, and result in velocity profiles variations that have significant relative differences, yet minor differences in absolute terms. It can be seen from Figure 102 that the profiles show good agreement, given the variability in bulk flow patterns shown in Figure 107 through to Figure 114.

The near-wall values are similar across grids. This is unsurprising, as the current set-up does not seek to resolve the boundary layer, but obtains temperature profiles and velocities through use of wall functions. This choice was made to prevent excessive vapour volume fractions in the near-wall cell from causing model instabilities, however further work is required to further refine the optimum grid size near the wall.

5.2.3 Base case results

Figure 106 through to Figure 114 show the results from the base case using the finer mesh. It can be seen that the simulation predicts the growth of boundary layers within the first 90 seconds, after which they become reasonably stable.

In the first 90 seconds the simulation predicts multiple small plumes rising from the bottom of the vessel, however from 90 seconds the flow patterns become more established and this is predicted to settle into one main plume which remains close to the centre of the vessel.

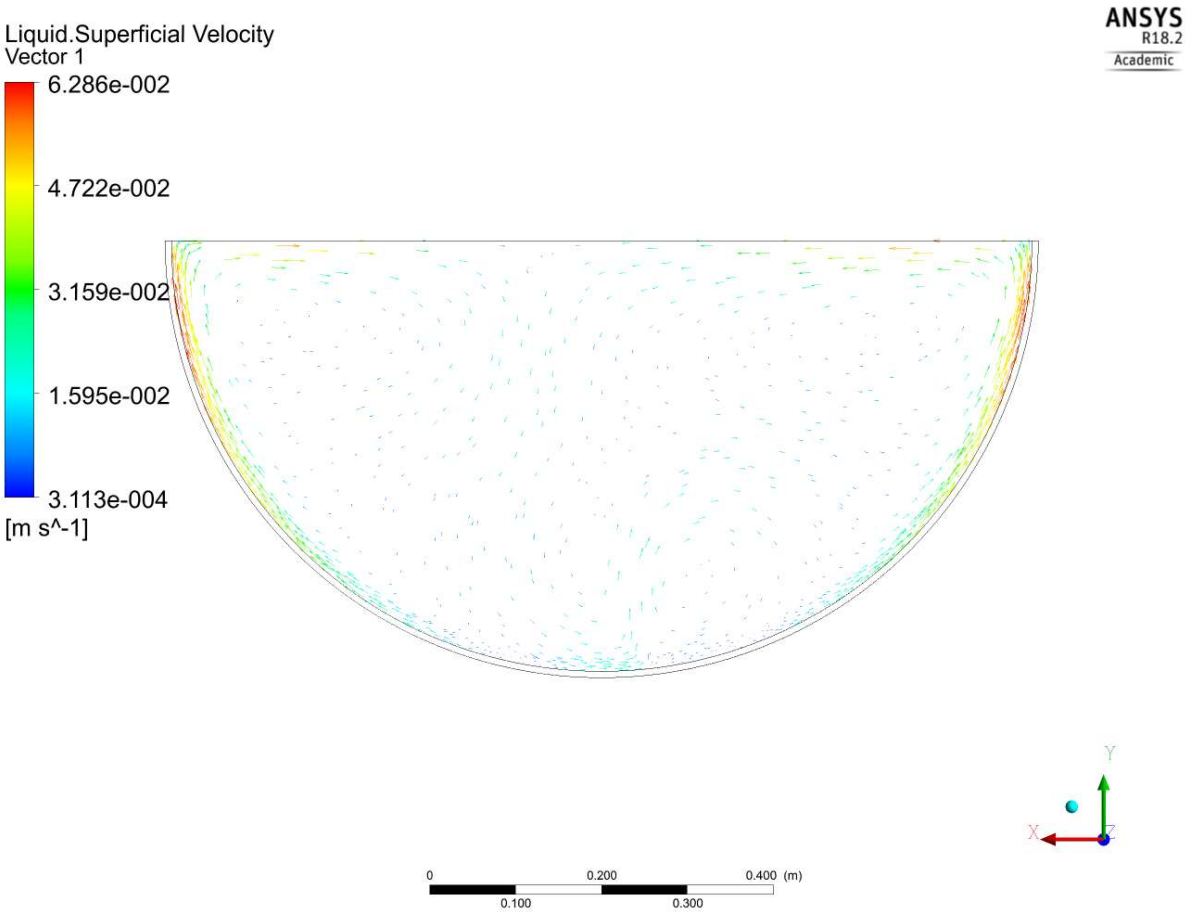

Figure 106 – Velocity vectors at 120 s, finer case

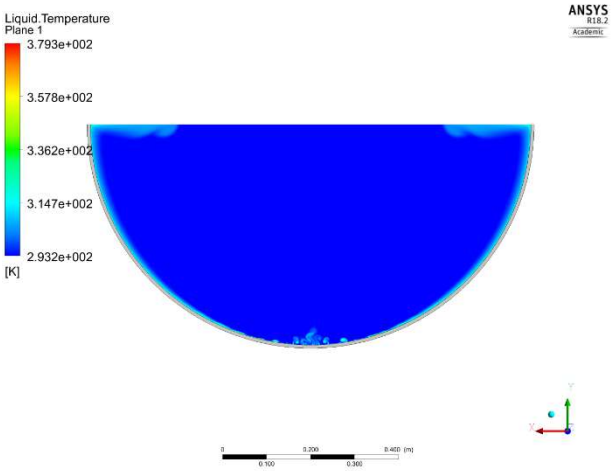

Figure 107 – Temperature, 30 s

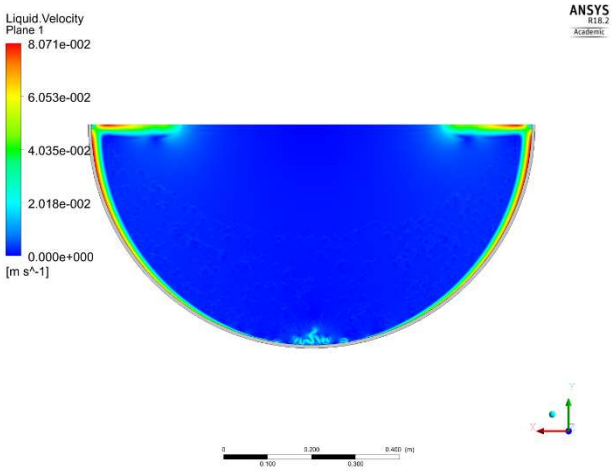

Figure 108 – Velocity, 30 s

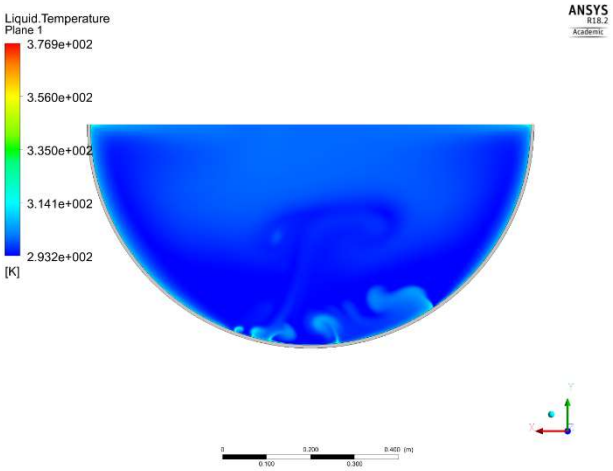

Figure 109 – Temperature, 60 s

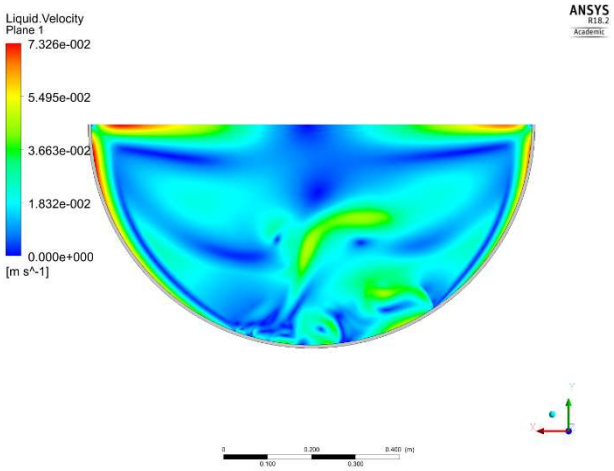

Figure 110 – Velocity, 60 s

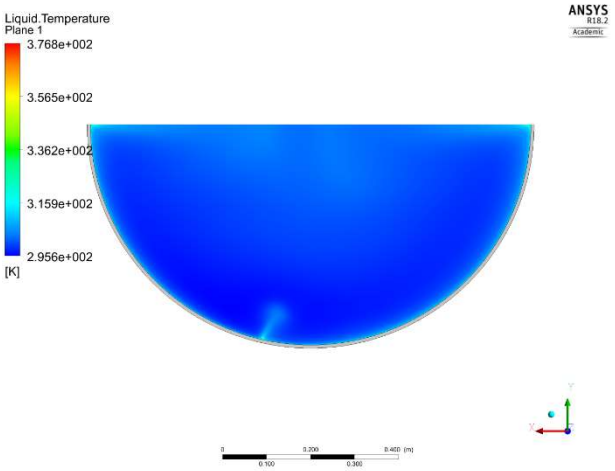

Figure 111 – Temperature, 90 s

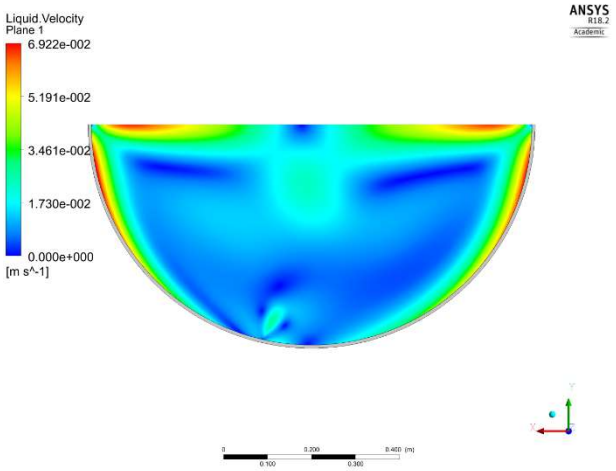

Figure 112 – Velocity, 90 s

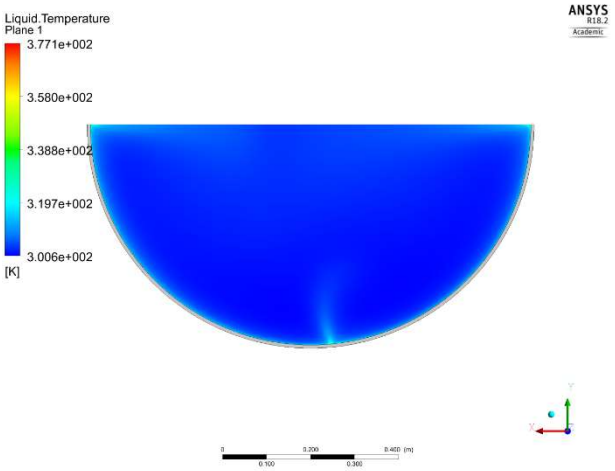

Figure 113 – Temperature, 120 s

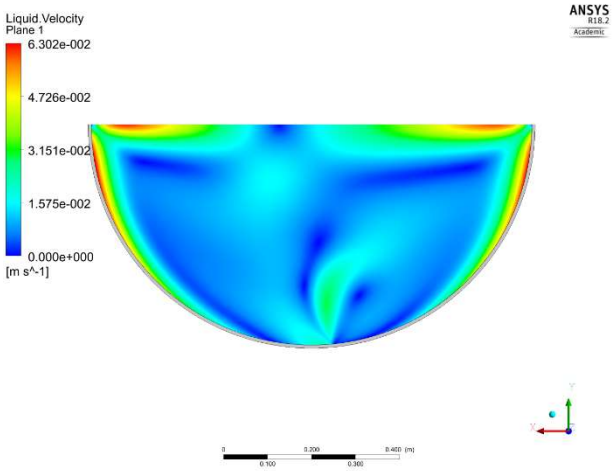

Figure 114 – Velocity, 120 s

5.2.4 Modified boiling characteristics results

The modified boiling statistics collectively increase the partitioned area of the wall influenced by bubbles yet reduce the rate of vapour mass generation significantly. Given the fixed heat flux boundary conditions the single-phase convective heat transfer via the non-bubble wall area must therefore increase. An increase in both temperature and velocities was therefore expected. Figure 115 shows the velocity vectors using the modified boiling characteristics. The maximum velocity at 120 seconds increased from approximately 6.3 mm/s to 9.9 mm/s. Figure 116 shows the temperature distribution. The maximum temperature at 120 seconds decreased from approximately 104°C to 91°C.

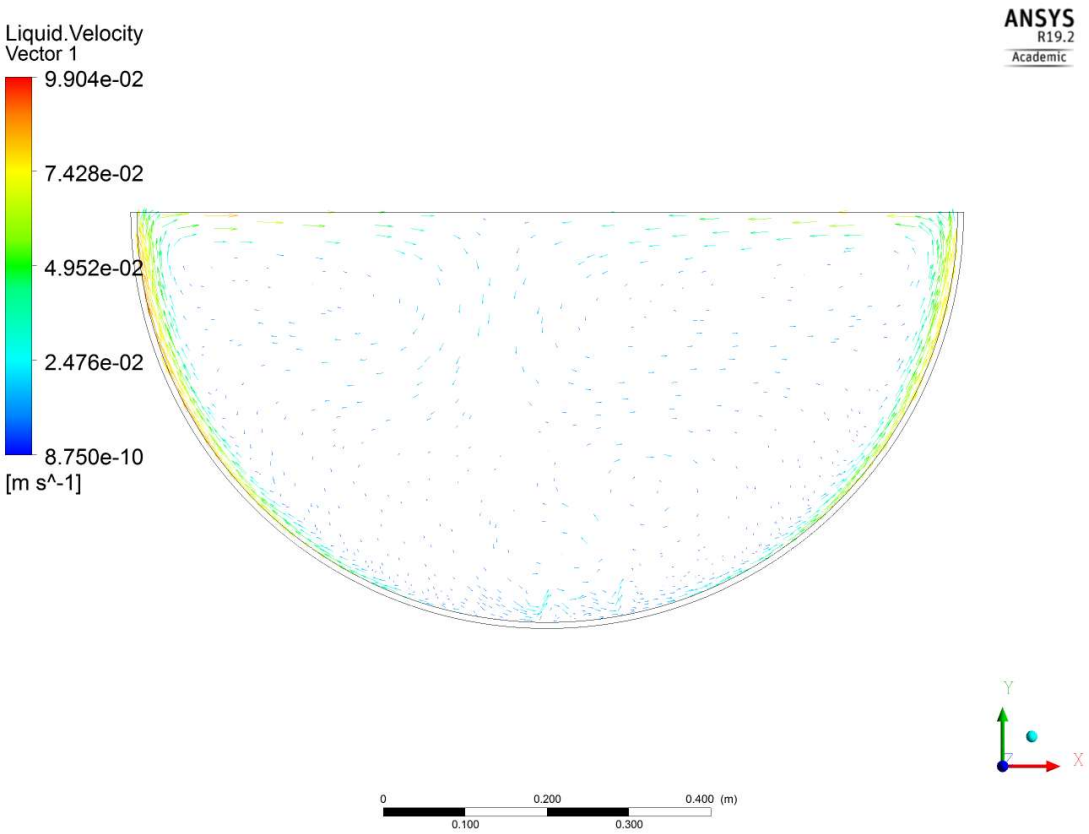

Figure 115 – Velocity vectors, 120 s, modified boiling characteristics

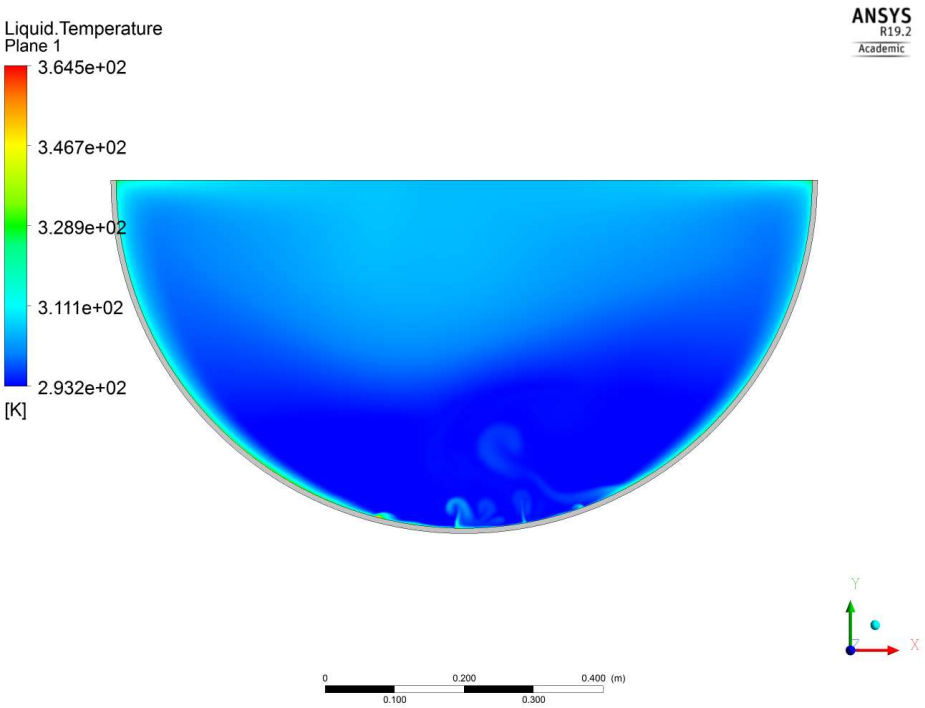

Figure 116 – Temperature, 120 s, modified boiling characteristics

The reduction in peak wall temperature to below that required for the onset of boiling requires further investigation. It could be an indication that either the model set-up or the boiling parameters used are incorrect, or it could demonstrate that heat transfer by single-phase convection was of a sufficient magnitude to maintain the wall temperature below that required for significant boiling.

5.2.5 Comparison with experimental data

The velocities and temperatures predicted are compared with those obtained by PIV and thermocouples within selected tests below. Each test differed from the simulation in terms of heat flux or fill level, making detailed quantitative comparisons against all tests of limited value. Comparison of the velocity and temperature profiles against selected tests are given in Figure 117 through to Figure 119.

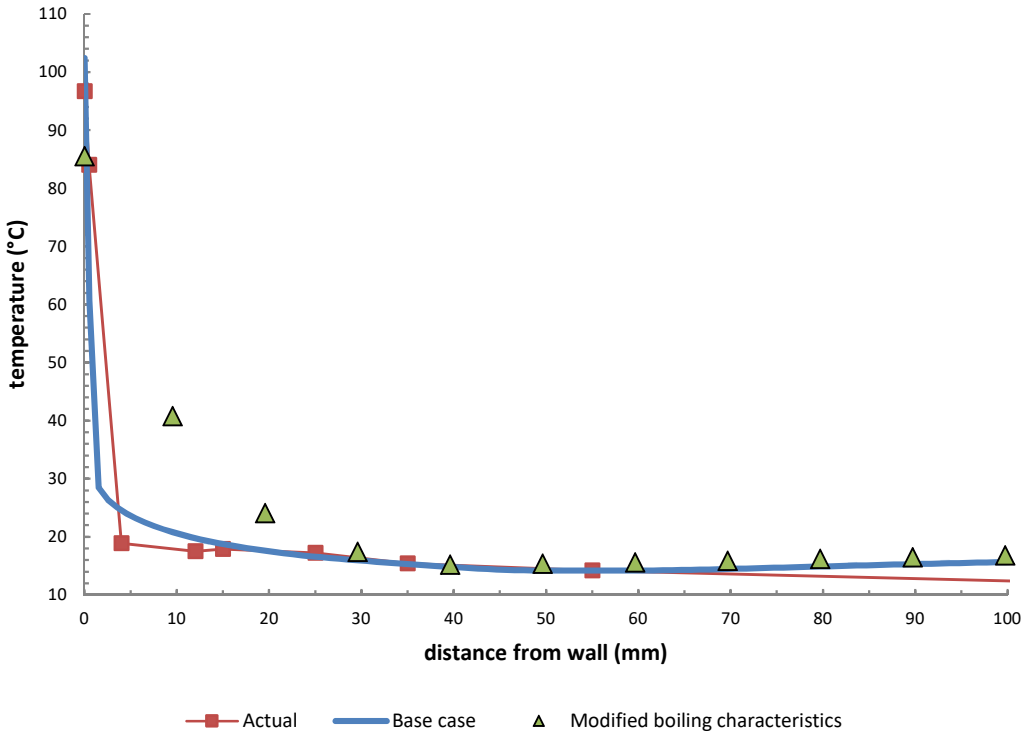

Figure 117 – Temperature comparison, test 22 (water, 62% fill, 67 kW/m^2), Station A - 135°, 60s (CFD cases shifted 6°C to match T22 actual starting temperature, excluding wall temperatures)

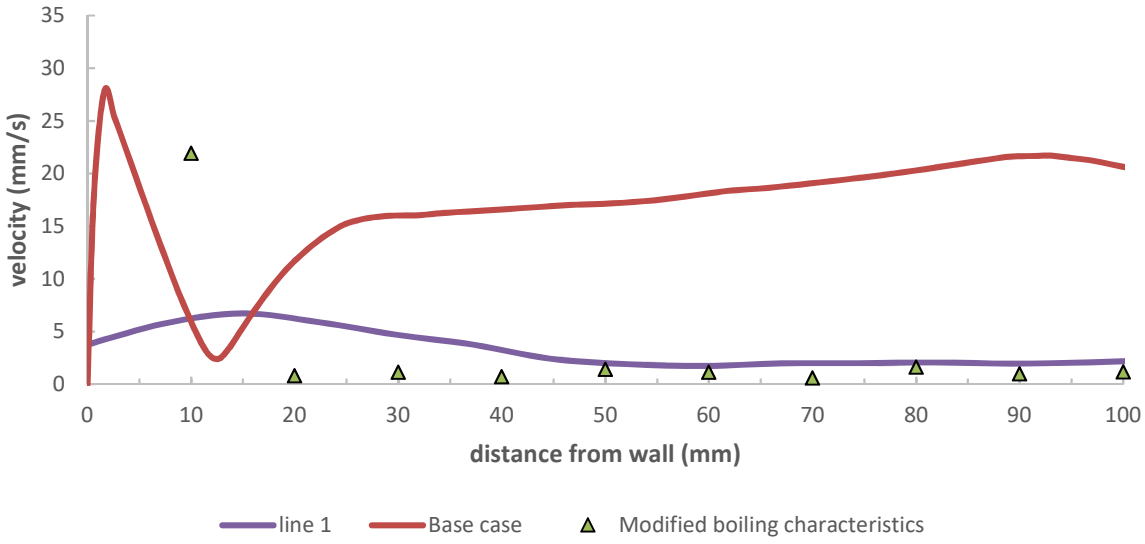

Figure 118 – Total velocity comparison, test 15 (water, 72% fill, 96 kW/m^2), 135°, 60 s

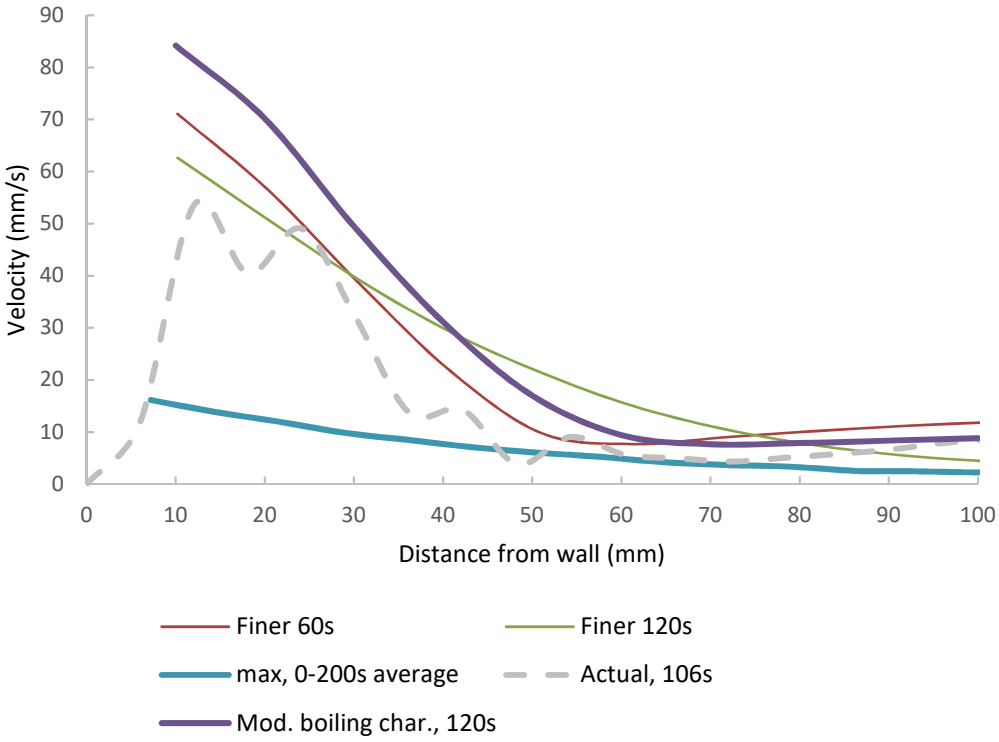

Figure 119 – Total velocity comparison, test 19 (water, 96% fill, 90kW/m^2), 90°, 60-120 s

The temperature profile of the base case shows the best match with the experimental data. Simulation results using the modified boiling characteristics resemble base case results at shorter durations before boiling has become significant. It

can be stated that the base case and modified case simulations represent simulations of significant boiling and insignificant boiling (with single phase convection dominant). The single-phase convection dominant simulation predicts a temperature profile that decreases more gradually, and a velocity profile that decreases less gradually, compared to when boiling is more significant. This can be explained by boiling reducing the heat transfer into the liquid phase, thereby reducing the thickness of the thermal boundary layer, and by the bubble-fluid interaction increasing the turbulence and acting to grow the velocity boundary layer. As the experimental results best match the base case scenario, it would indicate that boiling is significant within 120 seconds of the test start.

Use of modified boiling characteristics should also avoid fixed values. They should be implemented via equations linked to the wall superheat to ensure boiling does not occur until wall temperatures reach a sufficiently high value. This would allow boiling cycles and avoid 'forced' boiling preventing the wall temperatures from reaching a realistic value, which may have occurred within the simulation described here. The measured fluid temperature values within 15mm of the wall are not predicted well by the simulations, which predict a more gradual rate of temperature decrease. However, changes in measurement distance from the vessel wall due to vessel deformation during tests may be partially responsible by increasing the distances compared to those shown. Both cases simulated show a thermal boundary layer that extends to 30-50 mm, similar to that observed in the thermocouple data throughout the test series.

The velocity profile measurements are difficult to compare, given the variability in measured values, however the simulation results exhibit significant deviations from the measured values. Figure 119 shows the simulated profiles do reflect the measured profile quite well at intermittent times between 90 and 120 seconds at 90°. They also predict the overall velocity boundary layer to be approximately 50-100 mm thick. In the absence of significant boiling, such as the base case at 60 seconds or the modified boiling characteristics at 120 seconds, the lower thickness of 50mm is expected. When boiling is more significant (base case at 120 seconds) then the velocity boundary layer predicted thickness is closer to 100mm, with a corresponding flattening of the temperature profile, which reflects the time-averaged results of test 19. The instability of the boundary layer and the numerous eddies forming and entraining warm liquid into the bulk fluid are not captured by the simulation. A significant portion of the instability observed in tests may be attributable to variations in the thermal boundary conditions, which give rise to instability in the flow patterns. It is unclear whether the model is accurately capturing the extent to which turbulence is present in the flow. Further work should focus on creating conditions with static boundary conditions, to provide for a meaningful quantitative comparison with the simulation.

5.3 References

ANSYS Inc., 2013. *ANSYS CFX-Solver Theory Guide,* Canonsburg, PA: s.n.

Burns, A., Frank, T., Hamill, I. & Shi, J.-M., 2004. *The Favre Averaged Drag Model for Turbulent Dispersion in Eulerian Multi-Phase Flows.* Yokohama, Japan, s.n.

Cole, R., 1960. A photographic study of pool boiling in the region of the critical heat flux. *AIChE J.*, 6 (4).

D'Aulisa, A. et al., 2014. CFD Modeling of LPG Vessels Under Fire Exposure Conditions. *AIChE J., 60,* p. 4292–4305.

Egorov, Y. & Menter, F., 2004. *Experimental implementation of the RPI boiling model in CFX-5.6,* s.l.: Technical Report ANSYS / TR-04-10.

Ishii, M. & Zuber, N., 1979. Drag Coefficient and Relative Velocity in Bubbly, Droplet or Particulate Flows. *AIChE J., 25,* pp. 843-855.

Krepper, E., Koncar, B. & Egorov, Y., 2007. CFD modelling of subcooled boiling- Concept, validation and application to fuel assembly design. *Nuclear Engineering and Design,* Volume 237.

Krepper, E., Rzehak, R., Lifante, C. & Frank, T., 2013. CFD for subcooled flow boiling: Coupling wall boiling and population balance models. *Nuclear Engineering and Design,* Volume 255.

Launder, B. E. & Spalding, D. B., 1974. The Numerical Computation of Turbulent Flows. *Computer Methods in Applied Mechanics and Engineering 3,* p. 269–289.

Lemmert, M. & Chawla, J. M., 1977. Influence of flow velocity on surface boiling heat transfer coefficient. *Heat Transfer in Boiling,* Volume 237.

Ranz, W. & Marshall, W., 1952. Evaporation from drops. *Chem. Eng. Progr. 48 (3),* p. 141–146.

Sato, Y., Sadatomi, M. & Sekoguchi, K., 1981. Momentum and heat transfer in two-phase bubbly flow. *International Journal of Multiphase Flow,* Volume 7.

Tolubinsky, V. I. & Kostanchuk, D. M., 1970. Vapour bubbles growth rate and heat transfer intensity at subcooled water boiling. *Heat Transfer,* Volume 5.

6 CONCLUSIONS

A review of experiments and modelling techniques of pressure vessel during fire concluded that in order to make substantial improvements in our ability to model vessel fire response, it is necessary to develop a robust numerical model and to obtain further experimental data for validation.

The aims of the current study were to design test apparatus capable of generating data suitable for validating numerical models, and to use this equipment to generate a substantial body of test evidence suitable for development and validation of improved models. A secondary aim was to investigate the potential of the Eulerian-Eulerian multiphase model with the RPI wall boiling model as a basis for future numerical model development.

6.1 Test equipment design

In advance of test equipment design, a review of existing vessel tests and pool fire conditions concluded that the following thermal boundary conditions are representative of a medium-large open hydrocarbon pool fire:

- Net heat flux to the vessel of 80-120 kW/m^2 (preferably >100 kW/m^2 to be conservative)
- Minimum radiative fraction to a cool object of 0.7
- Full engulfment in flame
- Sufficient uniformity of heating to ensure all parts of an empty vessel are capable of reaching a minimum temperature of 700°C
- Use of a propane or butane burner arrangement to allow control over the degree of engulfment, rapid start-up and rapid termination of the test.
- Calibration testing prior to actual vessel test to assess the net heat flux to the vessel and the degree of uniformity
- Reasonable resistance to wind effects, or wind effects quantified and limitations applied to test conditions.

The test apparatus has allowed for unprecedented characterisation of the thermohydraulic behaviour of fluids within a pressure vessel during fire engulfment on an industrial-scale. The unique full-bore glass window, with a pressure equalisation system to ensure window integrity, has permitted PIV measurements to be obtained within a full-scale vessel during fire engulfment for the first time.

The equipment is re-configurable and re-usable. It has partially achieved the aim of demonstrating the capability of accurately characterising the thermohydraulic behaviour of fluid inside a vessel, while showing potential for achieving

significantly better data through refinements to the instrumentation and techniques used. Numerous recommendations have been made relating to this (see section 7).

Results have already provided insight into the thermohydraulic behaviour of full-containment vessels with water as a test fluid, highlighting the importance of adequately accounting for bubbly flow effects and wall boiling within simulations.

6.2 Fire characterisation

A novel methodology has been described to quantify the fire conditions used to test hazardous materials pressure vessels. The method uses data from directional flame thermometers, a water-cooled calorimeter, and a thermal imaging camera. It brings an improvement over previous methods in being able to calculate both the flame temperature and emissivity independently. It can also be used to confirm that the fire total heat flux to a cool surface and the radiation fraction for that heat flux is in an acceptable range when using liquid propane burners to simulate a liquid hydrocarbon pool fire. There is some uncertainty in the analysis, which should be considered when using the method, and further validation is also needed.

Characterisation of the fires across season one and two showed a significant variability in the flame engulfment and heat flux to the vessel. In comparison with the target conditions, the average flame emissivity and radiative fraction are lower than desired, as evident from DFT temperatures of approximately 830^{o}C. It is expected that a DFT temperature of around 870^{o}C is required to achieve a radiative fraction of 0.8. This is likely to be realised through an increase in the flame thickness. Further work should improve the thermal boundary conditions, either by improved burner design or by replacing the fire with an alternative heating source (e.g., radiant panels or electrical heating).

6.3 Generation of fluid behaviour data

Regrettably, limited success has been achieved relating to the second primary aim of generating an extensive dataset for numerical model validation. Time constraints, combined with operator error, prematurely ended the second test season before pressurised tests with PIV and de-aerated fluid or fluids other than water could be performed. However, the equipment has proven to be capable of operating 3 tests a day, demonstrating the potential for productivity during future work.

Unfortunately, the fires generated in the current study were incompatible with the level of consistency needed to perform quantitative comparisons with numerical models. The dataset generated within the current study is therefore of limited value for simulation validation at the present time. Further data with tightly controlled boundary conditions is

required to assess the performance of specific aspects of the model. It is hoped that future models may benefit from comparison with data generated during the current study, to assess the difference between idealised boundary conditions and variable boundary conditions. The data contained within this study could be re-assessed to create thermal boundary condition profiles that vary with time.

Despite the variability in thermal boundary conditions, the data and observations generated during the current study have given a deeper understanding of the fluid behaviour during fire engulfment. Insight into boundary layer thickness, regions of instability, the presence of eddies, the influence of boiling, and the mechanisms by which the bulk fluid heats have been gained.

It is concluded that modelling the pressure rise as the vapour saturation pressure of the liquid surface temperature, and that modelling the liquid surface temperature in terms of natural convection, does not capture all significant mechanisms that drive pressurisation. Even when the natural convection model is robust, for example using 3D CFD simulations, it cannot explain the variation in pressurisation rate observed between the tests in the current study and other tests in literature. Wall-boiling and radiative heating of the vapour and liquid surface are proposed as phenomena which may have significant influence on the rate of pressurisation. Further work is recommended to study their influence.

6.4 Heat transfer and boundary layer correlations

The current study has highlighted the complexity of the thermohydraulic processes occurring within a pressure vessel exposed to fire. The phenomena of turbulent free convection and partial nucleate pool boiling have been extensively studied. However, the interaction between the two under the conditions experienced in pressure vessels containing a subcooled liquid remains poorly understood.

Analysis of the test data has led to recommendations on correlations for Nusselt number to express the heat transfer coefficient. It is concluded that a modification to the correlation proposed by Schmidt (1956) to include the vessel diameter and fill level gives an improvement on existing correlations for the water and ethanol tests conducted with the current study. The modified correlation has the form:

$$Nu = 0.178\, Ra^{*0.257}$$

Where a modified Rayleigh number is used as described in equation 4.3 to remove the unknown temperature term (following the method proposed by Lienhard & Lienhard (2017)).

It is concluded that a dimensionless profile based on a logarithmic relationship can give a reasonable prediction of the thermal boundary layer profile over the turbulent outer region of the thermal boundary layer and extending into the bulk fluid. The dimensionless form of the profile is:

$$\theta^x = C \ln (y^x) + D$$

where values for constants C and D have been proposed related to the fluid Prandtl number and the vessel dimensions. The method of non-dimensionalising the data proposed by Hoelling & Herwig (2005) is recommended due to it being based on fluid properties and avoiding use of the wall shear stress, which is difficult to discern with accuracy.

No conclusions can be drawn within the near-wall thermal boundary layer due to limitations in equipment design. Further work is needed to understand the effect that the geometry of the vessel has on the thermal and velocity profiles in the boundary layers, at a range of void fractions. Further work is required to characterise the region close to the wall in more detail (within 1 mm for temperature profiles and within 5 mm for velocity profiles) to allow for improved wall functions to be developed. Recommendations to this effect are given in section 7.

It is concluded that the velocity boundary layer profiles are poorly predicted by existing dimensionless relationships. It is recommended that existing dimensionless correlations for velocity boundary layer thickness are not used for modelling purposes, with emphasis placed on obtaining actual test data, until further work is conducted and an improved velocity boundary layer profile can be established.

6.5 Boiling analysis

The heat flux partition method was applied to the subcooled water pool boiling scenario present in the current study, requiring description of key bubble characteristics for modelling purposes. It is concluded that the most commonly applied sub-models (i.e., the default models in ANSYS CFX and Fluent) for bubble departure diameter, departure frequency and nucleation site density did not give a good match with the measured values.

It is concluded that the existing sub-models that give the best match with the experimental data of the current study are those for nucleation site density *N*, bubble departure diameter *D*, and departure frequency *f* by Kocamustafaogullari & Ishii (1983), Unal (1976) and Petrovic, et al., (2004), respectively.

Alternative combinations that give reasonable results are Lemmert & Chawla (1977), Tolubinsky & Kostanchuk (1970) and Petrovic, et al., (2004), or Kocamustafaogullari & Ishii (1983), Tolubinsky & Kostanchuk (1970) and Petrovic, et al., (2004).

6.6 Numerical modelling

A two-dimensional simulation of water in a 50% fill configuration has been set-up in CFX using two different configurations of boiling parameters. A base case used default bubble characteristic properties and a modified case used values measured during the current study. A grid independence study was performed, showing good agreement between the three grids.

The base case simulation showed reasonable agreement with measured temperature values, given the limitations of the instrumentation used and uncertainties over the accuracy of stated distances from the wall. Both simulations showed a lower rate of temperature change in the region 1-10 mm from the wall than captured by the experiments. Improved instrumentation may result in a better match between experimental data and simulation results, however it is probable that further refinement of the model is necessary. Alternative wall functions may improve simulation results. Examples of modified wall temperature profiles include those proposed in section 4.5.1, and which would likely result in a higher rate of initial temperature decrease. The degree to which boiling occurs was shown to have a significant effect on the temperature and velocity profiles through comparison of the base case and the modified case.

The velocity profile shows an intermittent good agreement with measured values. However, given the variability in experimental data this must not be considered a validation of the results. Further data should be obtained. Overall, the simulations show a much more stable system, with no eddies forming on a significant scale at the edge of the boundary layer and the region of instability at the bottom of the vessel settling into a main plume centrally located. This may be attributed to the stability of the boundary conditions in the simulation (in contrast to the variability in the thermal boundary conditions in the experimental programme). Improving the stability of experimental boundary conditions is expected to reduce the system instability, but no conclusions can be drawn at present on whether the simulations are accurately capturing the bubble-induced turbulence, or whether eddies would be present to the same size and in the same number with a more stable system.

The turbulence model must be considered in view of the bubble influence on the flow, and alternative models tested. Turbulence models that do not require the use of wall functions (such as the k-ω SST model) are recommended for further study.

The vapour void fraction predicted by simulations cannot be compared against experimental values due to limitations in the instrumentation in the current study. Further work should include void fraction measurements to determine whether vapour volume fraction measurements are reasonable, and in turn whether the quantity of vapour reaching the liquid surface in bubbles makes a significant contribution to the rate of pressure rise. Calculations of theoretical void fractions

and bubble condensation rates indicate the vapour contribution to be minimal. However, this is contradicted by visual observations of numerous bubbles being present in the flow after 120 seconds. Future work should investigate bulk fluid vapour volume fraction in more detail, and ensure adequate de-aeration of all test fluid prior to commencement.

Further numerical modelling studies should perform comparisons between the bubble characteristic sub-model combinations described in section 6.5 and the default options found within ANSYS CFX or Fluent. The use of constant bubble characteristics based on experimental values measured by averaging over a time-window within the test was found to give simulation results that match poorly with the measured temperature profiles. It is possible that the use of fixed values may artificially enforce heat transfer due to phase change at the wall before the wall temperature reaches a sufficiently high value for boiling to occur in practice. Increased measurement of bubble properties is recommended for future work to allow them to be expressed as functions of the wall superheat and implemented as user-defined functions. Alternatively, the large thermal boundary layers predicted in the simulation may be prevented from occurring in practice due to the variability of the thermal boundary conditions causing eddies and unsteady flow effects that act to reduce the boundary layer thickness. Future work must prioritise improvement in application of stable thermal boundary conditions if a quantitative comparison is to be made with the numerical model.

Overall, it is concluded that the approach described in the current study has demonstrated potential for future improvements in simulation capabilities of pressure vessels. An improvement over the default model set-up has not been achieved within the current study, however numerous recommendations are given as means of improving correlation with future test data. There is cause for optimism that the boundary layers can be adequately predicted, which would imply that thermal stratification can be adequately predicted. Further work should compare modifications to the model to determine the settings that provide the best correlation with experimental data obtained from the equipment.

6.7 Summary of performance against objectives

In assessing the performance of the current study against the main project objectives, it is concluded that:

- Test equipment has been successfully designed, built and used to characterise the thermohydraulic behaviour inside a pressure vessel in fire. Although limited success has been achieved in resolving flow characteristics and boundary layer properties, the equipment shows promise for significant improvements in characterisation during future work through improvements to instrumentation.
- Limited success has been made in generating data suitable for validation of numerical models. Variations in thermal boundary conditions have been too great, and the tests performed have been limited to fluids that are

liquid at ambient temperature and pressure. However, the productivity and potential of the equipment has been demonstrated, with recommendations given to generate suitable data in future work.

- Some success has been achieved in assessing the potential of the Eu-Eu multiphase modelling approach with the RPI wall boiling model as a future platform for simulation of pressure vessels. The basic model has reasonably recreated the boundary layer data measured during experiments, and grid independence has been demonstrated. Experimentally derived bubble characteristics did not give an improvement over the default bubble characteristic models within CFX, however recommendations have been made for use of alternative sub-models and for the capture and implementation of experimental values in future work. Differences in thermal boundary conditions prevent more detailed comparisons of velocity profiles, temperature profiles and pressurisation at this time. Despite this, further recommendations are given for future model improvements ahead of the generation of suitable validation test evidence.

7 RECOMMENDATIONS FOR FURTHER WORK

7.1 Practical work

The recommendations can be divided into those which can be implemented with the current test vessel, and those which should be considered if designing a new test vessel.

7.1.1 Modifications to existing test vessel and equipment (excluding instrumentation)

- A larger tube should be used to join the test ends to allow vacuum to be drawn faster without risk of creating a pressure difference across the window
- All lights and cameras should be remotely operable and capable of data download, minimising the frequency at which the tank is opened
- Additional pan/tilt heads should be sourced to permit greater flexibility of in-test measurements
- Separate power connections should be used for the LEDS, laser and cameras to allow better control of operation
- A motorised table for the laser would improve safety by allowing remote adjustments to the positioning of the light sheet
- Main flange tightening bolts should have a smooth shank and protective tape where the glass sits, to reduce chips at the hole edges
- Bolts used should be effectively greased to ease application of torque to the flange
- A camera with a wide field of view during filling would allow remote monitoring and reduce the chance of filling incidents
- All fittings used on the vessel should be of a consistent type and standard, capable of being sourced locally
- The Durasteel and Promaglaf flame shield performed excellently, however the permanent exposure to weather conditions and fire led to loss of Promaglaf from the wall, which in turn was difficult to remove from the BAM test facility water tanks and pump filters. An alternative insulation material to Promaglaf that would not cause site specific issues should be sourced
- The flame shield primary supports should be moved from the middle (close to the glass) to the outside edge, to improve working conditions and the ability to torque the flange

- The facility should be moved away from BAM test pad B to a dedicated concrete pad, where it can remain without impeding the ability of the BAM facility to use test pad B, and without the requirement of being ready to remove at short notice
- Radiant panels or electrical heating wires should be tested as alternative heat sources, to recreate a constant heat flux in a manner not subject to environmentally-induced variations

7.1.2 Modifications to instrumentation

- A dual-tip conductivity probe should be used to determine void fraction near the wall, as a means of validating boiling sub-model parameters obtained
- Thermocouples were not fixed to the wall to avoid direct conduction. However, the tank deformation was greater than expected and the distances from the wall cannot be considered accurate during a test. An alternative method of fixing to the wall that minimises conduction must be devised and implemented
- A limited number of micro-thermocouples should be used to characterise the boundary layer with better resolution
- A pressure transducer capable of sub-atmospheric pressure should be connected to the test end, to allow estimation of the residual dissolved air within the test fluid during degasification
- PIV particles should be fluorescent and a different colour to the laser light. An appropriate filter should be used to minimise the effect of light scatter at the wall

7.1.3 Modifications to future test vessel designs

- Future vessels should be constructed from stainless steel to avoid the need to protect the interior from corrosion. This would improve knowledge of the boiling surface and improve clarity of images
- A larger manway on the camera end would improve ease and precision when setting up the PIV system and cameras
- A manway on the test end should be considered, to facilitate cleaning and minor adjustment of instrumentation without the need to open the primary flange. It should include a removable support frame that would allow the flange to be opened without the need for a fork-lift truck or crane

- Feedthroughs on the test end should consist of a smaller number of larger diameter items (e.g. ¾" or 1") positioned closer to the elliptical end of the vessel
- Additional feedthroughs are required on the equipment end to provide remote control and power to equipment individually

7.1.4 Further test programmes

The premature end to season two prevented tests that combined PIV, pressurisation, and test fluid de-aeration. Further work should include all three of these aspects as standard

- All future tests should use de-aerated test fluids, either by application of a vacuum pump, or by preparation of the test fluid by appropriate means.
- The PIV set-up was shown to be functional at approximately 400 kPa (3 barg) prior to the end of the test season. Future tests should include PIV but be allowed to pressurise up to the capability of the system
- Future tests should combine PIV measurements, thermal measurements, and void fraction measurements, with the latter being used to assess boiling models implemented in numerical codes
- PIV action should be simulated to assess the magnitude of two-phase swell on PRV opening
- Different levels of subcooling should be tested, including the use of pressure liquefied gases to include very low subcooling

7.2 Modelling

The basic Eulerian-Eulerian two-fluid model described within the current study has shown potential for being able to simulate the boundary layers formed within the specific geometry of a pressure vessel. Unfortunately, boundary condition variations during the experimental programme make a detailed, quantitative comparison redundant at this time. Further work should be invested in improving the test data available, however there are still improvements that can be made to the vessel model itself, ahead of future a-priori studies.

7.2.1 Grid refinement

The current study has demonstrated grid independence, especially in the near-wall region. However, the current grid did not seek to resolve the boundary layer to avoid an unrealistic vapour volume fraction. ANSYS recommend at least 10 cells within the boundary layer to resolve it effectively (e.g., a $y^+<30$), which would imply a grid density of approximately 10 to 20 times greater in the inflation layer than that used in the simulation. Full resolution of the boundary layer would require the near wall cell to fall within the viscous sub-layer ($y^+<5$).

Future grids should investigate the smallest near-wall control volume size that permits convergence, and perform a grid independence study that assesses the influence of the inflation layer independently.

7.2.2 Turbulence model

The use of refined grids near the wall should be accompanied by the SST k-ω turbulence model, which has been successfully used by numerous authors in subcooled boiling studies (see section 2.3). It is a blend of the k-ω model near the wall and the k-ε model in the outer part of the boundary layer and the bulk fluid. It is capable of resolving the whole boundary layer up to the wall.

The contribution of the vapour phase to the turbulence should also be investigated once vapour void fraction data is available. In addition to the enhanced eddy viscosity approach used in the current study, some researchers have successfully included contribution terms directly in the governing equations.

7.2.3 Fluid properties

The current model used fixed fluid properties to reduce the likelihood of convergence issues (typically occurring with high vapour volume fractions in the near-wall cells). Future work should investigate the stability of the model when variable fluid properties are enabled.

7.2.4 Boiling model

The RPI model is well-established as a platform for modelling wall boiling, however it is known to be highly dependent on the sub-models used for bubble characteristics to achieve accurate results. The simulation should be repeated with the alternative combinations of sub-models for nucleation site density, departure frequency and departure diameter as discussed in section 4.6.5. In particular, it is recommended that simulations use a combination of models by Kocamustafaogullari & Ishii (1983) for N, Petrovic, et al., (2004) for f, and both Tolubinsky & Kostanchuk (1970) and Unal (1976) for D_b.

Experimental values for bubble characteristics should be increased, and the results used to develop models relating the characteristics to the degree of wall superheating, to ensure models can accommodate the possibility of boiling cycles.

Some researchers have implemented multiple size group models to accommodate a range of bubble diameters within the flow. Further work should assess the effect such results have on the simulation output for different degrees of subcooling (as the effect may be insignificant at high degrees of subcooling, given the expected rapid condensation of most bubbles).

7.2.5 Non-drag force models

The basic model described herein did not include models for the lift force (a shear induced force that acts to push bubbles towards the wall) or the wall lubrication force (that acts to push it away). Accurate specification of these forces is important in getting a realistic vapour volume fraction in the near-wall grid cells. Future simulations should enable the non-drag force models and compare the results with void fraction data obtained from further experiments

7.2.6 Recommendations for development of simplified models

Non-numerical models, such as zone models or integral models, typically require the implementation of empirical parameters that are derived from experiments of validated numerical models, as a means of simplifying and capturing the complex interactions and phenomena that take place within the vessel.

Simplified model improvements since the advent of multi-zone models in the early 1980s have focussed on capturing the rate of growth of the hot, stratified fluid layer.

Experimental work in this study has shown that the heat transfer to the cool bulk fluid can be described by four main mechanisms. It is proposed that a simplified model be investigated to assess the rate of heat transfer from the boundary to the bulk, via the following mechanisms:

1. Convection at the bottom of the vessel in the region of instabilities and plumes, simulated by correlations of convection on an upward horizontal plate
2. Bubble condensation within the bulk fluid, based on the heat flux partitioning wall boiling model and established bubble velocity and condensation rate equations
3. Heat transfer from the boundary to the bulk by turbulent action, simulated by a turbulent conduction method
4. Heat transfer from the fluid surface down to the bulk by convection

The inclusion of a wall boiling model based on the heat flux partitioning model could also predict the contribution of vapour escaping from the liquid surface to the pressurisation rate. It remains unclear whether there is a significant contribution to the pressure rise caused by the direct addition of vapour molecules to the vapour space, particularly when there is a high degree of subcooling. This should be addressed in further work.

8 APPENDICES

8.1 APPENDIX 1 – Directional flame thermometer construction and conduction losses

8.1.1 Statement of contribution

The directional flame thermometers were designed and supplied by Queen's University, Ontario, Canada.

8.1.2 Description

The directional flame thermometers were designed to withstand temperatures of 1100°C for a period of 15 minutes. The design aimed to give the instruments sight of the fire in a hemispherical direction.

They consisted of a Type K thermocouple centrally attached to the rear-surface of fire-facing steel plate. Rear-surface ceramic blanket insulation (Promaglaf in the current study) ensured the instrument reaches a temperature close to the black-body equivalent fire temperature in the hemispherical direction viewed by the instrument.

The plate used was carbon steel at 0.3 mm thick. The front plate dimensions were 80mm x 80mm (excluding the lower lip for fixing screws). To permit assembly, the steel plate was wrapped around the edges of the insulation to allow it to be attached to a rear surface. It is recognized that this increases the field-of-view of the instrument beyond truly hemispherical, however, the inaccuracy introduced is considered acceptable given the uncertainty in the subject of measurement (i.e. the fire).

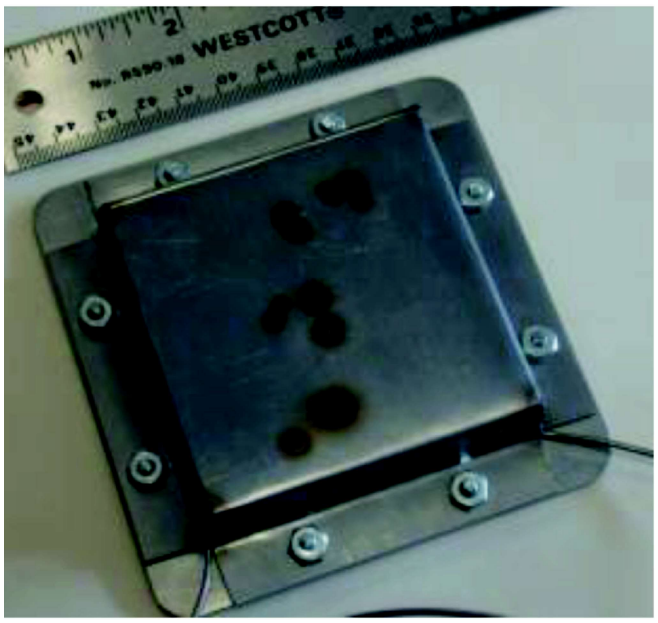

Figure 120 – Directional flame thermometer

8.1.3 DFT conduction losses study

An estimate of the heat lost by conduction through the ceramic blanket is given below. A simulation through a cross-section of the DFT was performed using a set of first-order backward (implicit) finite difference equations solved simultaneously. Iteration was used to achieve convergence across temperature varying material properties and to handle radiation exchange at surfaces. The basic equation for a node, j, exposed to radiative, convective and conductive heat exchange with surrounding nodes I,k,m,n is given by equation 1.

$$\left(\frac{1}{R_{ij}}+\frac{1}{R_{kj}}+\frac{1}{R_{nj}}+\frac{1}{R_{mj}}+hA_i+hA_k+hA_m+hA_n+A_i\sigma\varepsilon_s T_j^3+A_k\sigma\varepsilon_s T_j^3+A_m\sigma\varepsilon_s T_j^3+A_n\sigma\varepsilon_s T_j^3\right)T_j =$$
$$\left(\frac{1}{R_{ij}}\right)T_i+\left(\frac{1}{R_{kj}}\right)T_k+\left(\frac{1}{R_{mj}}\right)T_m+\left(\frac{1}{R_{nj}}\right)T_n+A_ihT_g+A_khT_g+A_mhT_g+A_nhT_g+$$
$$A_i\sigma\varepsilon_f\varepsilon_s T_f^4+A_k\sigma\varepsilon_f\varepsilon_s T_f^4+A_m\sigma\varepsilon_f\varepsilon_s T_f^4+A_n\sigma\varepsilon_f\varepsilon_s T_f^4 \quad [+Aq_{constant}]$$

The geometry of the DFT cross-section was recreated as shown in Figure 121.

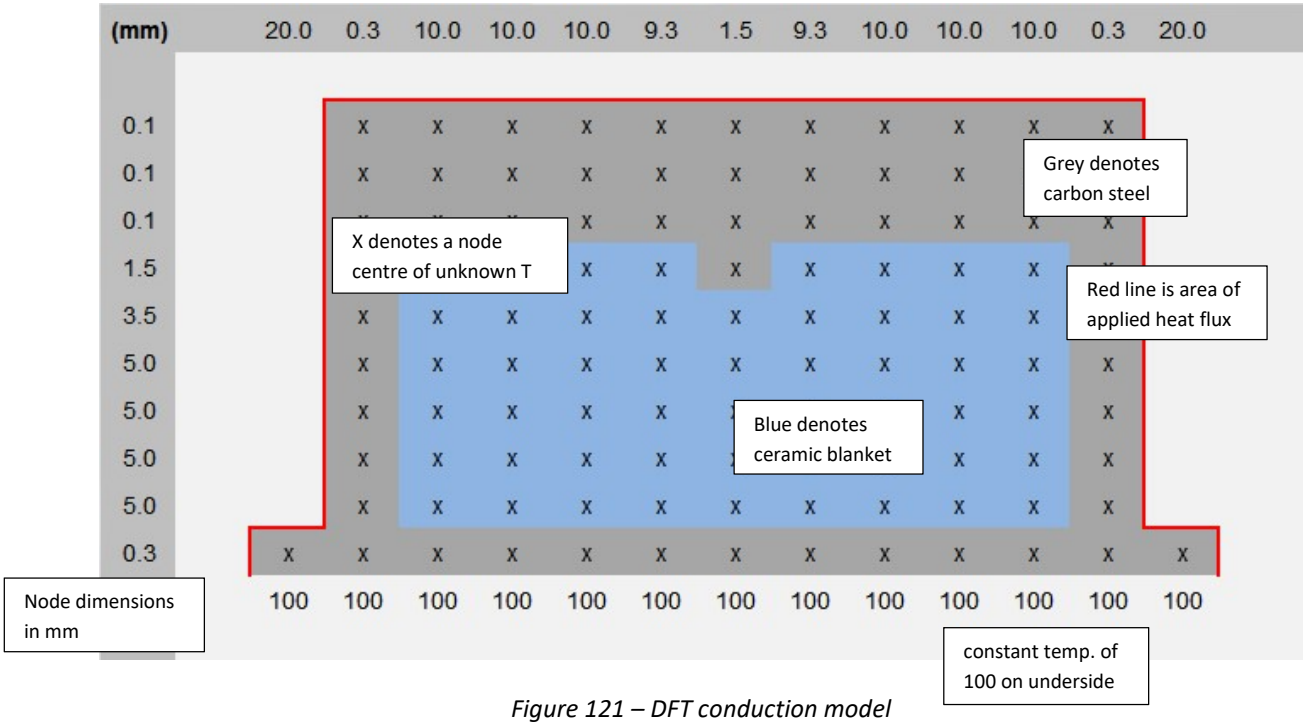

Figure 121 – DFT conduction model

The ceramic blanket material properties used in the simulation are given in Table 44. The carbon steel properties can be found in Eurocode 3: Design of steel structures - Part 1-2: General rules -Structural fire design (1993). A surface emissivity of 0.85 was used for the steel.

Table 44 - Ceramic blanket material properties

Temperature (°C)	Thermal conductivity (W/m.K)	Density (kg/m3)	Specific heat (J/kg.K)
0	0.0	128	1130
100	0.0	128	1130
200	0.1	128	1130
300	0.1	128	1130
400	0.1	128	1130
500	0.1	128	1130
600	0.2	128	1130
800	0.2	128	1130
1200	0.4	128	1130
1300	0.4	128	1130

Results

The simulation was run with two heating regimes and three back-face temperatures. The results of the six permutations are given in Table 45. Figure 122 shows an example output from a simulation (with heating regime 2 from table 45). The TC temperatures are taken from the metallic node at the top of the ceramic insulation. The simulations indicate that the TC readings will under-estimate the blackbody equivalent surface temperature by 1-2%.

Table 45 – DFT simulation results

	Heating Regime 1	**-Heating Regime 2**
	T_f: 1100°C, ε_f 0.3, h 30 W/m^{2}K	T_f: 1100°C, ε_f 0.4, h 25 W/m^{2}K
Net flux to a cool object	93	102
Steady state temperature of an adiabatic surface	788	844
Back-face temperature	**TC temperature**	
100°C	774	830
300°C	776	832
500°C	779	835

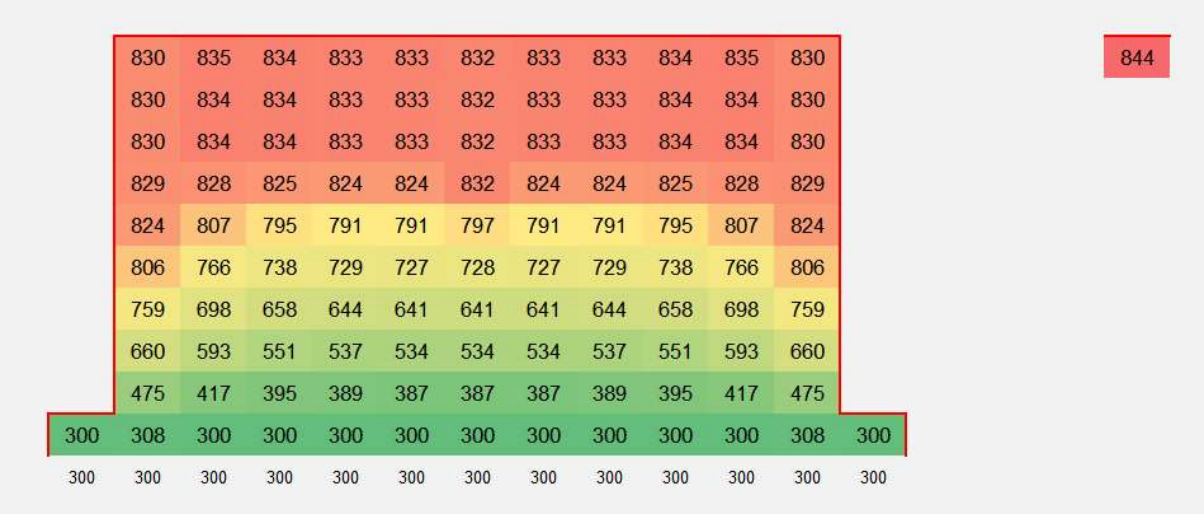

Figure 122 – 2D Conduction study of DFT

8.2 APPENDIX 2 – Pressure compensation system

8.2.1 Statement of contribution

The pressure compensation system was designed, sourced, built and initially tested by Queen's University, Ontario.

8.2.2 Equipment

The pressure compensation system was assembled from the following equipment:

- ¾ inch ball valve with air actuator for on/off control of air flow into tank
- ¾ inch ball valve with air actuator for on/off control of air flow out of tank
- -2.5 to + 2.5 psig differential pressure transducer
- 0-500 psig pressure transducer for tank pressure
- 0-500 psig pressure transducer for air supply pressure
- A National Instruments (NI) USB 6341 data acquisition and control (DAC) system to monitor and control tank pressure and control opening and closing of valves
- A Windows 10 PC to run the DAC
- 9 Barg air or nitrogen supply to fill tank and for driving valves

The system also uses the following wires for power and control.

- 5 V for control of valve 1 (from DAC)
- 5 V for control of valve 2 (from DAC)
- 240 V 50 Hz AC power for valve solenoids
- 10-28 V DC for three pressure transducers

Figure 123 shows the power box, with the following cables:

- black 240 V supply
- black switched 240 V, one to each valve solenoid
- blue Ethernet wire to two relays for control of two valves

Figure 124 and Figure 125 show the data acquisition system and ethernet box, respectively, with cables relaying signals from the three pressure transducers and controlling the two relays. Figure 126 shows the ball valves used. Figure 127 shows the differential pressure transducer and the vessel test end pressure transducer.

8.2.3 System tuning

The minimum change in pressure on opening of the vent or fill valves is determined by the capacity of the connecting pipes and the opening and closing time of the valves, which is affected by the supply pressure. A supply pressure of 9 barg was found to give an open and closing time of 0.5 seconds.

Reductions in pressure change can be further affected by using restrictors in the pipework. Pipe of a range of diameters were tested to allow the minimum pressure rise per valve cycle to be adjusted according to the expected rate of pressure rise in the tank.

Figure 123 – Control box

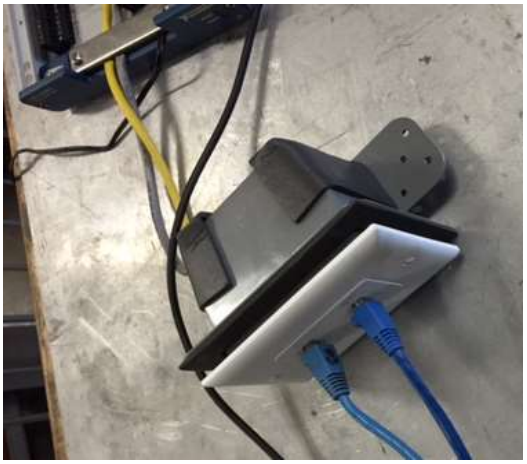

Figure 125 – Connection box

Figure 124 – DAC

Figure 127 – Directional pressure transducer

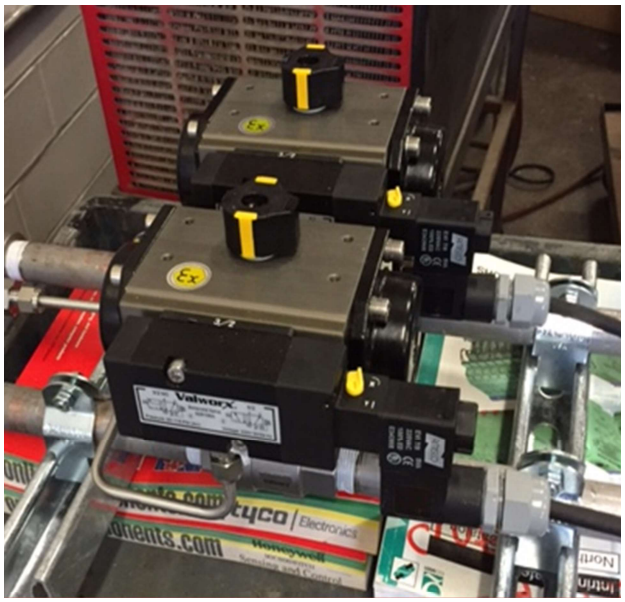

Figure 126 – Control valves

8.3 APPENDIX 3 - PIV scale calculations

During post-processing of PIV images, it proved impossible to obtain a scale from the series of chalk guidelines made in the tank for that purpose. The chalk line was not visible on the monochrome Flea 3 cameras.

The scale was instead determined from the curvature of the illuminated arc, where the laser sheet hit the wall. The known radius of the tank can be related to the chord length forming a segment with the arc by equation A3.1.

$$R = \frac{h}{2} + \frac{c^2}{8h} \qquad (A3.1)$$

Where

R is the radius of the tank, equal to 500.5mm

h is the segment height

c is the chord length

By measuring *h* and *c* overlaid on an image (see Figure 128 for an indicative example), and expressing *c* as a multiple of *h*, both unknowns in equation 1 can be determined. The accuracy of this method is estimated at +/- 4%, based on a range of possible chords drawn on an image from test 19 to test the sensitivity to chord subjectivity. It should be noted that the camera was not exactly perpendicular to the laser sheet, despite efforts to achieve this. Distortion effects have not been accounted for but will be present, resulting in an unquantified degree of additional inaccuracy in the calculation.

Once a chord length has been determined, it is used to scale an image. The results of this calculation are given in Table 46 for tests that generated PIV data suitable for analysis.

Table 46 – PIV images scale

Test	Flea3 Camera	Image size (pixels w x h)	Pixel equivalent size (mm)
15 & 16	1	1600 x 1200	0.31
16	2	1920 x 1080	0.35
19 & 22	1	1600 x 1200	0.37
19 & 22	2	1920 x 1080	0.45

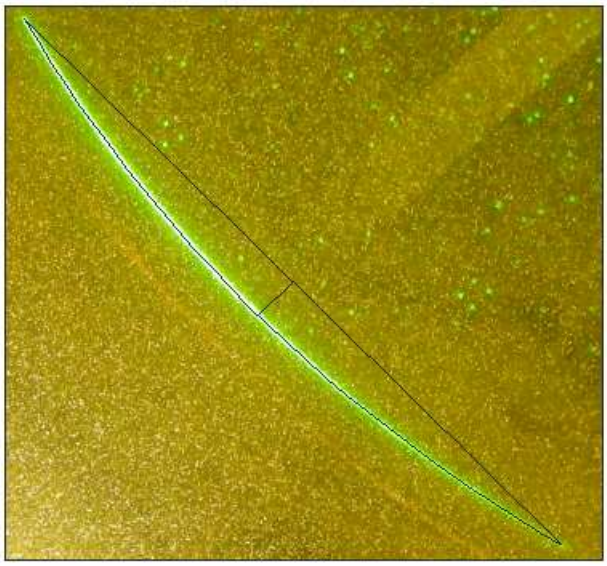

Figure 128 – PIV scale image

8.4 APPENDIX 4 – Relevant IR thermography theory

An infrared camera measures the radiance of an emitter over an area defined by the field of view and pixel size. Each pixel is, in effect, a separate measurement. The camera converts the measured radiance to that of the object being viewed by considering the emissivity of the object, the transmissivity of the atmosphere and any correction due to temperature change in the camera. The basic formula for this is:

$$I_{measured} = I\left(T_{obj}\right).\tau.\varepsilon + \mathrm{I}(T_{sur}).(1-\varepsilon).\tau + I(T_{atm}).(1-\tau) \quad \text{(A4.1)}$$

where:

τ is the transmissivity

ε is the emissivity

T is temperature (K)

I is the radiance (W/m2.sr)

The camera lens defines the solid angle through which the radiation is received, and therefore radiance is independent of the view factor of the emitter to the camera, so long as the emitter surface is not smaller than the resolution of a pixel.

IR cameras are typically calibrated against the object designed to exhibit effective black body behaviour, at a range of temperatures suitable for the camera range. The camera temperature range and focal length must be set by the user prior to measurements being taken. The surface emissivity and atmospheric transmissivity can be adjusted after recording in accompanying software.

The radiation from flames can be approximated as the radiation from a volume of gas of appropriate emissivity. Radiation from gases is a function of the absorptivity of the gas and the radiation path length (the thickness of the gas). The absorptivity of a flame can be approximated using Beers law of exponential decay as:

$$\alpha_\lambda = 1 - e^{-\kappa_\lambda L} \quad \text{(A4.2)}$$

Where:

α is the absorptivity (assumed equal to the emissivity)

κ is the absorption coefficient (1/m)

L is the thickness of the flame

Assuming the flames exhibits grey behaviour (having a spectral emissivity and absorption that is independent of the wavelength, λ) and that Kirchhoff's law is applicable (in its most simplistic form, the emissivity is equal to the absorptivity), the flame emissivity as seen by the IR camera can be described as:

$$\varepsilon_{fire-line} = 1 - \mathrm{e}^{-\kappa \mathrm{L}} \tag{A4.3}$$

In instances where the flame is adjoining a surface, the above is valid for a hemisphere of gas radiating to the surface. When the geometry of the flame cannot be approximated as a hemisphere, the mean beam length concept must be used. This provides a correlation for gas emissivity when applied to alternative geometries, replacing L with L_e. For radiation between two infinite parallel planes (which is closest to the flame-calorimeter interaction described in the present study):

$L_e = 1.8\ L$ (Bergman, et al., 2011)

The flame emissivity as seen by an object adjoining the flame can, therefore, be approximated as:

$$\varepsilon_{fire-vol} = 1 - e^{-\kappa\ 1.8L} \tag{A4.4}$$

The radiant energy emitted from a fire can be given by:

$$q'' = \varepsilon_{gas}\sigma T_{gas}^4 \tag{A4.5}$$

where the gas emissivity is determined from either equation A4.3 or A4.4, as appropriate.